Thermophysical properties of liquid Ti-Al-V alloys under oxygen influence

Von der Fakultät für Georessourcen und Materialtechnik der Rheinisch-Westfälischen Technischen Hochschule Aachen

zur Erlangung des akademischen Grades eines

Doktors der Ingenieurswissenschaften

genehmigte Dissertation

vorgelegt von

Benedikt Reiplinger, M.Sc.

Berichter: Herr PD Dr. rer. nat. Jürgen Brillo

Herr Univ.-Prof. Dr.-Ing. Andreas Bührig-Polaczek

Tag der mündlichen Prüfung: 07.08.2025

Diese Dissertation ist auf den Internetseiten der Universitätsbibliothek online verfügbar

Abstract

In this work, reliable systematic thermophysical property data on density and surface tension under the influence of oxygen is presented for pure liquid aluminum, titanium and vanadium, for the liquid binary alloys Al-Ti, Al-V and Ti-V as well as for one section through the ternary Al-Ti-V system. Compiling this data serves three distinct purposes. Firstly, the foundation of a thermophysical data base for the ternary Al-Ti-V is laid. Secondly, this thermophysical data helps gaining a fundamental insight into the general mixing behavior in this widely used alloy system. Lastly, the obtained data is investigated under the influence of oxygen both to reassess the validity of the previously developed data foundation and to understand the fundamental interaction of oxygen with the liquid Al-Ti-V system and liquid metals in general. To provide appropriate experimental techniques for both density and surface tension measurements, a new, specialized electromagnetic levitation furnace (EML) is constructed. Electromagnetic levitation is a container-less measurement technique which circumvents many experimental challenges associated with traditional container-based measurement methods when investigating highly reactive metal melts such as the liquid Al-Ti-V system. With the EML, the Al-Ti-V samples can be processed without the risk of contamination, allowing for a higher undercooling and higher measurement precision. Combining the well-established EML setup with a heating laser as well as a novel oxygen control system (OCS) allows for highly precise measurements of the thermophysical properties under the influence of oxygen by changing the oxygen partial pressure present in the process atmosphere during the experiment.

Density and surface tension are measured as a function of temperature for the pure components, the Al-V and the Ti-V system as well as for one ternary $Al_xTi_{(1-x)0.5}V_{(1-x)0.5}$ section. From the temperature dependent measurements, the compositional dependence of the density and surface tension can be determined for all different sub-systems. Using this approach, a comprehensive dataset was generated for the Al-Ti-V system, considering previous investigations. Subsequently, different established thermodynamic models for the binary systems were compared against the measured data. The results were then used to gain a more fundamental insight into the general mixing mechanisms, including segregation, of the three elements. Evaluating different thermodynamic models against the obtained data allows for an optimized prediction of the thermophysical properties of the binary, liquid sub-systems. The groundwork for an equally comprehensive prediction capability for the complete Al-Ti-V system, was set by exemplary expanding the established models by the ternary $Al_xTi_{(1-x)0.5}V_{(1-x)0.5}$ section.

The OCS is the key instrument to evaluate the influence of oxygen on the thermophysical properties of the Al-Ti-V system. To fully understand the operation principles of the OCS, for which an instrument similar in construction is also intended to expand the EML facility onboard the international space station (ISS), several system investigations were carried out. These lay the foundation for future research involving the OCS on earth and on board the ISS. After successfully integrating the OCS to the EML furnace on ground and establishing a general understanding of its operation, first oxygen dependent measurements were carried out for pure liquid vanadium. The oxygen influence was exemplary investigated on pure liquid vanadium in two different ways. First, the oxygen partial pressure of the process atmosphere was adjusted while simultaneously measuring the surface tension. Subsequently, the oxygen mole fraction of the measured sample was changed by adding oxide powder to the pure vanadium during sample preparation. The results were used to reevaluate the previous thermophysical property measurements against the background of oxygen influence and to gain first insights into the interaction mechanisms between liquid vanadium and oxygen. The first oxygen dependent measurements confirm the reliability of the developed thermophysical database and the prediction quality of the employed models. For liquid vanadium oxygen has only a minor influence on the surface tension for comparably high oxygen concentrations of up to 1 at.-%. Strong similarities can be found in this regard when comparing liquid vanadium with liquid titanium. The vast differences in the interaction with oxygen of liquid vanadium (liquid titanium respectively) and liquid aluminum opens up many exciting research possibilities.

Kurzfassung

Diese Arbeit liefert systematische, temperatur- und kompositionsabhängige Daten zu Dichte und Oberflächenspannung unter dem Einfluss von Sauerstoff für pures flüssiges Aluminium, Titan, Vanadium, die binären Subsysteme Ti-V und Al-V sowie für einen Schnitt durch das ternäre Al-Ti-V System. Dabei werden drei verknüpfte Ziele verfolgt um ein besseres Verständnis für das flüssige Al-Ti-V System zu erlangen. Zunächst soll eine verlässliche und umfassende Datensammlung für das ternäre System zur Verwendung dritter erstellt werden. Zusätzlich werden die erhobenen Daten genutzt um ein tiergehendes Verständnis für das fundamentale Mischungsverhalten des Al-Ti-V Systems zu erlangen. Abschließend werden verschiedene Messmethoden etabliert um die Messdaten vor dem Hintergrund des Sauerstoffeinflusses zu evaluieren, um sowohl ihre Verlässlichkeit zu gewährleisten, als auch erste Erkenntnisse zur grundlegenden Interaktion zwischen flüssigem Al-Ti-V und Sauerstoff zu sammeln.

Bei dem Al-Ti-V System handelt es sich um ein hochschmelzendes, hochreaktives Legierungssystem. Traditionelle, tiegelbasierte Messverfahren tragen daher ein erhöhtes Risiko der Kontamination mit sich. Um diese zu umgehen wurde eine neuartige, spezialisierte elektromagnetische Levitationsanlage (EML) konstruiert und aufgebaut. Mit dem EML können hochreaktive Metallschmelzen wie das Al-Ti-V System tiegelfrei prozessiert werden, was höhere erreichbare Unterkühlungen und eine höhere Messgenauigkeit ermöglicht. In Kombination mit einem neuartigen Sauerstoffkontrollsystem (Oxygen Control System, OCS), welches eine präzise Steuerung des Sauerstoffpartialdrucks in der Prozessatmosphäre ermöglicht, sind so hochpräzise Messungen von Dichte und Oberflächenspannung unter dem Einfluss von Sauerstoff möglich.

Dichte und Oberflächenspannung wurden für die reinen Elemente, die binären Subsysteme und den Schnitt durch das ternäre System als Funktion der Temperatur und der Probenzusammensetzung gemessen. Aufbauend auf bereits existierenden Untersuchungen zum Al-Ti System konnte so eine flächendeckende Datenbasis für das flüssige Al-Ti-V System erzeugt werden. Anschließend wurden die Daten mithilfe verschiedener etablierter thermodynamischer Modelle analysiert um möglichst präzise Vorhersagen der untersuchten Eigenschaften zu ermöglichen. Gleichzeitig wurden die Ergebnisse genutzt um ein tieferes Verständnis der grundlegenden Mischungsinteraktionen innerhalb des Al-Ti-V Systems zu gewinnen.

Das OCS ist ein Schlüsselinstrument, wenn es darum geht, den Sauerstoffeinfluss auf die thermophysikalischen Eigenschaften wie Dichte und Oberflächenspannung zu untersuchen. Ein System ähnlicher Bauweise soll daher die EML-Anlage an Bord der Internationalen Raumstation (ISS) erweitern. Um die Messmöglichkeiten und -herausforderungen des OCS genauer zu untersuchen, wurden im Zuge dieser Arbeit verschiedene Systemtests durchgeführt. Nach der erfolgreichen Integration des OCS in die EML Anlage wurden anschließend exemplarische Messungen der Oberflächenspannung von flüssigem Vanadium unter verschiedenen Sauerstoffpartialdrücken durchgeführt. Neben dem Einfluss des Sauerstoffgehalts der Prozessatmosphäre wurde auch der Einfluss von Sauerstoff im Probenvolumen auf die Oberflächenspannung von flüssigem Vanadium untersucht. Dazu wurden Proben verschiedener Sauerstoffgehälter durch Legieren von reinem Vanadium mit Vanadiumoxid Pulver präpariert und anschließend im EML prozessiert. Die Ergebnisse wurden genutzt um die vorangegangenen Messergebnisse bezüglich des Sauerstoff Einflusses zu bewerten. Außerdem wurden die grundlegenden Interaktionsmechanismen zwischen Sauerstoff und flüssigem Vanadium untersucht und mit dem Verhalten der anderen Systemkomponenten Aluminium und Titan bei Anwesenheit von Sauerstoff verglichen. Die so gefundenen Ähnlichkeiten zwischen Vanadium und Titan, sowie die Unterschiede zwischen Vanadium und Aluminium in der Interaktion mit Sauerstoff, wurden genutzt um zahlreiche hochinteressante weiterführenden Forschungsmöglichkeiten zu identifizieren.

Publications

During the course of this dissertation the following papers were published:

B. Reiplinger and J. Brillo (2022) Density and excess volume of the liquid Ti-V system measured in electromagnetic levitation, *J Mater Sci,* 57, pp. 7954-7964, https://doi.org/10.1007/s10853-022-07090-

B. Reiplinger, Y. Plevachuk and J. Brillo (2022) Surface tension of liquid Ti, V and their binary alloys measured by electromagnetic levitation, *J Mater Sci,* 57, pp. 21828-21840, https://doi.org/10.1007/s10853-022-07995-y

B. Reiplinger, Y. Plevachuk and J. Brillo (2023) Experimental study of density, molar volume and surface tension of the liquid Ti-V system measured in electromagnetic levitation, *HT-HP*, 52, pp. 175-190

B. Reiplinger, Y. Seimiya, J. Brillo and S. Ozawa (2024) Density and surface tension of liquid Al,V and their binary alloys measured by electromagnetic levitation, *J Mater Sci, 59, pp. 13183-13199,* https://doi.org/10.1007/s10853-024-09951-4

Acknowledgements

First of all, I owe immense gratitude to my family, Margitte Roth-Reiplinger, Peter Reiplinger und Nicolas Reiplinger, for creating a supportive environment, which gave me the freedom to purse everything in life without the fear of failing. Thank you for every advice given, for every helping hand lend and for every sacrifice made.

Secondly, I would like to thank Tara Höcherl for providing an affectionate home to return to after work. Thank you for being my safe-haven during the last three years.

I am very grateful to PD. Dr. Jürgen Brillo for his contagious enthusiasm towards the research topic and science in general, which sparked my joy about working as a scientist. His experience and guidance during the last three years made this work possible. Thank you for the many fascinating discussions on and off topic. Thank you for giving me the opportunity, convidence and trust to visit numerous international conferences and participate in two parabolic flight campaigns.

To all my colleagues at DLR who became dear friends over the course of time and helped me with every professional and personal struggle there was, thank you very much for making the institute more than just a workplace, but a place I enjoyed coming to each and every day. Among many I would like to especially thank Asbjørn Krüger, Melanie Clozel, Dr. Gwendolyn Bracker, Katharina Dammer, Dr. Fan Yang, Dr. Elke Sondermann, Dr. Johanna Wilden, Dr. Toni Schiller, Dr. Thomas Werner and Dr. Lucas Kreuzer.

I dearly appreciate the effort and patience of the workshop team, Konstantin Afanasev, Matthias Nell, Horst Esser and Till Trompetter who were a tremendous help right from the get go of the work.

I also owe a great deal of gratitude to the Tempus Parabolic flight team, Dr. Dirk Bräuer, Dr. Mitja Beckers, Tiberius Blumberg, Dr. Georg Lohöfer and Dr. Stephan Schneider, for the constant support during and after both flight campaigns.

Last but not least I would like to thank Prof. Dr.-Ing. Andreas Bührig-Polaczek for his willingness to be the secondary referee of my work and Prof. Dr. Andreas Meyer and Prof. Dr. Daniela Zander for the opportunity to work at the Intitute of Material Physics in Space at the German Aerospace Center.

Contents

1. Introduction

The ability to produce and process metals is linked so closely to the human evolution, that whole eras are named after metals like copper, bronze or iron. Since the first copper was worked with, roughly 10.000 years ago [1], metals have been the motor of human civilizational advancement. Historically, having a metallurgic technological advantage was equivalent with military superiority. Civilistations holding the highest performing metal alloys thrived while others withered. Today the importance of metallugical know- how has shifted from the military sector more towards economical and scientific areas. Material innovations make nations economical globally competitive. Simultaneously, this evergrowing demand for economical growth, which is closely linked with a soaring fabrication of metal products, is largely responsible for many challenges we as a society face today. Around 6 percent of the global CO_2 emissions are associated with metal manufacturing [2]. To takle the advancing global warming, it is inevitable to massively reduce the CO_2 emmisions produced during metallurgical processes. To achieve this goal industry and science have to work hand in hand to develop new alloy systems, new recyling pahtways and new low-energy processing routes. Science helps pushing the improvement of already existing metallic materials and processes as well as the development of new alloy systems forward. Although on a smaller scale, the present work is part of this ambitious endeveour.

1.1 Motivation and Research Questions

Precisely describing the scientific motivation behind the present work is a challenge since this work has aspects that fit into the category of fundamental research as well as aspects that are better categorized by applied research. This section will therefore try setting three major research goals by answering the central questions behind the scientific motivation of this work.

Why thermophysical properties?

When looking at the title of this work, the first question that comes to mind is: What is the motivation behind investigating thermophysical properties? Thermophysical properties are the tool to combine fundamental and applied research for liquid metal melts.

On the one hand a systematical data collection of thermophysical properties, in this case density and surface tension, can help improving existing production processes and alloy systems and make the development of new procedures and materials possible. Surface tension and density are crucial properties when designing and modelling casting processes [3] or developing new manufacturing processes such as additive manufacturing [4]. For the design and optimization of metal production processes simulations are essential tools. Already in the 1960s digital computers were used to solve casting process related problems [5]. Systematical and reliable thermophysical data, such as surface tension and density, is an absolute necessity for these simulations involving metal melts. Additionally, the properties need to be provided as a function of temperature, since the temperatures during, for example casting processes, vary vastly from temperatures well above the melting temperature to room temperature.

On the other hand, knowledge of the thermophysical properties such as density and surface tension allow a more fundamental understanding of the mixing behavior and interaction mechanisms of multicomponent metallic melts. Additionally, a sufficient thermophysical database enables the development and improvement of meaningful prediction models.

These considerations lead to the first two provisionally research goals of this work:

1. Systematical data collection for density and surface tension as a function of the temperature.
2. Evaluation of the obtained data in the context of already existing thermophysical prediction models to gain a deeper understanding towards the fundamental mixing behavior.

With the answers to the following research questions, these goals can be expanded and specified towards the final research goals. These research goals are now applied to a specific alloy system. Accordingly, the next question to be answered is the question of the right alloy system for the investigations.

Why Al-Ti-V ?

Ti-alloys are amongst the most promising newly upcoming alloy-systems for high performance industrial applications, with first alloys being developed in the late 1940s [6]. With a combination of highly favorable properties ranging from high specific strength over excellent heat and corrosion resistivity to their low density and superior biocompatibility, Ti-alloys might be perfectly suited to tackle the emerging ecological and economical challenges in modern metal production.

The first industrial sector that comes into the field of view when discussing Ti-alloys is aerospace. Reduction in energy and cost often is often the focus when discussing leading-edge aerospace developments. As structural materials in aircrafts, Ti-alloys help to achieve the high performance demands while simultaneously reducing the operating costs by combining the high structural strength of steels or Ni-based super alloys with the low weight of Al-alloys. Their superior temperature resistance makes Ti-alloys even more sought-after for high temperature applications such as aircraft and gas turbine engines. Around 7 % of the structural weight of the fuselage of the Airbus A340/A330 are allocated to Ti-alloys, which is roughly the same share as for steels [7]. However, for the jet engine this share increases to around one third, making Ti-alloys the second most used material group only to Ni-based superalloys [7]. In space applications, their high long-term chemical stability gives Ti-alloys an advantage over high strength steels when choosing structural materials for fuel tanks in launch vehicles.

When looking for earthbound applications of Ti-alloys, biomedical applications immediately catch the eye. With a continuously aging world population, the need for bio-device applicable materials is on a steady rise. Studies predict, that by 2030 approximately 272.000 total hip replacements will be performed annually worldwide [8]. The risk of implant loosening and resorption of natural bone can be reduced by choosing a highly biocompatible joint material with an elastic modulus similar to that of natural bone, such as different Ti-alloys [9]. The high wear and corrosion resistance of these Ti-alloys also help to reduce bone cell death caused by wear debris at the bone-implant stem interface. Therefore, Ti-alloys help drastically reduce the need for revision surgery.

One of the most recent area of application for titanium-based alloys is additive manufacturing. Additive manufacturing can help revolutionize metal manufacturing from rapid prototype development, to small series production all the way to mass production. With the perspective of near-net-shape forming in a single production step, additive manufacturing becomes especially interesting for materials that are traditionally hard to machine, such as Ti-alloys and other super alloys [10]. The high shaping flexibility of additive manufacturing processes can drastically reduce the processing costs of Ti-alloys and therefore broaden their application sectors [11].

In this context, considering the importance of thermophysical data discussed under the previous question, it is very surprising how scares the available thermophysical data for the liquid Al-Ti-V system is. While thermophysical data for the pure elements is still available, the available data becomes less for the binary sub systems Al-Ti, Al-V and Ti-V while there is almost no systematical research available for the ternary system.

For pure liquid Al surface tension [12, 13, 14, 15, 16] and density [13, 14, 16, 17] data is available over a wide temperature range, measured with various methods. For liquid titanium slightly less density [13, 18, 14, 19] and surface tension [13, 14, 16] data is available. This can partially be attributed to the high melting temperature and reactivity and the associated measurement difficulties for liquid titanium. These difficulties will be addressed more in-depth in the next question concerned with the measurement technique chosen in this work. The trend of less available data continues for both density [18, 20, 21, 22] and surface tension [23, 24] for liquid vanadium. The rarity of available data for liquid vanadium can be explained by the high melting temperature, high reactivity and comparably little industrial applications for pure vanadium.

For the binary sub-systems Al-Ti, Al-V and Ti-V the available data is getting even less. Al-Ti is the most studied system with many previous works carried out at our institute [13, 25, 26, 27]. The works by Wessing [13, 26] and Brillo [25] are the spiritual predecessors of this work. For liquid Al-V and Ti-V no systematical thermophysical property measurements could be found. The same can be said for the ternary Al-Ti-V system. Even though for selected ternary alloys like Ti-6Al-4V [28, 29] thermophysical data exists, no systematical investigation could be found.

With these findings the previously set up research goals can be specified:

1. Systematical data collection for density and surface tension as a function of the temperature **for pure liquid Al, Ti, V, its binary alloys and selected ternary sections**.
2. Evaluation of the obtained data in the context of already existing thermophysical **data** and prediction models to gain a deeper understanding towards the fundamental mixing behavior.

The rarity of available reliable data was partially attributed to the difficulties in processing high melting, highly reactive melts such as Al, Ti, V and their alloys. Therefore, the next question that is addressed is the question of the appropriate measurement technique.

Why electromagnetic levitation?

With the liquid Al-Ti-V system chosen as the system to be examined, the question for the right processing technique still remains. Reliable and precise measurement data is indispensable when evaluating predictive models as it is one of the above already established research goals of this work. Model and prediction quality usually rise with the quality of measured data.

Accurate experimental data is very hard to obtain when working with liquid metals at elevated temperatures. Three general experimental challenges can be identified when investigating the thermophysical properties of liquid metal melts. These challenges, being the high desired temperature ranges, the high reactivity of the melts and the risk of sample contamination, are all intertwined and influence each other. The higher the temperature, the higher the chemical reactivity of the metallic sample which eventually leads to a higher risk of contamination.

Especially in the case of this work, with titanium (1941 K) and vanadium (2183 K) having very high melting temperatures, it is hard to find suitable sample containers for traditional container-based processing methods such as Archimedean method for density [30]. The traditional container-based measurement techniques (an overview can be found in Ref. [30]) are originally designed for measurements at low temperatures. As mentioned above, a higher temperature usually leads to a higher sample reactivity. In the case of the present system this is true for all three components Al,Ti and V, which are extremely reactive at elevated temperatures. Upon increasing the measurement temperature well above the melting point it becomes nearly impossible to avoid chemical reactions with container or crucible walls. Thus, an accurate measurement of the thermophysical properties becomes impossible. A collection of surface tension data by Keene [31] showed a scatter of almost 20% between conventional

container-based methods. On the other hand, container-based techniques also shorten the experimentally achievable temperature. Contact with container walls or a crucible enable heterogeneous nucleation when cooling the metal melt, reducing the achievable undercooling. Even if a suitable container-based measurement technique can be found, the experimental temperature ranges for liquid metals are usually very small. In some cases, for example Ti [32] and V [31], measurements can only be carried out at a single selected temperature.

The electromagnetic levitation (EML) provides the possibility to process highly reactive metal melts such as Al, Ti and V at elevated temperatures [33]. The container-less nature of the measurement technique helps minimize contamination due to reactions with walls and crucibles [34]. The simultaneous inductive heating of the sample allows for achievable temperatures way above the liquidus temperature, while the elimination of heterogeneous nucleation gives access to an undercooling of several hundred K below the liquidus temperature [35]. Therefore, electromagnetic levitation allow for accurate and reliable thermophysical property measurements over a wide temperature range, for the highly reactive Al-Ti-V system investigated in this work.

The first research goal can be formulated as:

1. Systematical, **accurate and reliable** data collection for density and surface tension as a function of the temperature for pure liquid Al, Ti, V, its binary alloys and selected ternary sections.

EML provides a great way to minimize contamination caused by contact with container walls. However, even in electromagnetic levitation, contact between the metal melt and the surrounding atmosphere can not be avoided. In this way oxygen contaminations, can still affect the sample. This, inevitably leads to the next central research question of this work.

Why oxygen?

Thermophysical properties are strongly dependent on the composition of the investigated sample. In the context of the above mentioned contact between the liquid sample and the surrounding atmosphere this holds especially true for the surface tension. Even the smallest number of surfactants or impurities can greatly impact the observed surface tension [36]. For liquid metals, oxygen is the most impactful surface active element when it comes to surface tension [36]. It has been reported, that even small oxygen mole fractions can greatly influence the surface tension of Al [37], Fe [38, 39], Cu [40, 41] and others. The elements of this work might be amongst the elements for which oxygen plays an especially big role. Aluminum shows a strong affinity towards oxygen resulting in a strong tendency to quickly form a thin but stable oxide layer already in the solid state [42]. Previous works suggest that this affinity to oxygen might be the reason for large disagreements in different experimental studies of the surface tension for liquid aluminum [43]. Liquid titanium also shows a high affinity towards oxygen, paired with a high solubility of oxygen (66.6 at.% bulk solubility at 2000 K [25]). Based on the combination of these two properties, previous works suggested that ‘completely oxygen free’ titanium does practically not exist [44]. Consequently, oxygen can hardly be avoided during the preparation of titanium containing samples. The influence must therefore always be considered when investigating the properties of titanium alloys.

That is the reason why the previous works on Al-Ti [13] at our institute, which are the foundation of this work, include investigations considering the influence of oxygen [26, 25]. From the previous considerations result two distinct possibilities for the presence of oxygen. Oxygen can be present in the surface layer or solved in the material volume. Experimentally, this can be investigated by either preparing samples with a specific bulk oxygen concentration (solved in volume) or by exposing the liquid sample to an atmosphere enriched in oxygen (oxygen present at the surface layer). While the previous works on aluminum suggest that oxygen in the surrounding atmosphere immediately translates

to a high oxygen atomic concentration in the sample surface layer [37, 42] and a subsequently changed surface tension, the same could not be observed for titanium. For titanium [26, 25] the surface tension was rather unaffected by the oxygen partial pressure of the surrounding atmosphere but could be heavily reduced by the addition of oxide powder during sample preparation. All this points towards different interactions of liquid metals with oxygen, which are not yet fully understood.

With the EML facility at DLR, which is equipped with a newly developed 'Oxygen Control System' (OCS), it is possible to monitor and adjust the oxygen partial pressure of the processing atmosphere during the container-less investigations. In this way, the interactions between liquid metals and oxygen, both in the bulk and the surrounding atmosphere can be investigated effectively. The OCS is such a valuable tool in investigating the influence of oxygen on the thermophysical properties of liquid metals, that the EML facility onboard the International Space Station (ISS) is expanded by a similar system in the near future. This work can not only help understanding the interactions between liquid metal melts, but it can also help build a scientific and experimental foundation for future investigations carried out on the ISS.

Summarized, oxygen must inevitably be considered when investigating the thermophysical properties of metallic melts. For this work this means, that all investigations surrounding the Al-Ti-V system must be evaluated against the background of possible oxygen influence. Hence a final research goal needs to be established:

3. Creating a foundation towards the evaluation of the previous findings against the background of oxygen influence and expanding the insight into the general interaction between metallic melts and oxygen utilizing the Oxygen Control System in combination with electromagnetic levitation.

1.2 Research Concept

From the motivational questions answered above, three central research goals are identified:

1. Systematical, accurate and reliable data collection for density and surface tension as a function of the temperature for pure liquid Al, Ti, V, its binary alloys and selected ternary sections.
2. Evaluation of the obtained data in the context of already existing thermophysical data and prediction models to gain a deeper understanding towards the fundamental mixing behavior.
3. Creating a foundation towards the evaluation of the previous findings against the background of oxygen influence and expanding the insight into the general interaction between metallic melts and oxygen utilizing the Oxygen Control System in combination with electromagnetic levitation.

Based on these scientific goals a research concept was developed. The foundation of the present research was created by the works on the Al-Ti system by Wessing [26, 13, 25] at the '*Institut für Materialphysik im Weltraum'*. This work was expanded to provide a more systematical approach towards the investigation of the ternary Al-Ti-V system.

In order to reach the first two research goals of systematic and reliable thermophysical property data for the Al-Ti-V system, a strategic concept, which is sketched in Figure 1, was developed. To characterize density and surface tension for the complete ternary Al-Ti-V system in a structured approach, the pure elements Al, Ti and V were chosen as starting points. By starting with the pure elements, the obtained results can be counter-checked against already existing literature data. This helps in evaluating the accuracy and reliability of the data included in the first goal. This could also be used as plausibility check and as a first calibration of the new experimental setup. Both properties were measured for all pure elements as a function of temperature.

Afterwards, the liquid binary sub systems Ti-V and Al-V were investigated for their density, surface tension and mixing behavior. Both density and surface tension were measured as a function of temperature and composition. Therefore, a sufficient number of individual alloys were measured over a broad temperature range, to adequate map the complete binary sub-system. Together with already existing data for the liquid Al-Ti [13] system these binaries form the framework for later investigations of the ternary system.

For both properties, density and surface tension and for both binary systems, models are developed to precisely reproduce the experimental data depending on the composition and temperature. These can then also be used to examine the general mixing behavior and identify possible trends. Combining the model calculations of the binary subsystems with the gained insights of the mixing behavior, first predictive calculations for the ternary system can be developed. These models can then be tested against individual experimental measurement results for the ternary system. The insights gained through the application of the thermophysical models onto the obtained measurement data are used to a deeper understanding of the general mixing behaviors in the binary systems and the ternary system. The model evaluations build the backbone in answering the second proposed research goal.

In a final step, the obtained results are re-visited from a point of view considering the oxygen influence. Again, the pure elements, specifically pure vanadium, was chosen as a starting point for the investigations. The oxygen mole fraction of pure vanadium was varied by adding oxide powder while preparing the sample and by changing the oxygen partial pressure in the processing atmosphere. For both cases, the surface tension is measured as a function of the temperature. The findings in working with the OCS system build a foundation towards future experimental work on the ISS utilizing a similarly working device. The obtained data can be used for understanding the measurement principle for an Oxygen Control System and as a starting point when investigating the thermophysical properties of other alloy systems in dependence of the oxygen partial pressure.

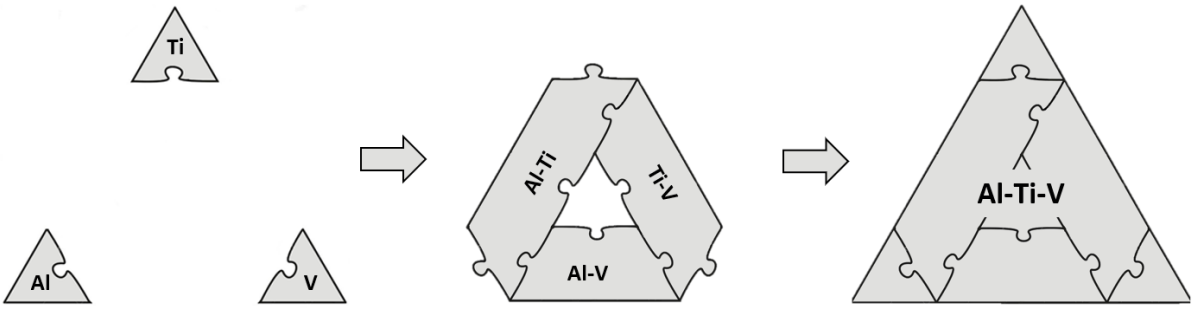

Figure 1: Strategic flow chart of the investigations regarding the thermophysical properties of the ternary Al-Ti-V system.

2. Theoretical Fundamentals

It is quite obvious that some theoretical fundamentals are needed if the introduced research goals want to be met. These fundamentals will be presented in the following section in three major parts. In the first one, a classification of Ti-alloys will be given to generate some compositional context since this works aims to provide a data collection for the Al-Ti-V system.

For the second research goal proposed in this work, the thermophysical properties should be used to gain some insight into the general mixing behavior of the Al-Ti-V system and thermodynamic models should provide predictive tools for these properties. This is only possible if the thermophysical properties investigated are well defined, their description is properly mathematically derived and if the respective models have been coherently introduced. This is the function of the second part of this chapter.

2.1 Classification of Ti-alloys

Pure titanium undergoes a lattice transformation from a hexagonal close-packed (hcp) α-structure to a body centered cubic (bcc) β-structure when above 1155.5 K. If an alloying element of titanium increases this phase transition temperature it is referred to as a "α stabilizer" otherwise it is called a "β stabilizer". Based upon which phase is present, technical Ti-alloys are classified in "α", "β" or "$\alpha + \beta$" Ti-alloys. For the sake of completeness, the titanium aluminide alloy group (commonly γ-Ti), which summarizes aluminum rich Al-Ti intermetallic compounds needs to be mentioned as well. Most non-transition metals are α stabilizers, upon which aluminum is the most prominent. In contrast to that most transition metals are stabilizers of the bcc β phase. Vanadium is one of the most industrial relevant of these alloying elements. A mixture of both alloying elements with titanium, Ti-6Al-4V is the most well-established titanium alloy consisting in equilibrium of both α and β phase. From an application stand-point, α alloys qualify for cryogenic uses since the hcp-structure lacks a ductile brittle transformation. With the bcc structure being prone to a ductile brittle transformation, β alloys are unsuited for low-temperature applications. However, they exhibit extreme high formability. For $\alpha + \beta$ alloys the mechanical properties can be adjusted over a rather broad range by appropriate heat treatments. They usually combine good machinability with high room-temperature strength and moderate high-temperature stability [45].

2.2 Thermophysical Properties

There is not a single exhaustive definition for what thermophysical properties are. Corresponding to the syllable “thermo” being the Greek word for heat, the term thermophysical properties is mostly used as an umbrella term for physical properties that change with temperature. However, thermophysical properties are only defined for homogeneous, single phase systems in equilibrium. While many thermophysical properties such as specific heat, thermal conductivity or thermal expansion can be described as responses to an external force, density (or molar volume) and surface tension are also considered thermophysical properties even though they don’t fall under this definition.

This chapter is intended to give the reader the necessary theoretical background to comprehend the analysis done for the experimentally gathered density and surface tension data. Besides an introduction into the thermodynamic formalisms of both density and surface tension, several model calculations will be introduced. Since most of the research conducted in this work revolves around multicomponent system it is necessary to introduce fundamental thermodynamic concepts for mixtures.

Starting for a single component system, the fundamental Gibbs free energy G can be expressed as [46]:

$$dG = Vdp - SdT \tag{1}$$

Here, V denotes the volume, p the pressure, S the entropy and T the temperature. Considering Eq. 1 at a constant temperature, the free energy of a phase increases with increasing pressure.

$$\left(\frac{\partial G}{\partial p}\right)_{\mathrm{T}} = V \tag{2}$$

The free energy of a multicomponent system will not remain constant during mixing. Therefore, the free energy of such a system can be described as:

$$G = \sum_{\mathrm{i}} x_{\mathrm{i}}\, G_{\mathrm{i}}^{0} + \Delta G \tag{3}$$

Where x_{i} is the mole fraction of component i and G_{i}^{0} is the Gibbs free energy of pure component i, while ΔG is the mixing free energy, which can be calculated from the heat of mixing ΔH_{mix} and mixing entropy ΔS_{mix} as $\Delta G = \Delta H_{\mathrm{mix}} - T\Delta S_{\mathrm{mix}}$ [46]. Both the heat of mixing and mixing entropy describe the difference in enthalpy and entropy between the unmixed and mixed state. For the simplest type of mixing, the ideal solution, the heat of mixing $\Delta H_{\mathrm{mix}} = 0$ equals zero. In that case the mixing free energy can be calculated as follows:

$$\Delta^{\mathrm{id}}G = RT \sum_{\mathrm{i}} x_{\mathrm{i}} \ln\left(x_{\mathrm{i}}\right) \tag{4}$$

In most cases mixing is either endothermic (heat absorbed during mixing) or exothermic (heat released during mixing). In such cases the model used for the ideal solution in Eq. 4 needs to be expanded by a so called excess free energy $^{\mathrm{E}}G$, which describes the difference in mixing free energy of the regular solution ΔG and the ideal solution $\Delta^{\mathrm{id}}G$. In result, the mixing free energy for a regular solution yields:

$$\Delta G = \Delta^{\mathrm{id}}G + {}^{\mathrm{E}}G = RT \sum_{i} x_{\mathrm{i}} \ln\left(x_{\mathrm{i}}\right) + {}^{\mathrm{E}}G \tag{5}$$

When applying Eq. 5 to Eq. 3 and the result to Eq. 2, the molar volume V of a regular solution results in

$$V = \sum_{\mathrm{i}} x_{\mathrm{i}} V_{\mathrm{i}} + \Delta V \qquad (6)$$

In this equation 6, V_{i} is the molar volume of pure component i and ΔV is the mixing molar volume, which in this work will more often be referred to as the molar excess volume ${}^{\mathrm{E}}V$. Eq. 5 mathematically illustrates that, if multiple components are mixed, while the mass m or amount of substance n of the solution is calculated as the sum of the corresponding components, the same is not true for the molar volume of the solution. An additional contribution ${}^{\mathrm{E}}V$, attributed to the particle interaction, has to be considered.

For mixtures that deviate from the ideal solution, in this work such mixtures will be called regular solutions, the excess free energy ${}^{\mathrm{E}}G$ can be described using a Redlich-Kister type polynomial [47]. For a binary mixture with components i and j this then reads as:

$${}^{\mathrm{E}}G = x_{\mathrm{i}} x_{\mathrm{j}} \sum_{v=0}^{N_{\mathrm{i,j}}} {}^{\mathrm{v}}L_{\mathrm{i,j}} (T)(x_{\mathrm{i}} - x_{\mathrm{j}})^{v} \qquad (7)$$

${}^{\mathrm{v}}L_{\mathrm{i,j}}$ is the binary interaction parameter accounting for the interactions between particles of species i and j, while v determines the order of the polynomial. Using Eq. 2 and Eq.7, a similar expression can be developed for the molar excess volume ${}^{\mathrm{E}}V$. For most binary cases, so too in this work, the first constituent $v = 0$ is sufficient to approximate the excess volume. Therefore, the parabolic trend of the molar excess volume, ${}^{\mathrm{E}}V_{\mathrm{i,j}}$, for a regular solution of two components i and j can be described by a term ${}^{0}V(T)$ as:

$${}^{E}V_{\mathrm{i,j}} \approx x_{\mathrm{i}} x_{\mathrm{j}} {}^{0}V(T) \qquad (8)$$

The same general derivation can be used for the molar excess volume of a ternary system. In the case of three components, the excess free energy, ${}^{\mathrm{E}}G$, has to be calculated using a Redlich-Kister-Muggianu form [48]:

$${}^{\mathrm{E}}G = \sum_{\mathrm{i<j}} x_{\mathrm{i}} x_{\mathrm{j}} \sum_{\mathrm{v}=0}^{N_{\mathrm{i,j}}} {}^{\mathrm{v}}L_{\mathrm{i,j}} (T)\left(x_{\mathrm{i}} - x_{\mathrm{j}}\right)^{\mathrm{v}} + {}^{\mathrm{T}}G\left(T, x_1, x_2, x_3\right) x_1 x_2 x_3 + \cdots \qquad (9)$$

The additional parameter ${}^{\mathrm{T}}G$ accounts for a possible ternary interaction. Subsequently, ${}^{\mathrm{T}}G$ transforms into a ternary parameter ${}^{\mathrm{T}}V$ when applying the derivation of the excess molar Volume with Eq. 2 onto Eq.9. The excess molar volume, ${}^{\mathrm{E}}V_{1,2,3}$, for a ternary system then reads:

$${}^{\mathrm{E}}V_{1,2,3} = \sum_{\mathrm{i<j}} {}^{\mathrm{E}}V_{\mathrm{i,j}}(T) + x_1 x_2 x_3 {}^{\mathrm{T}}V(T) \qquad (10)$$

The left term ${}^{\mathrm{E}}V_{\mathrm{i,j}}(T)$ is identical with the excess molar volume of the binary system and can be determined with Eq. 8 from an individual measurement. If the ternary interaction is very small, e.g. ${}^{\mathrm{T}}G \approx 0$, the excess free energy for the ternary system can be deduced from the binary sub systems.

2.2.1 Density and Molar Volume

For a single phase the density is defined by the mass *m* divided by the volume *V*. Respecting the previous derivations, for a mixture consisting of *i* components with molar masses M_i and mole fractions x_i the density can be written as:

$$\rho = \frac{\sum_\mathrm{i} x_\mathrm{i} M_\mathrm{i}}{\sum_\mathrm{i} x_\mathrm{i} \frac{M_\mathrm{i}}{\rho_\mathrm{i}} + {}^{\mathrm{E}}V} \qquad (11)$$

with $\rho_\mathrm{i} = M_\mathrm{i}/V_\mathrm{i}$ being the density of the pure component *i*.

Molar volume and density both depend on the temperature. If the density obeys a linear behavior, which is the case for all densities measured in this work, the temperature dependency can be derived from the volume expansion coefficient in the following form:

$$\rho(T) = \rho_\mathrm{L} + \rho_\mathrm{T}(T - T_\mathrm{L}) \qquad (12)$$

In this formalism ρ_L is the density at the liquidus temperature, ρ_T the linear temperature coefficient and T_L is the liquidus temperature.

2.2.2 Surface Tension

Before looking into the thermodynamic modeling which is done to analyze the experimentally gathered surface tension data in this work, it is first needed to define what a surface is and how it is described. In common language, the term ‘surface’ relates to a special case of interface between a solid and a gas or a liquid and a gas. The interface of a system is often defined in contrast to the (bulk) phase of the system. Usually a phase in a material system is defined as a homogeneous part of the system with uniform intensive properties, separated from other parts of the system by a distinct boundary. Subsequently, an interface in a system containing different phases must be the area where the intensive properties show discontinuity. Based on the description of the interface the surface tension can be defined. The further definitions of surface tension differ, depending on which approach is taken in its description. The surface tension can be described in three different ways: related to the difference in pressure between two sides of a curved surface, resulting from a difference in net binding energy due to a changing atomic distribution near the interface or for a liquid as the free energy change per surface area change. Only the thermodynamic definition of the surface tension will be further discussed in greater detail. More information regarding the remaining approaches can be found in [14] and [49].

2.2.3 Gibbs Method

Gibbs described the thermodynamics of a surface by introducing a so-called dividing surface [49]. The dividing surface is the hypothetically introduced plane separating two homogeneous phases in the area where the local properties show a continuous variation normal to the surface [50]. Figure 2 schematically shows the position of the dividing surface separating a liquid bulk phase (B) from a gas (G).

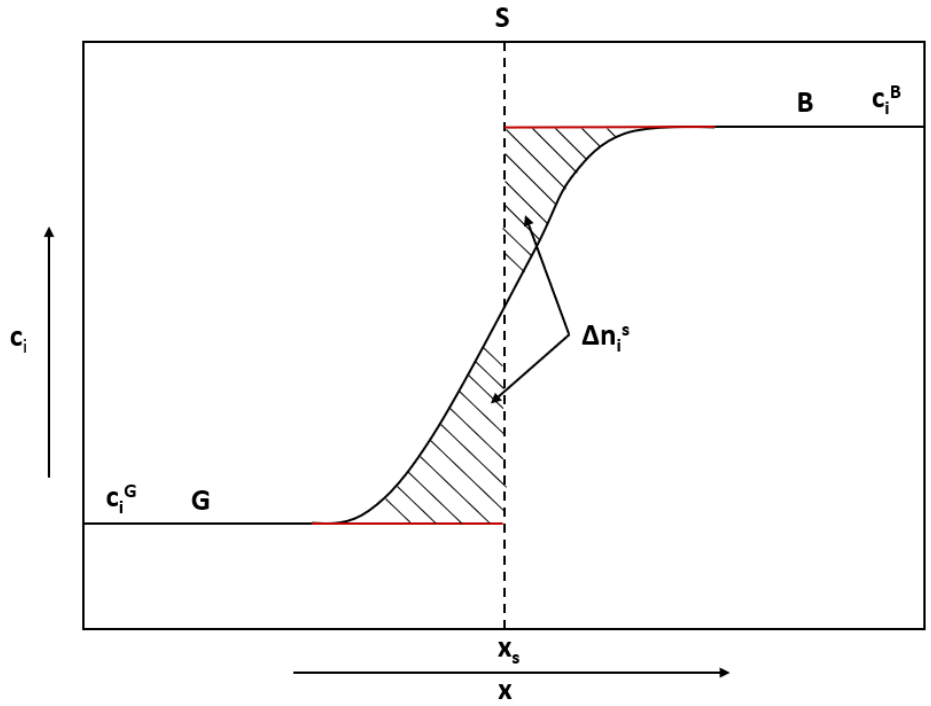

Figure 2: Schematic depiction of the Gibbs dividing surface S between a gas phase (G) and a liquid bulk phase (B) including the number of moles in the gas (n_G), in the liquid (n_B) and the excess number of moles Δn_i^s.

Theoretically, the Gibbs dividing surface has no thickness [14], but realistically the intensive properties (in Figure 2 the concentration of component *i* is shown as an example), which show a discontinuity at the dividing surface, do not change abruptly but continuously. This property transition zone results for the example in Figure 2 in a deviation of the total number of moles in the system from the sum $n_i^G + n_i^B$ of moles in the gas and in the liquid respectively. This deviation Δn_i^s is called the excess number of moles. When considering, that the total number of moles in the system is n_i, the volume of the liquid is V^B, the volume of the gas is V^G and the number of moles in the gas and liquid can be calculated as $n_i^G = c_i^G \cdot V^G$ and $n_i^B = x_i^B \cdot V^B$ respectively, one can write the excess number of moles as [49]:

$$\Delta n_i^s = n_i - (x_i^B \cdot V^B + x_i^G \cdot V^G) \qquad (13)$$

In a similar fashion surface excess can be defined for several thermodynamic quantities such as internal energy U^s, entropy S^s, Gibbs free energy G^s or Helmholtz energy F^s [49].

$$F^s = F - (f_i^B \cdot V^B + f_i^G \cdot V^G) \qquad (14)$$

Eq. 14 shows the Helmholtz energy as an example. In this equation f_i^B is the Helmholtz energy per unit volume of liquid phase and f_i^G the Helmholtz energy per unit volume of gas phase. With this it becomes obvious that the Gibbs method utilizes excess surface quantities (the differences of intensive properties at the interface with respect to the bulk) and integrates them at the dividing surface in order to describe the thermodynamics of the surface. It needs to be mentioned, that the dimension and sign of the excess quantities heavily depends on the position of the dividing surface. There have been approaches to negate this dependence, but since those are both, highly complex and not strictly relevant for this work they will not be discussed. Instead more information about the positional dependence can be found in [49] and [50].

2.2.4 Thermodynamics of the Surface Tension

The surface tension can be introduced by applying the first law of thermodynamics to the surface of a single-phase liquid, which was introduced earlier following Gibbs definition of the dividing plane. In an equilibrium the change in surface internal energy dU^s due to a change in surface dA can be expressed as:

$$dU^{\mathrm{s}} = TdS^{\mathrm{s}} + \gamma dA \qquad (15)$$

With γ being the surface tension and γdA being the work needed to increase the surface by dA. S^s is the interfacial excess entropy. When introducing the total differentiation of the Helmholtz energy of the surface ($F^s = U^s - TS^{\mathrm{s}}$) as:

$$dF^{\mathrm{s}} = dU^{\mathrm{s}} - TdS^{\mathrm{s}} - S^{\mathrm{s}}dT \qquad (16)$$

And inserting Eq. 15, one can obtain the surface tension as:

$$\gamma = \left(\frac{\partial F^{\mathrm{s}}}{\partial A}\right)_{\mathrm{T}} = f^{\mathrm{s}} \qquad (17)$$

Graphically speaking, according to the definition of the Helmholtz energy ($f^{\mathrm{s}} = u^{\mathrm{s}} - Ts^{\mathrm{s}}$), the surface tension consists of the excess internal energy per surface area and the excess entropy of the interface.

A different formalistic approach yielding the same information results in the so-called Gibbs-Duhem relation for surfaces:

$$S^{\mathrm{s}}dT - V^{\mathrm{s}}dP + Ad\gamma + \sum_{\mathrm{i}}^{N} \Delta x_{\mathrm{i}}^{\mathrm{S}} d\mu_{\mathrm{i}} = 0 \qquad (18)$$

Eq. (18) follows from the definition of the surface tension, γ, as a change in free energy, *G,* when the surface area, *A* is increased.

$$\gamma = \left.\frac{\partial G}{\partial A}\right|_{\mathrm{P,V,T}} \qquad (19)$$

From Eq. 17 and the definition of the Helmholtz energy, further insight into the temperature dependence of the surface tension can be gained. When partially differentiating with respect to the temperature the following correlation for the temperature coefficient of the surface tension γ_{T} is obtained (the same can be achieved from Eq. 18):

$$\gamma_{\mathrm{T}} = \left(\frac{\partial \gamma}{\partial T}\right) = \left(\frac{\partial f^{\mathrm{s}}}{\partial T}\right) = -s^{\mathrm{s}} \qquad (20)$$

Therefore, it can be deduced, that the temperature coefficient equals the negative surface excess entropy per unit volume. Moreover, several empirical models have been developed to reproduce the temperature dependence of the surface tension. The Katayama-Guggenheim [51] equation is widely regarded as one of the most useful:

$$\gamma = \gamma_0 \left(1 - \frac{T}{T_{\mathrm{c}}}\right)^{\frac{11}{9}} \qquad (21)$$

Here γ_0 is a constant that relates to the type of liquid and T_{c} is the critical temperature. At the critical temperature the distinction between liquid and gas becomes impossible, which means the surface tension

equals zero. In this work however, the surface tension is usually investigated at temperatures well below T_c. In those cases, the surface tension depends linearly on the temperature, allowing for a correlation similar to that deducted for the density in Eq. (12):

$$\gamma(T) = \gamma_L + \gamma_T(T - T_L) \tag{22}$$

In the case of the surface tension, γ_L denotes the surface tension at the liquidus temperature and γ_T the temperature coefficient.

2.3 Thermodynamic Models

Now that the surface and the surface tension are introduced thermodynamically, the model calculations that are employed in this work can be introduced. This section will largely follow the concepts developed by Kaptay in [52] and [53]. This approach is chosen because Kaptay derived his models in a very educational way from the fundamental Gibbs thermodynamics solely by introducing the partial surface area as a new property. Therefore, the equations are derived without the use of the Gibbs adsorption equation which removes the restrictions initially imposed on the thickness and structure of the solution surface. Moreover, the alternative models used in this work can be incorporated into his considerations as borderline cases.

2.3.1 The Renovated Butler Model

In Kaptay's work [53] all his considerations are based upon the thermodynamic definition of the surface tension by Gibbs.

$$\gamma = \left(\frac{dG}{dA}\right)_{p,T,n_i} \tag{23}$$

Here *A* is the absolute surface area of the liquid phase and *G* is the absolute Gibbs free energy. It should be noted that Eq. 23 is equal to Eq. 20 for constant temperature and pressure. Eq. 23 can be integrated with the boundary sets $A = 0$, $G = G_b$ and $A = A$, $G = G$, where G_b is the total absolute bulk Gibbs free energy. Then, the following form is obtained:

$$G = G_b + A\gamma \tag{24}$$

The main aspect of Kaptay's work is the introduction of the partial surface tension when applying Eq. 23 and 24 to a multicomponent liquid solution. He defined the partial surface tension of one component *i,* in such a multicomponent liquid solution accordance with Eq. 23 as:

$$\gamma_i = \left(\frac{dG_i}{dA_i}\right) \tag{25}$$

There, A_i is the partial surface area of component *i* and G_i the partial absolute Gibbs energy. The sum of the respective quantities for each component yield the integral absolute area *A* and Gibbs energy *G* respectively. The partial absolute Gibbs energy of component *i* in the liquid solution state G_i is connected to the partial absolute Gibbs energy of the pure liquid state G_i^0 via:

$$G_i = G_i^0 + \Delta G_i \tag{26}$$

accounting for the partial absolute mixing Gibbs energy ΔG_i when component *i* changes from the standard pure liquid state to the liquid solution state. Now, as for the absolute surface tension in Eq. 23, an integration of the partial surface (Eq. 24) tension leads to:

$$G_\mathrm{i} = G_\mathrm{b,i} + A_\mathrm{i}\gamma_\mathrm{i} \qquad (27)$$

$G_\mathrm{b,i}$ is the partial absolute bulk Gibbs free energy of component *i* and results from the boundary condition of the integration ($G_\mathrm{i} = G_\mathrm{b,i}$ and $G_\mathrm{i} = G_\mathrm{i}$). Summation over all *N* partial quantities leads to:

$$G = \sum_\mathrm{i}^\mathrm{N} G_\mathrm{i} = \sum_\mathrm{i}^\mathrm{N} G_\mathrm{b,i} + \sum_\mathrm{i}^\mathrm{N} A_\mathrm{i}\gamma_\mathrm{i} = G_\mathrm{b} + \sum_\mathrm{i}^\mathrm{N} A_\mathrm{i}\gamma_\mathrm{i} \qquad (28)$$

with G_b as the total partial absolute bulk Gibbs free energy. Since both Eq. 24 and 27 are equal, following equation can be positioned:

$$A\gamma = \sum_\mathrm{i}^\mathrm{N} A_\mathrm{i}\gamma = \sum_\mathrm{i}^\mathrm{N} A_\mathrm{i}\gamma_\mathrm{i} \qquad (29)$$

The simplest solution of this equation is:

$$\gamma = \gamma_\mathrm{i} = \cdots = \gamma_\mathrm{N} \qquad (30)$$

This expression is called the Renovated Butler equation [53]. The term 'Renovated' is added due to the expression's similarities with the Conventional Butler equation which will be introduced later. It is directly developed from the fundamental thermodynamic definition of the surface tension by Gibbs, by introducing the partial surface tension of a single component *i* in a multicomponent liquid solution. Therefore, in contrast to the Conventional Butler equation, there are no additional structural assumptions implied for the liquid.

To apply Eq. 30 to the experimental gathered data of this work a more practical form of Eq. 30 has to be found. Kaptay [53] derived such an expression for the partial surface tension γ_i as:

$$\gamma_\mathrm{i} = \gamma_\mathrm{i}^0 \frac{\omega_\mathrm{i}^0}{\omega_\mathrm{i}} + \frac{RT}{\omega_\mathrm{i}} ln\left(\frac{a_\mathrm{i}^S}{a_\mathrm{i}^B}\right) \qquad (31)$$

Here γ_i^0 is the surface tension of component *i* in pure liquid *i,* while ω_i^0 is the molar surface area of component *i* in pure liquid *i.* In contrast to that ω_i is the partial molar surface area of component *i* in the solution. For a binary solution *i-j,* ω_i can be calculated using the following expression:

$$\omega_\mathrm{i} = \omega_\mathrm{i}^0 + (x_\mathrm{j}^S)^2 L_\omega \qquad (32)$$

Where x_j^S is the mole fraction of component *j* in the surface and L_ω is the so called interaction surface area. The parameter L_ω contains the contribution of the molar excess volume ^0V introduced in Eq. 8.

$$L_\omega = N_\mathrm{Av}^{\frac{1}{3}} (^0V)^{2/3} \qquad (33)$$

N_Av is the Avogadro number.

Finally, when introducing the partial molar excess Gibbs free energy for bulk $^E g_i^B(T, x_i^B)$ and surface $^\mathrm{E} g_\mathrm{i}^\mathrm{S}(T, x_\mathrm{i}^\mathrm{S})$, a concluding formalism for the partial surface tension of component *i* in the solution can be derived depending on the mole fraction of component *i* in the bulk x_i^B and the surface x_i^S.

$$\gamma_\mathrm{i} = \gamma_\mathrm{i}^0 \frac{\omega_\mathrm{i}^0}{\omega_\mathrm{i}} + \frac{RT}{\omega_\mathrm{i}} ln\left(\frac{x_\mathrm{i}^\mathrm{S}}{x_\mathrm{i}^\mathrm{B}}\right) + \frac{1}{\omega_\mathrm{i}} (^\mathrm{E} G_\mathrm{i}^\mathrm{S}(T, x_\mathrm{i}^\mathrm{S}) - {}^\mathrm{E} G_\mathrm{i}^\mathrm{B}(T, x_\mathrm{i}^\mathrm{B})) \qquad (34)$$

Usually model description as introduced in Eq. 7 are used to describe the partial molar excess Gibbs free energy for the bulk. For the partial molar excess Gibbs energy for the surface a similar mathematical description is chosen, but as a function of the surface composition x_i^S instead of the bulk composition x_i^B.

Eqs. 30 and 34 can be combined to calculate the surface tension and the surface composition of a multicomponent liquid alloys. Together, they form the Renovated Butler model.

2.3.2 The Conventional Butler Model

Before Kaptay developed the Renovated Butler model, a slightly different analytical model to predict the surface tension of multicomponent melts was established as the 'Butler model'. To better distinguish between both models the latter shall be referred to as 'Conventional Butler model' in this work. The Conventional Butler model differs from the fundamental Gibbs description of the surface since it considers the surface as a separate thermodynamic phase with its own composition and chemical potential. Specifically, the Conventional Butler model considers the surface to be a separate phase in thermodynamic equilibrium with the bulk phase. Since both phases (bulk and surface) are in thermodynamic equilibrium, the model formalism of the Conventional Butler model can be developed from equalizing the chemical potentials. Thereby, the chemical potential for the surface phase has the same general functional form than the chemical potential of the bulk phase plus an additional contribution from the surface tension. However, the contribution not originating from the surface tension includes a factor $(0 < \beta \leq 1)$ accounting for the changed coordination of atoms in the monoatomic surface layer. By equating the chemical potential of the bulk and the chemical potential of the surface the Conventional Butler equation for a binary liquid A-B system reads:

$$\gamma = \gamma_{\mathrm{A}}^{0} + \frac{RT}{\omega_{\mathrm{A}}^{0}} ln\left(\frac{a_{\mathrm{A}}^{\mathrm{S}}}{a_{\mathrm{A}}^{\mathrm{B}}}\right) = \gamma_{\mathrm{B}}^{0} + \frac{RT}{\omega_{\mathrm{B}}^{0}} ln\left(\frac{a_{\mathrm{B}}^{\mathrm{S}}}{a_{\mathrm{B}}^{\mathrm{B}}}\right) \qquad (35)$$

It becomes obvious, that the Conventional Butler equation in Eq. 35 becomes equal to Eq. 31 derived by Kaptay in the Renovated Butler model, when the partial molar surfaces areas in the solution can be assumed equal to the molar surface areas in the pure liquid for the respective components. Therefore, Eq. (35) is a limiting case of Eq. (34). As expressed in Eq. 32 this can be done when the excess volume is rather small. As done for Eq. 34, Eq. (35) can be written in a more applicable form:

$$\gamma = \gamma_{\mathrm{A}}^{0} + \frac{RT}{\omega_{\mathrm{A}}^{0}} ln\left(\frac{x_{\mathrm{A}}^{\mathrm{S}}}{x_{\mathrm{A}}^{\mathrm{B}}}\right) + \frac{1}{\omega_{\mathrm{A}}^{0}} \left(\,^{\mathrm{E}}G_{\mathrm{A}}^{\mathrm{S}}(T, x_{\mathrm{i}}^{\mathrm{S}}) - \,^{\mathrm{E}}G_{\mathrm{A}}^{\mathrm{B}}(T, x_{\mathrm{i}}^{\mathrm{B}})\right) \qquad (36)$$

Just like for the Renovated Butler model in sec. 3.2.1, the excess Gibbs free energies can be modeled using existing data bases following Eq. 9. Thereby, the excess free energy can be calculated using the same formalism used for the bulk (Eq. 9) for the surface mole fraction $x_{\mathrm{i}}^{\mathrm{S}}$ instead of the bulk mole fraction $x_{\mathrm{i}}^{\mathrm{B}}$ when an additional factor $\beta = 0.83$ is included. For a binary alloy, it follows:

$$\,^{\mathrm{E}}G^{\mathrm{S}} = \beta * \sum_{\mathrm{i<j}} x_{\mathrm{i}}^{\mathrm{S}}{}_{i} x_{\mathrm{j}}^{\mathrm{S}} \sum_{\mathrm{v=0}}^{\mathrm{N_{i,j}}} \,^{v}L_{\mathrm{i,j}} (T)\left(x_{\mathrm{i}}^{\mathrm{S}} - x_{\mathrm{j}}^{\mathrm{S}}\right)^{v} \qquad (37)$$

β accounts for the different coordination of atoms located in the surface and was chosen to be 0.83 in accordance with [54]. The partial molar excess free energies, $\,^{\mathrm{E}}G_{\mathrm{i}} = \frac{\partial\,^{E}G}{\partial n_{\mathrm{i}}}$, can be calculated from these integral free energies for both the surface and the bulk. For a binary system, with $x_{\mathrm{A}} + x_{\mathrm{B}} = 1$, this reads as:

$$
\begin{aligned}
{}^{\mathrm{E}}G_A^{\square} &= {}^{\mathrm{E}}G - x_{\mathrm{B}}\frac{\partial\,{}^{\mathrm{E}}G}{\partial x_{\mathrm{B}}} \\
{}^{\mathrm{E}}G_{\mathrm{B}}^{\square} &= {}^{\mathrm{E}}G + (1-x_{\mathrm{B}})\frac{\partial\,{}^{\mathrm{E}}G}{\partial x_{\mathrm{B}}}
\end{aligned}
\qquad (38)
$$

For a ternary system the partial free excess energies can be calculated in a similar fashion as a taylor series until the first link. The equations then read as:

$$
\begin{aligned}
{}^{\mathrm{E}}G_{\mathrm{A}}^{\square} &= {}^{\mathrm{E}}G + (1-x_{\mathrm{A}})\frac{\partial\,{}^{\mathrm{E}}G}{\partial x_{\mathrm{A}}} - x_{\mathrm{B}}\frac{\partial\,{}^{\mathrm{E}}G}{\partial x_{\mathrm{B}}} - x_{\mathrm{C}}\frac{\partial\,{}^{\mathrm{E}}G}{\partial x_{\mathrm{C}}} \\
{}^{\mathrm{E}}G_{\mathrm{B}}^{\square} &= {}^{\mathrm{E}}G - x_{\mathrm{A}}\frac{\partial\,{}^{\mathrm{E}}G}{\partial x_{\mathrm{A}}} + (1-x_{\mathrm{B}})\frac{\partial\,{}^{\mathrm{E}}G}{\partial x_{\mathrm{B}}} - x_{\mathrm{C}}\frac{\partial\,{}^{\mathrm{E}}G}{\partial x_{\mathrm{C}}}\,\square \\
&\ldots
\end{aligned}
\qquad (39)
$$

With the excess Gibbs free energies for bulk and surface known for a binary liquid system, two equations describing the surface tension based on the partial quantities for both pure elements as a function of the bulk and surface composition can be developed and set equal. Subsequently, the surface tension and surface composition can be calculated. The calculations follow the same pattern for the ternary system.

2.3.3 The Ideal Solution as Limiting Case

Both the Renovated and the Conventional Butler model are able to predict the surface tension and composition of multicomponent liquid solution. Both models have been introduced for non-ideally mixing solutions, including possible excess quantities. In the frame of this work ideal mixing behavior of a liquid alloy is regarded as the limiting case in which the excess quantities vanish. Alloys that mix non-ideally are referred to as regular solution, while systems that mix ideal are called ideal solutions. For an ideal solution, the excess quantities in Eq. 34 and 36 vanish when predicting the surface tension of the system with the respective model. For the Conventional Butler model Eq. 36 for a liquid binary solution thereby changes to:

$$
\gamma = \gamma_{\mathrm{A}}^{0} + \frac{RT}{\omega}\,ln\left(\frac{x_{\mathrm{A}}^{\mathrm{S}}}{x_{\mathrm{A}}^{\mathrm{B}}}\right) = \gamma_{\mathrm{B}}^{0} + \frac{RT}{\omega}\,ln\left(\frac{1-x_{\mathrm{B}}^{\mathrm{S}}}{1-x_{\mathrm{B}}^{\mathrm{B}}}\right) \qquad (40)
$$

Here it was further assumed, that all areas $\omega_{\mathrm{i}}^{0} = \omega_{\mathrm{j}}^{0} \equiv \omega$ are equal. The expression above can be solved analytically for the surface mole fraction $x_{\mathrm{A}}^{\mathrm{S}}$.

$$
x_{\mathrm{A}}^{\mathrm{S}} = \frac{x_{\mathrm{A}}^{\mathrm{B}}}{x_{\mathrm{A}}^{\mathrm{B}} + (1-x_{\mathrm{A}}^{\mathrm{B}})S_{\mathrm{e}}(T)} \qquad (41)
$$

The introduced factor $S_{\mathrm{e}} = \exp\left((\gamma_{\mathrm{A}} - \gamma_{\mathrm{B}})\omega/RT\right)$, describes the segregation in the system. Segregation describes the phenomenon, that the component with the smaller surface tension will enrich in the surface phase as the system tends to minimize its total energy. In reverse, the element with the higher surface tension will deplete in the surface phase. Segregation effects already occur in ideal solutions.

An analytical solution for the Renovated Butler model for an ideal solution following a similar approach would not yield any added value. The assumption of all areas being equal, made for the Conventional Butler model above would circumvent the main difference in both models. For clarity and simplicity, all calculations for ideal solutions are made on the basis of the Conventional Butler model using the approach introduced above.

For many systems however, this assumption oversimplifies the real thermodynamic situation. For regular solutions (only terms of the 1st order ($v = 1$) need to be considered in Eq. 9 and Eq. 37) the excess partial free energies do not vanish. In those cases, Eqs. 34 and 36 hold. It will be mentioned for each case in this work which mixing type was assumed when using either model.

2.3.4 The Egry Model

Egry [55] incorporated compound formation into the lastly introduced ideal solution case of the Conventional Butler model. He assumed, that in a binary system that forms intermetallic phases, some atomic clusters of the intermetallic composition exist until temperatures slightly above the liquidus temperature T_{L}. These clusters consequently change the surface composition by binding components that would otherwise segregate to the surface phase (see segregation above). Egry modified the segregation factor S_{e} in the Conventional Butler model for an ideal solution to consider this change in surface composition. He included a second factor $f_{\mathrm{Se}} * (n+m)(x_{\mathrm{A}}^{\mathrm{B}})^{\mathrm{n}}(x_{\mathrm{B}}^{\mathrm{B}})^{\mathrm{m}}$ so that the deviation from the ideal behavior is largest at the concentration of the intermetallic phase $\mathrm{A_nB_m}$ chosen as the cluster blueprint. The resulting segregation factor then reads as:

$$S_{\mathrm{e}}(T) = \exp\left(\frac{(\gamma_{\mathrm{A}}-\gamma_{\mathrm{B}})\omega - f_{\mathrm{Se}}*(n+m)(x_{\mathrm{A}}^{\mathrm{B}})^{n}(x_{\mathrm{B}}^{\mathrm{B}})^{m}}{RT}\right) \qquad (42)$$

With f_{Se} being an adjustable parameter related to the single bond energy in the compound. In some cases, it might also be advisable to include ω as a second fitting parameter to achieve a better accordance with the obtained data.

With the Egry model and the ideal and regular solution case for Regular and Conventional Butler model, in total 5 different thermodynamic models are introduced in this work. Their similar formalisms emphasize their common origin. However, for each model different assumptions are made, since they are developed for different applications. Therefore, all will be tested against the experimentally gained data.

With the thermophysical properties described and the thermodynamic models introduced an adequate framework has been set to be filled with experimental data which will be used to fulfil the goals of this work. For a good scientific practice, it is essential to precisely describe the methods used to obtain any sort of data. This description will be done in the next section.

2.4 The Role of Oxygen

Oxygen is one of the surfactants with the strongest effect on the surface tension of metallic melts [25, 26, 36]. Already small amounts of oxygen in the sample or the surrounding atmosphere can greatly reduce the surface tension of liquid alloys and impede the reliability of the experimental data. At the same time, the interactions between the liquid phase and oxygen are immensely complex. Chemisorption, adsorption specified by a chemical bond between the adsorbate (oxygen) and the adsorbent (liquid metal), convection processes such as Marangoni flow (in the liquid phase or at the surface), diffusion processes or oxide formation are just a few phenomena that need to be considered when investigating the interaction between a liquid metal droplet and oxygen [56]. Whether oxygen adsorbs on the surface, evaporates from the surface, is oxides are forming or if oxygen is dissolved in the bulk depends on temperature and oxygen partial pressure in the process atmosphere [57].

The *Gibbs isotherm*, derived from *Gibbs-Duhem relation of surfaces* in Eq. 18, describes the adsorption of oxygen on a liquid surface at constant temperature and pressure. It reads:

$$d\gamma + \sum_{i}^{N} \Gamma_i d\mu_i = 0 \qquad (43)$$

In this equation $\Gamma_i = \Delta x_i^S / A$ denotes the adsorption of component *i* per surface area *A*. The chemical potential, μ_i, of component *i* can be described as a function of the standard chemical potential of the bulk state, μ_i^0, the molar gas constant, *R,* the temperature, *T*, and the activity, α_i:

$$\mu_i = \mu_i^0 + RTln(\alpha_i) \qquad (44)$$

Langmuir derived a semi-empirical isotherm for a unary adsorbate system where the adsorption takes place at single adsorption sites independent of the atomic arrangement and the surface coverage of the species. The Langmuir isotherm reads:

$$\frac{\theta_i}{1-\theta_i} = K_{ad}\alpha_i \qquad (45)$$

Where, $\theta_i = \Gamma_i/\Gamma_i^0$, is the surface coverage (the fraction of adsorption sites occupied) and K_{ad} is the equilibrium constant. In the context of this work it is an important note, that the equivalent of the oxygen partial pressure for the liquid phase is the activity, α_i. Eq. (45) only holds true for non-dissociative adsorption and desorption. Eq. 43-45 can be combined to write [14, 58, 59]:

$$\frac{d\gamma}{dln(\alpha_i)} = -\sum_{i}^{N} RT\theta_i \frac{K_{ad}\alpha_i}{1+K_{ad}\alpha_i} \qquad (46)$$

Integration of Eq. 46 yields the Belton/Szyszkowski equation:

$$\gamma = \gamma^{pure} - RT\Gamma_i^0 \ln(1 + K_{ad}\alpha_i) \qquad (47)$$

When one integration limit is taken as the pure solvent. With Eq. (47) the influence of the oxygen adsorption on the surface tension can be calculated with the known surface tension of the pure liquid metal adsorbent, γ^{pure}. It is highly practical in the framework of this investigations to express the activity, α_i, through the (oxygen) partial pressure.

$$\alpha_{\mathrm{i}} = \sqrt{\frac{P_{\mathrm{O}_2}}{P^0_{\mathrm{O}_2}}} \qquad (48)$$

Above, $P^0_{\mathrm{O}_2} = 10^{-5}(\mathrm{Pa}) = 1\mathrm{bar}$ is defined as the standard oxygen state. Eq. (49) accounts for the difference between oxygen in the gas phase, O_2, and adsorbed oxygen in the melt, O_{ad}, following the reaction $\frac{1}{2}\mathrm{O}_2(\mathrm{g}) \leftrightarrow \mathrm{O}_{\mathrm{ad}}$. If the oxygen partial pressure $P_{\mathrm{O}_2} \leq P^{\mathrm{sat}}_{\mathrm{O}_2}$ is below the saturation oxygen partial pressure, $P^{\mathrm{sat}}_{\mathrm{O}_2}$, Eq. 48 and Eq. 47 can be combined to describe the surface tension as a function of the oxygen partial pressure:

$$\gamma = \gamma^{\mathrm{pure}} - RT\Gamma^0_{\mathrm{i}} \ln\left(1 + K_{\mathrm{ad}} f_{\mathrm{i}} \sqrt{P_{\mathrm{O}_2}}\right) \qquad (49)$$

In Eq. 49, f_{i} is the activity constant for oxygen in the molten component *i* [60]. If oxygen obeys *Henry's law* (which is valid to assume since the oxygen concentration in the liquid is dilute, therefore the assumption is valid) in the molten metal, $f_{\mathrm{i}} = 1$ can be assumed.

Oxide formation is another phenomenon which needs to be considered when investigating the surface tension of liquid metals under the influence of oxygen. The driving force (Gibbs free energy) of oxide formation is depicted as a function of temperature and oxygen partial pressure in the so-called Ellingham diagram [61] shown in Figure 3. With the help of the Ellingham diagram, the equilibrium partial pressure for metal and oxide can be determined at a specific temperature. If the experimental partial pressure is higher, the sample is oxidized, if not the sample will be reduced. In Figure 3 several metal/oxide pairings are depicted as straight lines (if the slope of a line changes, a phase transition of any of the components occurs). The lower the line lies, the more stable the oxide is. To determine the equilibrium partial pressure for a specific temperature, first the corresponding position on the straight line in the Ellingham diagram has to be found for that temperature. Afterwards the top left '0' point has to be connected with the corresponding temperature point with a straight line. The extension of this line yields the equilibrium partial pressure. Figure 3 shows that for the Al-Ti-V system, Al forms the most stable oxides, Al_2O_3, followed by TiO_2 for titanium and V_2O_5 for vanadium.

For an oxide formation reaction, the Gibbs free energy, ΔG, can be connected to the equilibrium constant, *K*, of the reaction as:

$$K = \frac{1}{\sqrt{P_{\mathrm{O}_2}}} = \exp\left(-\frac{\Delta G}{RT}\right) \qquad (50)$$

In the Ellingham diagram the Gibbs free energy of (oxide) formation ($\Delta G = \Delta H - T\Delta S$) is plotted versus the logarithmic oxygen partial pressure and $1/T$.

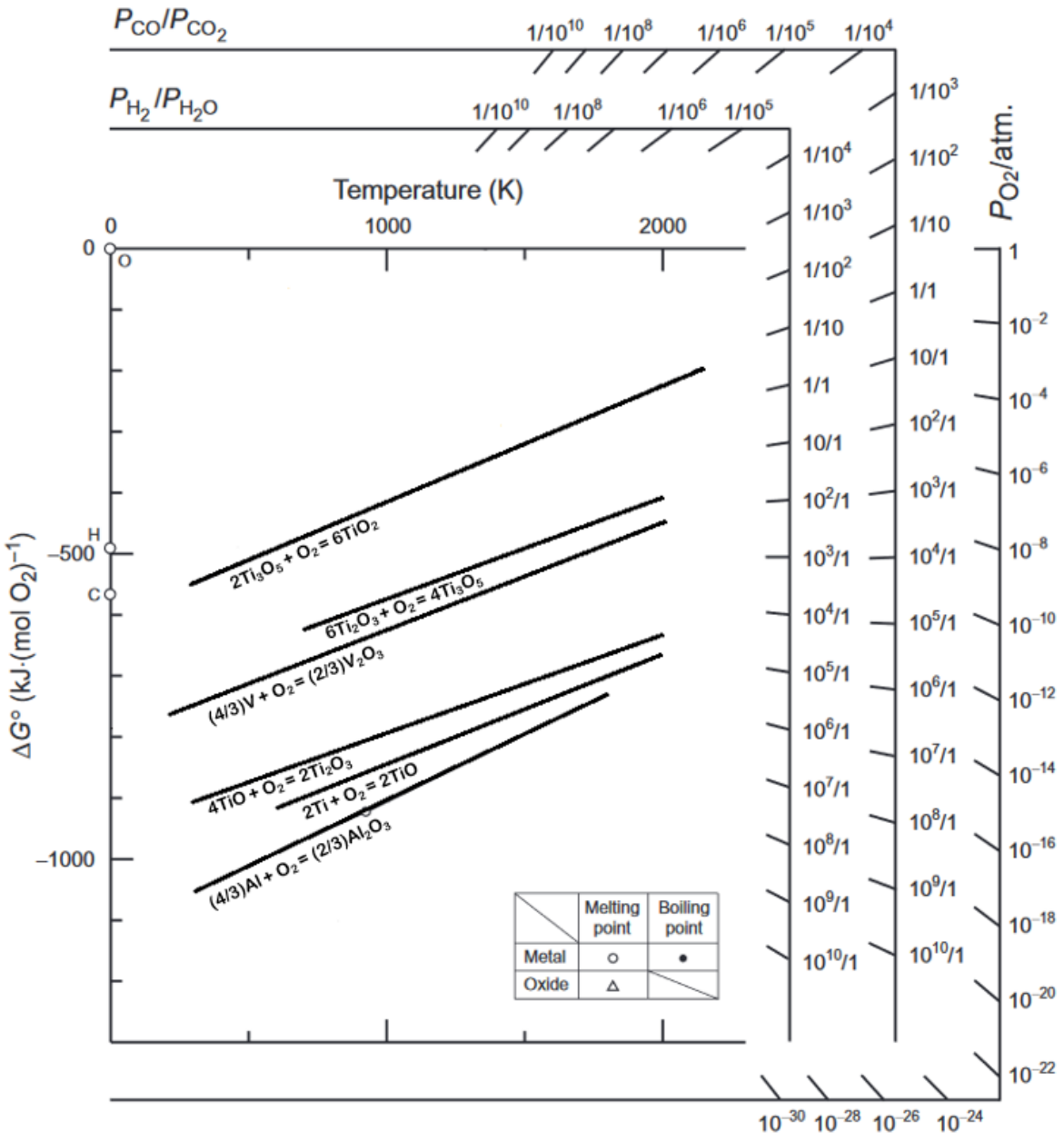

Figure 3:Ellingham diagram showing the Standard free energy of formation of different oxides as a function of temperature and oxygen partial pressure for different Al, Ti and V oxides. The diagram was constructed following Ref. [61] and [62].

2.4.1 Oxygen Model Calculations

Monoatomic model

Previous works [25] already investigated the surface tension of liquid titanium in the presence of oxygen. In that work, a simple model based on the conventional Butler model (see section 2.3.2) was developed to predict the surface tension for a binary ideal solution of a liquid metal and oxygen. For this purpose, the so-called 'Butler-Belton isotherm' has been introduced by combining the Belton equation and the conventional Butler model. It reads:

$$\overset{\mathrm{id}}{\square}\gamma_{\infty} = \gamma_{\mathrm{metal}} - \frac{RT}{A_{\mathrm{metal}}} \ln\left(1 + (\overset{\mathrm{id}}{\square}K(T) - 1)x_{\infty}\right) \qquad (51)$$

With $\overset{\mathrm{id}}{\square}K(T)$ being the equilibrium constant of the ideal solution and x_{∞} the equilibrium oxygen bulk mole fraction. Eq. (51) is only valid if the system is in equilibrium (∞ subscript). As mentioned in the last section, the Belton equation can be derived by combining the Gibbs-adsorption isotherm with the Langmuir isotherm (see section 2.4). A more detailed derivation of Eq. (51) can be found in [25, 63]. This model assumes, that the melt is made up of only metal and oxygen atoms in homogeneous distribution. It is therefore labeled the monoatomic model. In the scope of this works Eq. (51) of the monoatomic model will be used analogously to calculate the surface tension of an ideal mixture of liquid vanadium and oxygen.

Associate model

To expand the calculations for a non-ideal model, Ref. [25] introduced excess free energy calculations based on a simple associate model. In the special use case of liquid titanium and oxygen, these excess free energy calculations were simply implemented into the monoatomic model under the assumption, that only 'TiO_2 -associates' form in the melt. For the titanium/oxygen application this simplification of only considering the associates for excess free energy calculations might be valid, but in the case of the vanadium/oxygen system the situation is much more complex. To describe the V-O liquid phase, multiple associates need to be considered. It is important to note at this point, that the associate species must not be confused with the oxides that are described by the same stochiometric formula. In contrast to an actual oxide compound, the term associate relates to pronounced short range ordering with hetero-coordination. In accordance with [64] four different coordination vanadium atoms need to be considered to describe the short-range ordering representing the VO, V_2O_3, VO_2 and V_2O_5 compositions. In this case, the monoatomic model is not applicable.

In [63] Brillo introduced a simple associate model based on the Butler equation which can be adapted for the liquid V-O system to read as follows:

$$\begin{aligned}
\gamma &= \gamma_{\mathrm{V}} + \frac{RT}{A_{\mathrm{V}}} \ln\left(\frac{x_{\mathrm{V}}^{\mathrm{S}}}{x_{\mathrm{V}}^{\mathrm{B}}}\right) + \frac{1}{A_{\mathrm{V}}} (\overset{\mathrm{E}}{\square}G_{\mathrm{V}}^{\mathrm{S}} - \overset{\mathrm{E}}{\square}G_{\mathrm{V}}^{\mathrm{B}}) \\
&= \gamma_{\mathrm{VO}} + \frac{RT}{A_{\mathrm{VO}}} \ln\left(\frac{x_{\mathrm{VO}}^{\mathrm{S}}}{x_{\mathrm{VO}}^{\mathrm{B}}}\right) + \frac{1}{A_{\mathrm{VO}}} (\overset{\mathrm{E}}{\square}G_{\mathrm{VO}}^{\mathrm{S}} - \overset{\mathrm{E}}{\square}G_{\mathrm{VO}}^{\mathrm{B}}) \qquad (52) \\
&= \dots \\
&= \gamma_{\mathrm{V_2O_5}} + \frac{RT}{A_{\mathrm{V_2O_5}}} \ln\left(\frac{x_{\mathrm{V_2O_5}}^{\mathrm{S}}}{x_{\mathrm{V_2O_5}}^{\mathrm{B}}}\right) + \frac{1}{A_{\mathrm{V_2O_5}}} (\overset{\mathrm{E}}{\square}G_{\mathrm{V_2O_5}}^{\mathrm{S}} - \overset{\mathrm{E}}{\square}G_{\mathrm{V_2O_5}}^{\mathrm{B}})
\end{aligned}$$

Analogue to the conventional Butler model x_V^S and x_V^B are the mole fractions of liquid vanadium in the surface and the bulk respectively. The same notation is chosen for the associate species. The same is true for the excess free energies for the surface ($^{E}G^{S}$) and the bulk phase ($^{E}G^{B}$). The excess energies can be calculated following Ref. [64]. As for the conventional Butler model the excess free energies for the surface follow the same formalisms as the bulk excess free energies but with an additional β factor (see section 2.3.1 and 2.3.2).

The complexity for the liquid V-O system lies in the determination of the mole fraction of each individual associate species. In an attempt to do so, a 'Metropolis' algorithm was employed in combination with the model parameters reported in Ref. [64] to determine the energetically favored associate distribution. Subsequently, the equation system (52) can be solved numerically.

It needs to be mentioned, that both the model and the Metropolis algorithm employed are far from optimized. However, the results achieved are in good enough agreement with the measured data to be mentioned in this work. In this way, the results can be further evaluated and a foundation for further model calculations is set.

3. Experimental Methods

The experimental data obtained in this work is the cornerstone of its purpose. On one hand, providing high quality data is a major goal of this work by itself. On the other hand, all investigations on interaction mechanisms, mixing behaviors and model predictions are based on the obtained data.

In this section, all practical methods used to gather high quality experimental data presented will be explained. Firstly, the sample preparation steps will be described from raw materials to the final sample that is investigated. Subsequently, all technical facilities and apparatuses in which the sample is processed will be discussed. Finally, every measurement technique will be explained.

With the fundamentals presented in this section the reader should be able to fully understand how the experimental results are obtained to an extend where the reader is able to duplicate the measurements carried out.

3.1 Sample Preparation

Since it is one major goal of this work to compile reliable experimental thermophysical data depending on alloy composition, it is mandatory to very carefully prepare samples with an exactly known alloy composition. Moreover, any kind of contamination has to be strictly avoided during the preparation process. High purity raw metals Ti (99.99 pct. provided by *Alpha Aesar*), Al (99.999 pct. provided by *Alpha Aesar*) and V (99.99 pct. provided by *Smart Elements*) are used in order to circumvent contamination with microelements. For the preparation of the samples containing different oxygen mole fractions, highly pure vanadium(V)-oxide powder (99.99 pct. provided by *Alpha Aesar*) is used.

The first step in sample preparation is to calculated the needed raw material masses for the desired alloy composition. The needed mass m_i for component i, can be calculated using the following equation:

$$m_\mathrm{i} = m_\mathrm{tot} \frac{M_\mathrm{i} x_\mathrm{i}}{\sum M_\mathrm{i} x_\mathrm{i}} \qquad (53)$$

In this case, m_tot is the desired total sample mass, M_i the molar mass of component i and x_i the mole fraction. An overview over the molar masses of the used substances, their purity and their respective melting temperatures can be found in table 1.

Table 1: Purity, Molar mass M_i and melting temperatures of the used raw materials.

Material	Purity [%]	Molar mass [g/mol]	Melting temperature [K]
Aluminium	99.999	26.982	933.3 [65]
Titanium	99.99	47.867	1941 [66]
Vanadium	99.99	50.942	2183 [66]
Vanadium(V)-oxide	99.99	181.88	963 [67]

Before the calculated masses are portioned for each component, any possible oxide layer is removed from the raw elements using SiC grinding paper. For Ti and V an IsoMet-High-Speed-Pro-Precision-Cutter is used to cut the desired masses. For Al, a wire cutter is sufficient. After weighting in the raw elements, a cleaning cycle using an ultrasonic bath and isopropanol is performed. For the preparation of

the samples with different oxygen mole fraction, the vanadium(V)-oxide powder was weighted in without a subsequent cleaning cycle.

Afterwards, an industrial *Compact Arc Melter MAM-1* from *Edmund Bühler GmBH* is used to alloy all components together. The individual raw materials are placed upon a water-cooled copper plate and molten together under a high purity argon (99.9999 vol pct. purity) protective gas atmosphere with a light arc originating from a tungsten electrode.

Since vanadium(V)-oxide starts to decompose around 2023 K, which is well below the melting point of pure vanadium, a special alloying route was designed for the samples containing oxide powder. Therefore, special vanadium containers are machined from the pure raw vanadium, as seen in Figure 3.

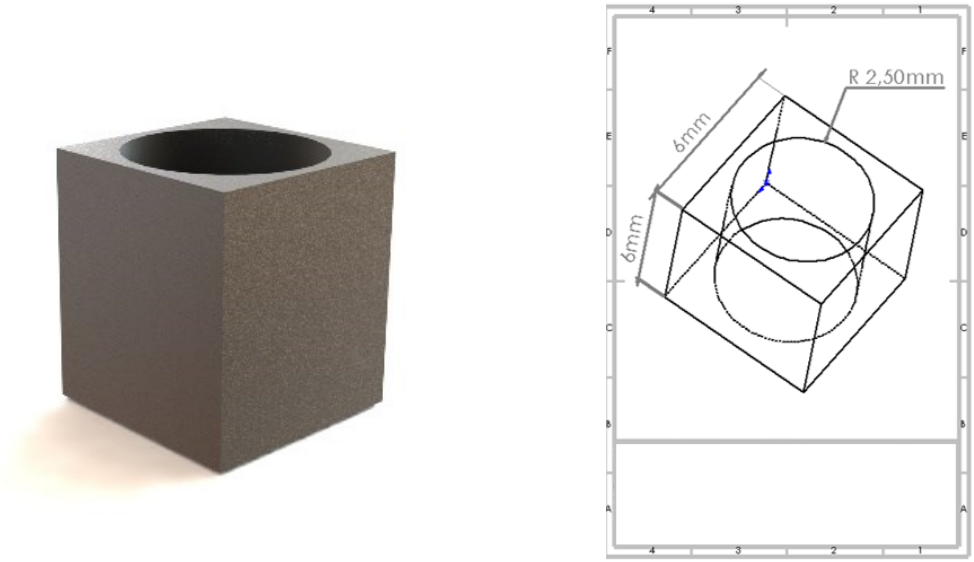

Figure 4: Render and Technical drawing of the special vanadium containers used to prepare the samples containing the vanadium(V)-oxide powder.

The containers are then filled with the exact amount of vanadium(V)-oxide powder needed before the powder is compacted with a precisely fitting steel stamp. Afterwards, the container with the powder is placed upside down on the copper plate of the arc melter. Next, the container is carefully molten, solving the powder in the melt before it can evaporate. The vanadium, vanadium oxide powder mixture is then allowed to cool down. In a final alloying step the mixture is molten again until it becomes homogeneous.

After completing the alloying process, the samples passes through an additional isopropanol cleaning cycle in the ultrasonic bath. After cleaning, the mass of each sample is measured with a *Mettler AT20* analytical micro balance and compared to the mass of all raw materials. If the difference in mass is larger than 0.25%, the sample is discarded. All samples are stored in isopropanol until measurement to prevent any oxidation.

3.2 Electromagnetic Levitation

Electromagnetic Levitation (EML) is often compared to “conventional techniques” for thermophysical property measurements. Most commonly, that expression refer to container-based measurement techniques where the investigated liquid is inside some sort of crucible or on a substrate. An extensive compilation of these conventional methods can be found in Ref. [30]. It is often argued, that the main drawback of these conventional techniques, especially when working with liquid metals at elevated temperatures, is the contact of the investigated liquid with the container or substrate. Liquid metals at high temperatures tend to be highly chemically reactive which raises several obstacles when working in a crucible or on a substrate. Before an experiment can even be started a suitable substrate material has to be found. Besides withstanding the needed temperatures, the material needs to be inert against the investigated melt. Otherwise contamination caused by chemical reactions at elevated temperatures, which can greatly influence the thermophysical properties of the sample, is risked. For extremely reactive and high melting alloys such as the Ti- and V- alloys investigated in this work no suitable material can be found. Therefore, container-less investigation methods, such as the electromagnetic levitation, are the only valid option for reasonable thermophysical property measurements.

The basic principle of electromagnetic levitation is rather simple. If a metallic, conductive sample is inserted into an alternating electromagnetic field, eddy currents are induced in the sample. This has two results. Firstly, the sample is heated due to the ohmic losses of the eddy currents and secondly a Levitation force acts upon the sample as a result of the interaction between the eddy currents and the external alternating electromagnetic field. This levitation force acts opposite to the gravitational forces and therefore levitates the sample. A schematic for the forces acting upon a levitating sample can be found in Figure 5. As common for the electromagnetic levitation the magnetic field is generated by a live copper coil in with the sample inserted into.

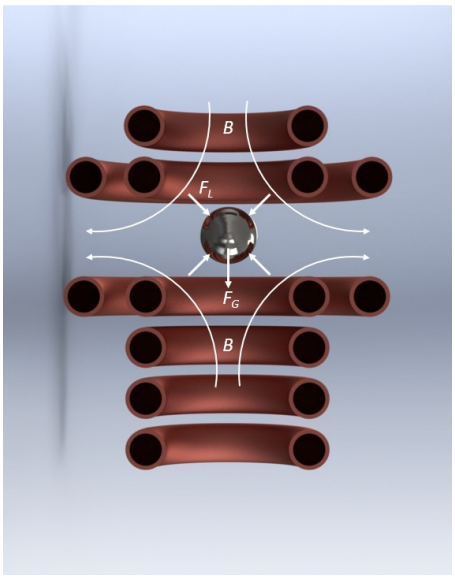

Figure 5: Schematic drawing of the forces acting upon a sample in the $\vec{B}$ field of a copper coil.

The mathematical description of the electromagnetic levitation is deduced in [68]. Under the assumption of a ferromagnetic, conductive, nearly spherical sample in a magnetic field, the equation for the Lorentz force $\overrightarrow{F_L}$ reads:

$$\overrightarrow{F_{\mathrm{L}}} = -\frac{4\pi R^3}{3\mu_0} G(q) \nabla \vec{B}^2 \qquad (54)$$

Here, R is the radius of the sample, μ_0 the magnetic permeability and $q = \frac{R}{\delta}$ is the ratio of the sample radius and the frequency ω dependent skin penetration depth $\delta = \sqrt{2/\omega\sigma\mu_0}$ of the $\vec{\mathrm{B}}$ field into the sample (with σ being the electric conductivity). The $G(q)$ function takes the penetration depth of the magnetic field $\vec{B}$ into account with:

$$G(q) = 1 - \frac{3}{2q} \frac{\sinh(2\mathrm{q}) - \sin(2\mathrm{q})}{\cosh(2q) - \cos(2q)} \qquad (55)$$

Several deductions that are useful for the experimental procedure can be made based on these mathematical descriptions. First, the levitation force acting upon the sample scales with $-\nabla\vec{B}^2$ and therefore is always directed linearly away from the field (see Figure 5). For a successful levitation the vertical component of the Lorentz force $\overrightarrow{F_{\mathrm{L}}}$ needs to equalize the gravitational force $\vec{F}_{\mathrm{g}} = \vec{g}\frac{4}{3}\pi r^3 \rho$ acting upon the sample. Together with Eqs. 54 and 55 it can be shown, that the levitation behavior of a sample strongly depends on its density. Especially when working with an alloy system with vastly different densities (Al has a very low density compared to Ti and V) it has to be considered experimentally, that samples with a low density levitate easier than those with a high density (assuming otherwise identical conditions). As shown in, the Lorentz force levitating the sample is always directed opposite to the field.

As introduced earlier, the second effect utilized for scientific electromagnetic levitation is the heating of the sample due to ohmic losses of the induced eddy currents. Just like the Lorentz force the heating power P_{H} introduced into the sample can be mathematically described in dependence of the magnetic field $\vec{B}$.

$$\overrightarrow{P_{\mathrm{H}}} = -\frac{4\pi R^3 \omega}{6\mu_0} H(q) \vec{B}^2 \qquad (56)$$

In this equation $H(q)$ acts similar to $G(q)$ in Eq. 54, describing the power absorption ratio of the sample.

$$H(q) = \mathrm{q}\frac{\sinh(2q) + \sin(2q)}{\cosh(2q) - \cos(2q)} - 1 \qquad (57)$$

A graphical display for the heating and positioning efficiency as a function of q is shown in Figure 6. The graph was taken from Ref. [69]. Examining the mathematical descriptions of the electromagnetic levitation for the edge case $q = 0$ one can see, that both $G(q)$ and $H(q)$ vanish and neither levitation nor heating is possible. A practical example for this case would be a perfect insulator. For the second edge case $q \to \infty$ only $H(q)$ equals zero while $G(q) > 0$. Therefore, in the case of a perfect conductor levitation is possible but no heating can be achieved. A practical experimental situation ranges somewhere between those extreme cases. From the formalisms above, it becomes evident that, if the physical properties of the sample change, e.g. when a different sample material is used, the ratio of heating power and levitation force has to be adjusted accordingly. This can be achieved by changing the frequency or power of the electromagnetic field (by doing so q is changed). Furthermore, the coil design (the number of windings and their geometry) is elementary for the gradient of the electromagnetic field and therefore also greatly influences the heating and positioning of the sample. More details on the exact mathematical description of the levitation [70] and heating [71] of an electromagnetically levitated metal sample can be found in the works of G. Lohöfer [70, 71].

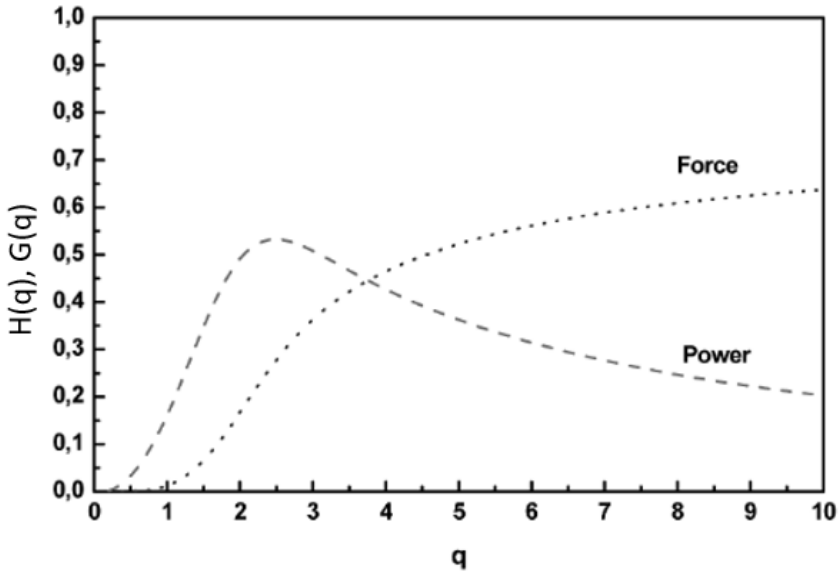

Figure 6: Effective Heating Power (H(q)) and Positioning Force (G(q)) in dependence of q [69]. An EML experiment is usually carried out where the two curves intersect.

3.2.1 DLR Cologne – EML

For most experiments of this work, two EML furnaces at the '*Institut für Materialphysik im Weltraum*' at the German Aerospace Center (DLR) in Cologne are used. Figure 7 shows a photograph of the EML apparatus used for oxygen dependent surface tension measurements in the DLR lab and an exploded view of the furnace chamber itself. The EML furnace used to measure the density is similar in design. The density measuring apparatus misses the Oxygen Control System and the Laser heating system which will be described in the following sections. The description given in this chapter applies for both EML furnaces.

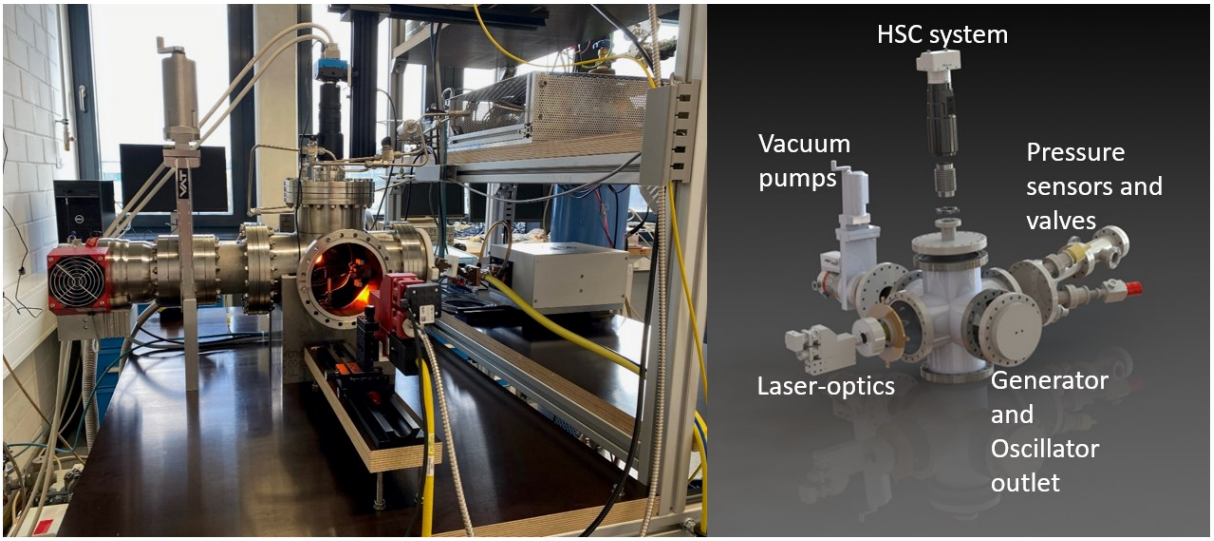

Figure 7: Photograph of the EML setup at the German Aerospace Center in Cologne Germany (left). Exploded view render of the furnace chamber with its several attachments (right).

The EML furnace as seen in Figure 7 was built as the first part of this work. The heart of the furnace is a water-cooled copper coil with a winding cross section that follows that of Figure 5. The coil is located

inside a CF DN 160 6-Way Cross which acts as the processing chamber (in the center in Figure 7, left and right). Before each experiment, the chamber is evacuated down to a pressure of about 10^{-6} mbar using a combination of a rotary pump and a high molecular pump. In doing so, any residual substances (air, adsorbed water, etc.) are removed from the furnace. Subsequently, the chamber is filled up with high-purity inert process gases (99.9999 vol. pct. purity Ar, He or a mixture of both) to about 750 hPa pressure. Several pressure sensors in addition to a magnetic valve system and an additional rotary pump ensure a constant pressure during processing.

Before the experiment, the nearly spherical sample (7 mm diameter; sample masses vary depending on density between 0.5 and 1.3 g) rests on a ceramic alumina sample holder inside the copper coil. To start the experiment, an alternating current of around 200 A with a frequency of 250 kHz is applied to the coil by a *Cobes 12 kW Generator*. As described earlier the sample is now being levitated and heated simultaneously and the sample holder can be withdrawn. Temperatures of up to 2700 K can be reached in this setup with a suitable sample material (e.g. V or Ti). Due to the nature of EML the positioning (levitation) and heating of the sample are not decoupled. To carry out temperature dependent measurements the samples are cooled by applying a variable, laminar He or Ar gas flow during the levitation. To measure the sample temperature during the experiment a two-color pyrometer by *Mergenthaler GmbH* is used. Since the sample emissivity changes with each sample material and is generally not known precisely, the following approximation derived from Wien's law [72] is used to determine the actual sample temperature T from the pyrometer signal T_P.

$$\frac{1}{T}-\frac{1}{T_\mathrm{P}}=\frac{1}{T_\mathrm{L}}-\frac{1}{T_\mathrm{L,P}} \qquad (58)$$

In Eq. 58 T_L is the liquidus temperature taken from literature and $T_\mathrm{P,L}$ is the liquidus temperature observed with the pyrometer. The apparent liquidus temperature $T_\mathrm{P,L}$ can be identified in the temperature-time log, as a sudden increase in slope, once the melting process is finished [73]. Eq. 58 is only valid, if the sample emissivity stays constant over the temperature range of the measurement for the pyrometer wavelength. For most metals Eq. 58 holds [74].

For many of the measurement techniques used in EML, both sample shape and fluid flow are of great interest. Since both are complex to such an extent that they created separate, comprehensive research areas, they will be only mentioned briefly while more profound references are given. As described and depicted in Figure 5, during levitation the sample is exposed to forces induced by the magnetic field. Matson et. al. [75] developed a numerical modeling of the electromagnetic forces exemplary for a levitated Co-Cu sample. The results for the electromagnetic force vector field (left side) and the velocity vector field (right side) are plotted in Figure 8 taken from Ref. [75].

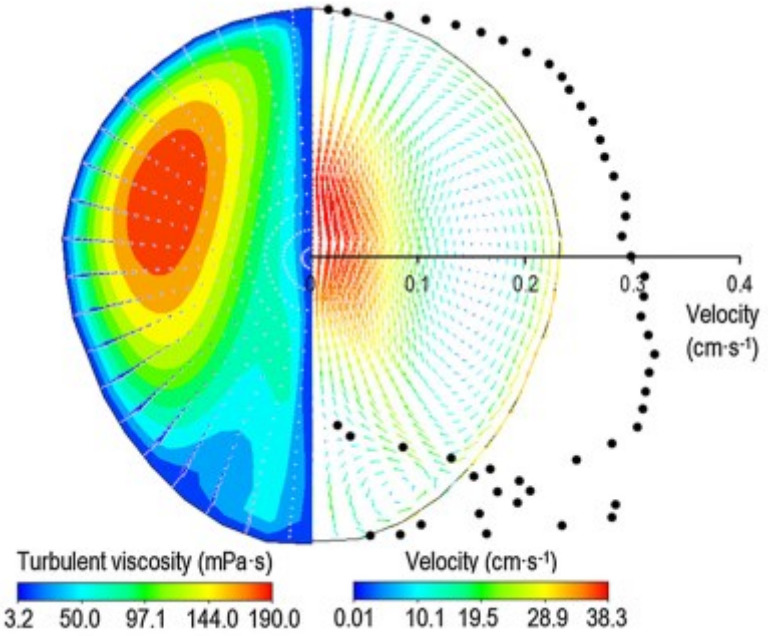

Figure 8: Magnetohydrodynamic modeling of a liquid $Co_{16}Cu_{84}$ sample during EML taken from Ref. [75]. On the left-hand side, the electromagnetic force vector field and turbulent viscosity are plotted. On the right, the velocity vector field and distribution of velocity along the surface (black dots) are depicted.

The first thing that becomes obvious, is that the sample shape deviates from a perfect sphere. A slighly simplified explanation is that the middle part of the sample experiences the most levitation forces.Therefore, one could imagine the liquid droplet as suspended on a virtual intersect through its middle with a half droplet floating on top and a half droplet hanging underneath. Sauerland [76] specifically investigated the sample shape during EML experimentally and mathematically. The devitaion of the liquid sample from an ideal sphere during EML needs to be taken into account when applying the measurement techniques that will be explained later.

Figure 8 also shows, that the flow in the sample is fully turbulent. The turbulent flow becomes more prominent when moving from the sample edges to the middle of the upper quadrant (see left side). Two circulation loops can be observed on the right side in Figure 8, one big one with a maximum in velocity near the sample center and a smaller loop near the lower pole. When kept in certain thresholds, this turbulent flow can be beneficial for the EML experiment, since it can lead to a sample homogenization. However, if the flow becomes too strong, it can lead to strong oscillations [77] and even sample rotation which in turn can prevent an accurate measurement. The turbulent flow inside the sample during terrestrial EML is also one of the reasons why a viscosity measurement is not possible in a ground based EML [78].

With its fundamentals in mind, it is easy to see the advantages EML offers compared to traditional measurement methods. Due to its nature the levitation process is intrinsically stable, meaning no active position control is needed. The turbulent flow inside the sample homogenizes the liquid droplet and at the same time induces spontaneous surface oscillations, which can in turn be used to investigate the surface tension of the liquid (described in more details later). With the implementation of a 12-kW generator the levitator makes extremely high temperatures accessible and enables processing over large temperature ranges from high overheating to deep undercooling.

3.3 Oxygen Control System - OCS

The setup described above equates to the standard EML setup used to measure thermophysical properties such as density and surface tension of liquid metals. Although this is one major aspect of this work, it is necessary to fulfill the entire scope of this work to expand the EML setup by a system to monitor and control the oxygen partial pressure in the process atmosphere. To investigate the influence oxygen has on the thermophysical properties of a liquid melt it is crucial to have precise knowledge of the oxygen in the surrounding atmosphere. The Oxygen Control System (OCS) used in this work not only does this but also allows to adjust the oxygen partial pressure of the process atmosphere in a range between 10^{-24} bar and 10^{-2} bar. Therefore, the measured properties can be measured as a function of the oxygen partial pressure during the experiment.

The OCS employed in this work was built as a prototype in a cooperation between *Clausthal University of Technology, DLR* and *Airbus Defense and Space GmbH (formerly Astrium-Space Transportation)* and is now a permanent loan to DLR. The core of its operation principle is a ceramic ionic O^{2-} conductor as shown in Figure 9. Yttrium-stabilized Zirconia (YSZ) tubes are chosen as the ionic conductor since they enable the O^{2-} transport through the ceramic at a moderate temperature while still suppressing the electronic conduction [79]. Three platinum electrodes are placed on the ceramic via vapor deposition whereas the furthest electrode to the right is extended onto the inside of the ceramic tube. At the operation temperature of the OCS, which is 600°C, the oxygen flux J_{O_2} through the ceramic is defined as:

$$J_{O_2} = \frac{I}{4F} \qquad (59)$$

where I is the electric current and F the Faraday constant. If the oxygen flow is small compared to the total gas flow through the tube the oxygen partial pressure in the tube p_{O_2} can be calculated as a function of the initial partial pressure in the carrier gas p_{O_2}, the total gas flow J_{tot} and the total pressure p_{tot} as:

$$p_{O_2} = p_{O_2}^0 + p_{\mathrm{tot}} \frac{J_{O_2}}{J_{\mathrm{tot}}} \qquad (60)$$

A difference in the oxygen partial pressure p_{O_2} inside the tube in regards to a reference $p_{O_2}^{\mathrm{ref}}$ leads to an electromotive force similar to the one in an electrochemical cell. This electromotive force can be calculated using the Nernst equation [79]:

$$E_{\mathrm{cell}} = \frac{RT}{4F} \ln\left(\frac{p_{O_2}}{p_{O_2}^{\mathrm{ref}}}\right) \qquad (61)$$

For the OCS the surrounding atmosphere acts as the reference gas, so that $p_{O_2}^{\mathrm{ref}} = 0.209\,\mathrm{bar}$. The reference oxygen partial pressure can be assumed to be constant since the introduced error is neglectable small. The oxygen pump depicted in Figure 9 uses this operation principle in both directions. The smaller electrode area ($\approx 3\ \mathrm{cm}^2$) closer to the gas in-/outlet acts as a sensor measuring a current and monitoring

the oxygen partial pressure p_{O_2} in the carrier gas. The bigger electrode area ($\approx 125\ \mathrm{cm}^2$) is used to induce an oxygen ion flow into the carrier gas by applying a current according to Eq. 61. It therefore acts as an oxygen pump increasing or decreasing the oxygen partial pressure in the carrier gas.

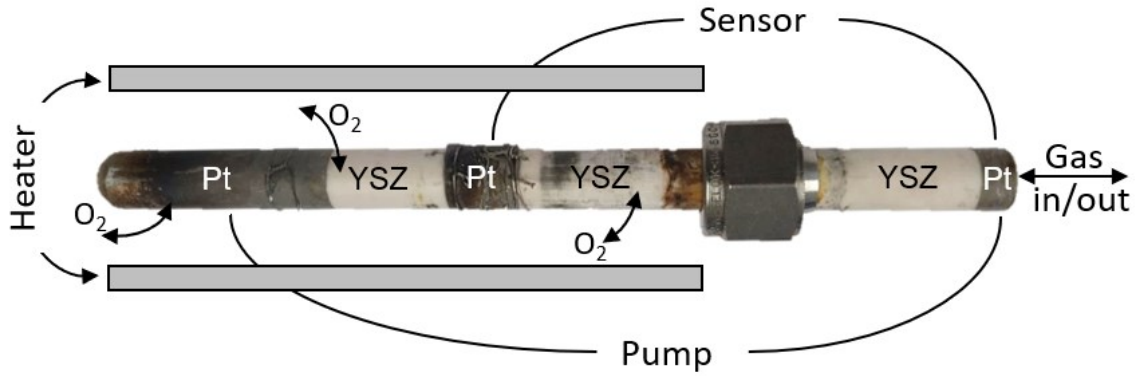

Figure 9: Yttrium-stabilized zirconia (YSZ) ceramic tube with platinum electrode (PT) areas devised as an oxygen ion pump. The carrier gas is let in and out of the tube via a smaller ceramic tube which is not depicted above. The oxygen partial pressure inside the carrier gas can be monitored by measuring the Nernst potential between the electrode areas labeled "sensor". The partial pressure can be increased or decreased by applying a current at the electrode areas labeled "pump".

The OCS system consists of two O^{2-} ion conductors whose operation principle was discussed above. The first one is depicted in Figure 9 and operates as both an oxygen pump and sensor. A second ceramic tube holds only a sensor platinum electrode area and enables the partial pressure measurement independent from the pump position. The pump/sensor combination will be referred to as the "pump unit" while the second ceramic tube will be referred to as the "sensor-unit" in this work. Both ionic conductors are encapsulated in thermal insulation blocks equipped with an electrical heater to ensure a uniform operation temperature of 600°C of the complete measurement are. Resistive temperature sensors are used to monitor the temperature close to the ceramic tubes.

Figure 10 shows a picture of the OCS which was taken while it was opened for maintenance. The gas flow from the EML processing chamber to and through the OCS is schematically marked. The gas flow is realized via a gas circulation pump attached between the EML processing chamber and the gas inlet of the OCS. Figure 10 shows both the "sensor"- and "pump"-unit inserted into the respective electrical heater. During operation, the ionic conductor/heater combinations are enclosed in large thermal insulation blocks, however Figure 10 shows only the lower half of these blocks for better comprehensibility. Since the EML furnace represents an environment with strong electromagnetic noise, electromagnetic interference (EMI) shielding for the entire OCS is needed. In Figure 10 most of the shielding has been removed except for the part in the right border of the picture. Additional heat and EMI shielding is mounted between each ceramic tube and the respective control electronics.

With the pump unit, an oxygen partial pressure between 10^{-24} and 10^{-2} bar can be adjusted in the processing chamber. For this purpose, a 40mA pumping current, whose polarity can be changed, is applied controlled by a PID algorithm. Since the oxygen partial pressure needs to be controlled over more than 20 orders of magnitude, a dynamic adjustment of PID parameters at different partial pressures was employed.

A device similar in construction is planned to be implemented into the EML facility onboard the International Space Station (ISS). Many design choices made for the experimental setup at DLR in Cologne are therefore made against the background of comparability between the two devices. In this way, the DLR facility can provide vital experimental ground support for the experiments planned in space.

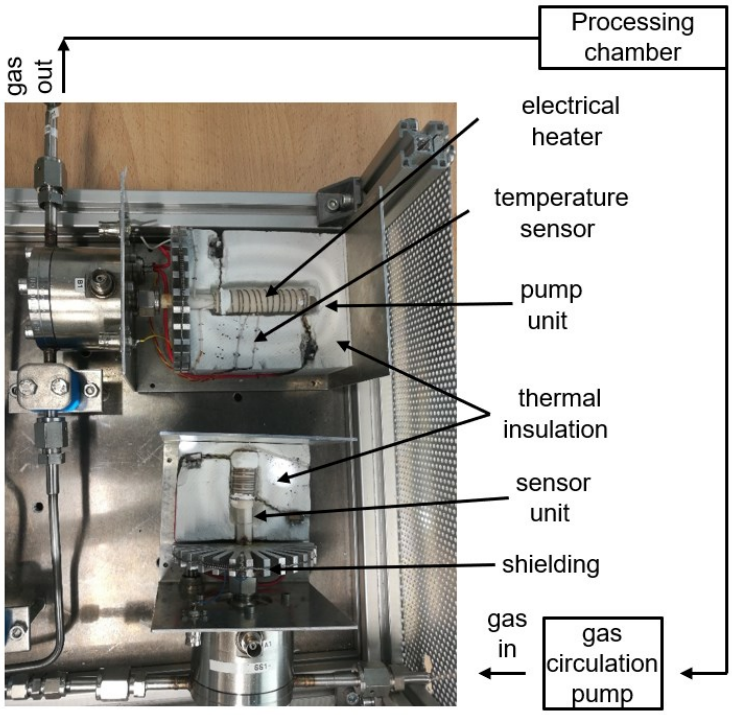

Figure 10: Photograph of the OCS during maintenance. The gas flow from and into the processing chamber is depicted schematically. Most of the thermal insulation as well as EMI shielding has been removed.

3.4 Laser Heating System

It was explained in 3.2.1, that the temperature control during EML experiments is usually realized by applying a constant laminar flow of inert cooling gas (Ar, He) to the liquid droplet. It is obvious that this is not possible, when the oxygen partial pressure of the surrounding atmosphere is of interest. The controlling of the oxygen partial pressure would be completely meaningless if the processing atmosphere is constantly changing due to the applied cooling gas. Adjusting and controlling the partial pressure would not be possible at all.

When aiming for EML experiments including meaningful OSC measurements, a different temperature control technique has to be applied. To achieve a temperature control without cooling gas, the EML furnace was expanded by a 100 W, 915 nm Diode Laser provided by *Mergenthaler GmbH*. The corresponding laser head can be seen in Figure 7 between the vacuum pumps and the generator and oscillator outlet. The general measurement idea was to design a coil (see 4.2) that would steadily levitate the investigated sample while barely melting the sample. The default temperature during levitation without any temperature control is therefore be slightly above the liquidus temperature. The sample temperature can subsequently be increased by increasing the laser power applied to the liquid droplet. To decrease the sample temperature the generator power can be reduced within a certain framework that still ensures a stable levitation. For liquid vanadium a temperature measurement range $\Delta T \approx 200°C$ can be achieved with this method.

Besides the laser fiber the laser head additionally holds both the two-color pyrometer and a normal camera for sample observation during processing. Due to laser power and the associated risks the EML furnace had to be fully encapsulated so that no laser light can escape during processing. To ensure that the capsulation is fixed properly, magnetic interlocks have been attached to all removable parts of the furnace. As soon as only one interlock is opened an operation of the laser is no longer possible.

3.5 TEMPUS – EML

TEMPUS-EML describes the electromagnetic levitation experiments carried during the DLR parabolic flight campaigns. Since TEMPUS – EML and the EML facility at DLR Cologne use mostly the same measurement principle, a detailed description of the TEMPUS – EML would contain countless redundancies. Instead, only the differences that are important for the analysis for the experimental results will be described in detail. A profound description of the experimental setup of the TEMPUS – EML can be found in Ref. [80].

Electromagnetic levitation in a microgravity environment changes two major fundamental aspects of the EML method introduced in 3.2. Under 'microgravity conditions' (during the parabolic flight) the sample only has to be positioned against $10^{-2}g$, with g being the gravitational acceleration. Therefore, the corresponding electromagnetic positioning field can have strong gradients which reduces the power absorbed by the sample by a factor of more than 100, compared to the terrestrial setup. This allows for an effective decoupling of the positioning and heating during the levitation. Additionally, many negative effects, such as evaporation or strong sample rotation, observed in terrestrial EML can be extenuated heavily. In the TEMPUS-EML ("Tiegelfreies Elektromagnetisches Prozessieren Unter Schwerelosigkeit") facility, two different coil systems generate two separate fields that superposition each other corresponding to Figure 11 taken from Ref. [81].

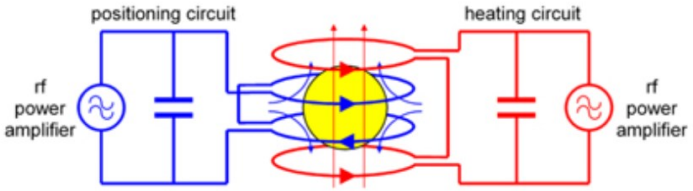

Figure 11:Two different circuits generate the positioning (blue) and the heating (red) magnetic field in the TEMPUS – EML facility. Schematic taken from [80].

Positioning is achieved with an alternating, symmetric quadrupole field with an oscillation frequency of 100 Hz. The heating circuit generates a high efficiency dipole field oscillating with a frequency of 400 Hz. Each circuit consists of a copper coil, a capacitor and a radiofrequency generator. With two separate circuits, the sample can be positioned and heated independently [80].

As a direct result, the turbulent flow, which was described in 3.2, is less pronounced when comparing the TEMPUS – EML (microgravity) facility to the DLR – EML (terrestrial). Therefore, the sample surface must be externally excited by short pulses from the heating coil in order to measure the surface tension with the oscillating drop method (which will be explained in sec. 3.6).

Additionally, some of the disadvantages and experimental difficulties, like magnetic sample shape deformation or strong sample rotation, for electromagnetic levitation under terrestrial condition can be bypassed in a microgravity environment.

To generate a microgravity environment, the TEMPUS – EML facility is installed onboard the Airbus 310 'Zero-G' operated by *NOVESPACE.* The aircraft performs parabolic flight maneuvers as depicted in Figure 12. During each parabola the aircraft enters an effective "freefall" where the sum of all forces, other than gravity, acting on the occupants and their experiments are reduced to almost nothing [82]. After a pull up and a 20 s hyper-gravity phase, the injection into this "freefall" usually happens at an aircraft angle of 47°. After a 22 second period of weightlessness, the aircraft is pulled out at a downwards angle of 42° entering another 20 second period of hyper-gravity (1.8g). Eventually, the aircraft is brought back into a horizontal orientation and steady flight is regained. A usual flight campaign consists of 3 flight days with 33 such parabolas each.

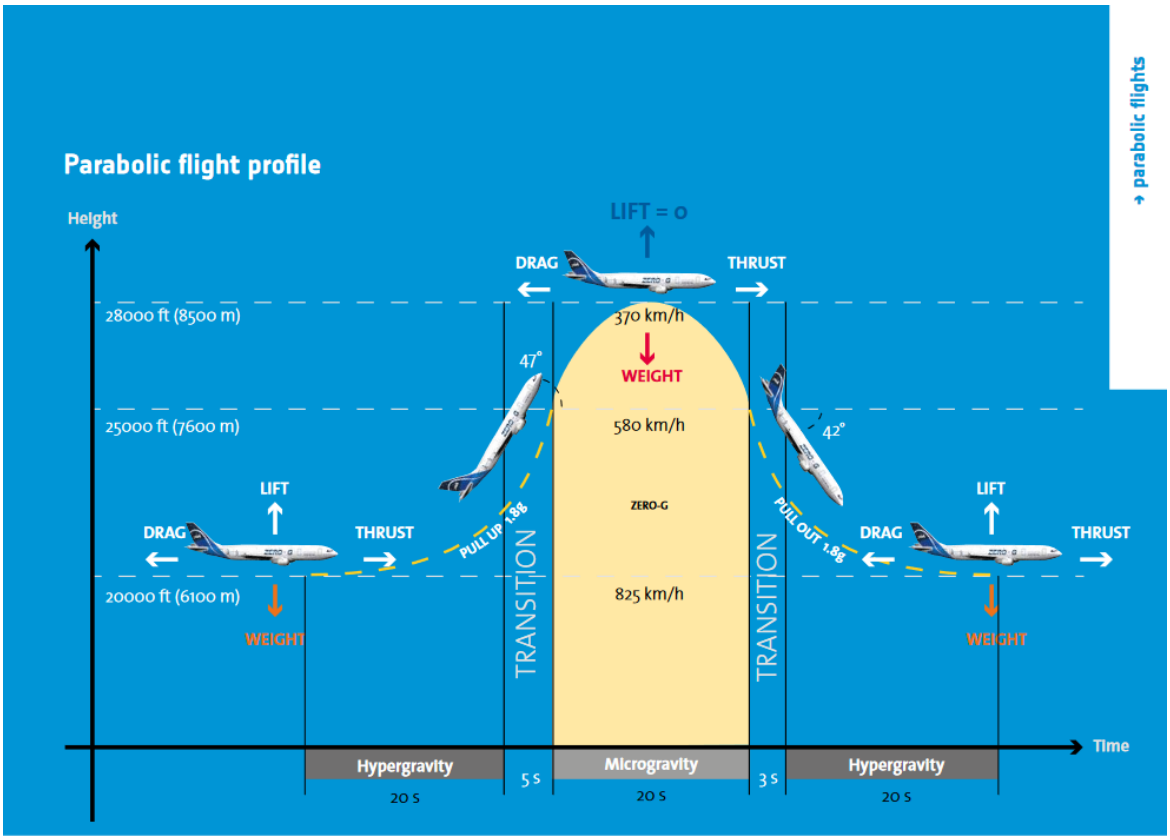

Figure 12: Schematic depiction of a single parabolic flight maneuver performed with the Airbus 310 "ZeroG" to achieve a 22 second weightlessness phase according to Ref. [82].

3.6 Optical Dilatometry

Previously, all means necessary for the levitation and temperature control of a sample have been described in great detail. With our liquid droplet molten and levitating, it is now necessary to specify the diagnostics used for the measurement of its thermophysical properties.

The density of a sample processed with EML is measured by precise determination of its volume V. With the sample mass m known from sample preparation (see 3.1), the density can be calculated as $\rho = m/V$. The "optical dilatometry" method is established as the main technique for the volume, and therefore density measurement during EML [14, 69, 83]. The experimental setup, as used in combination with electromagnetic levitation, is schematically plotted in Figure 13 a). To measure the sample volume during levitation, a shadowgraph image of the sample is cast onto a CCD camera chip. Therefore, a polarized, parallel laser beam (HeNe) is directed onto the sample. Laser light source, sample and CCD camera share the same, horizontal, optical axis. The optical elements (lens, pinhole and polarizer) ensure that only non-scattered light originating from the laser reaches the camera chip. Lens (80mm) and pinhole ($\emptyset = 0.5$ mm) together act as an optical Fourier Filter, while the polarizer varies the light intensity and the interference filter removes any thermal radiation from the sample. The shadowgraph images are captured with a *Mikrotron MC1302* (resolution: 1280 x 1024; frame rate: 100 frames per second) and transferred to an image processing software. The second camera observing the sample through the coil axis is used for error correction and will be explained in more detail later. Figure 13 b) shows an exemplary image. Atop and below the sample in the image center, the shadow cast by the copper coil can be seen. For each image taken an edge detection algorithm determines the sample edge. In Figure 13 c) the area of interest (dotted area), the near-edge area (filled grey area), the sample center (pink dot) and the sample edge curve (solid pink line) are depicted.

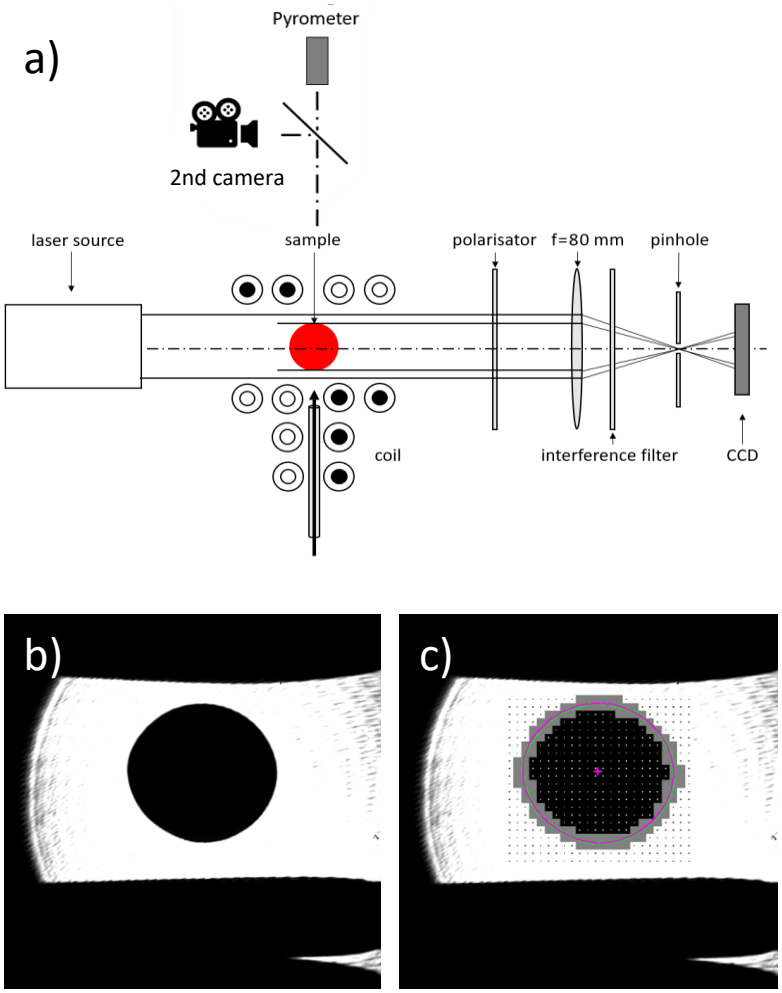

Figure 13: Top: Schematic of the optical elements in the experimental setup of the optical dilatometry method during EML. Bottom: a) Shadow graph image taken during the optical dilatometry measurement; b) edge detection with the image processing software.

To determine the edge curve, each pixel in the area of interest is either identified as an edge pixel or bulk pixel. A pixel is identified as an edge pixel if the derivative of the light intensity is larger than a threshold and forms a local maximum. Otherwise, the pixel is a bulk pixel, or doesn't belong to the sample (depending on the intensity). The edge curve $R(\varphi)$ is described in polar coordinates with the radius R from the droplet center as a function of the azimuthal angle φ [83]. In sec. 3.2 it was explained that a liquid droplet is exposed to oscillations during EML. Therefore, the sample shape in single frames can deviate from the equilibrium shape. As long as these deviations are small compared to the equilibrium shape they can be compensated by averaging over a larger number of frames. In this work the edge curves have been averaged over 2500 frames.

The averaged edge curve is then fitted by Legendre polynomials of an order ≤ 6 according to the following equation:

$$\langle R(\varphi)\rangle = \sum_{i=0}^{6} a_i \Pi_i(\cos(\varphi)) \qquad (62)$$

Here Π_i is the ith Legendre polynomial, a_i is the series coefficient and $\langle \dots \rangle$ marks time averaging for each separate angle φ. With this averaged edge curve Radius $\langle R(\varphi)\rangle$, the sample volume in pixel-units V_P can be calculated when assuming rotational symmetry of the liquid droplet around the vertical axis:

$$V_P = \frac{2}{3}\pi \int_0^{\pi} \langle R(\varphi)\rangle^3 \sin(\varphi)\, d\varphi \qquad (63)$$

The actual sample volume V in cm^3 can be derived from the pixel volume V_P by executing a calibration with metal balls of precisely known volume (RB-4.762/GW20 DIN 5401). The calibration yields a dimensionless scaling factor u which then leads to the sample volume as $V = u * V_P$.

The density is measured in this work during incremental cooling from temperatures well above the liquidus temperature. A 40 s isothermal hold is performed before each measurement, to ensure that the sample has reached thermal equilibrium. Exemplary density data measured in EML is shown in Figure 14. The density of liquid vanadium is measured over approximately 350 K. Each data point represents a measurement over 2500 frames after the afore mentioned 40 s isothermal hold. The liquidus temperature, T_L, of vanadium (2183 K) was marked to show, that a sample undercooling of around 150 K is possible while still obtaining valid density data. The measured data is compared to literature data from Ishikawa et al. measured in electrostatic levitation [18]. The measured data compares well with the literature data regarding the experimental error.

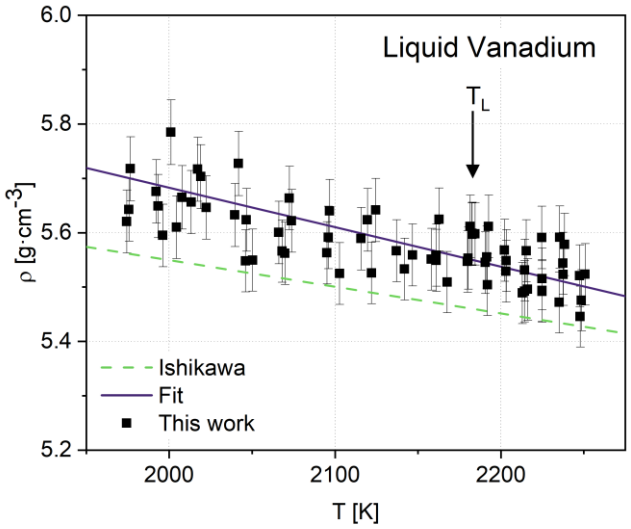

Figure 14: Density of liquid vanadium as a function of temperature. The dashed line shows data measured in electrostatic levitation by Ishikawa et al. [18] for comparison.

To develop a reliable error estimation of the measurement technique, the different contributions to the experimental error have to be identified and assessed. The main error sources for the optical dilatometry method are errors in mass, calibration, volume calculation, temperature as well as a strong lateral sample movement or a strong sample rotation distorting the rotational symmetry. Table 2 shows the main error sources and their impact on the density measurement in EML.

Table 2:Error sources, the appropriate parameter, their order of magnitude as well as their impact on the density measurement via optical dilatometry.

Error source	Parameter	Order of magnitude	Impact on density measurement
Evaporation	m	≤ 0.3%	critical
Calibration	u	≤ 0.6%	critical
Temperature reading	T	≤ 1% (±10 K)	uncritical
Sample rotation	V_p	≤ 0.8%	critical
Purity conditions	x_O	≤1%	medium
Lateral sample movements		≤ 1.25%	uncritical

The error in mass is mainly attributed to evaporation during electromagnetic levitation. Especially, processing for a longer time at temperatures far above the liquidus temperature can lead to sample evaporation. To bypass this, the samples are weighted before and after levitation and measurements with a sample mass loss $\Delta m \geq 0.3\%$ are discarded. The error in volume calculation and calibration are closely intertwined since the calibration is needed to calculate the real sample volume form the sample pixel volume. A calibration is carried out before and after each individual levitation experiment. The deviation in the scaling factor, u, is $\Delta u \leq 0.6\%$. For the error approximation of the pixel volume several volume measurements of calibration bodies (RB-4.762/GW20 DIN 5401) with different known volume have been carried out. The observed deviation is added to the uncertainty of the calibration bodies made by the manufacturer. This results in an error $\frac{\Delta V_\mathrm{p}}{V_\mathrm{p}} \leq 0.8\%$ for the volume calculation. The error associated with the temperature ΔT measurement can be estimated by the measurement error given by the pyrometer manufacturer (±10 K ≈ 1%). For the density measurement itself the error in the temperature reading is rather uncritical, but it has to be considered when evaluating the temperature dependence (e.g. linear fits) of the density.

From the previous considerations the total error for the density measurement can be estimated using a propagation of uncertainty approach according to the following equation:

$$\frac{\Delta\rho^2}{\rho^2} = \frac{\Delta m^2}{m^2} + \frac{\Delta u^2}{u} + \frac{\Delta V_\mathrm{p}^2}{V_\mathrm{p}^2} + \left(\frac{\partial V_\mathrm{p}}{\partial T}\right)^2 \frac{\Delta T^2}{V_\mathrm{p}^2} \qquad (64)$$

In accordance with Ref. [73], the total measurement error for the density measurement with optical dilatometry during electromagnetic levitation is approximately ±1%.

Table 2 additionally mentions purity conditions as a possible error source. Section 3.1describes what measures are taken to avoid any kind of contamination during sample preparation. Since impurities do not impact the density measurement itself and since several precautions are installed to keep them at a minimum, they have not been considered in this calculation.

However, special attention needs to be paid to the sample shape and movement during the levitation process. The density calculation according to Eq. (63) are only valid, if the preceding assumption of averaged rotational symmetry is upheld. In Ref. [84] an expansion to the optical dilatometry method explained above is introduced to measure the density of samples that violate the symmetry assumption. Therefore, a second camera is employed in a perpendicular axis to the original optical axis as shown in Figure 13. The second camera measures the sample edge curve independently to determine an asymmetry factor. The sample volume can then be calculated similar to Eq. (63) but with the inclusion of the asymmetry factor. This new optical method is used to ensure the axial symmetry of the levitated samples on a test basis. Figure 15 shows such an exemplary test in the case of the density measurement of pure liquid titanium as a function of the temperature.

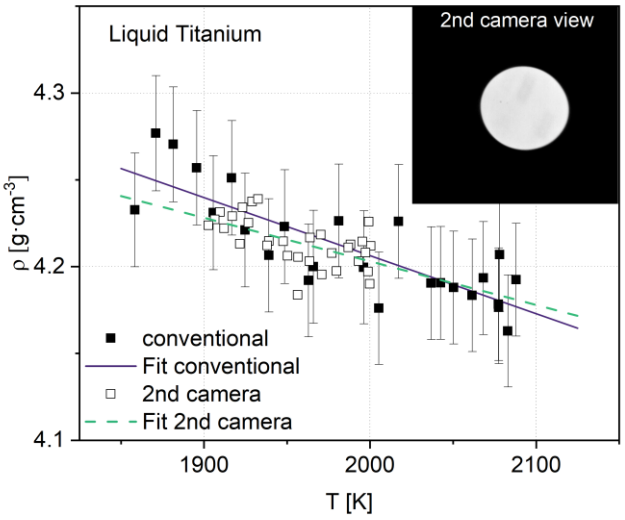

Figure 15: Density measured with the 'classic' optical dilatometry method (filled squares) compared with the density measured with the 'second camera' method (hollow squares). The solid line represents a linear fit for the 'classic' method and the dashed line a fit for the 'second camera' method respectively. The insert in the top right corner shows a single frame recorded with the second camera.

The filled squares represent data points measured with the 'classic' optical dilatometry method utilizing only one camera, while the hollow squares represent data measured with the 'second camera' method. Linear fits are included for both 'classic' (solid line) and 'second camera' method (dashed line). The difference in density measured with both methods is neglectable and therefore the axial symmetry of the time average sample can be assumed.

Similar spot checks have been carried out for different samples. No mentionable difference was found. To keep the experimental effort in a manageable framework, this work mainly focuses mainly on the 'classic' method for the density determination.

3.7 Oscillating Drop Method

The oscillating drop method is a surface tension and viscosity measurement technique for levitating liquid droplets. It has been successfully applied by many previous works [15, 25, 33, 70, 85, 86] using different levitation techniques both under terrestrial and under microgravity conditions. In terrestrial EML it is only possible to measure the surface tension using the oscillating drop method (see sec. 3.2.1). The fundamental condition for this measurement method is, that the liquid sample performs oscillations around its equilibrium shape, with the surface tension being the spring constant. The frequencies of this oscillations can then be related to the surface tension.

Lord Rayleigh provided 1879 [87] a major contribution to the calculation of the surface tension, γ, of a spherical, non-rotating droplet of mass, m, as a function of the oscillation frequency, $\omega_{l,m}$,:

$$\omega_{l,m}^2 = l(l+2)(l-1)\frac{4\pi}{3M}\gamma \qquad (65)$$

In Eq. 65 l describes the oscillation mode and M the sample mass. Due to the spherical symmetry there is a complete degeneracy of the oscillation modes, leading to $2l+1$ possible oscillation modes with identical frequency for every index l.

To illustrate the different oscillation modes, every deformation of a sphere can be described as a sum of multiple spherical harmonics $Y_{\mathrm{l,m}}(\theta, \varphi, t)$:

$$R(\theta, \varphi, t) = \sum_{\mathrm{l}=0} \sum_{\mathrm{m}=-\mathrm{l}}^{+\mathrm{l}} a_{\mathrm{l,m}}(t) Y_{\mathrm{l,m}}(\theta, \varphi, t) \qquad (66)$$

In this equation R is the droplet radius as a function of the polar angle θ, the azimuthal angle φ and the time. Here $a_{\mathrm{l,m}}(t)$ is the time dependent deformation.

For the oscillation corresponding to mode $l = 0$, Eq. (66) yields $R(\theta, \varphi, t) = a_0(t)$ which is the equivalent to an isotropic expansion or contraction of the droplet. For an incompressible liquid droplet this is not compatible with the conservation of mass.

For mode $l = 1$ and small oscillation amplitudes, the resulting oscillation is best described as a translational movement of the entire droplet. Although, this is important for the measurement process, the translational movement does not contain information about the surface tension.

There are five different deformation modes for $l = 2$ ($m = -2, -1, 0, 1, 2$). It is the first fundamental oscillation mode that contributes to the surface tension calculation according to Eq. (66). A geometrical illustration can be found in Figure 16 taken from Ref. [88]. A more detailed mathematical description of the different oscillation modes can be found in Ref. [76] and [88]. In a force-free environment and for a spherical, non-rotating sample the $l = 2$ holds a 5-fold degeneracy at one frequency, $\omega_{2,0}$, which is usually called the Rayleigh frequency, ω_{R}:

$$\omega_{\mathrm{R}}^2 = \frac{32\pi}{3M}\gamma \qquad (67)$$

Expected values for the Rayleigh frequency of samples with a mass of 1g lie around 40 Hz [69]. In electromagnetic levitation experiments under microgravity conditions the preconditions for Eq. 67 are met. Therefore, it has been successfully used to calculate the surface tension from the observed oscillation frequency for such experiments [33, 89, 90].

However, under terrestrial conditions the levitated droplets are no longer force free with the gravitational force and a magnetic force acting upon them. As discussed earlier and depicted in Figure 8, the samples are in result no longer perfectly spherical. Therefore, the spherical symmetry needs to be replaced by a cylindrical symmetry. As a result, the degeneracy of the Rayleigh frequency is lifted and a set of three distinct frequencies $\omega_{2,0}$, $\omega_{2,\pm1}$ and $\omega_{2,\pm2}$ become apparent, with $\omega_{2,\pm1}$ and $\omega_{2,\pm2}$ still being twofold degenerate [91]. In practical levitation devices the coil is usually made from a single copper tube. This results in a coil ‘in-‘ and ‘outlet’ which in turn leads to slight inhomogeneities in the magnetic field. Therefore, additional forces act upon the droplet, which can lead to a sample rotation. Additional sample deformations and the so introduced centrifugal force can further influence the surface oscillations. Busse [92] showed in 1984 that a sample rotation leads to the degeneration being lifted for the oscillation modes $\omega_{2,\pm1}$ and $\omega_{2,\pm2}$. If the rotation frequency, Ω_{rot}, of the sample around its vertical axis is smaller than the oscillation frequencies observed, the frequencies are being shifted by $\frac{m}{2}\Omega_{\mathrm{rot}}$.

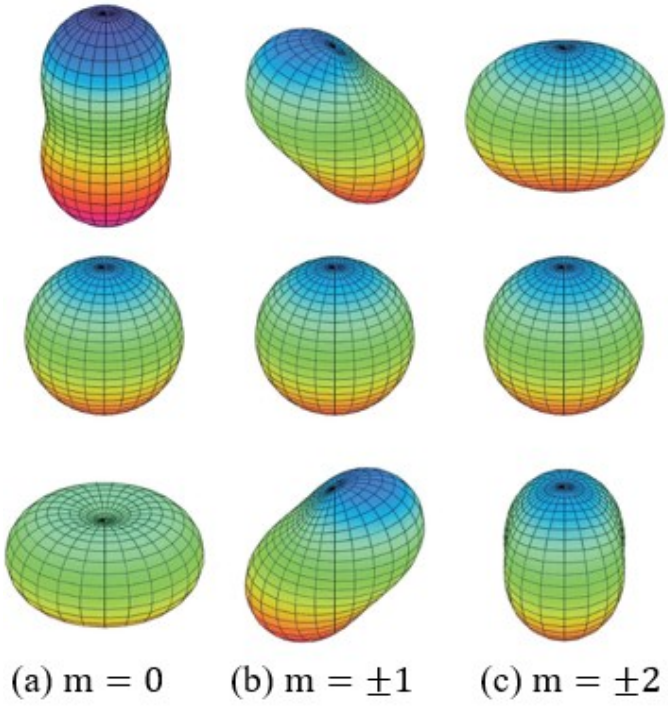

Figure 16: Geometrical illustration of the oscillations of mode $l = 2$ taken from Ref. [88]. For each index pair m, the illustration shows the maximum displacement (top and bottom) around the spherical rest position (middle).

Cummings and Blackburn [91] developed a formalism that combines the five distinct frequencies that are visible in the oscillation spectrum for a sample levitated under terrestrial conditions. In result a more practical equation could be developed in Ref. [69].With the following equation, the surface tension can be calculated as a summation of the frequencies observed during an experiment:

$$\gamma = \frac{3M}{160\pi}\left(\sum_{m=-2}^{2} {\omega^*_{2,m}}^2 - 1.9\overline{\omega_{Tr}{}^2} - 0.3\left(\frac{g}{a\overline{\omega_{Tr}{}^2}}\right)^2\right) \qquad (68)$$

In this equation, M is the sample mass, a the sample radius (if the sample is approximated as a sphere), g the gravitational acceleration and $\omega^*_{2,m}$ are the frequencies shifted by sample rotation. The $\overline{\omega_{Tr}{}^2}$ term is introduced as a correction for the magnetic pressure. It is mean square of the translation frequencies, $\omega_{x,y,z}$, as $\overline{\omega_{Tr}{}^2} = 1/3(\omega_x^2 + \omega_y^2 + \omega_z^2)$. The frequencies ω_x and ω_y are determined from the horizontal translation of the droplet centre, while ω_z is extracted from the spectrum of the apparent droplet area, which changes with vertical movement of the sample due to the changing distance between the sample and the high-speed camera. A mathematically more detailed description for the correction factor can be found in Ref. [76]. Typical frequencies $\omega_{x,y,z}$, lie between 5 and 20 Hz, with the rule of thumb: $\omega_z \approx 2\omega_x \approx 2\omega_y$.

A schematic of the setup used to record the oscillation frequencies of a levitated droplet is depicted in Figure 17. In contrast to the density determination, for the surface tension measurements high-speed videos are recorded of the sample from a top point of view. For electromagnetic levitation, it is usually safe to assume, that the surface oscillations are constantly excited over the experimental duration due to the fluid flow inside the sample (see section 3.2) without an external excitation.

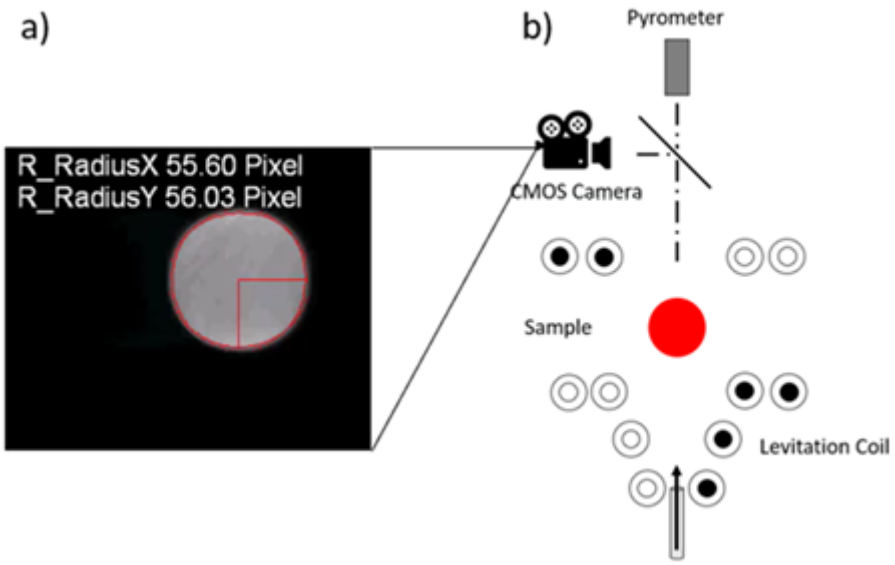

Figure 17: Schematic setup (b) to measure the surface tension of a levitating liquid metal droplet via oscillating drop method. The insert (a) shows a recorded high-speed frame, the detected edge curve and the two perpendicular radii for the frequency determination.

During a conventional experiment, short videos of the sample are recorded during an isothermal hold in stepwise cooling, similar to the density determination. The EML – DLR cologne setup utilizes a *Microtron EoSens Cl MC 1362* camera to record these videos. Usually, 4096 frames with a resolution of 400 x 400 pixels are recorded at a framerate of 400Hz.

Subsequently, a custom video analysis software extracts several parameters needed for the oscillation frequency determination. For each frame, the center of mass position, $(x_0(t), y_0(t))$, the visible sample area $A(t)$ and two perpendicular radii (see Figure 17 a), $r_x(t)$ and $r_y(t)$, are determined. In an additional step these results are transformed via a Fast Fourier Transformation (FFT) to obtain the spectra for the horizontal translation (FFT$(x_0(t), y_0(t))$), the area (FFT$(A(t))$ as well as the sum (FFT$(r_x(t) + r_y(t))$) and the difference (FFT$(r_x(t) - r_y(t))$) of the two radii [76].

A typical result for the translation and area spectra can be found in Figure 18. From these spectra the frequencies, $\omega_{x,y,z}$, needed for the magnetic pressure correction are extracted. In Figure 18 the individual frequencies have already been marked with the corresponding index *x,y* or *z*. The frequencies ω_x and ω_y lie around 12.5 Hz with a small deviation of 0.5 Hz between them. This difference indicates a slight deviation of the copper coil used in the setup from a perfect symmetrical geometry. For a perfectly symmetrical coil both frequencies would be identical. The vertical sample movement frequency needs to be derived from the FFT of the visible sample area. As the sample moves “up and down” along the z-axis, in this case towards and away from the camera on the optical axis (compare Figure 17), the visible area increases (if the sample is closer to the camera) or decreases. Therefore, the frequency ω_z becomes apparent as a minor peak in FFT(A(t)). In Figure 18 this frequency is marked with the index *z*. As the peak is not heavily pronounced, it can sometimes be hard to identify. In those cases, the rule of thumb $\omega_z \approx 2\omega_x \approx 2\omega_y$ can be helpful.

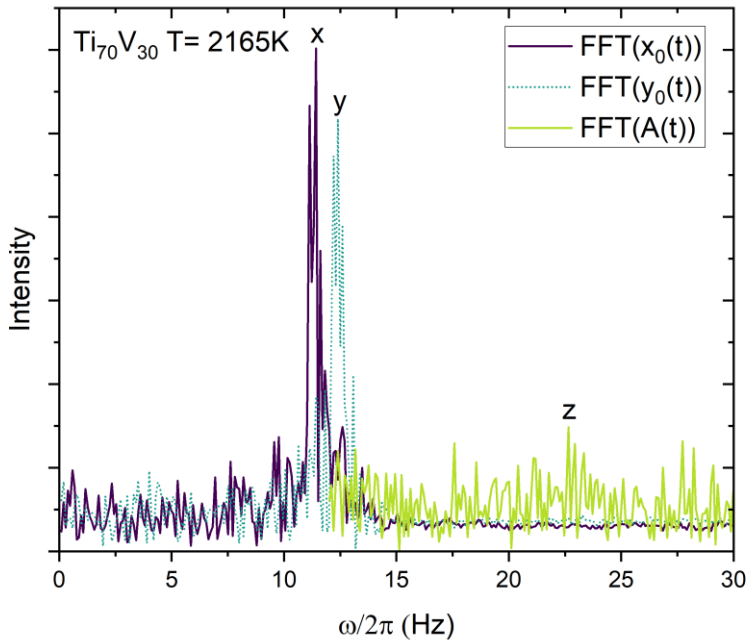

Figure 18: Spectra of the translational sample movement frequencies in x(t) (dark) and y(t) (dotted) direction. The frequency spectrum of the visible sample area A(t) (light) is added to identify the sample frequency in z-direction. The peaks corresponding to the modes are marked with x,y and z. The spectra were recorded for a $Ti_{70}V_{30}$ sample at 2165 K.

Figure 19 shows the frequency spectra of the sum (FFT(r_x+r_y); dotted) and the difference (FFT(r_x-r_y); solid) of the two perpendicular sample radii r_x and r_y (see Figure 17 a). The sum and difference spectra are displayed to facilitate the identification of the five distinct oscillation frequencies, ω_m, needed to successfully apply Eq. 68. By displaying the sum and the difference of two perpendicular radii as the signal, simple geometrical considerations can be employed to selectively mask different oscillation modes, which heavily simplifies the peak identification.

Figure 16 a) illustrates the symmetry with respect to the z-axis for the $\omega_{2,0}$ mode. Since the sample is observed with a camera positioned in the z-axis and since both perpendicular radii are always equal for a rotational symmetrical sample, the $\omega_{2,0}$ mode will vanish in the difference, FFT(r_x-r_y), signal. To identify the $\omega_{2,0}$ mode a peak has to be found in the sum signal, FFT(r_x+r_y), that does not appear in the difference signal, FFT(r_x-r_y). In Figure 19 the $\omega_{2,0}$ peak can be found at 43.2 Hz, appearing only in the sum signal.

To identify the $\omega_{2,+2}$ and $\omega_{2,-2}$ modes, the point symmetry of the oscillation depicted in Figure 16 c) can be used. Imagining a projection of the sample onto a plane perpendicular to the z-axis, it becomes evident, that the expansion in one radius direction is exactly equal to the contraction in the other radius direction, keeping the sum constant. Since in the FFT only signals that vary with time appear and the sum of both perpendicular radii is constant over time, the $\omega_{2,\pm2}$ modes are effectively masked in the FFT sum plot. The $\omega_{2,\pm2}$ peaks can be found in Figure 19 at 37.9 and 41.0 Hz respectively only in the FFT difference.

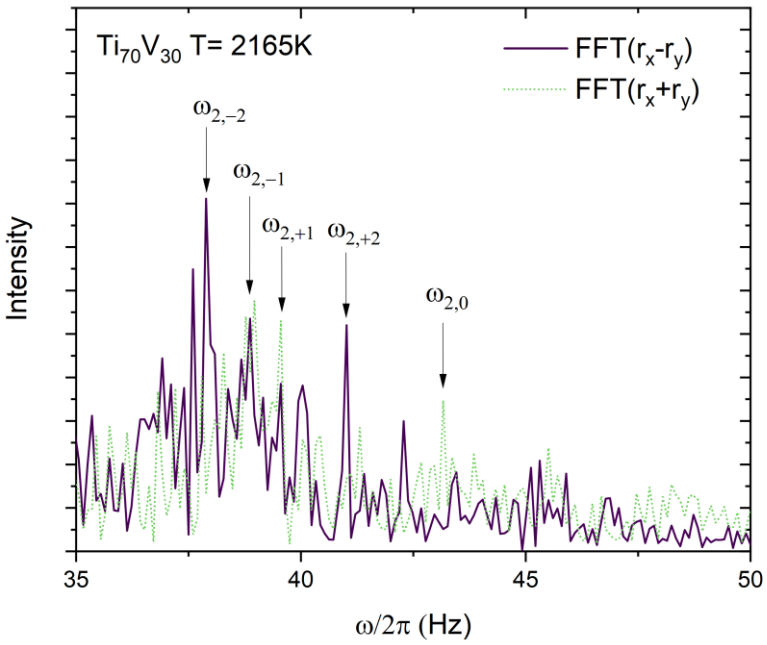

Figure 19: Frequency spectra of the sum (FFT(r_x+r_y); dotted) and the difference (FFT(r_x-r_y); solid) of the two perpendicular sample radii r_x and r_y used to determine the sample surface oscillations. The spectra were recorded for a $Ti_{70}V_{30}$ sample at 2165 K.

The $\omega_{2,\pm1}$ peaks can now simply be identified as the two peaks that can be masked in neither spectrum. Figure 19 shows the two $\omega_{2,\pm1}$ peaks, which are prominent in both the sum and the difference, at 38.8 and 39.5 Hz. With five distinct peaks identified, as done in Figure 19, Eq. 68 can now be employed to calculated the surface tension of the sample at the present temperature.

Since all necessary tools for the surface tension and density measurement are now explained, it is a good opportunity to quickly recap the general measurement procedure. First, the sample is placed onto an alumina specimen holder and put into the copper coil inside the EML furnace. Afterwards, the processing chamber is evacuated down to a pressure of approximately 10^{-6} mbar and subsequently filled back up again with a protective inert gas atmosphere of Ar or He. Now the generator is switched on and the power is carefully increased until the sample is levitated and fully molten. A stepwise cooling process is now initiated by stepwise increasing the cooling gas flow through the alumina specimen holder that now act as a gas nozzle. During the isothermal holds of the stepwise cooling, either density, surface tension measurements or both are conducted. For the surface tension high speed videos of the sample are recorded with the axial camera, for the density shadowgraph images are captured with the radial camera. This procedure is continued until the sample is fully solidified. In a final step, the sample is landed back onto the specimen holder and retrieved from the EML furnace for further examinations.

For an error estimation of the oscillating drop method, a similar scheme as for the density can be used. The conservative approach is to estimate numerical errors for each parameter in Eq. 68. The error in temperature for surface tension is identical with the error in temperature for the density measurements, since the same experimental setup is used. The same can be said for the mass error. Again, samples have been weighted before and after measurement and samples with a mass loss, $\Delta m \geq 0.3\%$ were discarded. The error in the in the frequency identification and reading, is estimated as 0.5 Hz. In accordance with most works utilizing the oscillating drop method [13, 14, 15, 93] the error for the surface tension measured with the oscillating drop method can be estimated as $\frac{\Delta\gamma}{\gamma} \leq 5\%$.

Table 3 shows an overview of the possible error sources for a surface tension measurement using the oscillating drop method.

Table 3: Qualitative error sources, the corresponding equation parameter and their impact on the surface tension measurement

Error source	Parameter	Order of magnitude for surface tension	Impact on surface tension measurement
Evaporation	m	$\leq 0.3\%$	severe
Temperature reading	T	≤ 1% (±10 K)	uncritical
Sample rotation	V_P	$\leq 2.5\%$	critical
Purity conditions	x_O	≤1%	severe
Lateral sample movements		$\leq 1.25\%$	uncritical

A strong sample rotation, which can be caused by a strong coil asymmetry, can lead to a strong sample deformation and violates the assumption of a non-rotating sample made for Eq. 68 to be valid. Strong sample rotations usually appear in the frequency spectra as a single extremely pronounced peak at double the rotation frequency. Lateral sample movement, which is accounted for in the correction for the magnetic pressure, is usually uncritical for the surface tension measurement. However, if the lateral sample movement gets too large, the sample might leave its equilibrium position in the copper coil, which can eventually lead to a sample loss during the levitation.

To ensure a reliable measurement, a steady levitation without strong lateral movement or sample rotation needs to be guaranteed. As mentioned in section 3.2 the coil geometry is vital for the heating and positioning of the sample during levitation. Before each measurement series, test levitations with the pure elements and an alloy of moderate composition of the investigated alloy system are carried out. The coil was slightly adjusted until a steady levitation was achieved for all tested samples.

The last experimental challenge that needs to be mentioned is sample purity and contamination. Previous works have shown, that surface active species can heavily influence the measured surface tension. In the case of pure liquid copper, the surface tension can be reduced by more than 30% if only a few ppm oxygen are in the sample [40]. It is therefore crucial to keep the processing atmosphere “clean” of oxygen, which is why the processing chamber is evacuated down to a pressure of 10^{-6} mbar and filled back up to 750 mbar with an inert noble gas, before each measurement. Additionally, any contamination with other surface-active species during sample preparation has to be avoided. If the purity conditions cannot be maintained a reliable measurement is not possible.

With the machines and methods explained all fundamentals needed to understand and interpret the experimental data are now provided. Every step in the lifecycle of a sample was explained in great detail, so that in the origin of the results presented in the next section can be understood.

4. Results and Discussion

The core of this work is the data obtained on density and surface tension for the liquid Al-Ti-V system. As mentioned earlier the data collection itself is one of the main purposes of this work as it is intended as a data reference for the ternary system for further expansion and use. To therefore make the data of this work as accessible as possible the next sections present all data obtained for density and surface tension. To achieve a convenient data collection, the data is organized corresponding to the property investigated, i.e. the data collection is separated in a density and a surface tension part. Within each property, the data is first presented for the pure elements, then for the binary sub-systems and finally for the section through the ternary system, following the research concept developed for this work.

The second main goal of this work is to obtain a deeper understanding of the mixing behavior in the Al-Ti-V system by comparing the data obtained to established thermodynamic models. Simultaneously, the models can be used to develop predictive tools for the density and surface tension of the Al-Ti-V system. To achieve this goal, both the density and surface tension data section is appended by a discussion part which applies different model to all the data obtained and interprets the data on this basis. The discussion part mirrors the data presentation part in its systematics. The investigations are expanded from the pure elements to the binaries, to the ternary system.

In the last section, the oxygen influence on the surface tension of pure liquid vanadium is investigated to fulfil the final goal of this work. By investigating the oxygen influence exemplary for pure vanadium, three tasks can be accomplished. First, a foundation for the experimental use of the novel Oxygen Control System can be laid, identifying the possibilities and challenges when using this newly developed measurement system. Secondly, the data obtained for liquid vanadium can be used to reevaluate the previously collected data regarding the oxygen influence during the ‘standard’ EML measurement. And lastly, the results help expanding the knowledge on the basic interactions between oxygen and liquid metal melts in the Al-Ti-V system.

4.1 Density

The density, and respectively the molar volume, of the pure elements is the cornerstone of any reliable investigation on binary and ternary alloy systems. Knowing the ideal molar volume, V_i, of a pure component i, is essential when analyzing the density for an alloy system corresponding to Eq. 8. Knowing the density of an alloy is essential when designing a manufacturing process or developing reliable models that predict the behavior of a metallic melts. The density of the pure components in turn, is vital when developing prediction models for the density of alloy systems. Precise knowledge of the density of the pure components is therefore often a basic requirement for many practical applications.

Apart from the practical relevance, the measurements of the pure elements can be used as a scientific assessment of the experimental setup, when comparing the obtained results with already existing literature data measured with different measurement methods and setups. Therefore, the density measurements of the pure elements, aluminum, titanium and vanadium were taken with great care and are presented here rather extensively. For each element the measured density is compared to literature data of different measurement methods. The measured densities are summarized in table form at the end of each sub-section for a convenient use.

4.1.1 Pure Elements

The precise knowledge of the temperature dependent density of pure liquid metals is essential for many practical and fundamental applications. This section is aimed to be a clear compilation of highly precise, temperature dependent density data for liquid aluminum, liquid vanadium and liquid titanium. The section is designed to offer quick and easy access to the measured density for further use. The density of each pure element can be found in a separate table at the end of each sub-section.

Al

Figure 20 shows the density measured as a function of the temperature for liquid aluminum with the optical dilatometry method (described in 3.6) in electromagnetic levitation. The density was measured over a temperature range of roughly 650 K. Undercooling was not achievable, meaning the lowest possible measurement temperature was slightly above the liquidus temperature. As expected, the density of liquid aluminum increases linearly form $2.12\ g{\cdot}cm^{-3}$ at 1700 K to $2.33\ g{\cdot}cm^{-3}$ at the liquidus temperature 933.3 K with decreasing temperature. A linear fit according to Eq. 12 is included. The corresponding fit parameters are summarized in table 4. The results are compared to previously published EML density measurements on liquid aluminum by Wessing et. al [13] (dashed line), density data measured with the sessile drop method by Levin [17] (dash-dotted line) and data recommended by literature review by Assael [94] (dotted line). The dashed, dash-dotted and dotted lines refer to the fit parameters ρ_L and ρ_T proposed by the respective works, rather than actual measured data.

The data of this work compares very well with the data measured by Wessing [13]. Both measurements were carried out in EML facilities with slightly different designs. The literature reference values proposed by Assael [94] are in good agreement with the measured data of this work for high temperatures. For temperatures around the liquidus temperature of aluminum, the suggested density lies slightly higher than the data measured in this work. The density measured with the sessile drop method lies slightly higher over the complete temperature range. Overall, a good agreement with already existing density data for liquid aluminum can be achieved. The linear fit parameters $\rho_L$and ρ_T of literature references are included in Table 5. The abbreviations used for the different measurement methods are explained in Table 4. For clarity, all upcoming abbreviations are also included in this table.

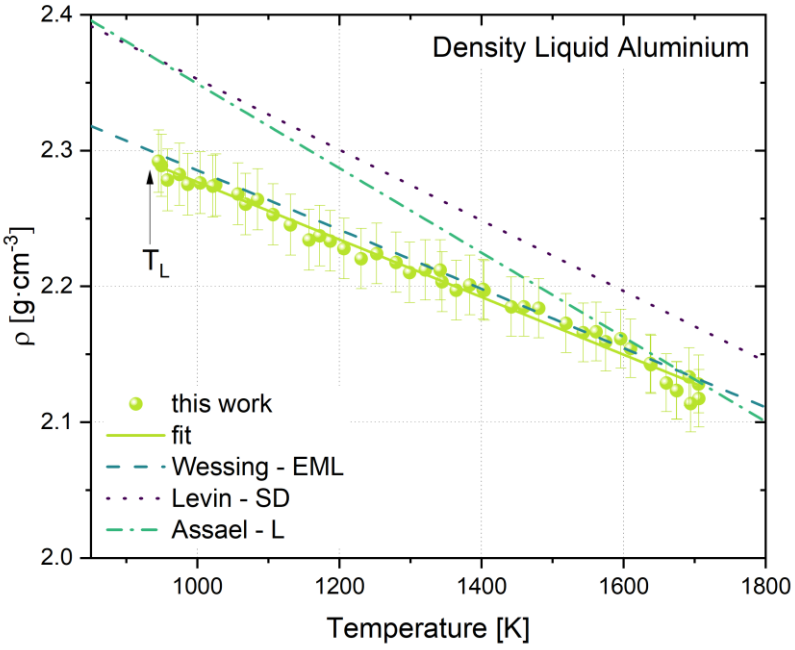

Figure 20: Density of liquid aluminum as a function of temperature. A linear fit according to Eq. 12 is included as solid line. The dashed line shows data measured in electromagnetic levitation by Wessing [13], the dotted line data measured with the sessile drop technique by Levin [17] and the dash-dotted line references data recommended from literature review by Assael [94].

Table 4: Abbreviations used for different measurement methods

Abbreviation	Name
EML	Electromagnetic Levitation
L	Recommendation from literature review
SD	Sessile Drop
XA	X-ray Absorption
ADL	Aerodynamic Levitation
OPH	Ohmic Pulse Heating
EW	Exploding Wire
MD	Molecular Dynamic Simulation
AM	Atomic Modelling

Table 5: Parameters T_L [94], ρ_L, ρ_T and $\rho(1800\ \mathrm{K})$ obtained for the pure liquid Al in this work compared to literature data obtained using different measurement techniques. The keys for the methods referenced can be found in table 4.

T_L – Aluminum [K]	ρ_L[g cm^{-3}]	ρ_T[10^{-4}g cm^{-3}K^{-1}]	$\rho(1800\ \mathrm{K})$[g cm^{-3}]	Reference	Method
933.3	2.33±0.12	-2.15±0.88	2.09	This work	EML
933.3	2.33±0.02	-2.18±0.32	2.09	[13]	EML
933.3	2.36±0.03	-3.30±0.03	2.02	[95]	EML
933.3	2.37±0.015	-3.11±0.2	2.05	[94]	L
933.3	2.37	-2.6	2.10	[96]	SD
933.3	2.37	-2.64	2.14	[97]	XA
933.3	2.4	-3.0	2.14	[98]	ADL
933.3	2.39	-2.99	2.13	[16]	OPH

Overall, the density for pure liquid aluminum at the liquidus temperature (933.3 K [94]) differs within a range of $\pm 1.5\%$ for all measurement techniques. The variation for the temperature coefficient is roughly 10 times higher. As described in section 3 the measurement of ρ_T is influenced by more sources of error, such as mass loss (evaporation) and temperature reading. For a precise measurement of the temperature coefficient a large experimentally accessible temperature range is necessary. In many cases, an expansion of the temperature range leads to the introduction of more error sources, such as heavier evaporation or stronger sample movement and rotation.

However, since ρ_T is comparably small the variance in ρ_T will not introduce a significant uncertainty for the density measurement over the experimentally achievable temperature ranges.

Ti

The density measured for pure liquid titanium is shown in Figure 21 as a function of the temperature. A reasonable measurement could be carried out over a temperature range of $\Delta T \approx 230$ K. In this experimental temperature range a steady levitation with no major evaporation was achieved. The liquidus temperature of 1941 K is marked in the figure. In contrast to pure liquid aluminum, an undercooling of roughly 100 K could be realized when processing titanium. The density measurement shows the expected linear decrease. The fit according to Eq. 12, $\rho_{\mathrm{Ti}}(T) = 4.21 \pm 0.03\ \mathrm{g\,cm^{-3}} - 3.45 \pm 0.3 \cdot 10^{-4}\mathrm{g\,cm^{-3}K^{-1}}$ is also included in the plot.

The measured data is compared to a selection of already published density data measured at different electromagnetic and electrostatic levitation (ESL) devices. The density data of this work lies well between the highest density reported in literature by Saito [20] et. al. measured in EML and the lowest density presented by Wang [99] measured in ESL. The density measured is in good agreement with previously published density data also measured in EML at the '*Institut für Materialphysik im Weltraum'* by Wessing [13]. Additionally, the density observed is almost identical to the ESL data reported by Zou [100]. A more complete comparison with even more literature data compared to the data of this work can be found in Table 6.

Overall, the density at the liquidus temperature, ρ_{L}, observed in this work compares well with already existing literature data.

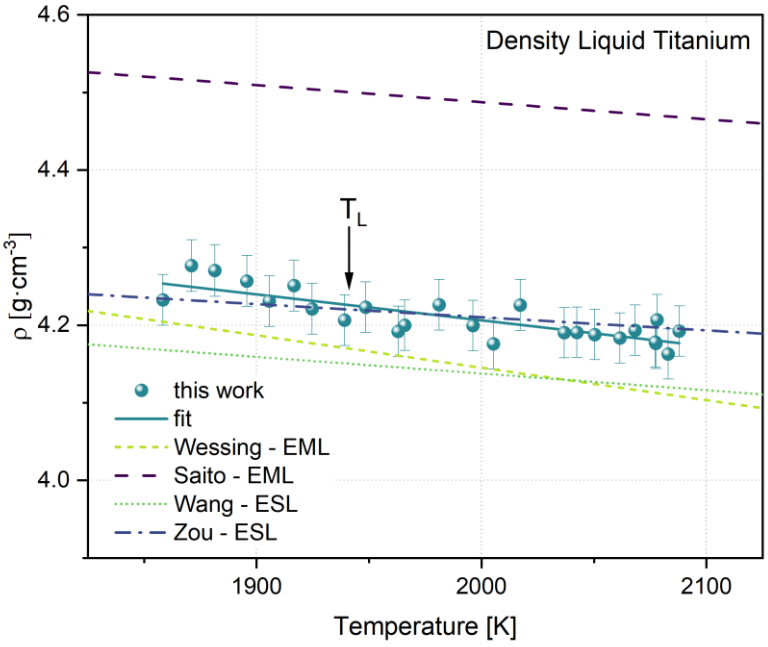

Figure 21: Density of pure liquid titanium as a function of temperature. A linear fit according to Eq. 9 is included as solid line. The short-dashed line shows data measured in electromagnetic levitation by Wessing [13], the dotted line shows data measured with the ESL by Wang [99], the dash-dotted line references ESL data by Zou [100] and the long-dashed line illustrates older EML data by Saito [20] .

Table 6: Parameters T_L [66], $\rho_{\square}L$, ρ_T and $\rho(1800\ \mathrm{K})$ obtained for the pure liquid titanium in this work compared to literature data obtained using different measurement techniques. The keys for the methods referenced can be found in Table 4.

T_L – Titan [K]	$\rho_L[\mathrm{g\ cm^{-3}}]$	$\rho_T[10^{-4}\mathrm{g\ cm^{-3}K^{-1}}]$	$\rho(1800\ \mathrm{K})[\mathrm{g\ cm^{-3}}]$	Reference	Method
1941	4.21±0.03	-3.45±0.30	4.25	This work	EML
1941	4.17±0.07	-4.18±3.02	4.23	[13]	EML
1941	4.5±0.06	-2.2	4.53	[20]	EML
1941	4.15	-2.15	4.18	[99]	MD
1941	4.29	-2.3	4.32	[101]	EW
1941	4.19±0.06	-2.3	4.22	[102]	ESL
1941	4.21±0.02	-5.08	4.28	[103]	ESL
1941	4.22	-1.69	4.24	[100]	ESL

V

The measured density of pure liquid vanadium is displayed in Figure 22 as a function of temperature. The experimentally achievable temperature ranges from $2250\ \mathrm{K} > T > 1975\ \mathrm{K}$. With the liquidus temperature $T_L = 2183\ \mathrm{K}$ (marked with the arrow in Figure 22), an undercooling of more than 200 K could be achieved.

Similar as for both pure aluminum and pure titanium the density declines linearly with increasing temperature. A linear fit according to Eq. 12 was carried out and is shown in Figure 22 as a solid line. The resulting linear fit parameters, ρ_L and ρ_T can be found in Table 7.

The experimental results are compared to existing literature EML data measured by Saito [20] and ESL data by Ishikawa et. al. [18]. The corresponding linear functions are included in Figure 22 as the dash-dotted line (EML, Saito) and the dotted line (ESL, Ishikawa) respectively. Additionally, a linear fit recommended by a recent literature review by Ntonti et. al. [104] was included as the dashed line. Both, the recommendation from literature review and the ESL measurements from Ishikawa lie within the experimental error of $\pm 1\%$ for the density measured in this work over the complete temperature range. Only the data by Saito lies roughly $0.3\ \mathrm{g{\cdot}cm^{-3}}$ lower than the measured density for pure liquid vanadium of the complete measurement range. Overall, the good agreement with already existing data confirms the assumption of a reasonable density measurement for pure liquid vanadium in the present electromagnetic levitation furnace. Compared to pure aluminum and pure titanium the literature data availability is much more scares for liquid vanadium.

The data obtained for liquid vanadium shows a slightly higher experimental scatter than the data collected for pure aluminum and titanium. This can be explained with the slightly more challenging levitation of vanadium. Because of its high melting point, it is harder to achieve a stable levitation of a fully visible liquid droplet. Eventually, a more turbulent levitation translates to an increased experimental error. However, the setup adjustments made (mostly coil adjustments) allowed for a reasonable density measurement.

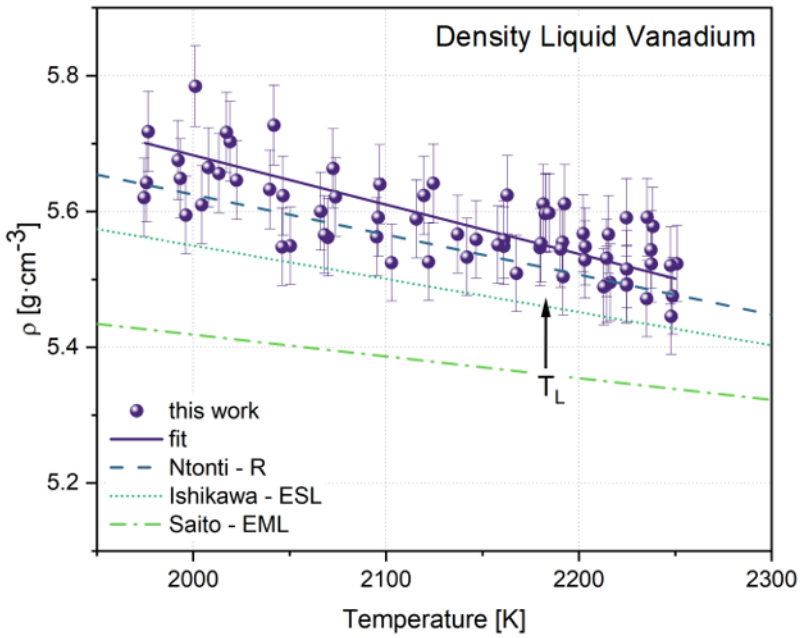

Figure 22: Density of pure liquid vanadium as a function of temperature. A linear fit according to Eq. 9 is included as solid line. The dashed line shows data recommended by literature review by Ntonti [104], the dotted line shows data measured with the ESL by Ishikawa [18] and the dash-dotted line references EML data by Saito [20].

Table 7: Parameters T_L [66], ρ_L, ρ_T and $\rho(1800\ \mathrm{K})$ obtained for the pure liquid vanadium in this work compared to literature data obtained using different measurement techniques. The keys for the methods referenced can be found in table 4.

T_L – Vanadium [K]	ρ_L[g cm^{-3}]	ρ_T[10^{-4}g cm^{-3}K^{-1}]	$\rho(1800\ \mathrm{K})$[g cm^{-3}]	Reference	Method
2183	5.55±0.03	-6.01±0.52	5.78	This work	EML
2183	5.36±0.09	-3.20	5.48	[20]	EML
2183	5.46	-4.9	5.65	[18]	ESL
2183	5.51±0.02	-5.89	5.73	[104]	R
2183	5.44	-4.5	5.61	[21]	R

When the compositional dependence of the mixing behavior of two or more components is investigated in this work, the molar volume of the pure components is usually needed. Therefore, Figure 23 gives an overview over the molar volume of the pure liquid elements as a function of temperature. Additionally, Figure 23 enables a comparison between the measured values for the individual elements.

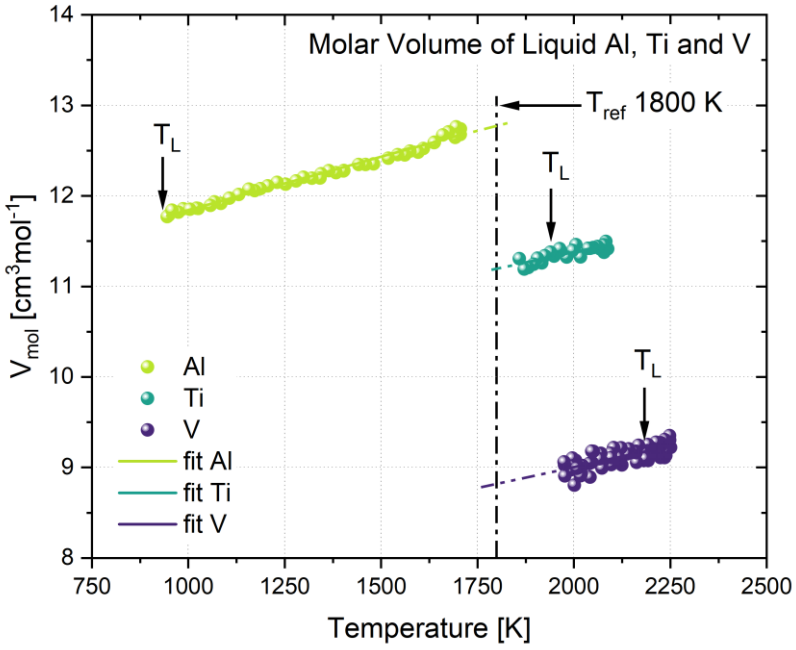

Figure 23:Molar volume of pure liquid aluminum, titanium and vanadium as a function of the temperature. The respective liquidus temperatures are marked for every element. The reference temperature (T_{ref} = 1800 K) for later comparisons is also marked.

Figure 23 also illustrates the different experimentally available temperature ranges for each element. These have their origin in the vastly different liquidus temperatures of the elements. The liquids temperatures and the maximum and minimum experimentally achievable temperatures are summarized together with the molar masses for each element in Table 8. Since the liquidus of aluminum is more than 1000 K below that of titanium and vanadium, evaporation of aluminum occurs before the temperature range of Ti and V can be reached. These differences have to be considered when designing the ideal experimental setup for each element and eventually for each different alloy.

Additionally, the different liquidus temperatures and subsequently different measurement temperatures complicate a comparison of the measured data. In this work a fixed temperature of 1800 K was chosen as a reference temperature for all compositions containing Al (see dash-dotted line in Figure 23), as it lies central in-between all measurement temperatures. However, it has to be considered, that this reference temperature lies outside the actual experimental range for the pure elements.

Table 8: Molar Mass M, liquidus temperature T_{liq} and maximum and minimum achievable temperature during EML, T_{max} and T_{min}, for the pure elements aluminum, titanium and vanadium.

Element	M [kg·mol^{-1}]	T_{liq} [K]	T_{max} [K]	T_{min} [K]
Al	26.98	933.3 [94]	1706	945
Ti	47.87	1941 [66]	2087	1858
V	50.94	2183 [66]	2247	1977

4.1.2 Binary Alloys

Even though the density of the pure elements is important fundamental knowledge for many continuing applications, industrial used metals are mostly alloy systems of varying complexity. Therefore, the density of the different alloys within the Al-Ti-V system is of even greater practical interest than that of the pure elements.

In this section the density measured for the binary alloys will be presented. The systematical approach remains the same as for the pure elements. The experimental data will be attributed to the appropriate binary sub-system. At the end of each binary system, an overview table will be given for the temperature dependent density of each investigated alloy composition.

Ti-V

Figure 24 shows the density measured for all tested alloy compositions in the binary Ti-V system versus the temperature. The data for pure Ti and V, discussed in sec. 4.1.1, is included as reference. Symbols of the same kind and color represent different measurements for different samples of the same alloy composition. The individual measurements follow the same systematical approach as the pure elements. Every composition shows a linear decrease in density with increasing temperature. Therefore, linear fits according to Eq. 12 could be carried out for every composition. The fits are included in Figure 24 as solid lines and the corresponding fit parameters are summarized in Table 9.

The densities observed for the alloys vary between the density of the pure elements over the complete temperature range. Overall, the density increases with increasing vanadium mole fraction. The achievable temperature range is very similar for all processed samples. All samples could be investigated over at least 250 K. All samples could be steadily levitated without major evaporation. The possible undercooling increased with increasing vanadium mole fraction, with alloys of intermediate composition displaying the highest possible temperature range.

To ensure the clarity of the plot, error bars were omitted. The experimental error is comparable to that of the pure elements. To compare the densities of the single alloys in the Ti-V system with each other, a reference temperature was fixed at 2023 K. Since no aluminum is present in the system a use of the afore mentioned reference temperature of 1800 K would be not useful. The reference temperature is marked in Figure 24 and included in Table 9.

Table 9 also includes the liquidus temperature T_L for every composition. The temperatures were taken from the phase diagram of Ti-V reported in Ref. [66]. The linear fit parameters reported in Table 9 correspond to the mean values of every measured sample.

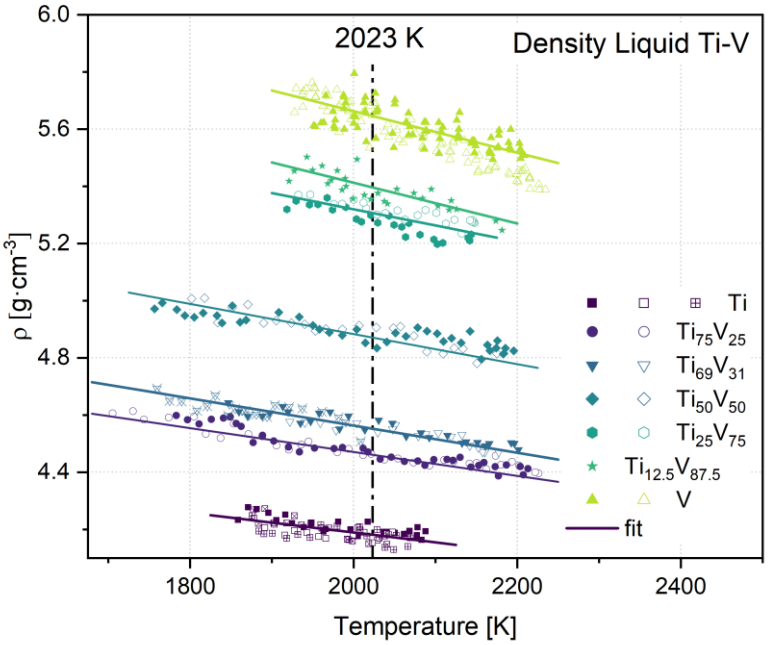

Figure 24: Density of the liquid Ti-V system versus the temperature. The solid lines represent the linear fits according to Eq. 9. The dash-dotted line marks the reference temperature 2023 K.

Table 9: Parameters T_L, ρ_L and ρ_T for every composition examined in the Ti-V system. Additionally, the isothermal densities for 2023 K *are shown.*

Composition	T_L[K]	ρ_L[g cm^{-3}]	ρ_T[10^{-4}g cm^{-3}K^{-1}]	ρ(2023 K)[g cm^{-3}]
Ti	1941	4.21	-3.92	4.17
$Ti_{75}V_{25}$	1883	4.54	-4.4	4.47
$Ti_{69}V_{31}$	1881	4.62	-4.75	4.55
$Ti_{50}V_{50}$	1893	4.93	-4.29	4.88
$Ti_{25}V_{75}$	2053	5.29	-5.67	5.31
$Ti_{12.5}V_{87.5}$	2088	5.43	-7.11	5.47
V	2183	5.55	-6.01	5.64

Al-V

The density was measured for ten different alloy compositions within the Al-V system. The experimental results are shown in Figure 25 together with the densities measured for the pure components Al and V (measured in 4.1.1) as a function of temperature. Each investigated composition is listed together with the corresponding liquidus temperature in Table 10. The $Al_{30}V_{70}$ sample could not be reasonably processed due to extreme evaporation during the levitation. All other compositions could be measured over a temperature range of roughly 200 K. In some cases, the maximum temperature had to be adjusted to avoid excessive evaporation. For this reason, some medium compositions exhibit an abridged experimental temperature range. For clarity error bars are only included for a single measurement in each measurement series.

As expected, the density of the alloy compositions lies within the density measured for the pure elements, with the density increasing with increasing vanadium mole fraction. Each alloy test series shows the usual linear decline in density with increasing temperature. Thus, a linear fit (Eq. 12) could be carried out for every series. The fits are included in Figure 25 and the fit parameters are summarized in Table 10.

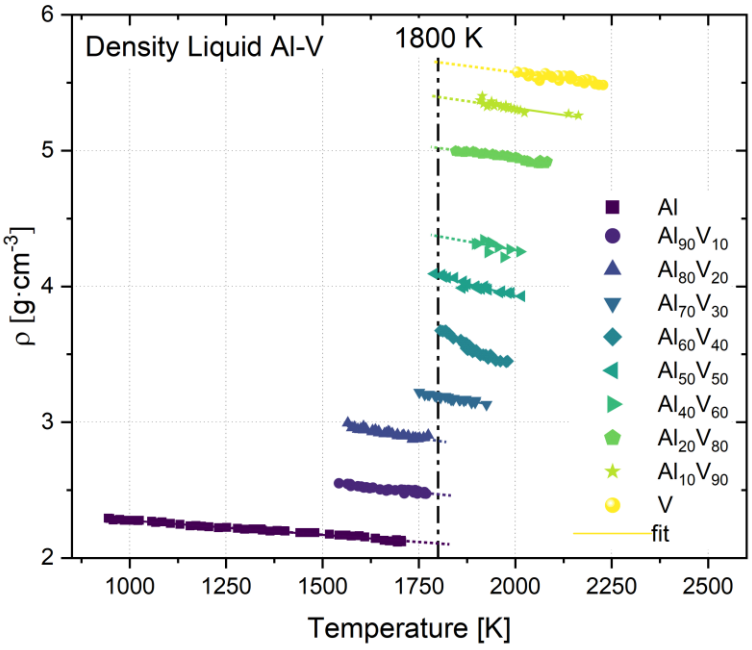

Figure 25: Density versus temperature for all investigated samples in the Al-V system. Linear fits following Eq. (12) are also included. The density decreases linearly with increasing temperature for all alloys. The density for the alloys lies between the density for the pure elements. The data is displayed without error bars for clarity reasons. The usual experimental error is ±1% as explained under sec. 4.4.

The experimental scatter observed in Figure 25 increases slightly towards medium alloy compositions of 50 at.% vanadium and aluminum. This can be attributed to a slightly less stable levitation for alloys of medium composition. However, the total scatter is still within the ±1 % experimental error associated with the optical dilatometry method in EML (see sec. 3.6).

For the Al-V system 1800 K was set as a reference temperature for further investigation since it lies well in the middle of the temperature ranges. The density as the reference temperature is also included in Table 10. Additionally, the liquidus temperature read out of the phase diagram given in Ref. [65] can also be found in Table 10.

Table 10: Parameters T_L, ρ_L, ρ_T and $\rho(1800\ \mathrm{K})$ for the density measurements carried out in the Al-V system. The liquidus temperatures were read out form the phase diagram given in Ref. [65].

Composition	T_L[K]	ρ_L[g cm^{-3}]	ρ_T[10^{-4}g cm^{-3}K^{-1}]	$\rho(1800\ \mathrm{K})$[g cm^{-3}]
V	2183	5.51±0.15	-3.56±0.07	5.586
$V_{90}Al_{10}$	2130.5	5.26±0.17	-4.08±1.28	5.325
$V_{80}Al_{20}$	2108	4.90±0.40	-3.99±0.44	4.953
$V_{60}Al_{40}$	2090.5	4.54±0.29	-5.27±1.15	4.387
$V_{50}Al_{50}$	2055.5	4.09±0.17	-4.58±1.07	4.010
$V_{40}Al_{60}$	1930.5	3.83±0.17	-4.95±1.38	3.422
$V_{30}Al_{70}$	1803	3.67±0.11	-3.70±0.52	3.125
$V_{20}Al_{80}$	1580.5	2.96±0.15	-4.61±0.57	2.782
$V_{10}Al_{90}$	1485.5	2.56±0.11	-2.91±0.41	2.419
Al	933.45	2.33±0.12	-2.15±0.88	2.099

Al-Ti

For the sake of completeness, the Al-Ti system needs to be mentioned here as well. Measurements on the density of the liquid Al-Ti have already been carried out at the *'Institut für Materialphysik im Weltraum'* before the beginning of this work. The data was adapted to fit the layout of this work. The data was taken from Ref. [13] and is shown in figure 26.

The density of the liquid Al-Ti system shows very similar trends to Al-V system. All samples could be measured over a temperature range of at least 300 K. The density decreases linearly with increasing temperature allowing for linear fits as discussed earlier. The corresponding fitting parameters can be found in Table 11. The density increases from pure aluminum, showing the lowest density, with increasing titanium mole fraction. Pure titanium shows the highest density.

A more detailed presentation of the density data can be found in Ref. [13]. For the measurements in [13] a different EML furnace was used. However, the same optical dilatometry setup was used and the same systematics were applied when analyzing the results. The experimental setup used in this work was designed to assure maximum comparability.

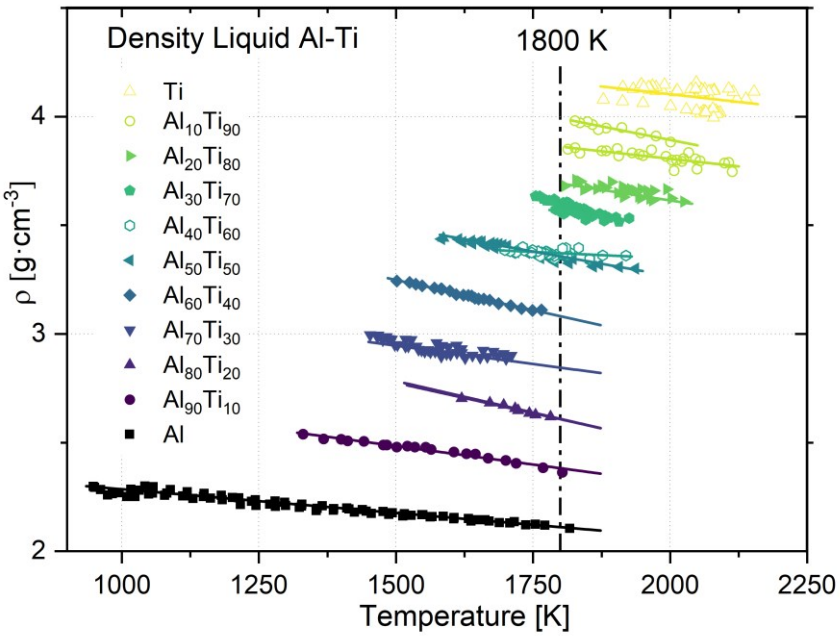

Figure 26: Density of the liquid Al-Ti system as a function of the temperature. The data was taken from Ref. [13] and adapted to the layout of the present work. Linear fits (Eq. (12)) are included as solid lines. The reference temperature was changed to 1800 K *in accordance with this work.*

Table 11: Parameters T_L, ρ_L, ρ_T *and* $\rho(1800\ K)$ *for the density measurements carried out in the Al-Ti system. The data was taken from Ref. [13].* $\rho(1800\ K)$ *was calculated (Eq. (12)) to fit the data into the framework of this work.*

Composition	T_L[K]	ρ_L[g cm^{-3}]	ρ_T[10^{-4}g cm^{-3}K^{-1}]	ρ(1800 K)[g cm^{-3}]
Ti	2183	4.12±0.04	-0.85±1.23	4.15
$Ti_{90}Al_{10}$	1962	3.87	-3.88	3.93
$Ti_{80}Al_{20}$	1948	3.65	-3.54	3.70
$Ti_{70}Al_{30}$	1915	3.53	-5.39	3.59
$Ti_{60}Al_{40}$	1853	3.37	-1.18	3.43
$Ti_{50}Al_{50}$	1757	3.36	-4.71	3.16
$Ti_{40}Al_{60}$	1721	3.13	-5.56	3.31
$Ti_{30}Al_{70}$	1689	2.90	-3.45	2.86
$Ti_{20}Al_{80}$	1654	2.69	-5.7	2.61
$Ti_{10}Al_{90}$	1562	2.46	-3.41	2.37
Al	933.45	2.30±0.02	-2.18±0.32	2.11

4.1.3 Ternary alloys

The first objective of this work, an extensive data collection for liquid Al-Ti-V alloys, is set to contribute to the long-term goal of creating a comprehensive thermophysical data base for the complete Al-Ti-V system. However, a complete, systematical study of the density for the ternary Al-Ti-V system would go well beyond the scope of this work. However, the investigations done for the binary system can fundamentally be expanded upon the ternary system. In this work a single section through the Al-Ti-V system is investigated. For this section the aluminum atomic concentration was varied from 0 to 100 at.% with the Ti to V ration being 1:1. The section is marked in the liquidus projection of the Al-Ti-V system taken from Ref. [105]. Based on this section, the fundamental question that will be investigated is, whether there is a ternary term (Eq. 9) that needs to be considered for the $Al_xTi_{0.5(1-x)}V_{0.5(1-x)}$ section or whether the density can be described based on the binary sub-systems alone. With this objective in mind, the section was chosen to start at pure vanadium, increasing the transition metal atomic concentration in 10 at.% steps while keeping the ratio between titanium and vanadium constant.

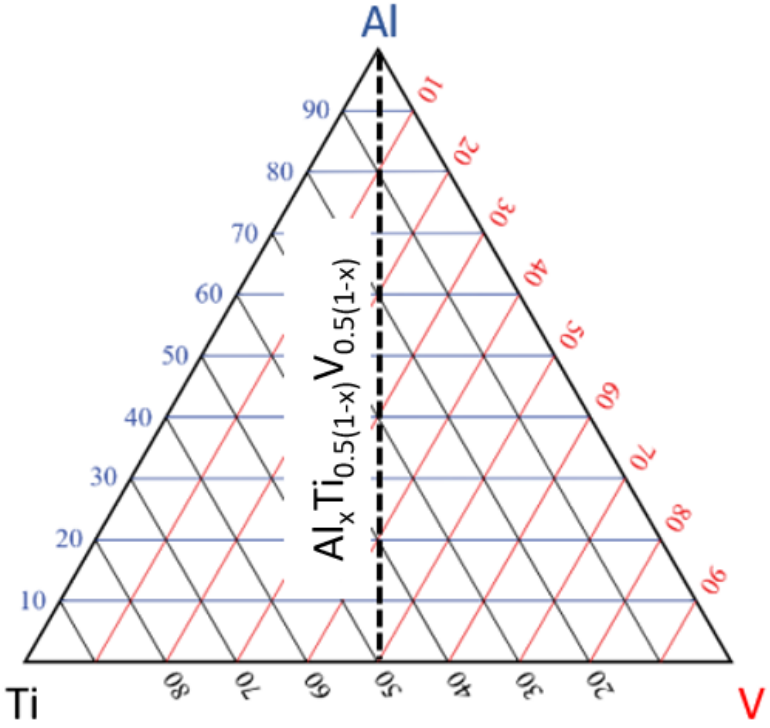

Figure 27: Al-Ti-V liquidus projection taken from Ref. [105] with the investigated section $Al_xTi_{0.5(1-x)}V_{0.5(1-x)}$ marked as the dashed line.

The density for the ternary system was measured analogously to the pure elements and the binary sub-systems. Samples of ten different compositions (10 at.% steps), following the section depicted in Figure 27, were prepared and analyzed using the optical dilatometry method. The resulting densities are plotted in Figure 28 against the temperature. To ensure reasonable measurements, the *'edge compositions'* Al and $Ti_{50}V_{50}$ were measured anew. Both measurements match very well with their previous counter parts (see sec. 4.1.1 Table 5 and 4.1.2 Table 9). Due to strong evaporation, a reasonable measurement for $Al_{60}Ti_{20}V_{20}$ was not possible. Every other composition in the system could be measured over a temperature range of at least 300 K.

Every composition investigated shows the already known linear decrease in density with increasing temperature. This allows for linear fits following Eq. 12, which are included in Figure 28 as solid lines. As for the binary systems the associated fit parameters, liquidus temperatures and densities at the

reference temperature of 1800 K are summarized in Table 12. The liquidus temperatures were calculated using the '*TCAL 5: TCS Al-based Database'* with the Thermo-Calc software.

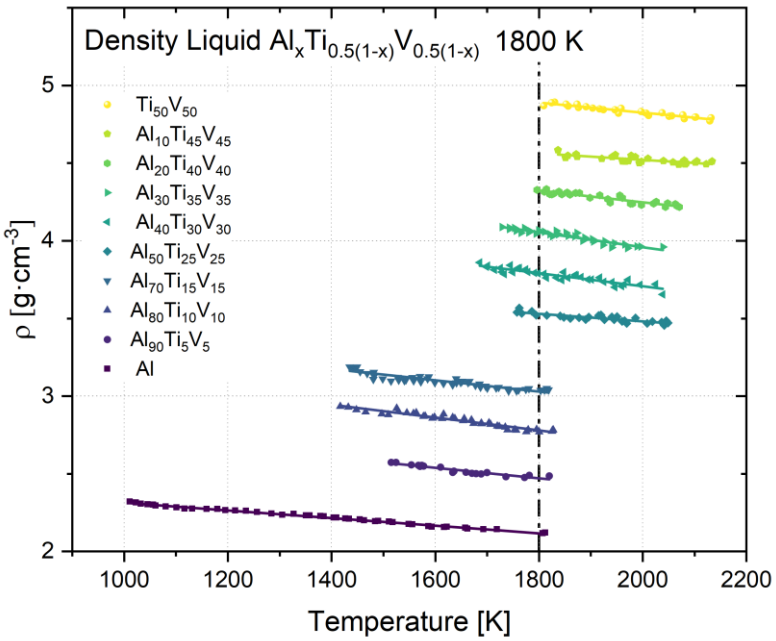

Figure 28: Density versus temperature for all investigated samples in the Al-Ti-V section. Linear fits following Eq. 12 are also included. The density decreases linearly with increasing temperature for all alloys. The density for the alloys lies between the density for pure aluminum and $Ti_{50}V_{50}$. The data is displayed without error bars for clarity reasons. The usual experimental error is ±1% as explained under sec. 3.6.

As expected the density for every alloy lies between the density observed for pure aluminum and $Ti_{50}V_{50}$. The density increases with decreasing aluminum mole fraction. Similarly, to the Al-V system, the experimental scatter increases slightly for medium compositions of 50 at.% aluminum. These samples usually also show a slightly less stable levitation.

As the system contains aluminum, 1800 K was chosen as a reference temperature for later analysis. The reference is included in Figure 28 as a dash-dotted line.

Table 12: Parameters T_L, ρ_L, ρ_T and $\rho(1800\ K)$ for the density measurements carried out in the Al-Ti-V section. The liquidus temperatures were calculated using the TCAL 5: TCS Al-based Database with the Thermo-Calc software.

Composition	T_L[K]	ρ_L[g cm^{-3}]	ρ_T[10^{-4}g cm^{-3}K^{-1}]	ρ(1800 K)[g cm^{-3}]
$Ti_{50}V_{50}$	1897	4.95±0.12	-3.26±0.39	5.586
$Al_{10}Ti_{45}V_{45}$	1976.3	4.59±0.11	-2.05±0.54	5.325
$Al_{20}Ti_{40}V_{40}$	2006.77	4.35±0.11	-3.72±0.36	4.953
$Al_{30}Ti_{35}V_{35}$	2009.6	4.08±0.19	-4.76±4.25	4.387
$Al_{40}Ti_{30}V_{30}$	1974.2	3.83±0.25	-4.20±0.59	4.010
$Al_{50}Ti_{25}V_{25}$	1875.9	3.58±0.13	-2.43±0.62	3.422
$Al_{70}Ti_{15}V_{15}$	1658	3.18±0.19	-3.66±0.60	3.125
$Al_{80}Ti_{10}V_{10}$	1656.6	2.95±0.12	-4.14±0.57	2.782
$Al_{90}Ti_5V_5$	1561	2.65±0.11	-3.40±0.32	2.419
Al	933.3	2.40±0.09	-2.46±0.10	2.099

4.2 Density – Discussion

The pure data collection is not the sole purpose of this work. Instead, the gathered data should be analyzed, to achieve to major objectives. First, the analysis should yield more information on the general mixing behavior in the Al-Ti-V system. Subsequently, calculation formalisms should be developed to predict the thermophysical properties, in this case for the density. Following the general research concept of this work (see 'Research Goals and Concept) this will be done in a 'bottom up' way, starting with the binary sub-systems working our way up to the exemplary ternary section.

Therefore, in this segment, the previously presented data will be analyzed. For the density this analysis will be made under three major aspects. Firstly, both the compositional (*A*) and temperature (*B*) dependence of the density will be investigated for each individual binary and ternary system. Subsequently, an attempt will be made to draw conclusion on the general mixing behavior of the present alloying elements to eventually formulate a mathematical model to predict the density in dependence of the alloy composition (*C*). This approach is first applied to the binary sub-systems. Subsequently, the findings for the binary systems will be compared to each other in order to gain further insight into the comprehensive ternary system. In a final step all previous findings will be applied to the analysis of the density data for the Al-Ti-V system.

Ti-V

A. Compositional Dependence

To investigate the compositional dependence, the density at a reference temperature, in this case 2023 K, is calculated from the linear fits carried out for each alloy composition measured. For the Ti-V system the corresponding fits and the appropriate densities can be found in Table 9. The resulting compositional dependence is shown in Figure 29 for increasing vanadium mole fractions. The dashed line represents the compositional dependence of an ideal mixture of Ti-V.

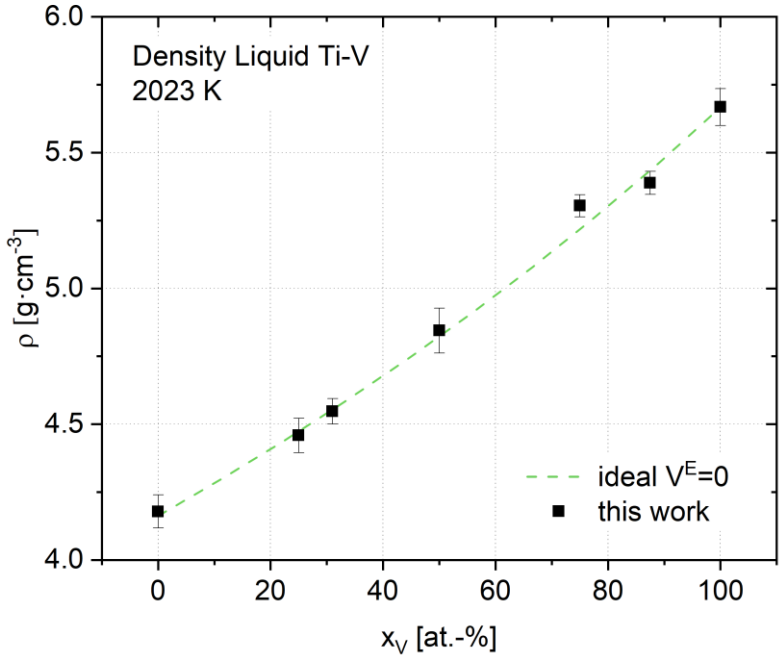

Figure 29: Isothermal density of liquid Ti-V at 2023 K *(1750 °C) as a function of the mole fraction* x_V*. The dashed line represents the density of an ideal solution calculation from the molar volume from equation 11.*

For an ideal solution of Ti and V equation 6 can be written as $V^{\mathrm{id}} = x_{\mathrm{Ti}}V_{\mathrm{Ti}} + x_{\mathrm{V}}V_{\mathrm{V}}$. The isothermal molar volume at the reference temperature (2023 K) can be calculated from the experimentally measured densities with the known molar masses for each alloy. The so obtained isothermal molar volume is plotted for increasing vanadium mole fraction in Figure 30. It is compared to the isothermal molar volume of an ideal mixture calculated following the equation above.

The greatest deviation of the measured molar volume to the calculated ideal molar volume at 2023 K is roughly 1.5 pct. for the sample containing 75 at.-% vanadium. This is well insight the experimental uncertainty and gives no indication for any excess volume. The Ti-V system shows no significant excess molar volume (see sec. 4.1.2) over the complete compositional range. It is therefore reasonable to assume an ideal mixing behavior in regards to the density for liquid Ti-V.

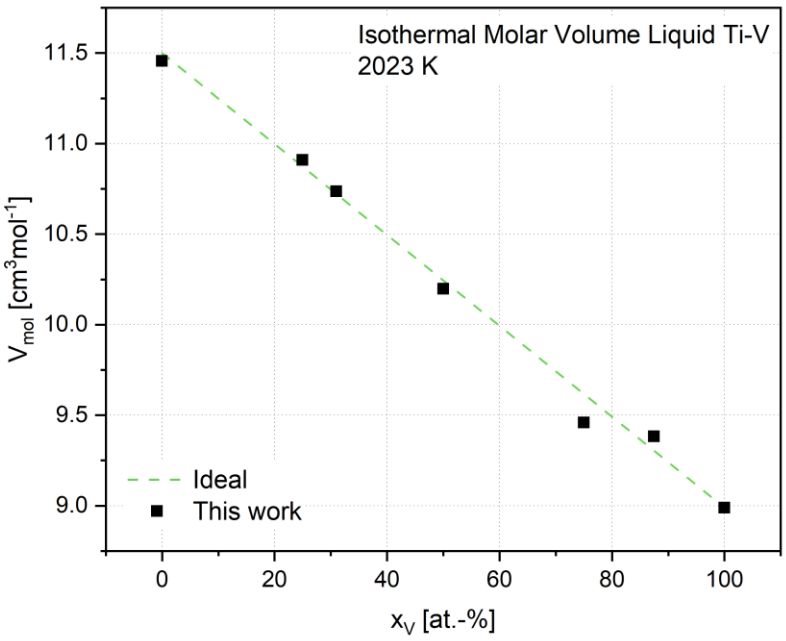

Figure 30: Isothermal molar volume at 2023 K *as a function of the V mole fraction* χ_V*. The dashed line represents the molar volume calculated for an ideal solution following Eq. 6.*

B. Temperature Dependence

To investigate the temperature dependence of the density for the liquid Ti-V system, the temperature coefficient ρ_T is plotted against the alloy composition in Figure 31. The coefficient decreases with increasing vanadium mole fraction. With the negative sign, this shows a stronger temperature dependence for alloys with higher vanadium atomic concentration, with pure vanadium showing the strongest temperature dependence. The temperature coefficient is negative for all investigated alloys, as one would expect for metallic samples.

Since ρ_T represents the differentiation of Eq. 11 and since the excess volume ^{E}V can be neglected for liquid Ti-V, the temperature coefficient can be expressed for this system as:

$$\rho_T = M \frac{[x_{Ti} \frac{M_{Ti}\rho_{T,Ti}}{\rho_{Ti}^2} + x_V \frac{M_V \rho_{T,V}}{\rho_V^2}]}{(V^{id})^2} \qquad (69)$$

Here $\rho_{T,Ti}$ and $\rho_{T,V}$ are the temperature coefficients for the pure titanium and vanadium. M_{Ti} and M_V are the molar volumes of the pure elements and M is the molar mass of the alloy $M = x_{Ti}M_{Ti} + x_V M_V$. It is worth mentioning that the temperature coefficient can be calculated for an ideal mixture, solely based of parameters of the pure elements.

The temperature coefficient for an ideal mixture following the equation above is included in Figure 31 as a dashed line. The calculated coefficient shows convincing agreement with the measured temperature coefficient, confirming the assumption of an ideal mixture of liquid Ti and V with respect to the density.

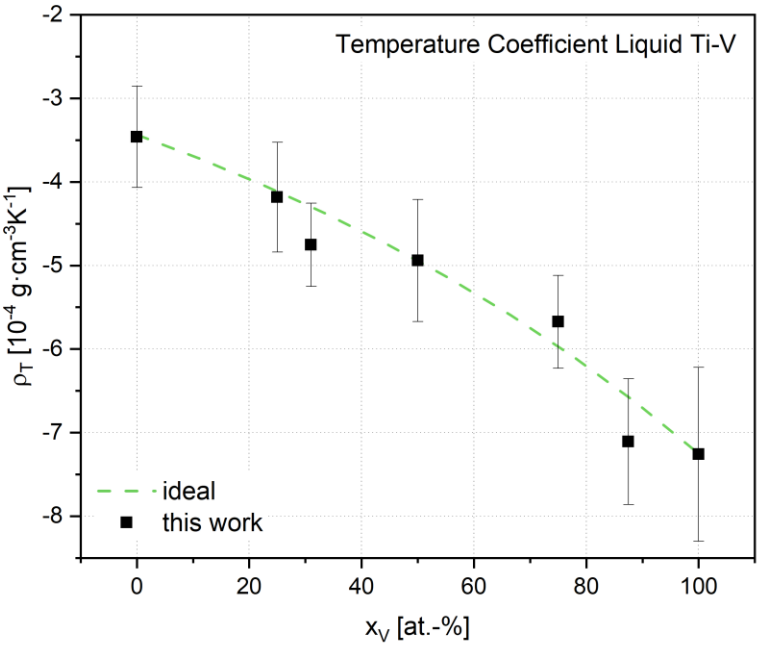

Figure 31: Temperature coefficient for the density calculation following the linear fit with Eq. 12, versus the V mole fraction x_V. The dashed line represents the temperature coefficient for an ideal mixture derived from the pure elements following equation 69.

C. Mixing Behavior

Up to now, there is no established mathematical expression to predict the excess volume of any liquid metallic alloy [14]. Ti-based alloys have shown vastly different excess voluminal and different mixing behavior respectively [13, 106]. In this work, no significant excess volume was observed regarding the density, molar volume and temperature coefficient.

Previous works suggest [14], that elements exhibiting similar electronic structures should display little to no excess volume and hence mix ideally. The findings of this work combined with the proximity of titanium and vanadium in the periodic table confirm these suggestions. Watanabe postulated a correlation between the excess volume of a system and its free energy for Pt-X [107] and Fe-Ni [108] melts. Recently, many different alloys were added to the framework of these works connecting excess volume with excess free energy [109]. For the Ti-V system calculations [110] yield only a minor positive excess energy. Eventually, the correlation by Watanabe predict no significant excess volume when implementing the excess free energy calculated for liquid Ti-V. The data measured in this work support these considerations.

In contrast to the findings by Watanabe, molecular dynamics simulations by Amore [85] find no correlation between the excess volume and the mixing behavior of an alloy system. According to those works, the mixing behavior rather results from the relation of repulsive and attractive interactions in chemical ordering. That would allow for all combinations in the sign of the excess volume and the observed enthalpy of mixing. Taking this approach, the lack of an excess volume for the liquid Ti-V system could be explained by an equilibrium of the repulsive and attractive interactions in the alloy system.

The data obtained in this work can lay the foundation for more simulation work to fully understand the mixing behavior of Ti-V.

Al-V

In the previous section the ideal mixing behavior between Ti-V was shown by a lack of excess volume. Their similar electronic structure (proximity in the periodic table) was one explanation attempt. The similarities make titanium and vanadium highly interesting when investigating their respective mixing behavior with aluminum. Following the previous logic, the question arises if titanium and vanadium are interchangeable when mixing with aluminum. A comparison between the mixing behavior of Al-V and Al-Ti can help answer this question and yield even more information on the mixing in the Al-Ti-V system. In the following section the data presented for the liquid Al-V system will be analyzed. The analysis and interpretation follows the same systematical approach as the analysis of the Ti-V density.

A. Compositional Dependence

For the compositional analysis, 1800 K was chosen as a reference temperature. Due to the large differences in melting temperatures for aluminum and vanadium, this temperature does not lie within the temperature range for all measured samples (see Figure 25). In such cases the density at the reference temperature was extrapolated from the obtained linear fits (see Table 10). The density decreases nearly linearly from 5.65 $g \cdot cm^{-3}$ for pure vanadium to 2.14 $g \cdot cm^{-3}$ for pure aluminum.

The density for an ideal mixture of Al and V is included as the dashed line. It is evident, that in contrast to the Ti-V system, the calculated ideal density and the density measured do not agree. Therefore, the excess volume in Eq. 6 cannot be neglected.

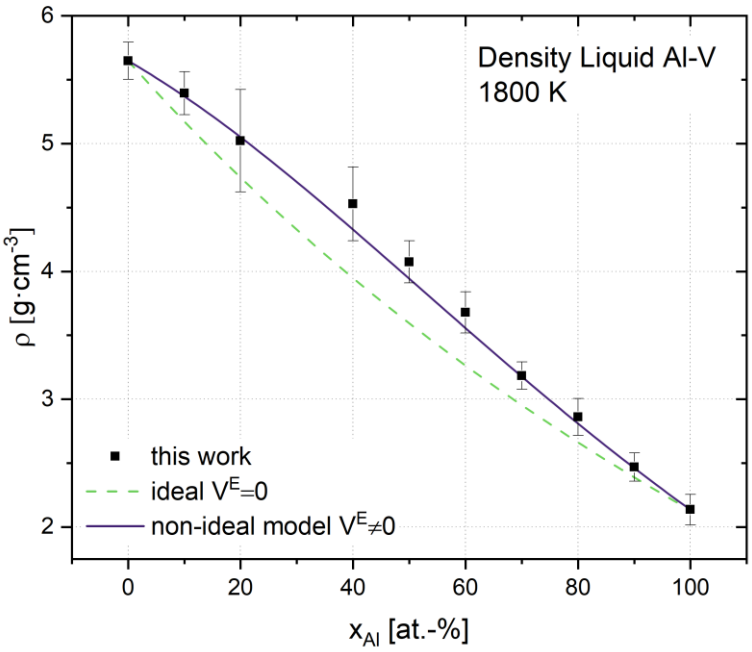

Figure 32: Density at the reference temperature 1800 K *versus the mole fraction of aluminum for the liquid Al-V system. Fits for the ideal solution (dotted line) and the regular solution (solid line) are also included. The density decreases nearly linearly with increasing aluminum mole fraction.*

To determine the excess volume for the liquid Al-V system, Figure 33 plots the molar volume measured against the mole fraction of aluminum. The molar volume increases convexly with increasing aluminum mole fraction from 9.02 $cm^3 \cdot mol^{-1}$ to 12.64 $cm^3 \cdot mol^{-1}$ below the ideal molar volume, showing the expected oppositional trend compared with the density.

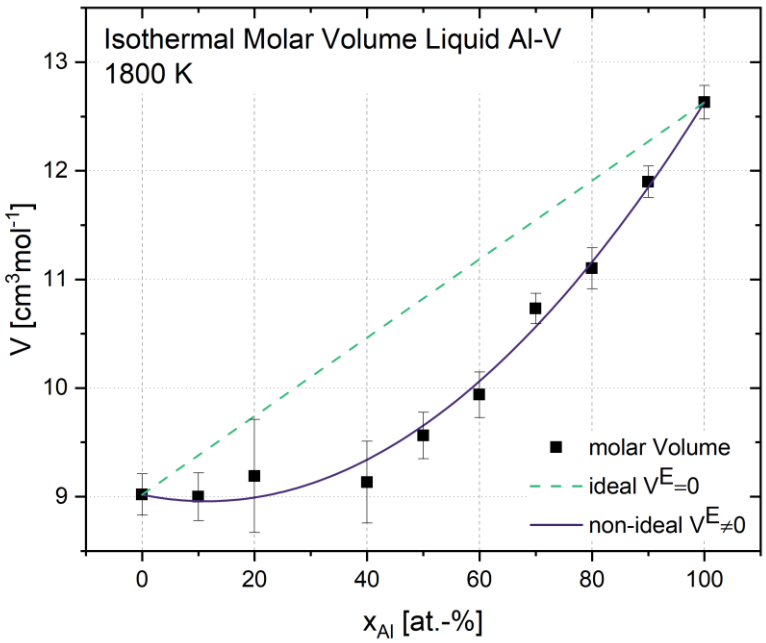

Figure 33: Molar volume for liquid Al-V at 1800 K *versus the aluminum mole fraction. Fits for the ideal (dashed line) and regular solution (solid line) are also included. The molar volume increases with increasing aluminum atomic concentration, but does not follow the linear behavior of the ideal solution.*

The excess volume is defined as the difference between the molar volume of an ideal solution and a non-ideal solution. Figure 34 displays this difference for the Al-V system against the aluminum atomic concentration. The so received excess volume as a function of the aluminum atomic concentration can be fitted with a Redlich-Kister polynomial following Eq. (8) and Eq. (9) respectively. For a binary system the excess volume can be described by only one, so called binary interaction parameter ${}^{0}_{\square}V(T)$ (see Eq. 8). The corresponding fit in Figure 34 yields ${}^{0}_{\square}V = -5.55\ \mathrm{cm^3 \cdot mol^{-1}}$. These findings can subsequently be used to calculate the molar volume and density for a regular solution of Al-V in dependence of the alloy composition. The calculations are included as solid lines in Figure 32 and Figure 33 respectively.

For both the density and the molar volume, the data of this work agrees better with the calculations for a regular solution than with the calculations for an ideal solution. The maximum observed excess volume for the Al-V system was 14% of the molar volume calculated for the ideal Al-V solution. This fits well with the findings of previous works investigating the density of liquid Al alloys. For Al-Ni [111] a binary interaction parameter of $-5.0\ \mathrm{cm^3 \cdot mol^{-1}}$ was suggested, for Al-Cu [95] $-3.37\ \mathrm{cm^3 \cdot mol^{-1}}$ and for Al-Cu [95] $-2.68\ \mathrm{cm^3 \cdot mol^{-1}}$ were found. This confirms the general trend, that Al alloys containing transition metals exhibit a negative excess volume and strong attractive interactions.

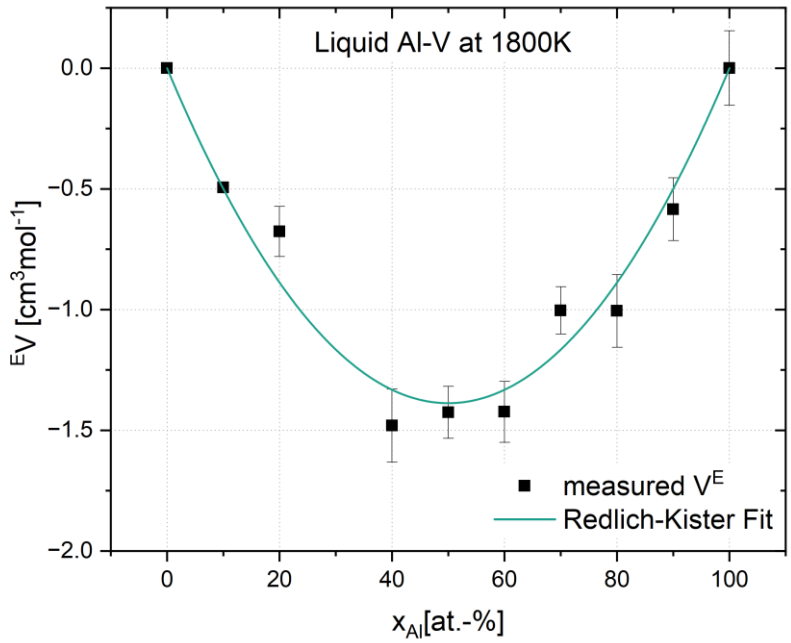

Figure 34: Excess volume versus the bulk mole fraction aluminum. A Redlich-Kister fit following Eq. (8) is included as a solid line. The corresponding binary interaction parameter is $^{0}V = -5.55\ \mathrm{cm^3 \cdot mol^{-1}}$.

B. Temperature Dependence

The temperature coefficient for liquid Al-V is shown in as a function of the aluminum atomic concentration in Figure 35. The coefficient shows a convex shape, with a minimum for medium aluminum atomic concentrations of around 40 at.-% aluminum. Figure 35 also shows the temperature coefficient for an ideal mixture of Al-V by neglecting the excess volume as a dashed line. It becomes apparent, that the excess volume cannot be neglected for Al-V. If the excess volume is included, the temperature coefficient for a regular, binary solution can be calculated as follows, if $\frac{\partial\, ^{E}V}{\partial T}$ is set to zero:

$$\rho_T = \frac{\sum_i x_i M_i * \sum_i x_i \frac{M_i \rho_{T,i}}{\rho_i^2}}{(V^{id} + {}^{E}V)^2} \qquad (70)$$

For the Al-V system the excess Volume V^E can be extracted from Figure 34. In Figure 35 the according calculation is included as a solid line. The observed trend can be much better reproduced this way. This verifies the non-ideal mixing of Al-V.

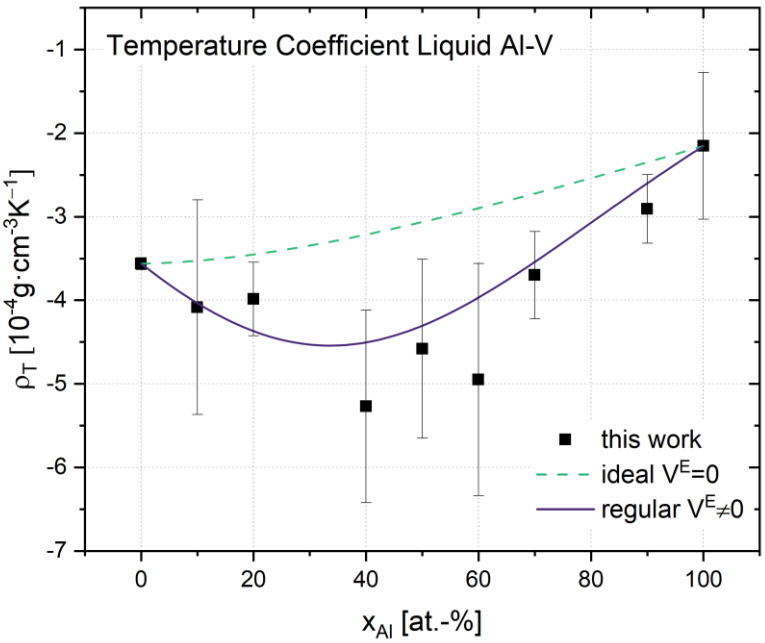

Figure 35: Temperature coefficient of liquid Al-V versus the bulk aluminum concentration. The dashed line represents the calculated volume for an ideal solution, the solid line the calculations for a regular solution.

The findings for the density, molar volume and the temperature coefficient carved out the non-ideal mixing of liquid Al-V. This compares well with the non-ideal mixing observed for several other Al-based alloys containing transition metals.

Comparing the non-ideal mixing behavior between Al-V with the ideal mixing behavior of Ti-V it is easy to assume that the non-ideality is connected to the differences in electronic structure of Al and V. As previously mentioned, it is very interesting to investigate a possible interchangeability of Ti and V when mixing with Al. Under those two previous assumptions, the Al-V and Al-Ti system should show a similar deviation from the ideal mixing behavior. Therefore, a comparison of the data measured in this work for the Al-V system and the data previously recorded by Wessing [13] for the Al-Ti system is highly interesting. To allow for a reasonable comparison, the compositional dependence of the density and molar volume of the Al-Ti system will be shown here briefly. The data is adapted to fit the style of this work. An in-depth analysis of the density and mixing behavior of liquid Ti-Al can be found in Ref. [13].

Al-Ti

Figure 36 and Figure 37 show the compositional dependence of the density and molar volume for the liquid Al-Ti system. Both properties show the same general trends as their counterparts for the Al-V system. It needs to be mentioned that in order for the data by Wessing [13] to fit into the systematic of this work, the reference temperature was changed to 1800 K.

Both density and molar volume deviate from the calculations made for the ideal solution. The ideal solution is included as the dashed line in the respective figures. For the excess volume calculation two different approaches were taken. In the first approach, one constituent was considered for Eq. 7, resulting in an excess molar calculation corresponding to Eq. 8. This is consistent with the approach of this work for the Al-V system. The molar volume resulting from this approach is included in Figure 37 as the

dash-dotted line. In a second approach a second constituent was considered for Eq. 7. The calculations for density and molar volume following this approach are included in the respective figures as solid lines.

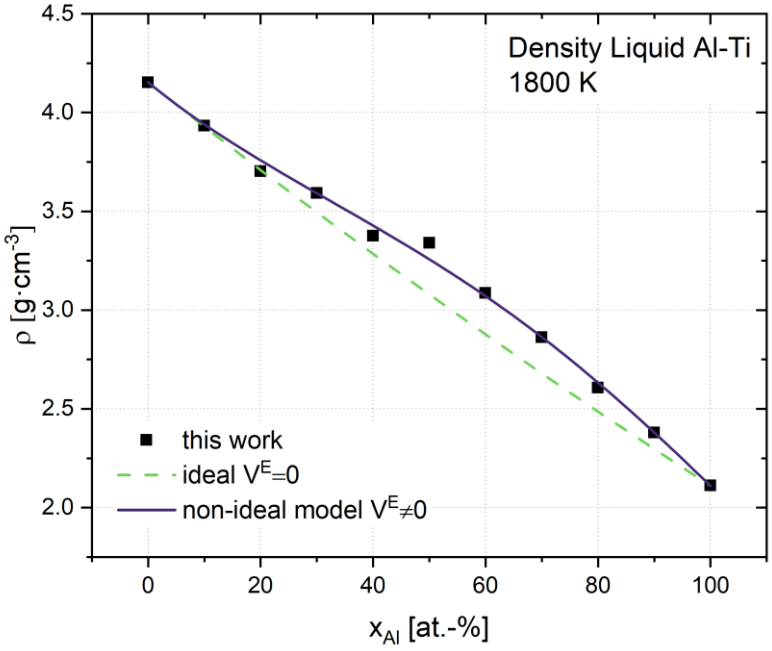

Figure 36: Density at the reference temperature 1800 K *versus the mole fraction of aluminum for the liquid Al-Ti system. Calculations for the ideal solution (dotted line) and the regular solution (solid line) are also included. The density decreases with increasing aluminum mole fraction.*

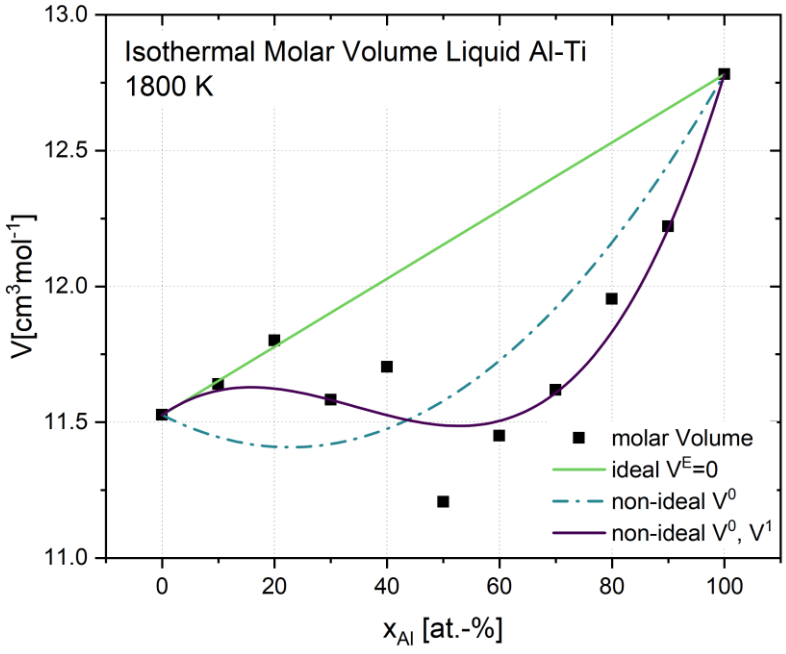

Figure 37: Molar volume for liquid Al-Ti at 1800 K *versus the aluminum mole fraction. Calculations for the ideal (dashed line) and regular solution (solid line) are also included. The molar volume increases with increasing aluminum atomic concentration, but does not follow the linear behavior of the ideal solution.*

Especially for high aluminum mole fractions Al-Ti and Al-V show very similar behavior regarding the density and molar volume. For low to medium aluminum mole fractions, the molar volume of Al-Ti mixtures seems to be best described when considering a second constituent for Eq. 7, while only one constituent is sufficient to describe the molar volume of Al-V over the complete compositional range.

C. Mixing Behavior

Since both Al-V and Al-Ti show similar behavior regarding density and molar volume it makes sense to discuss their mixing behavior here, in a combined section.

The most promising approach is to compare the excess volume observed for the Al-V system with the one observed for the Al-Ti system. This was done in Figure 38 at the fixed reference temperature of 1800 K. The corresponding interaction parameters from the Redlich-Kister type polynomial fit for each system can be found in Table 13. It is important to note that, as indicated in in Figure 37, the excess volume for the Al-Ti system was fitted using the first two constituents ($\upsilon = 1$) for a Redlich-Kister type polynomial fit. In contrast to that, for the Al-V system a fit using only the first constituent ($\upsilon = 0$) is sufficient. This was done, as the excess volume of the Al-Ti system is better described using a second order polynomial. This way, the data presented here for Al-Ti is still in accordance with [13].

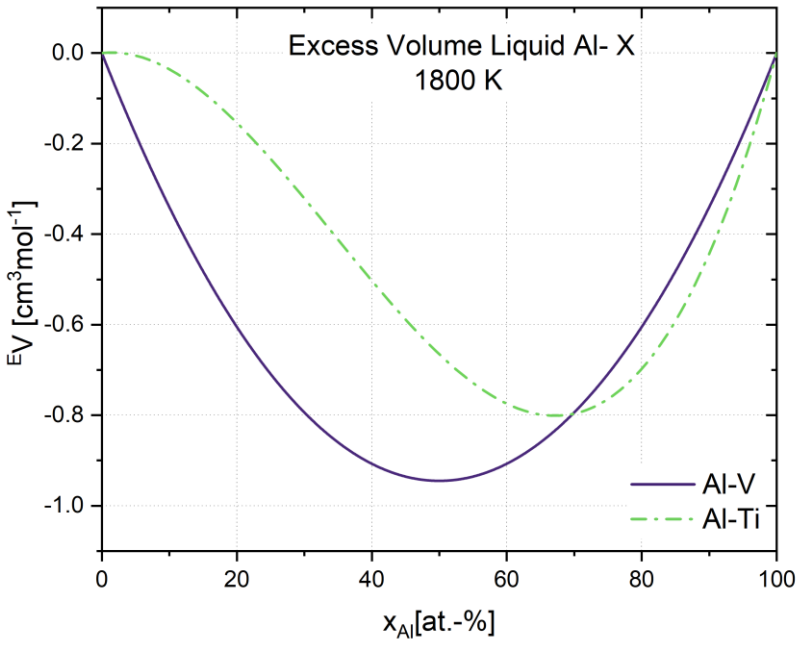

Figure 38: Comparison of the excess volume versus the aluminum mole fraction of the liquid Al-V and liquid Al-Ti system at 1800 K. *The data for Al-Ti was taken from Ref. [13]. Note that for the Redlich Kister type fit is of second order for Al-Ti and of first order for Al-V.*

Table 13: Parameters for the Redlich-Kister type fit of the excess volume for liquid Al-Ti [13] and liquid Al-V. Al-Ti is best described when considering two constituents. For liquid Al-V one is sufficient.

System	v	${}^{v}V(1800\ \mathrm{K})\ [\mathrm{cm^3 mol^{-1}}]$
Al-V	0	-5.55
Al-Ti	0	-2.11
Al-Ti	1	-2.57

Both alloy systems show a pronounced negative excess volume over the complete compositional range. Compared to the molar volume calculated for the ideal solution Al-Ti shows half the percentage excess volume ($V^{\mathrm{E}}/V^{\mathrm{id}}$) of Al-V, with the maximum observed excess volume for Al-Ti being 6.4%. As discussed earlier, Al-V showed a percentage excess volume of 14%. For aluminum atomic concentrations greater than 60 at.-% the trend of the excess volume is almost identical for both systems. For lower aluminum mole fractions the excess volume of liquid Al-V is lower than the excess volume of Al-Ti.

The comparison of the excess volume of both systems further strengthens the assumption of a similar mixing behavior of V and Ti due to their chemical similarities. Especially, when alloyed with aluminum both elements act almost interchangeable in their mixing behavior.

When attempting the classification of the Al-V and Al-Ti alloy system with regards to their mixing behavior into already existing classes (as done for the Ti-V system) proposed by Ref. [14], both alloys show strong attractive interaction and display a negative excess volume. This mixing behavior is very common for Al-based alloys.

Al-Ti-V

For the ternary Al-Ti-V the same schematic approach as for the binary sub system was applied to investigate the mixing behavior with regards to the density. However, the investigation of the complete ternary system is not feasible. The scientific focus is therefore changed from a comprehensive investigation to a more generalized approach. The most interesting question is, if the density of the ternary system can be calculated from the previously investigated binary sub-systems. Mathematically expressed, this translates to the question if the ternary term in Eq. 10 needs to be considered.

To answer this question, Figure 39 shows the molar volume measured for the $\mathrm{Al_xTi_{(1-x)0.5}V_{(1-x)0.5}}$ section through the ternary system as a function of the aluminum atomic concentration. The measured molar volume for the boundaries of pure aluminum and $\mathrm{Ti_{50}V_{50}}$ match very well with the previously recorded values. The measured molar volume lies within the boundary cases for all investigated alloys. The molar volume calculated for an ideal mixture of $\mathrm{Al_xTi_{(1-x)0.5}V_{(1-x)0.5}}$ without any excess volume is included as a dashed line. As expected the data is not very well represented by the ideal calculations.

Additionally, different calculations for ${}^{\mathrm{E}}V \neq 0$ are included as solid and dash-dotted line in Figure 39. The dash-dotted line represents calculations following Eq. 10 but neglecting the ternary term including ${}^{\mathrm{T}}V$. These calculations are solely derived from the excess volume of the binary sub-system Al-Ti, Al-V and Ti-V. Using this approach, the observed molar volume is under estimated for aluminum atomic concentrations smaller than 50 at.-% while overestimating the molar volume for higher aluminum atomic concentrations. In this case, the knowledge of the binary sub-systems is not sufficient to accurate describe the ternary system.

For the solid line in Figure 39 the additional ternary interaction parameter was considered, when applying Eq. 9. If a positive interaction parameter, $^{T}V = 9.76\ cm^3 \cdot mol^{-1}$, is considered, the observed molar volume can be much better described over the complete compositional range.

With this in mind, the compositional dependence of the measured $Al_xTi_{(1-x)0.5}V_{(1-x)0.5}$ section through the ternary system is displayed in Figure 40. The observed density decreases with increasing aluminum mole fraction, with pure aluminum showing the lowest density. The ternary section shows very similar behavior compared to the binary sub-systems Al-Ti and Al-V. The similarities between the ternary and the binary Al-Ti are especially prominent.

Figure 40 also includes calculations for the ideal solution (dashed line) and the regular solution considering a ternary interaction parameter when calculating the excess volume (solid line). The density is underestimated by the ideal calculations, especially for medium aluminum atomic concentrations around 50 at.-%. The data is much better reproduced by the calculations done for the regular solution.

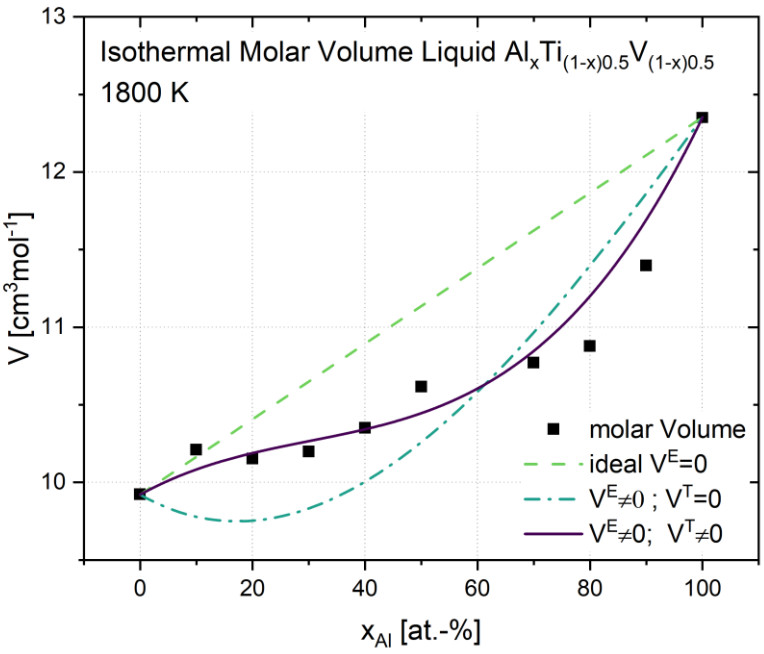

Figure 39: Molar Volume for the liquid $Al_xTi_{(1-x)0.5}V_{(1-x)0.5}$ section at 1800 K *versus the aluminum mole fraction. Fits for the ideal (dashed line) and regular solution (solid line) are also included. The molar volume increases with increasing aluminum mole fraction, but does not follow the linear behavior of the ideal solution.*

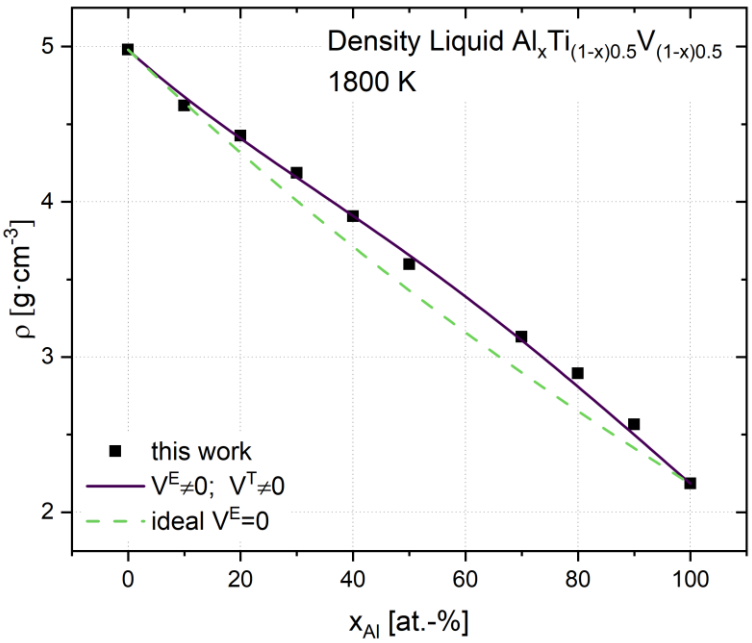

Figure 40: Density at the reference temperature 1800 K *versus the aluminum mole fraction for the liquid Al-Ti-V section. Fits for the ideal solution (dotted line) and the regular solution (solid line) are also included. The density decreases with increasing aluminum mole fraction. The measured density is best reproduced with when considering a ternary interaction parameter in Eq. 10.*

The $Al_xTi_{(1-x)0.5}V_{(1-x)0.5}$ section can best be compared with its binary sub-systems Al-Ti and Al-V when investigating the excess volume. Figure 41 shows a comparison of the excess volume for $Al_xTi_{(1-x)0.5}V_{(1-x)0.5}$ and both binary systems. The excess volume shows a great resemblance between the excess volume observed for Al-Ti and $Al_xTi_{(1-x)0.5}V_{(1-x)0.5}$, especially for low aluminum mole fractions. At first glance, the excess volume of $Al_xTi_{(1-x)0.5}V_{(1-x)0.5}$ seems to be a mix between the excess volume of the two binary systems Al-Ti and Al-V.

These findings make the previously constructed assumption of the interchangeability between Ti and V when mixing with aluminum even more possible. The similarities in the excess volume for Al-Ti and Al-V translate likewise to the ternary Al-Ti-V section investigated in this work. However, when taking a closer look at the excess volume in Figure 41 and the molar volume of Al-Ti-V and Al-Ti (Figure 36 and Figure 38), it becomes evident, that Al-Ti and Al-Ti-V share more similarities than Al-V and Al-Ti-V. This indicates a dominant influence of Ti in ternary alloys. It appears, that the ternary interaction term for the $Al_xTi_{(1-x)0.5}V_{(1-x)0.5}$ calculations almost compensates the effect of Al-V in the ternary system for aluminum atomic concentrations smaller than 60 at.-%. The ternary term conveys the similarities in excess volume for Al-Ti and $Al_xTi_{(1-x)0.5}V_{(1-x)0.5}$. Therefore, further investigations need to show if this applies to the complete Al-Ti-V system or if this section forms an exception.

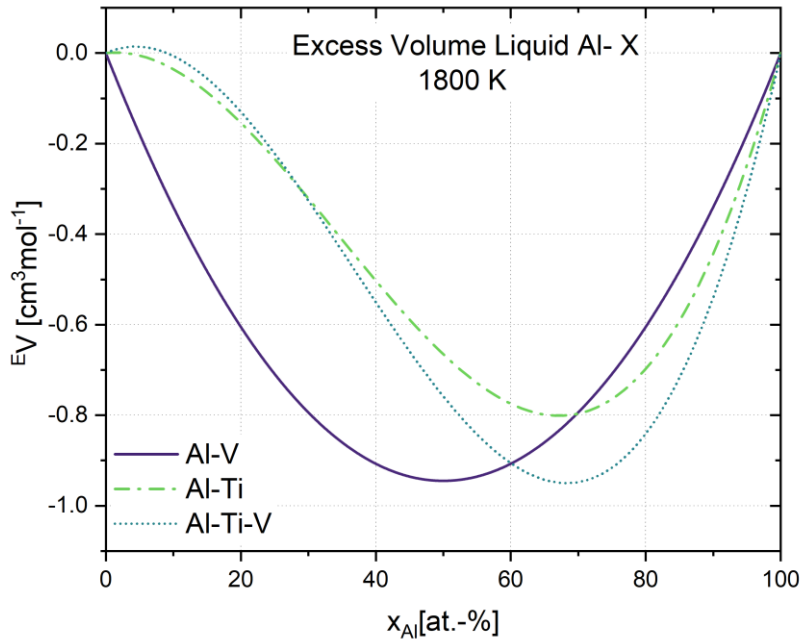

Figure 41: Comparison of the excess volume versus the aluminum mole fraction of the binary liquid Al-V and Al-Ti systems with the ternary $Al_xTi_{(1-x)0.5}V_{(1-x)0.5}$ *section at* 1800 K. *The data for Al-Ti was taken from Ref. [13].*

Previous investigations on ternary alloy systems containing aluminum have shown, that the ternary interaction parameter ${}^{T}_{\square}V$ can have strongly varying influences on the density. With ${}^{T}_{\square}V = 9.76\ \mathrm{cm^3 \cdot mol^{-1}}$, being strongly positive, the ternary interaction parameter compensates the effect of both binary sub-systems which each show a negative excess volume. This leads to the conclusion, that the strong attractive interactions between these transition metals are weakened in the ternary system compared to the binary systems.

Table 14 shows that, for Ag-Al-Cu [112] ${}^{T}_{\square}V$ can be neglected, and the density can be calculated from the binary interaction parameters of the sub-systems alone. In contrast to that, for the Al-Cu-Si system [113] the ternary interaction parameter ${}^{T}_{\square}V = 19.7\mathrm{cm^3 \cdot mol^{-1}}$ can have a quite extensive impact on the density. The ternary section investigated in this work falls into the latter category. With ${}^{T}_{\square}V = 9.76\ \mathrm{cm^3 \cdot mol^{-1}}$, being strongly positive, the ternary interaction parameter compensates the effect of both binary sub-systems which each show a negative excess volume.

Table 14: Ternary volume interaction parameter ${}^{T}_{\square}V$ *for different Al containing ternary systems.*

System	${}^{T}_{\square}V$ [$\mathrm{cm^3 mol^{-1}}$]	Reference
Al-Cu-Si	19.7	[113]
Al-Ag-Cu	0	[112]
Al-Ti-V	9.76	This work

The investigations on the density of the ternary Al-Ti-V systems show very well how this work intends to function. A systematic data collection can be found at the beginning of the chapter sorted by the elements and alloys investigated. This data collection is the foundation of the subsequent interpretation. Starting from the binary alloys the mixing behavior is examined. Each binary sub-system builds a single layer that contributes to the understanding of the ternary system. After measuring the pure elements, the Ti-V system was investigated. An ideal mixing behavior was observed which was attributed to the

similarities in electronic structure and the proximity in the periodic table. The hypothesis of a similar mixing behavior of Ti and V was translated to the investigations of Al-V and Al-Ti. The comparison of both Al binaries could further strengthen this assumption. Step by step, these findings were applied to the ternary system and an exemplary section through the Al-Ti-V system was measured to compare to the considerations made. As expected, a ternary term is needed to accurately describe the density data measured for the ternary. The similarities between the results obtained for Al-Ti/Al-V and Al-Ti-V support the hypothesis of an interchangeability between Ti and V, but indicate a dominance of Ti in the ternary system.

These insights into the mixing behavior of the Al-Ti-V system were gained by comparing several established thermodynamic models against the measured data. In doing so, while the mixing behavior was investigated, powerful predictive tools for the temperature and composition dependent density (molar volume) were developed, achieving another set objective of this work.

4.3 Surface Tension

The same goals that stand for the density investigations also stand for the surface tension investigations. Therefore, the analysis of the surface tension for the Al-Ti-V system will be carried out following the same schematic structure as the density investigations.

First the measured surface tension data will be presented for the pure elements, the binary sub systems and a section through the ternary system. In order to fulfill the scientific claim of this work to provide reliable reference data, the data will be summarized in, easily accessible, tabular form at the end of each section.

In a second step the obtained data will be discussed for the binary alloys and the ternary section. Within each individual part, the discussion will follow the structure introduced in the density discussion (sec. 4.1). Compositional dependence (*A*) and temperature dependence (*B*) will be discussed first. Finally, any possible conclusions towards the mixing behavior and possible modeling (*C*) will be drawn.

This approach ensures that a comprehensive, precise data collection, a capable model development and a gain in knowledge is achieved.

4.3.1 Pure Elements

The analysis of the pure elements serves two purposes. First, the measured surface tension data can expand and validate the already existing data bases for the pure elements. Additionally, by comparing the measured results with existing literature data a benchmark can be generated on how well our results compare to literature data. The measurement method employed in this work (sec. 3.7) can thereby be validated to some extent.

Al

The surface tension of pure liquid aluminum as a function of the temperature is shown in Figure 42. The experimental temperature range was 500 K. Undercooling could not be achieved. The surface tension decreases linearly with increasing temperature allowing for a linear fit according to Eq. 22. Reference data using electromagnetic levitation [13], sessile drop method [31] and literature review [54] is included as dashed, dotted and dash-dotted line respectively. The corresponding fit parameters for the literature data and the data measured in this work can be found in Table 15. Additionally, Table 15 also includes a wider variety of literature data, which was left out of Figure 42 for clarity reasons. A key for the corresponding measurement techniques can be found in Table 4.

The measured data is in overall very good agreement with the data measured by Wessing [13]. These measurements were taken with the same method but in a different EML furnace. The data of this work lies slightly higher. Data measured using the sessile drop techniques [31] lies slightly higher over the complete temperature range, while values recommended from literature [21] review lie lower than the data of this work.

Overall the surface tension for liquid aluminum measured in this work compares very well to already existing literature data. Naturally, the surface tension observed with different measurement methods differs more with increasing temperature, since the experimental handling usually becomes more challenging for temperatures greatly exceeding the melting point. In the vicinity of the liquidus temperature of aluminum (933 K) the values are in good agreement.

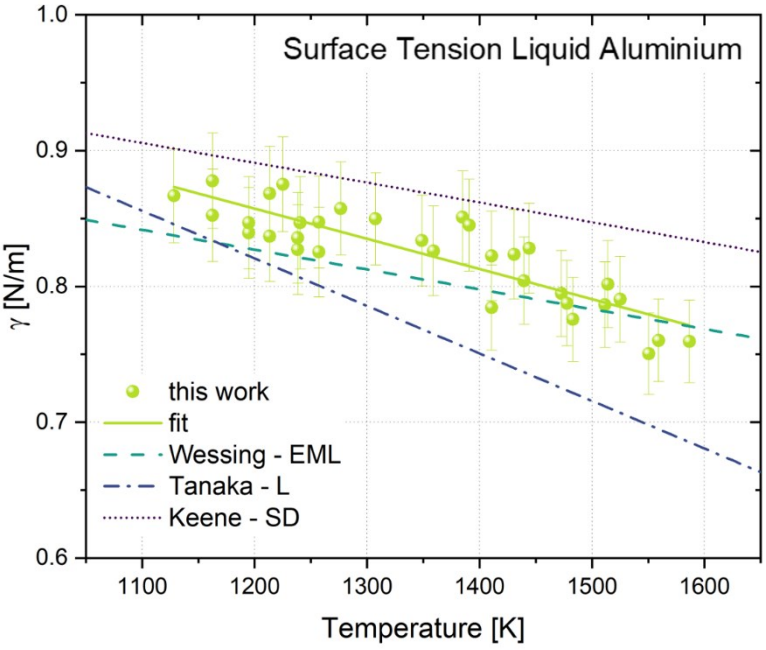

Figure 42: Surface tension measured as a function of the temperature for pure liquid aluminum. A linear fit following Eq. 22 is shown as solid line. Different reference data using different measurement techniques is included as dashed (Wessing – EML, Ref. [13]), dash-dotted (Tanaka – L, Ref. [54]) and dotted line (Keene – SD, Ref. [31]).

Table 15: Parameters γ_L, γ_T and $\gamma(1800\ \mathrm{K})$ for pure liquid Al compared to literature data obtained with different measurement techniques. The key for methods can be found in Table 4.

Composition	$\gamma_L[\mathrm{Nm^{-1}}]$	$\gamma_T[10^{-4}\mathrm{Nm^{-1}K^{-1}}]$	$\gamma(1800\ \mathrm{K})[\mathrm{Nm^{-1}}]$	Reference	Method
Al	0.916±0.04	-2.22±0.59	0.723	This work	EML
Al	0.866±0.03	-1.46±0.4	0.739	[15]	EML
Al	0.914	-3.5	0.611	[54]	L
Al	0.930	-1.46	0.803	[31]	SD
Al	0.916	-1.05	0.825	[43]	MD
Al	1.024	-2.74	0.787	[98]	ADL
Al	0.825	-0.5	0.782	[31]	BP

Ti

Figure 43 shows the surface tension measured for pure liquid titanium as a function of the temperature. The maximum possible temperature was 2300 K, while the lowest reachable temperature was 1850 K. An undercooling of almost 100 K was achievable, with the liquidus temperature (1941 K) being marked in the chart. The surface tension exhibits a linear decline with increasing temperature. Therefore, a linear fit following Eq. 22 was carried out.

Besides the measured data, Figure 43 also contains reference data as linear functions of the form according to Eq. 22. The corresponding parameters, both for the reference data and the linear fit of this work can be found in Table 16. Additional reference data was added to Table 16, but left out of Figure 43 for sake of clarity.

The measured surface tension was compared against different literature data measured in electromagnetic and electrostatic levitation events. As expected the findings of this work compare very well with data previously measured at the *'Institut für Materialphysik im Weltraum'* by Wessing [13], even though a different levitation apparatus was used for both measurements. The data of this work lies slightly lower, but well within the experimental error over the complete temperature range. The same can be said for the reference data measured in ESL by Paradis et. al. [103]. Zhou [114] measured on average 6% higher surface tension.

For liquid titanium a stable levitation was possible for the complete temperature range. No major evaporation could be observed during the levitation.

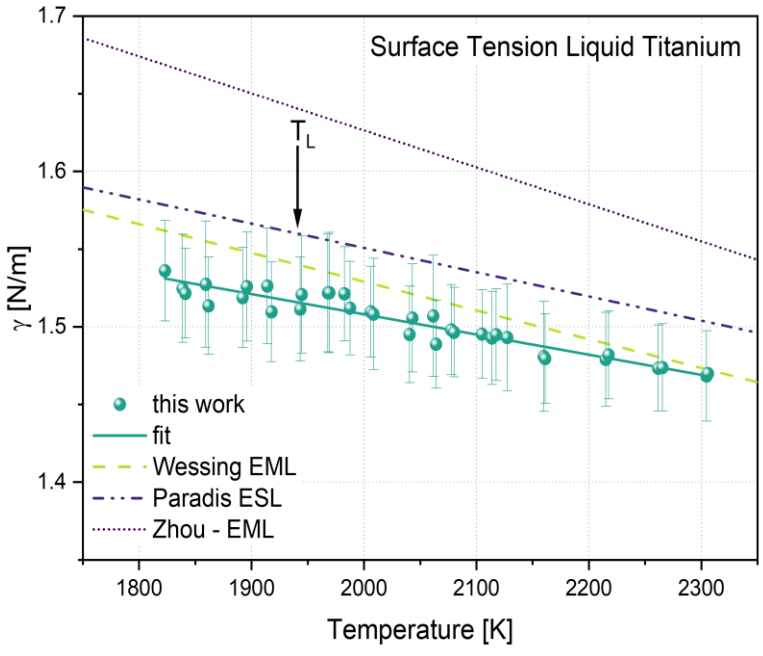

Figure 43: Surface tension measured as a function of the temperature for pure liquid titanium. A linear fit following Eq. 22 is shown as solid line. Different reference data using different measurement techniques is included as dashed (Wessing – EML, Ref. [13]), dash-dotted (Paradis - ESL, Ref. [103]) and dotted line (Zhou – EML, Ref. [114]).

Table 16: Parameters γ_L, γ_T and $\gamma(1800\ \mathrm{K})$ for pure liquid Ti compared to literature data obtained with different measurement techniques. The key for methods can be found in Table 4.

Composition	$\gamma_L[\mathrm{Nm^{-1}}]$	$\gamma_T[10^{-4}\mathrm{Nm^{-1}K^{-1}}]$	$\gamma(1800\ \mathrm{K})[\mathrm{Nm^{-1}}]$	Reference	Method
Ti	1.52±0.01	-1.77±0.3	0.723	This work	EML
Ti	1.56±0.02	-1.65±0.95	0.739	[13]	EML
Ti	1.557±0.08	-1.56±0.8	0.611	[115]	ESL
Ti	1.64	-2.38	0.803	[114]	EML
Ti	1.49	-1.7	0.825	[116]	EML
Ti	1.65	-	-	[32]	PD
Ti	1.65	-2.6	0.782	[54]	R

V

Figure 44 shows the temperature dependent surface tension of pure liquid vanadium measured in this work. Due to its high melting point, the sample mass was the biggest for the vanadium samples. This causes a slightly increased sample movement during levitation and subsequently to a slightly higher experimental scatter and error. A reasonable measurement could be carried out over almost 400 K with a maximum temperature of 2300 K and a maximum undercooling of roughly 300 K. At 2300 K liquid vanadium started to show evaporation. Therefore, the temperature was limited to 2300 K and the time spent at elevated temperatures was kept as short as possible.

As for all tested pure elements, a linear decrease in surface tension can be observed for increasing temperature. The linear fit according to Eq. 22 is included as solid line. The resulting fit parameters can be found in Table 17.

A comprehensive literature comparison for the surface tension of liquid vanadium is quite hard, since temperature dependent data is scarce for vanadium. The only experimental data available was measured by Okada [24] in ESL. The data of this work compares remarkably well against the ESL data. The measured surface tension at the liquidus temperature is almost identical. The only other reported temperature dependent surface tension is based on atomic modeling by Lu [117]. The surface tension predicted by their model lies lower but within the experimental error of this work. It needs to be noted, that the models employed by Lu [117] are based on experimentally available data, among other experiments, on the data measured by Okada [24]. Apart from those two works, surface tension data for liquid vanadium is mainly available at the liquidus temperature measured by the pendant drop method and not as a function of the temperature. The values for the surface tension at the liquidus temperature, the temperature coefficient and the surface tension at the reference temperature are summarized in Table 17 if available.

The rarity of experimental, temperature dependent surface tension data shows how important the first research goal (a comprehensive data collection) of this work is. Overall the data of this work compares well with the sparsely available literature data. Therefore, it can be assumed that valid surface tension measurements are obtained.

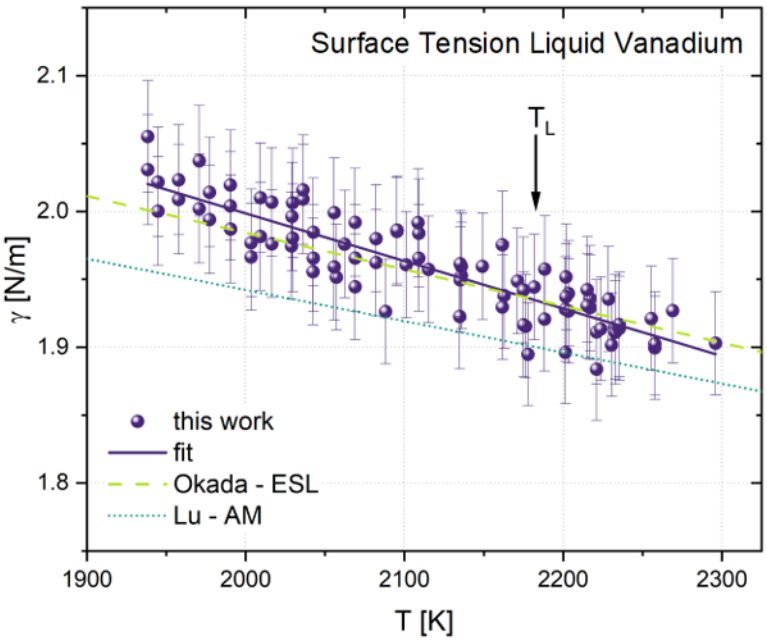

Figure 44: Surface tension measured as a function of the temperature for pure liquid vanadium. A linear fit following Eq. 22 is shown as solid line. Different reference data using different measurement techniques is included as dashed (Okada – ESL Ref. [24]) and dotted line (Lu – AM, Ref. [117]).

Table 17: Parameters γ_L, γ_T and $\gamma(1800\ \mathrm{K})$ for pure liquid V compared to literature data obtained with different measurement techniques. The key for methods can be found in Table 4.

Composition	$\gamma_L[\mathrm{Nm^{-1}}]$	$\gamma_T[10^{-4}\mathrm{Nm^{-1}K^{-1}}]$	$\gamma(1800\ \mathrm{K})[\mathrm{Nm^{-1}}]$	Reference	Method
V	1.934±0.07	-3.51±0.66	2.069	This work	EML
V	1.935±0.06	-2.7	2.038	[24]	ESL
V	1.902	-2.3	1.990	[117]	AM
V	1.950	-	-	[31]	PD
V	1.850	-	-	[31]	PD

4.3.2 Binary Alloys

With the pure elements measured and the experimental method validated, the next step is to investigate the binary sub-systems.

In this section the measured surface tension data for the binary sub-systems Ti-V, Al-V and Al-Ti will be presented. The approach remains the same. First, the surface tension for all measured composition will be shown and subsequently the obtained surface tension and temperature coefficient will be summarized in tabular form. Using this approach, a comprehensive well-arranged data collection is developed.

Ti-V

Figure 45 shows the surface tension versus the temperature for all measured alloy compositions in the liquid Ti-V system. The pure elements Ti and V are included for reference. The maximum and minimum achievable temperature slightly differ for the individual compositions, but all samples could be measured over at least 400 K. A moderate undercooling was possible for all compositions. All alloys show a linear decrease in surface tension with increasing temperature. A linear fit according to Eq. 22 is included for each data set. The obtained fit parameters are summarized at the end of the section in Table 18.

All investigated samples could be levitated steadily over the temperature range, allowing for a reasonable oscillating drop measurement for all samples. Almost no change in the levitation behavior could be observed for the Ti-V system, which can in part be attributed to the similar melting temperatures of Ti and V. The liquidus temperatures, T_L, for all tested compositions are included in Table 18. The temperatures were read out of the phase diagram presented in Ref. [66].

The observed surface tension lies within the values of the pure elements for all alloys tested. The surface tension increases for the alloys with increasing vanadium mole fraction. Since no aluminum is present in the binary system, a reference temperature of 2100 K was chosen since it lays well in the middle of all experimental temperature ranges. The reference temperature is marked in Figure 45 as a dash-dotted line.

To provide a clearer depiction, the error bars associated with the individual measurement are left out of Figure 45. The experimental error lies within $\pm 5\%$ for each measurement, as introduced in sec. 3.7.

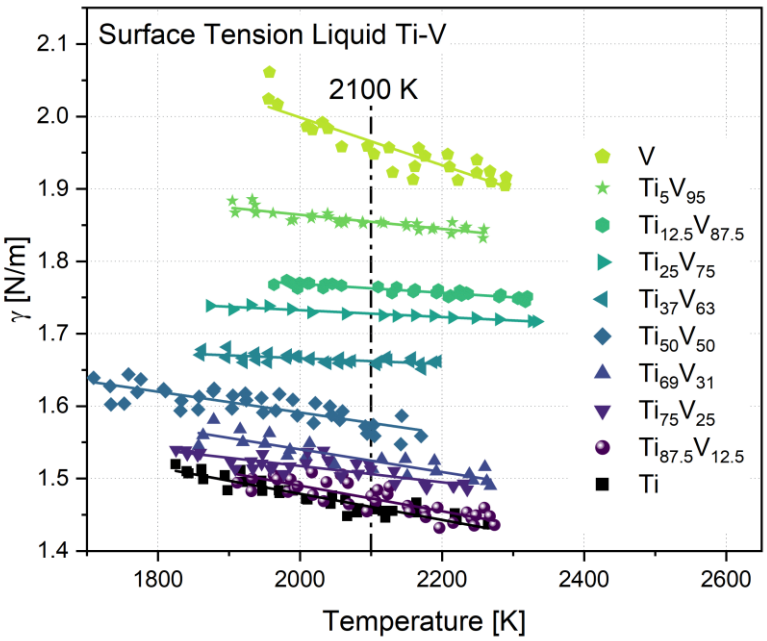

Figure 45: Surface tension of all investigated binary Ti-V alloys as a function of the temperature. The surface tension of pure Ti and V is included for reference. Linear fits following Eq.22 are included as solid lines. The reference temperature of 2100 K *for future analysis is marked as a dash-dotted line.*

Table 18: Parameters T_L, γ_L, γ_T *and* $\gamma(2100\,K)$ *for all investigated compositions within the Ti-V system. The liquidus temperatures,* T_L, *were taken from the phase diagram introduced in [66].*

Composition	T_L[K]	γ_L[Nm^{-1}]	γ_T[10^{-4}Nm^{-1}K^{-1}]	γ(2100 K)[Nm^{-1}]
Ti	2183	1.94±0.07	-3.29±0.7	1.967
Ti_5V_{95}	2173	1.85±0.02	-9.78±0.25	1.855
$Ti_{12.5}V_{87.5}$	2113	1.76±0.01	-6.64±0.5	1.759
$Ti_{25}V_{75}$	2023	1.72±0.01	-5.49±0.4	1.712
$Ti_{37.5}V_{62.5}$	1937	1.67±0.02	-3.64±0.43	1.667
$Ti_{50}V_{50}$	1913	1.61±0.08	-1.41±0.42	1.580
$Ti_{69}V_{31}$	1881	1.56±0.05	-1.57±0.39	1.525
$Ti_{75}V_{25}$	1893	1.53±0.04	-1.12±0.35	1.506
$Ti_{87.5}V_{12.5}$	1913	1.51±0.04	-1.77±0.5	1.473
V	1941	1.52±0.01	-1.77±0.3	1.461

Al-V

Figure 46 shows the temperature dependent surface tension for all investigated compositions in the liquid Al-V system. As usual the measurements for both pure elements are also included. The strong discrepancy between the liquidus temperatures of aluminum (933 K) and vanadium (2183 K) made the steady levitation for some alloy compositions more difficult and shortened the experimentally accessible temperature range in same cases. As mentioned in section 3.2, the levitation and heating behavior during the experiment is highly dependent on the coil geometry as well as the sample material. In the case of the Al-V system the coil needs to steadily levitate aluminum while also being able to fully melt vanadium. Since heating and positioning are not decoupled achieving both can be challenging and, in some cases, compromises regarding the accessible temperature range need to be made. The edge compositions with alloying atomic concentrations less than 20 at.-% could usually be steadily levitated and measured over a 300 K temperature range or more.

Alloys with aluminum atomic concentrations between 70 at.-% and 30 at.-% showed pronounced evaporation at elevated temperatures. This can potentially be explained by a strong evaporation of aluminum before the tested sample is fully molten. To counteract this evaporation, the levitation experiment was designed to heat up the sample as quickly as possible. Additionally, for samples that exhibited the most prominent evaporation, the maximum temperature was adjusted to a point where no significant evaporation was observed. These measures cause the different temperature ranges depicted in Figure 46.

Pure aluminum shows the lowest observed surface tension ($0.724\ \mathrm{Nm^{-1}}$ at T_L) while pure vanadium ($2.069\ \mathrm{Nm^{-1}}$at T_L) shows the highest surface tension for all measured samples. All alloy compositions lie between the pure elements. All measurements show a linear decline in surface tension with increasing temperature. The subsequent linear fits in accordance with Eq. 22 are included for each tested sample as a solid line. The corresponding fit parameters γ_L and γ_T are summarized in Table 19 together with the liquidus temperature for each composition and the surface tension at the reference temperature of 1800 K.

The liquidus temperatures for the different composition were taken from the Al-V phase diagram presented in Ref. [65]. It needs to be mentioned, that the reference temperature chosen for further evaluation does not fall into the experimentally achievable temperature range for all measurements made. In the following analysis, the surface tension at the reference temperature is obtained by extrapolating the measured surface tension to 1800 K via the obtained fit parameters.

As for all other overview graphs, the error bars were omitted to provide a clearer comparison of the surface tension for the different compositions. The usual experimental error was estimated to be $\pm 5\%$ in section 3.7

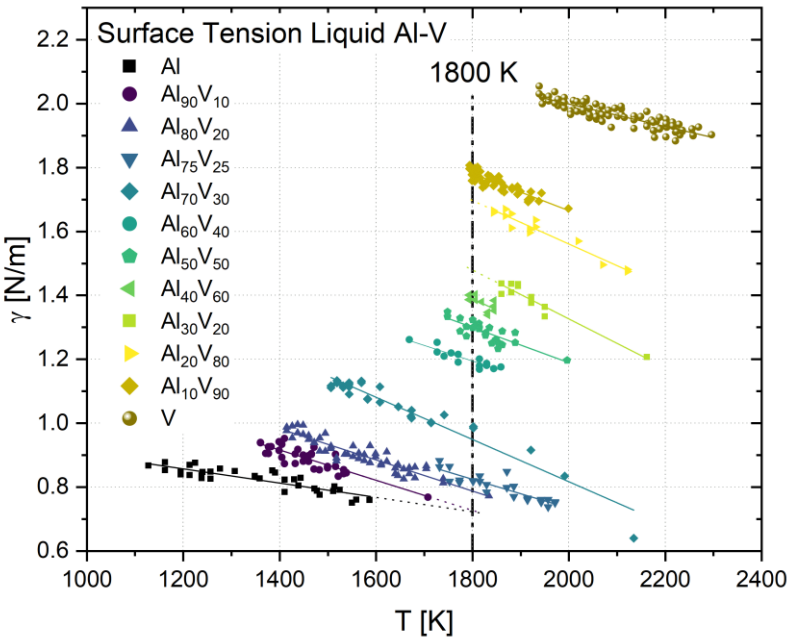

Figure 46: Surface tension versus temperature of all investigated alloys in the Al-V system. Surface tension decreases linearly with increasing temperature for all investigated samples. Linear fits according to Eq. 22 are included for every measurement as solid lines. Error bars have been left out for clarity reasons. As explained in sec. 3.7 the experimental error is ±5%.

Table 19: Parameters T_L,γ_L, γ_T and $\gamma(1800\ K)$ for all compositions measured in the Al-V system.

Composition	T_L[K]	γ_L[Nm^{-1}]	γ_T[10^{-4}Nm^{-1}K^{-1}]	γ(1800 K)[Nm^{-1}]
V	2183	1.935±0.07	-3.51±0.66	2.069
$V_{90}Al_{10}$	2162	1.572±0.09	-5.789±0.75	1.781
$V_{80}Al_{20}$	2138	1.468±0.09	-6.772±0.88	1.696
$V_{70}Al_{30}$	2107	1.245±0.08	-7.651±1.00	1.479
$V_{60}Al_{40}$	2045	1.214±0.07	-7.186±0.93	1.390
$V_{50}Al_{50}$	1949	1.219±0.08	-5.656±0.74	1.303
$V_{40}Al_{60}$	1810	1.190±0.08	-4.879±0.64	1.194
$V_{30}Al_{70}$	1663	1.048±0.07	-5.218±0.68	0.976
$V_{25}Al_{75}$	1548	0.939±0.04	-4.517±0.58	0.824
$V_{20}Al_{80}$	1548	0.911±0.04	-4.874±0.63	0.787
$V_{10}Al_{90}$	1460	0.888±0.03	-4.735±0.62	0.726
Al	933	0.916±0.04	-2.223±0.59	0.723

Al-Ti

The surface tension for Al-Ti system was measured by Wessing [13]. The results are presented here for completeness' sake and for comparison to the Al-V and Ti-V system. The measurements were carried out in a different EML furnace using the same measurement principle of the oscillating drop method. A precise experimental setup description can be found in [13, 26]. The data is presented to fit the layout of the current work.

The Al-Ti shows the same general trend as both of binary sub-systems. The surface tension for all alloys lies within the values for the pure elements. In Ref. [13] the same analytical approach was chosen. Linear fits were carried out for all measurements taken. The resulting fit parameters are summarized in Table 20.

The reference temperature was changed to 1800 K in order to fit into the framework of this work and allow for easier comparisons. As for the Al-V system it has to be kept in mind, that the reference temperature is not within the experimental temperature range for all compositions tested. In those cases, the surface tension values were extrapolated.

A more detailed description of the data can be found in [13, 26].

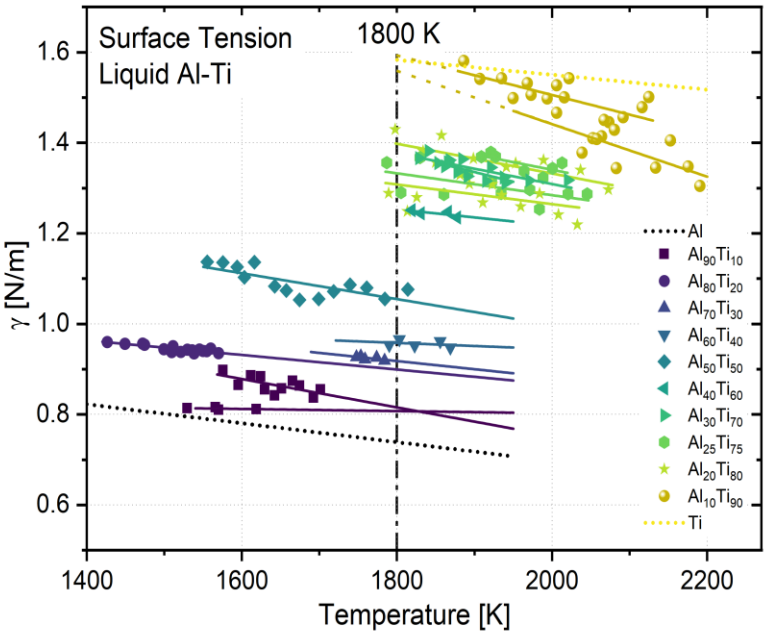

Figure 47: Surface tension versus temperature of all investigated alloys in the Al-Ti system. Values measured for the pure elements are included as dotted lines. Linear fits according to Eq. 22 are included for every measurement as solid lines. The data presented has been adapted from [13] to the layout of this work.

Table 20: Parameters T_L,γ_L, γ_T and $\gamma(1800\ \mathrm{K})$ for all compositions in the Al-Ti system. Data has been adapted from [13] to fit the layout of this work.

Composition	T_L[K]	$\gamma_L[\mathrm{Nm^{-1}}]$	$\gamma_T[10^{-4}\mathrm{Nm^{-1}K^{-1}}]$	$\gamma(1800\ \mathrm{K})[\mathrm{Nm^{-1}}]$
Ti	2183	1.56	-1.65±0.95	1.621
$Ti_{90}Al_{10}$	1962	1.52	-4.34	1.590
$Ti_{90}Al_{10}$	1962	1.46	-5.81	1.554
$Ti_{80}Al_{20}$	1948	1.35	-3.29	1.398
$Ti_{80}Al_{20}$	1948	1.28	-2.18	1.312
$Ti_{75}Al_{25}$	1941	1.30	-2.42	1.334
$Ti_{75}Al_{25}$	1941	1.36	-3.38	1.407
$Ti_{70}Al_{30}$	1915	1.34	-3.38	1.378
$Ti_{70}Al_{30}$	1915	1.33	-4.24	1.378
$Ti_{60}Al_{40}$	1853	1.24	-1.79	1.249
$Ti_{50}Al_{50}$	1757	1.07	-2.86	1.057
$Ti_{40}Al_{60}$	1721	0.96	-0.68	0.954
$Ti_{30}Al_{70}$	1689	0.94	-1.80	0.920
$Ti_{20}Al_{80}$	1654	0.92	-1.61	0.896
$Ti_{10}Al_{90}$	1562	0.89	-3.14	0.815
$Ti_{10}Al_{90}$	1562	0.81	-0.23	0.804
Al	933	0.916±0.04	-2.223±0.59	0.723

4.3.3 Ternary Alloys

For the analysis of the ternary alloys, the same section $Al_xTi_{0.5(1-x)}V_{0.5(1-x)}$ through the Al-Ti-V system was chosen as investigated in 5.1.3. Therefore, the same liquidus temperatures, calculated using the TCAL 5: TCS Al-based Database with the Thermo-Calc software, could be used.

Figure 48 shows the surface tension measured for all alloys in the $Al_xTi_{0.5(1-x)}V_{0.5(1-x)}$ section through the ternary system as a function of the temperature. For the edge compositions of pure Al and $Ti_{50}V_{50}$ the measurements of the ternary system are compared with the measurements taken in 4.3.1 and 4.3.2. Both are nearly identical to the previous measurements as the experimental setup was not changed. As expected Al shows the lowest and $Ti_{50}V_{50}$ shows the highest surface tension measured for the ternary alloys.

All samples tested could be steadily levitated to ensure a reasonable surface tension measurement. Samples that previously showed signs of heavy evaporation, were cooled after melting to a temperature were no significant evaporation was observed.

All alloys tested show a linear decrease in surface tension with increasing temperature. Fits according to Eq. 22 are included as solid lines for each measurement taken. The resulting fit parameters as well as the liquidus temperatures and the surface tension at the reference temperature are summarized in Table 21. As for all systems containing aluminum 1800 K was chosen as a reference temperature for future analysis. The reference temperature is included as dash-dotted line in Figure 48.

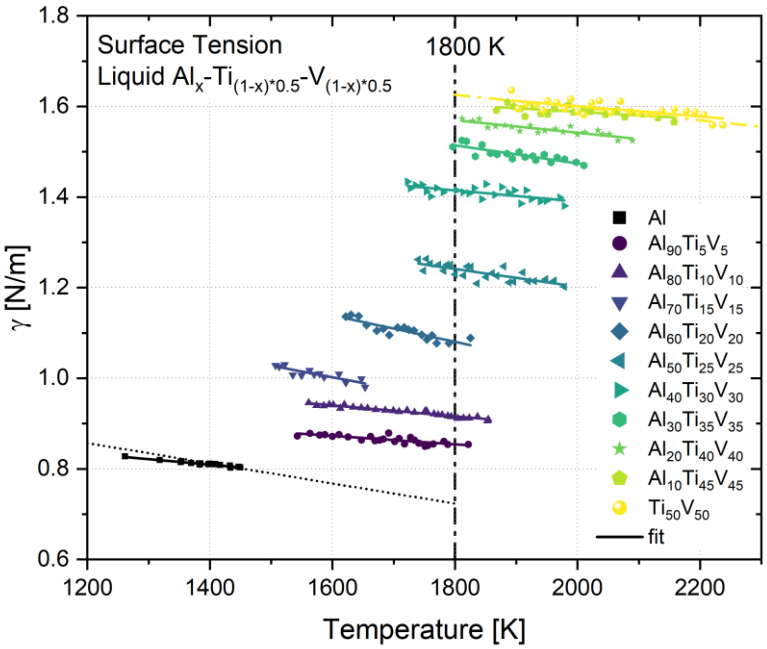

Figure 48: Surface tension versus temperature of all investigated alloys in the Al-Ti-V section. Surface tension decreases linearly with increasing temperature for all investigated samples. Linear fits according to Eq. 22 are included for every measurement as solid lines. Error bars have been left out for clarity reasons. As explained in 4.5 the experimental error is ±5%. The dotted line and dash-dotted line refer to the surface tension measured for pure Al and $Ti_{50}V_{50}$ in sec. 4.3.1 and 4.3.2.

Table 21: Parameters T_L,γ_L, γ_T and $\gamma(1800\ \mathrm{K})$ for all compositions measured in the $Al_xTi_{0.5(1-x)}V_{0.5(1-x)}$ section. The liquidus temperatures were calculated using the TCAL 5: TCS Al-based Database with the Thermo-Calc software.

Composition	T_L[K]	$\gamma_L[\mathrm{Nm^{-1}}]$	$\gamma_T[10^{-4}\mathrm{Nm^{-1}K^{-1}}]$	$\gamma(1800\ \mathrm{K})[\mathrm{Nm^{-1}}]$
$Ti_{50}V_{50}$	1897.5	1.612	-1.13	1.84
$Al_{10}Ti_{45}V_{45}$	1976.4	1.591	-0.80	1.76
$Al_{20}Ti_{40}V_{40}$	2006.7	1.541	-1.39	1.85
$Al_{30}Ti_{35}V_{35}$	2009.6	1.472	-1.99	1.91
$Al_{40}Ti_{30}V_{30}$	1974.2	1.393	-1.23	1.66
$Al_{50}Ti_{25}V_{25}$	1875.9	1.227	-1.96	1.61
$Al_{60}Ti_{20}V_{20}$	1684.6	1.114	-2.92	1.57
$Al_{70}Ti_{15}V_{15}$	1658.7	0.987	-2.57	1.38
$Al_{80}Ti_{10}V_{10}$	1656.6	0.934	-1.21	1.12
$Al_{90}Ti_5V_5$	1561	0.877	-0.93	1.00
Al	933	0.866	-1.22	0.87

4.4 Surface Tension – Discussion

The discussion of the surface tension results will be conducted mostly analogously to the discussion of the density data in 5.2. Compositional (*A*) and temperature (*B*) dependence will be discussed first. Subsequently, the mixing behavior (*C*) of the alloys will be discussed based on the surface tension findings. Therefore, different models that were introduced in sec. 3.3 are employed to describe the measured data and draw conclusions on the segregation behavior of the different alloy systems. This approach is applied to both the Ti-V and Al-V system. The previously existing findings for the Al-Ti system [13] are compared against both systems investigated in this work. Lastly, an attempt is made to expand this approach onto the section through the ternary Al-Ti-V system.

Ti-V

The results presented in this section are mostly adapted from [23] to fit the framework of this work.

A. Compositional dependence

Figure 49 shows the isothermal surface tension of liquid Ti-V at the reference temperature of 2100 K, as a function of the titanium bulk composition x^{B}_{Ti}. As usual, the surface tension was calculated using the linear fit parameters summarized in Table 18. For liquid Ti-V, the reference temperature lies within the temperature range for all measurements.

A monotonous decrease of the surface tension can be observed with increasing Ti mole fraction, with pure vanadium showing the highest (1.97 N/m) and pure titanium the lowest (1.46 N/m) surface tension. In section 4.3, several thermodynamic models have been introduced to describe the surface tension behavior of alloy systems. Figure 49 includes calculations for the Conventional Butler model both for the ideal solution case and the regular (non-ideal) solution. For these calculations ${}^{0}_{Ti}V$ and ${}^{0}_{V}V$ are needed for Eq. 33. Both can be derived from the corresponding density data introduced in sec. 5.1 and 5.2. In Figure 49 it becomes obvious that there is no significant difference in the data description by the ideal and regular solution model.

The general trend of the experimental data is very well reproduced by the Conventional Butler model for the ideal solution. Therefore, it can be assumed, that the liquid Ti-V system mixes ideally with regards to the surface tension. This assumption is further strengthened when carrying out the calculations following the Conventional Butler model for the regular solution. Using parameters from [118] to calculate the excess Gibbs energies for bulk and surface following a Redlich-Kister approach, the resulting excess energies are very small. Thus, the difference in the calculations for ideal and regular solution are neglectable. Theoretically, with the excess Gibbs energies being different from zero, the mixing behavior of liquid Ti-V is not strictly ideal, but they are so small, that there is no practical difference between the ideal and regular solution. In that sense, the mixing behavior of liquid Ti-V will be regarded as ideal concerning the surface tension.

B. Temperature dependence

The temperature dependence is illustrated in Figure 50, showing the temperature coefficient γ_T for liquid Ti-V at the reference temperature of 2100 K as a function of the Ti atomic concentration. The temperature coefficient is negative for all compositions measured. As the compositional dependence curve in Figure 49 is steeper for the pure elements and flatter for alloy compositions, the temperature coefficient is stronger negative for pure elements and closer to zero for alloys.

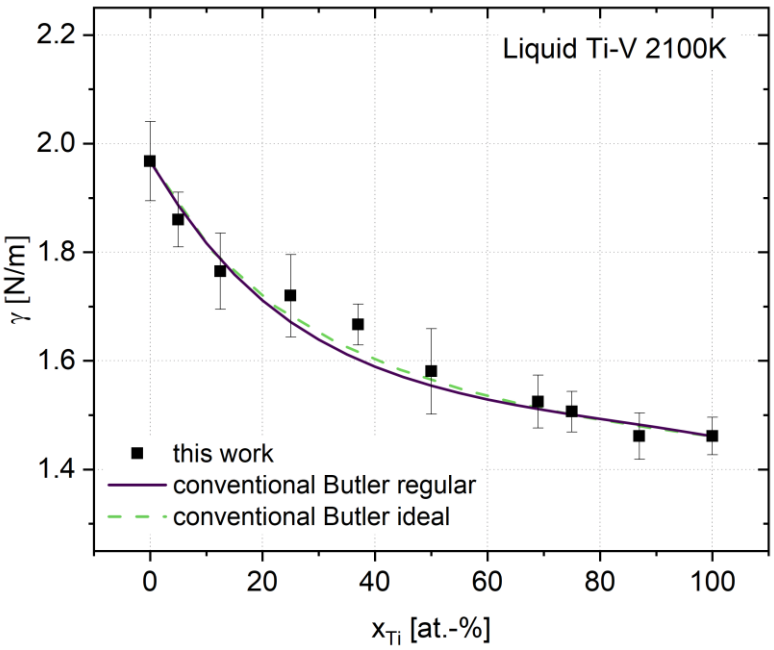

Figure 49: Isothermal surface tension of liquid Ti-V at 2100 K *as a function of the titanium bulk composition* x^{B}_{Ti}. *The dashed line shows the surface tension calculated following Eq. 40 for the ideal Butler model. The solid line represents the calculations for the regular (non-ideal) Butler model.*

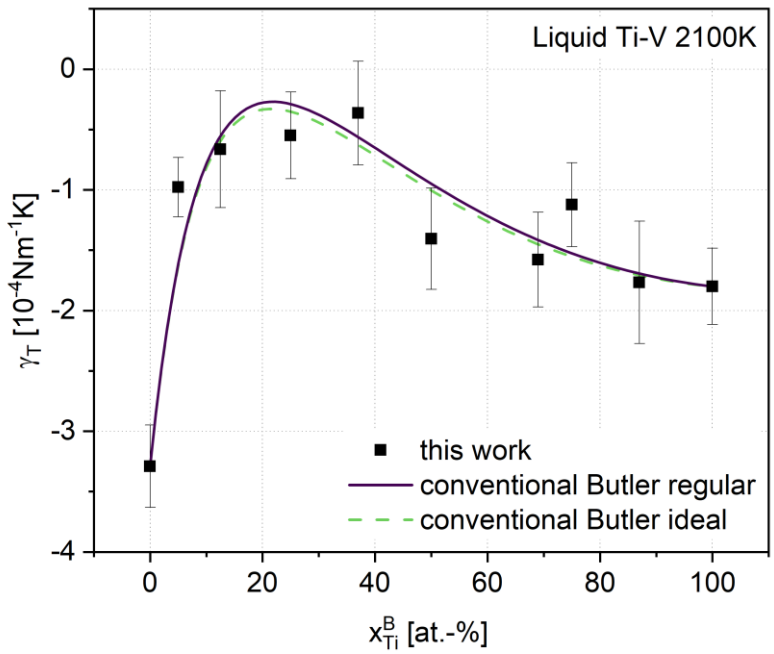

Figure 50: Temperature coefficient γ_T *for the liquid Ti-V system at* 2100 K *as a function of the titanium mole fraction. Calculations for the Conventional Butler model regarding the ideal and regular solution are included as dashed and solid line respectively.*

Upon increasing the vanadium mole fraction, the coefficient increases steeply towards a maximum at $x^{B}_{Ti} \approx 37$at.-%, before settling into the value for pure titanium. This progression suggests a smaller surface entropy for the alloys what could be interpreted as a higher degree of order for the alloys compared to the pure elements.

The comparison of the experimentally obtained temperature coefficient with those calculated for the Conventional Butler model of the ideal and regular solution show the same trend as observed for the compositional dependence in section (*A).* The calculations for the ideal case (dashed line) and the regular case (solid line) both reproduce the data qualitatively and quantitatively. Additionally, the calculations suggest a maximum of the temperature coefficient at lower Ti atomic concentrations (around x^{B}_{Ti} = 20 at.-%) than the experimental data. As for the compositional dependence, no significant difference between the two cases for the Conventional Butler model can be observed in the temperature coefficient. Again, an ideal mixture is observed for liquid Ti-V.

C. Mixing Behavior

The mixing behavior regarding the surface tension agrees well with the previous findings of an ideal mixture between Ti and V observed for the density. The same arguments of a similar electronic structure and both being d-transition metals can be made when investigating the ideal behavior of the surface tension. The hypothesis of an ideal mixture of Ti-V caused by their proximity in the periodic table holds true, since no significant excess surface tension is found.

In predicting the surface tension of the alloy system, the Conventional Butler model simultaneously models the surface composition of the molten sample. In most binary metallic liquids, the surface depletes in one species to minimize its overall energy. This effect is called segregation. The thermodynamic modelling of the surface tension at the same time includes information about the segregation in the investigated alloy system.

Figure 51 compares the segregation of the titanium alloys Ti-V, Ti-Al [13] and Ti-Cu [116] based on the thermodynamic model that best described the surface tension of the respective system. The surface concentration of the segregating species is plotted against the bulk concentration of the segregating species for the three different Ti-alloys. All alloys show a similar trend. However, in the case of Ti-Al and Ti-Cu the Conventional Butler model of the regular solution was used, since it best modeled the respective surface tension. Additionally, for Ti-Al and Ti-Cu aluminum and copper segregate to the surface during mixing, while for Ti-V, titanium is the segregating species. Usually, the component with the smaller surface free energy segregates to the surface, to minimize the systems overall energy.

The extent to which segregation occurs can be linked to the excess free energy, ^{E}G. Systems that show a positive excess free energy, $^{E}G > 0$, tend to demix showing strong segregation, while the opposite is true for systems with negative excess free energy, $^{E}G < 0$. All Ti-alloys investigated at our institute, much like most titanium alloys, show a negative excess free energy and therefore only moderate segregation. The excess free energy calculated for Ti-V is close to zero but still negative. Ti-V therefore fits the classification made in [14].

While the general extent of segregation is similar for all three Ti-alloys the segregating species depends on the alloying element. Figure 52 compares the segregation of the Ti-V system against the Ti-Al system by showing the bulk Ti composition against the Ti atomic concentration of the surface layer. Two things become evident from Figure 52. Firstly, in the case of Ti-V the surface enriches in titanium, while it depletes in titanium for the Ti-Al system, which was somewhat expected since vanadium shows a higher surface tension than titanium. Secondly, in contrast to Ti-V the Ti-Al system exhibits a strong difference in the calculations for the ideal and regular case of the Conventional Butler model. The ideality of the mixing for Ti-based alloys, much like the segregating species, seems to depend on the alloying element.

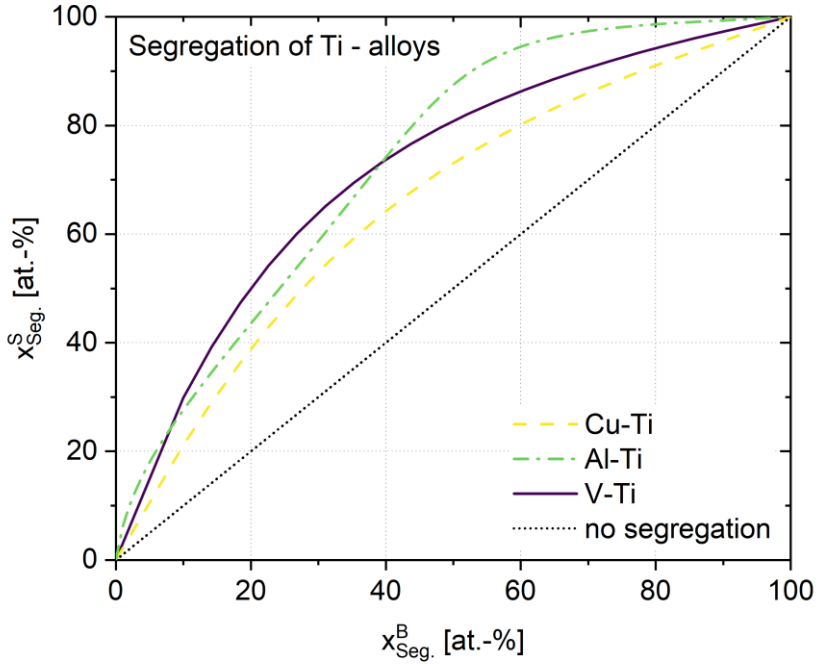

Figure 51: Calculated surface composition of the segregating species of different Ti-based alloys at 2100 K *as a function of the bulk composition of the segregating species. For Ti-V the ideal Conventional Butler model is employed and Ti is the segregating species. For Ti-Al [13] and Ti-Cu [116] aluminum and copper are the segregating species. For both alloys the regular case of the Conventional Butler model describes the surface tension data best and is hence used for the calculations.*

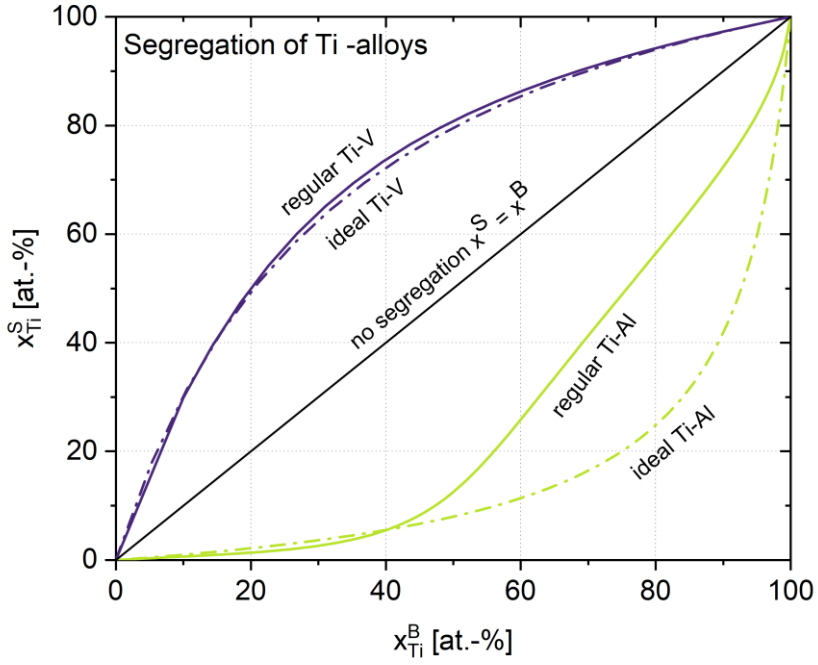

Figure 52: Titanium mole fraction of the surface layer versus the bulk titanium mole fraction for liquid Ti-V and Ti-Al at 2100 K. *The solid lines represent the calculations for the regular case of the Conventional Butler model while the dash-dotted lines show the calculations for the ideal case.*

Al-V

A. Compositional Dependence

As previously carried out, the compositional dependence is investigated by determining the surface tension for each tested alloy at the reference temperature of 1800 K with the linear fits done in sec. 5.3.2. Figure 53 shows the resulting isothermal surface tension as a function of the aluminum mole fraction. All alloy samples show a surface tension between those of the pure elements. Pure vanadium shows the highest measured surface tension of 2.069 Nm^{-1} and pure aluminum the lowest surface tension of to 0.723 Nm^{-1}.

Several thermodynamic models introduced in 3.3, are included in Figure 53 to reproduce the measured data. The previous Ti-V system showed ideal behavior when regarding the surface tension and was therefore best described by the mathematically most basic model, the Conventional Butler model in the ideal case. The calculations for this model according to Eq. 40 are represented by the dashed line. In this case the surface tension of the mixture is calculated purely from the bulk composition and the surface tension of the pure elements. Considering the findings for the density in 5.2 and the highly non-ideal behavior observed, it is little surprising, that the surface tension of the liquid Al-V system is not well reproduced by this model. As for the density, the surface tension of Al-V is underestimated by the calculations carried out for the ideal case. It can be assumed that the Al-V system behaves non-ideal for the surface tension as well as for the density.

When including the excess free energies to account for the non-ideal behavior of the system into the calculations for the Conventional Butler model (Eq. 36) the predicted surface tension is represented by the dotted-line in Figure 53. The experimental data is way better represented when considering the non-ideal system behavior. The Redlich-Kister parameters are taken from [119] and summarized in Table 22. For aluminum atomic concentrations smaller then 20 at.-% as well as more than 70 at.-% aluminum the measured data is very well represented by the Conventional Butler model for the regular solution. For aluminum atomic concentrations between 20 and 70 at.-% the surface tension is underestimated by the chosen model.

The next model tested against the measured data is the Renovated Butler model introduced by Kaptay [120] and summarized in 3.3.1. The calculations for this model are based on Eq. 34. For the Renovated Butler model, the ideal case was not considered, since it was previously shown that the liquid Al-V does not show ideal behavior regarding density and surface tension. All calculations labeled ‘Renovated Butler’ therefore refer to the non-ideal (regular) case. The Renovated Butler model is depicted in Figure 53 as the solid line. The Renovated Butler model describes the measured surface tension better than the Conventional Butler model for aluminum atomic concentrations between 20 and 70 at.-% and is still in reasonable agreement for the edge compositions.

The last model included in Figure 53 is the Egry model introduced in 3.3.4. The calculations for this model are based on the segregation factor described in Eq. 42. It was assumed, that AlV_3 is the main species segregating. The results of the calculations are added as the dash-dotted line. The Egry model shows the best agreement with the measured data for medium aluminum mole fractions, while having the worst accordance with the data for the edge compositions.

All thermodynamic models for the regular solution are in reasonable agreement with the measured data. From the different model formalisms, the differences between the model calculations can be pinned down to the mathematical description of the surface area. The quality of the modeling can therefore be linked to the quality of the surface area description. Additionally, it should be mentioned that the Redlich-Kister parameters can have an impact on the model quality. Considering Eqs. (34) and (36) an inadequate description of the excess Gibbs energy, ^{E}G, (resulting from variying Redlich-Kister

parameters) can lead to an apparent change in the assumed surface area. Ref. [119] the most recent thermodynamically assessment was used. However, different assessments yield different parameters.

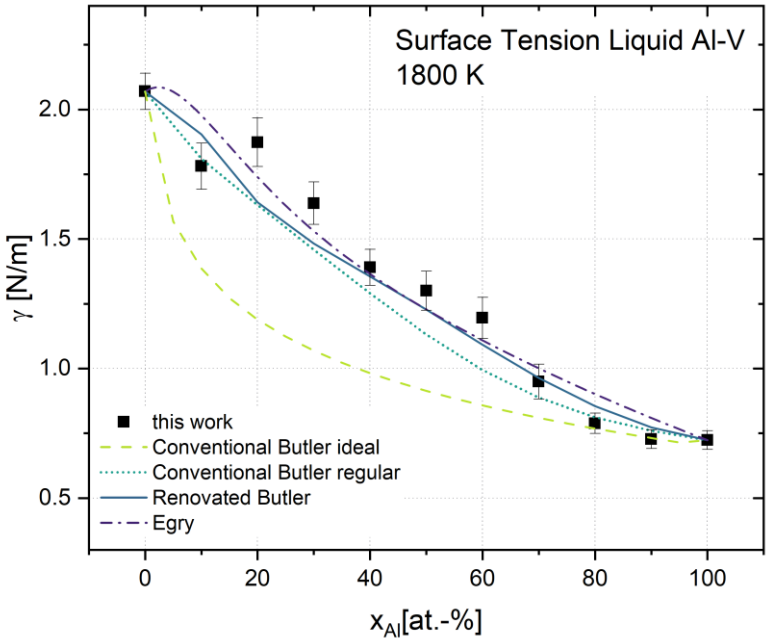

Figure 53: Isothermal surface tension of liquid Al-V at the reference temperature of 1800 K *as a function of the aluminum mole fraction. Calculations for the Conventional Bulter model of the ideal case, according to Eq. 40 are included as dashed line. The Conventional Butler model for the regular solution following Eq. 36 is shown as the dotted line. The Renovated Butler model (Eq. 34) is shown as a solid line and the Egry model (Eq. 42) is shown as dash-dotted line.*

Table 22: Redlich-Kister parameters ${}^{0}L_{\mathrm{Al,V}}(T)$ *and* ${}^{1}L_{\mathrm{Al,V}}(T)$ *for the liquid Al-V [119] and Al-Ti [13] system.*

System	Parameter	Value	Unit
Al-V	${}^{0}L_{\mathrm{Al,V}}(T)$	$-57725 + 9 \cdot T$	J mol^{-1}
	${}^{1}L_{\mathrm{Al,V}}(T)$	$-18000 + 8 \cdot T$	J mol^{-1}
Al-Ti	${}^{0}L_{\mathrm{Al,Ti}}(T)$	$-118048 + 41.972 \cdot T$	J mol^{-1}
	${}^{1}L_{\mathrm{Al,Ti}}(T)$	$-23613 + 19.704 \cdot T$	J mol^{-1}

B. Temperature Dependence

The temperature dependence of the surface tension can be analyzed for the liquid Al-V system by investigating the temperature coefficient, γ_T. Figure 54 shows the temperature coefficient at 1800 K for the Al-V system as a function of the bulk aluminum mole fraction. The compositional edges show the lowest temperature dependence in the surface tension, while a maximum in terms of amount can be observed for roughly 30 at.-% aluminum atomic concentration. As the surface tension, the temperature coefficient of the surface tension can also be predicted by the thermodynamic models used in this work. To do so, the surface tension is calculated using both the Conventional Butler model for the ideal case and the Renovated butler model for the non-ideal (regular) case at two different temperatures (1790 K and 1810 K). The temperature coefficient can than be obtained as the quotient of the surface tension difference and the temperature difference, $\gamma_T \approx (\gamma(1810\ \mathrm{K}) - \gamma(1790\ \mathrm{K}))/20\mathrm{K}$.

The calculations for the Conventional (ideal) Butler model are shown as the dashed line and the Renovated Butler model calculations for the non-ideal case are shown as the dash-dotted line. For aluminum atomic concentrations lower than 50 at.-% the temperature coefficients are overestimated by the ideal Conventional Butler model. The measured temperature coefficients are way better represented by the calculations carried out for the ideal case. Figure 54 greatly illustrates the highly non-ideal behavior of the liquid Al-V systems regarding the surface tension.

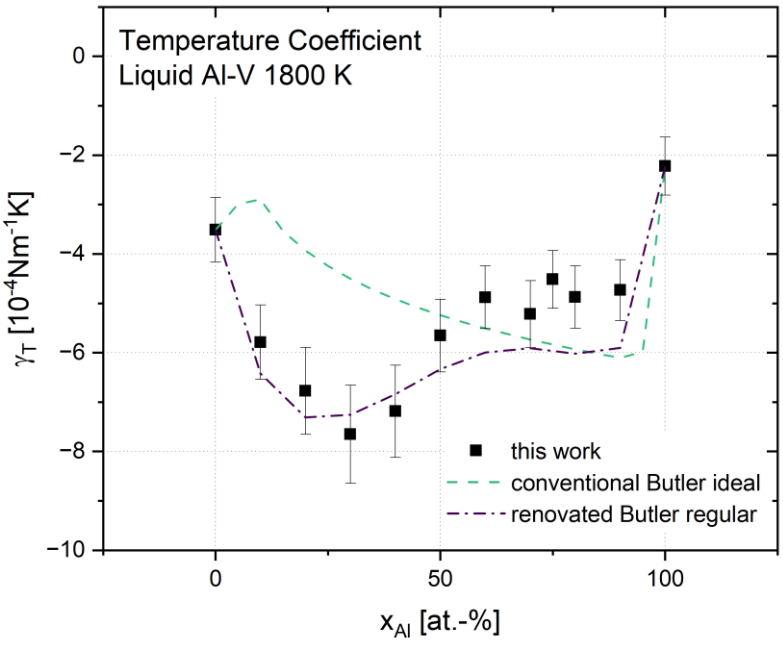

Figure 54: Temperature coefficients measured at 1800 K *for the liquid Al-V system as a function of the bulk aluminum mole fraction. The modeled coefficients with the Conventional Butler model for the ideal solution and the Renovated Butler model for the regular solution are shown as dashed and dash-dotted line respectively.*

Al-Ti

As done for the density discussion of both Al-Ti and Al-V it makes most sense to show some of the surface tension data measured for Al-Ti by Wessing [13] at this point. This is important both for the completeness sake and since the mixing behavior of liquid Al-V will be analyzed mostly by comparison with Al-Ti. All data shown here was previously published by Wessing [13] and was adapted to fit the layout of this work.

A. Compositional Dependence

Figure 55 shows the compositional dependence of the surface tension for the liquid Al-Ti system at 1800 K. The experimental data is compared to several thermodynamic models included as solid, dashed and dotted line. More detailed information on the modelling procedure can be found in [13]. The Chatain model is not considered in this work.

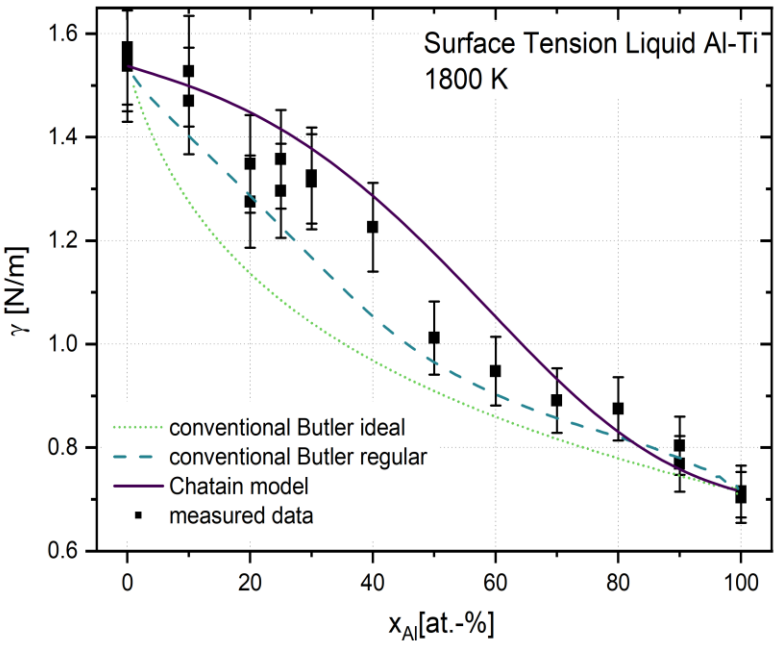

Figure 55: Isothermal surface tension for the liquid Al-Ti system at 1800 K *as a function of the aluminum mole fraction. The measured data was compared to the Conventional Butler model for the ideal and regular case and the Chatain model. The data was adapted from [13] to fit the layout of this work.*

B. Temperature Dependence

Figure 56 shows the experimentally measured temperature coefficients as a function of the bulk aluminum mole fraction. The data is compared to the modeled temperature coefficients by both the Conventional Butler model for the regular solution (dashed line) and the Chatain model (solid line). A comprehensive discussion of the compositional and temperature dependence of the surface tension for liquid Al-Ti can be found in [13].

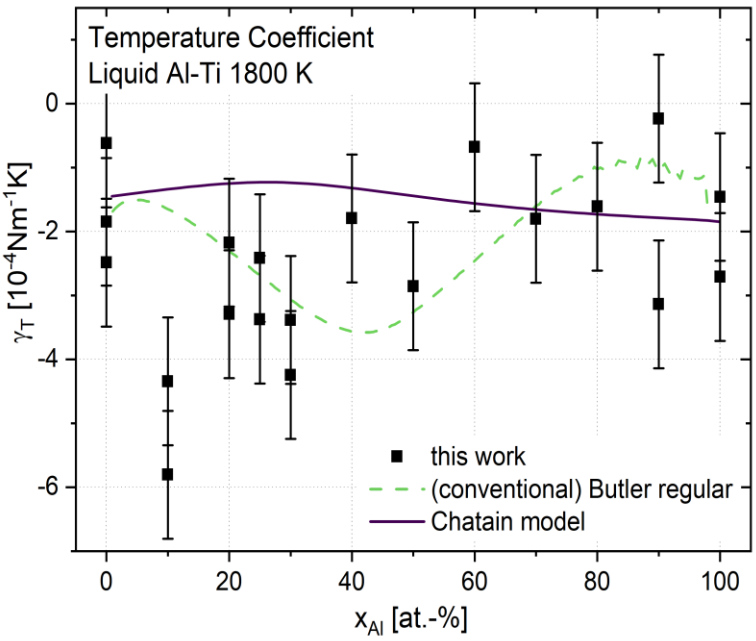

Figure 56: Temperature coefficients measured at 1800 K *for the liquid Al-Ti system as a function of the bulk aluminum mole fraction. The modeled coefficients with the Conventional Butler model for the regular solution and the Chatain model are shown as dashed and solid line respectively.*

C. Mixing Behavior

As done earlier, the compositional and temperature dependence of the surface tension can be used to gain some insight into the general mixing behavior of the binary systems Al-Ti and Al-V in accordance with the 2nd postulated research goal.

It was already explained, that the thermodynamic models employed not only predict the surface tension of the investigated alloy system but also the surface composition of the respective alloy. In this way, the segregation can be investigated for the binary mixtures. As expected, the predicted segregation varies with the thermodynamic model chosen. The differences in the segregation prediction can be observed in Figure 57, where the aluminum mole fraction of the surface of the liquid droplet is modeled as a function of the bulk aluminum mole fraction with the Conventional Butler model for the ideal solution, the Renovated Butler model for the regular solution and the Egry model for compound formation. As expected, all models predict a segregation of aluminum to the droplet surface. All curves lie above the dash-dotted diagonal line representing an equal aluminum atomic concentration of bulk and surface. Since surface tension can be viewed as excess surface energy per unit surface area [14], an enrichment of the surface layer in aluminum, which has the lower surface tension in the binary system, can be expected as a minimization of the systems free energy per surface area.

In this context, it can be easily understood, that the Conventional Butler model for the ideal solution predicts the strongest surface segregation of aluminum since it underestimates the compositional surface tension (compare Figure 53). As pointed out earlier, the Al-V system does not behave like an ideal system and instead exhibits attractive interactions ($^{E}g < 0$), a much less prominent segregation is predicted by both the Renovated Butler model for the regular solution as well as by the Egry model. Similar to their prediction of the surface tension in Figure 53, both models predict a very similar surface

segregation for a bulk aluminum atomic concentration up to 40 at.-%. Above this threshold, the Renovated Butler model for the regular solution predicts slightly more aluminum in the surface layer. Regarding the good agreement with the Renovated Butler model with the experimental surface tension data, especially for high aluminum bulk mole fraction, it is reasonable to assume that segregation is best described by the Renovated Butler model for the regular solution.

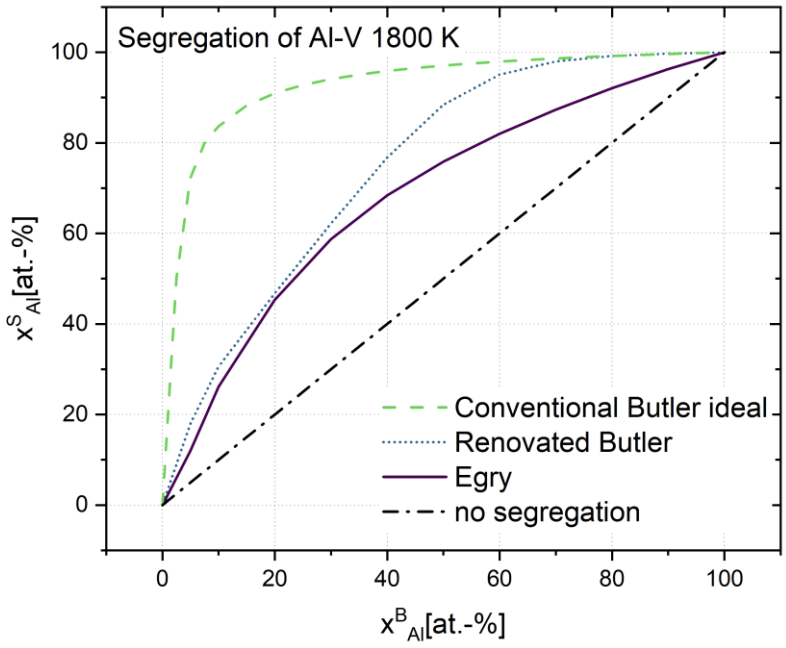

Figure 57: Surface composition of the liquid Al-V system at 1800 K *as a function of the aluminum bulk mole fraction. Data for the ideal Conventional (Eq.36) and regular Renovated Butler model (Eq.34), as well as data for the Egry model (Eq.42) are presented.*

The segregation is a great aspect to utilize when comparing the mixing behavior of different alloy systems. Comparing the mixing behavior of different, similar binary subsystems can help understanding the mixing behavior in more complex systems and therefore help achieve the 2nd research goal proposed in this work for the ternary Al-Ti-V system. In the context of this work, it is elementary to compare the mixing of Al-V with the mixing of Al-Ti.

Earlier in this work, a similar behavior of Ti and V was postulated when mixing with Al. Figure 58 compares the segregation behavior of Al in the two binary systems Al-V and Al-Ti. The graph shows the aluminum surface mole fraction predicted by the Conventional Butler model for the ideal and non-ideal solution as a function of the bulk aluminum mole fraction. The calculations for the Al-V systems are displayed as the solid lines, while the calculations for the Al-Ti system are shown as dashed lines. Both systems show a very similar segregation behavior. The non-ideal models describe both systems best. The segregation proposed by these models are almost identical for the two systems. The theory of similar mixing of Ti and V with Al is strengthened by the similar surface mole fraction of Al when varying the bulk mole fraction of Al.

With respect to the 2nd research goal of this work, these finding indicate an interchangeability of Ti and V when mixing with Al regarding the general mixing behavior of the binary systems. Connecting this with the findings, of the ideal mixing of Ti with V, the similar mixing behaviors of both elements with liquid Al could potentially be justified by the similar electronic structures of Ti and V. Further studies need to be carried out to further prove this hypothesis.

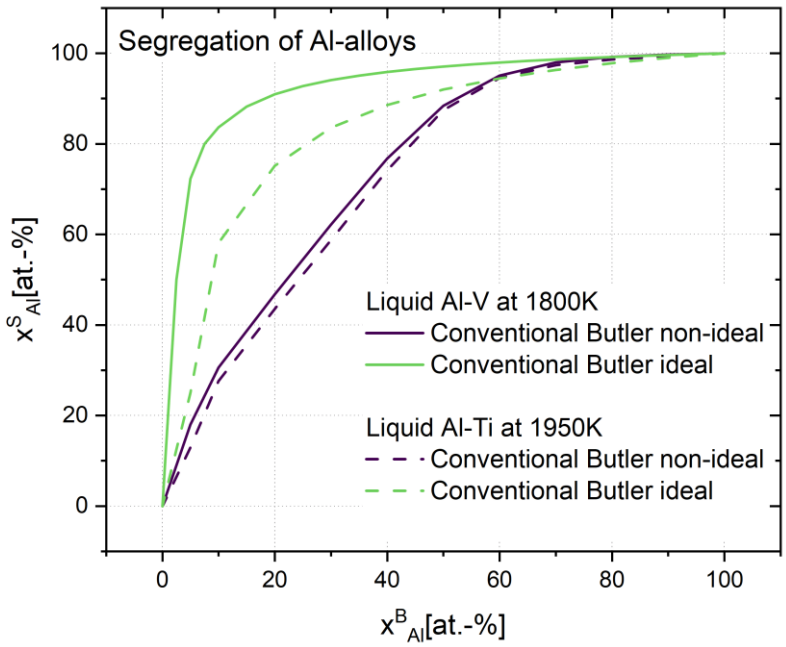

Figure 58: Surface composition of the Al-V (solid lines) system and the Al-Ti (dashed lines) system at 1800 K *as a function of the bulk mole fraction of aluminum. The composition has been calculated in accordance with the ideal and regular Butler model for both alloy systems.*

Al-Ti-V

One reason for investigating the binary subsystems was to understand the mixing behavior of the ternary Al-Ti-V system. In the concept, developed at the beginning of this work, it was stated that the general approach in doing so is by combining the findings for all binary sub-systems to form the foundation towards understanding the ternary system.

This is done exemplary in the following for one section through the ternary Al-Ti-V system, since a systematical investigation of the complete ternary would go well beyond the scope of this work. The general question that this work aims to answer remains the same as for the density investigations of the ternary system. For the example of the surface tension this translates to:

Can the surface tension of a ternary alloy be predicted solely from the quantities measured for the binary sub-systems?

To answer this question, the same schematic approach as for the binary systems was chosen. The surface tension for the $Al_xTi_{(1-x)0.5}V_{(1-x)0.5}$ section was compared at the reference temperature of 1800 K. The results are shown in Figure 59 as a function of the bulk aluminum mole fraction. The experimentally obtained surface tension is now being compared to different solutions of the Conventional Butler model. First, the Conventional Butler model was solved without considering a ternary term in the excess Gibbs energy in Eq. 9. The excess Gibbs energy can be calculated solely as the sum of all the excess Gibbs energies observed for the binary systems in that case. For the chosen ternary section, this reduces to the excess Gibbs energy for the Al-Ti and Al-V system as the Ti-V was found to mix nearly ideally. The result is included as the dashed line. For high aluminum atomic concentrations over 60 at.-% the agreement with the measured surface tension is good, but for lower aluminum mole fractions the surface tension is underestimated. Afterwards, the Conventional Butler model was solved considering a ternary term in the excess Gibbs energy in Eq. 9. The corresponding parameters were taken from [121] and are display in Table 23. The dash-dotted line shows the results for the Conventional Butler model considering a ternary term. The agreement could be expanded up to 50 at.-% aluminum when considering a ternary contribution, but for lower aluminum mole fractions the surface tension is still underestimated.

For both previous calculations the partial excess free energy of the surface was calculated using the identical mathematical expression as for the partial excess free energy of the bulk, simply by adding the factor $\beta = 0.66$ accounting for the different coordination of surface atoms compared to bulk atoms [54]. Usually, an atomic factor of $\beta = 0.83$ is a good average to describe most system [14]. For all binary systems the surface tension could be modelled well using this proposed factor $\beta = 0.83$. However for the ternary system the agreement of both model calculations with the experimental data were significantly improved by changing this factor to $\beta = 0.66$ which has proven advantages for different Al-based alloys [14].This could indicate, that the coordination of surface atom or the surface structure changes for the ternary system compared with its binary sub-systems. However, numerous other factors, such as changing binding energy, rearrangement of atom configurations and many more [122], can change the value of β, too.

These findings can be used to answer the previously asked question of how to model the ternary system based upon its binary sub-systems. It could be shown, that in the case of the chosen section through the ternary system, a ternary term needs to be considered for the calculation of the excess Gibbs energy. Therefore, the ternary section cannot be modelled solely form the binary sub-systems.

This in turn contributes to the 2nd proposed research goal. It was shown that the mixing of the ternary system does not directly follow from the mixing of its binary sub-system. It can be assumed, that the general mixing behavior changes from the binary to the ternary system. At first glance this forms a contrast to the previously proposed hypothesis of an interchangeable mixing of Ti and V with Al. One

would assume, that if Ti and V mix similarly with Al, the mixing behavior of the chosen section would not differ significant from the mixing of Al-Ti or Al-V.

The best agreement witch the measured data can be obtained when using a factor $\beta = 0$ for the model calculations. It is important to keep in mind that simultaneously a ternary interaction parameter $G_T^E \neq 0$ needs to be considered. The model calculations using $\beta = 0$ and $G_T^E \neq 0$ are shown in Figure 59 as a solid black line. A factor $\beta = 0$ appears to be no physical in combination with $G_T^E \neq 0$ at first sight, as it suggests, that the surface acts as an ideal solution while the bulk of the sample still is a regular solution. However, it might also be possible that Redlich-Kister approach for calculating the excess Gibbs energy might reach its limitations for the ternary system. In that case, a different modelling approach utilizing a quasi-chemical compound formation model might lead to better modelling accuracy. Additionally, a variation in the modelling success using excess Gibbs energy contributions may indicate insufficient thermodynamic assessments for the Al-Ti-V system, as the calculations of the excess Gibbs energies are based upon these assessments. In summary, more work is needed to fully understand and accurately model the mixing behavior of the Al-Ti-V system.

The surface composition of the ternary alloys predicted by the thermodynamic modelling can help understand this phenomenon. Figure 60 shows the surface mole fraction of each alloy component as a function of the bulk aluminum mole fraction predicted by the Conventional Butler equation considering the ternary term and using the factor $\beta = 0.66$. As expected from the surface tensions of pure Al, Ti and V and the surface energy minimization driving segregation, Al is the main component in the surface layer followed by Ti and V. For bulk aluminum concentrations higher than 40 at.-% the surface composition shows the expected behavior for the $Al_xTi_{(1-x)0.5}V_{(1-x)0.5}$ section, considering the segregation behavior of the binary Al-Ti and Al-V system. The surface enriches heavily in aluminum and Ti and V are almost present in a 1:1 ratio with a slight excess of Ti. In this aluminum mole fraction area, the measured surface tension is still in reasonable agreement with the Butler equations neglecting the ternary term (see Figure 59).

For aluminum atomic concentrations up to 25 at.-%, Ti and V show different segregation behavior, with the surface depleting in Ti and enriching slightly in V, which stands in contrast to the energy minimization since pure liquid V has a higher surface tension than pure Ti. In this area the differences between the calculations neglecting and considering a ternary contribution become more and more apparent. The different segregation behavior and the resulting compositional changes in the surface can be a first indicator for a changed mixing of Ti and V with Al for low aluminum mole fractions. This apparent conflict together with the changing factor β can be the starting point of interesting future investigations towards further expansion the 2nd proposed research goal of this work to fully understand the mixing behavior of the Al-Ti-V system.

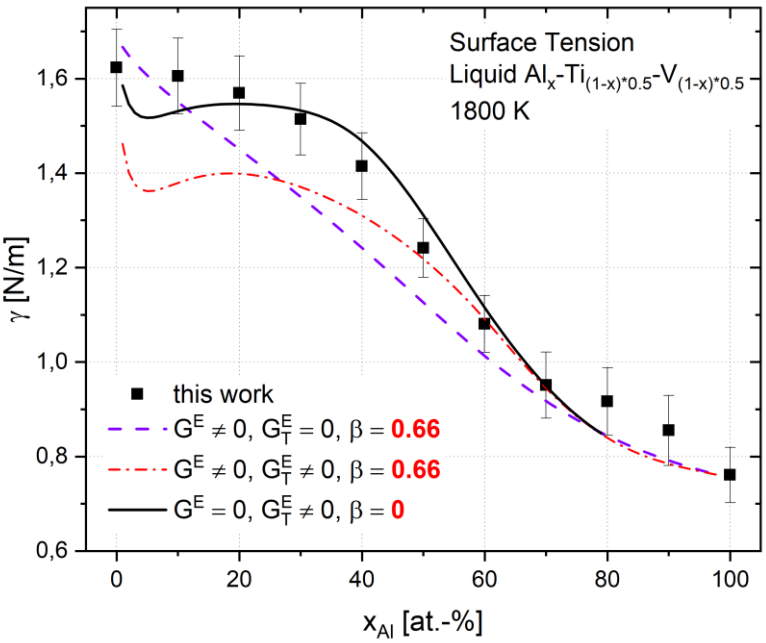

Figure 59: Isothermal surface tension for the liquid $Al_xTi_{(1-x)0.5}V_{(1-x)0.5}$ section as a function of the bulk aluminum mole fraction at 1800 K. *The experimental data is compared to different solutions of the Conventional Butler model. In some cases, the ternary term for the excess Gibbs energy in Eq. 9 was neglected and in some cases the ternary term was considered. Additionally, the factor β was varied between 0 and 0.66 to calculate the excess Gibbs energy of the surface.*

Table 23: Optimized thermodynamic parameters for the liquid Al-Ti-V system taken from Ref. [121].

Phase	Parameter	Value	Unit
Liquid	${}^0L_{Al,Ti,V}$	−550000	J mol^{-1}
	${}^1L_{Al,Ti,V}$	−50000	J mol^{-1}
	${}^2L_{Al,Ti,V}$	390000	J mol^{-1}

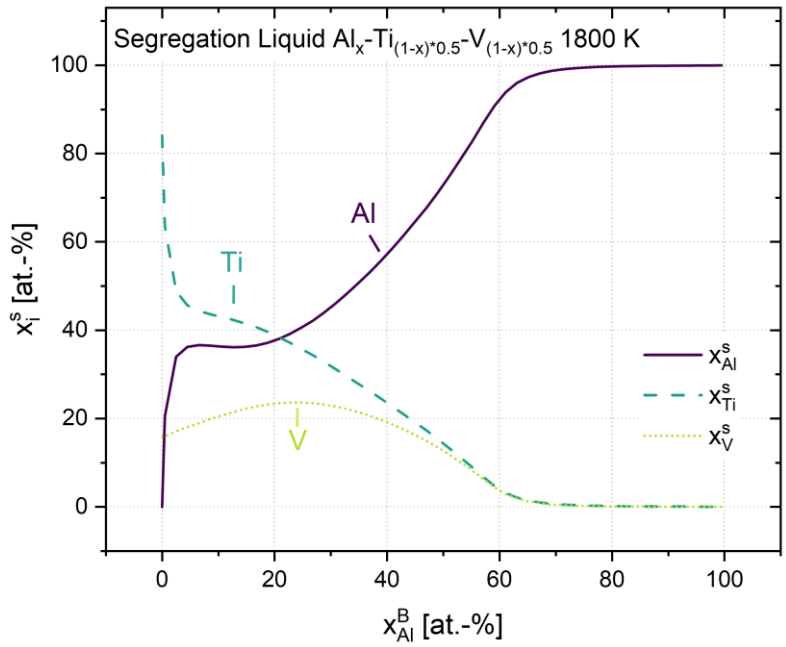

Figure 60: Surface quantity of Al, Ti and V as a function of the bulk aluminum mole fraction obtained by solving the Conventional Butler model considering the ternary term and a factor $\beta = 0.66$.

4.5 Oxygen Influence

The previous chapters were mainly focused on fulfilling the 1st and 2nd proposed research goal, namely building a thermophysical property data base for the Al-Ti-V system and using the obtained data to gain insights into the mixing behavior of the system. With such systematical measurements, investigating the potentially crucial influence of oxygen on the before measured thermophysical properties is highly interesting. Understanding a possible oxygen influence can greatly enhance the scientific value and industrial applicability. With the oxygen influence being considered the thermophysical data measured can truly be called accurate and reliable. Simultaneously, the presence of oxygen can alter all assumptions made based on these thermophysical properties. Therefore, investigating the oxygen influence is not only necessary to reach the 3rd and final goal of this work, it is also essential to consolidate the investigations carried out so far.

To achieve the third and final proposed goal of this work thermophysical property data depending on the oxygen presence is necessary. Such data can only be obtained through a reliable and well understood experimental method. Such a method was created by implementing the OCS into the EML setup at DLR in cologne. The practical implementation is described in section 3.3. In order to gain meaningful insights from the thermophysical property data generated with this novel setup, the measurement principle of the OCS in combination with the EML needs to be studied. The following section aims to provide the needed insights by performing elaborated ‘pre-experiments’ working out the operational functions of the OCS in the EML setup.

After the experimental method is established, several sections are dedicated to the investigation of the oxygen influence on the surface tension of liquid vanadium.

4.5.1 Results – OCS Operation

The oxygen control system used in this work is not comparable to a commercially available sensor unit. There is no standardized operation or calibration procedure. In its design, the OCS used in this work is one of only a few comparable systems worldwide. Especially, with its wide operating range reaching to extremely low oxygen partial pressures (10^{-20} bar) it cannot be compared to conventional sensors and controllers such as industrial temperature sensors or mass flow controllers.

It is therefore crucial, to understand the measurement principle and the possible interactions with any experiment carried out. With a device as complex as the OCS this would fill a PhD thesis of its own and would certainly extend the scope of this work by far. Rather than fully investigating the potential and challenges of the OCS it is therefore the aim of this work to provide a foundation of both systematical data and experimental data which future investigations can build upon. Simultaneously, these first fundamental findings are integrated into the framework of this work to help evaluate the influence of oxygen on the previous findings.

The systematic investigations on the OCS are particularly important considering that a system very similar in design is scheduled to be installed in the EML onboard the International Space Station (ISS) in the near future. This work can be a first reference for the researchers planning and carrying out their experiments onboard the ISS as well as a foundation for further ground support programs.

Two steps are performed in order to establish a functional understanding of the OCS in the EML environment. First, OCS ‘reference measurements’ are carried out without a levitation experiment being carried out. Through this approach any influences of the experimental conditions on the measurement results can be excluded and the capabilities and challenges of the OCS as a measurement system can be carved out. In a second step, first levitation experiments on simple model systems, in this case pure

liquid vanadium, are carried out with the OCS running to investigate the basic interactions between the EML and the OCS.

To gain a first, very basic idea of the general measurement principle the 'bypass' configuration is chosen. In this configuration, the gas flow is solely circulating through the OCS, contrary to the gas flow depicted in Figure 10, by bypassing the EML processing chamber. Figure 61 shows the result of this first 'bypass' test.

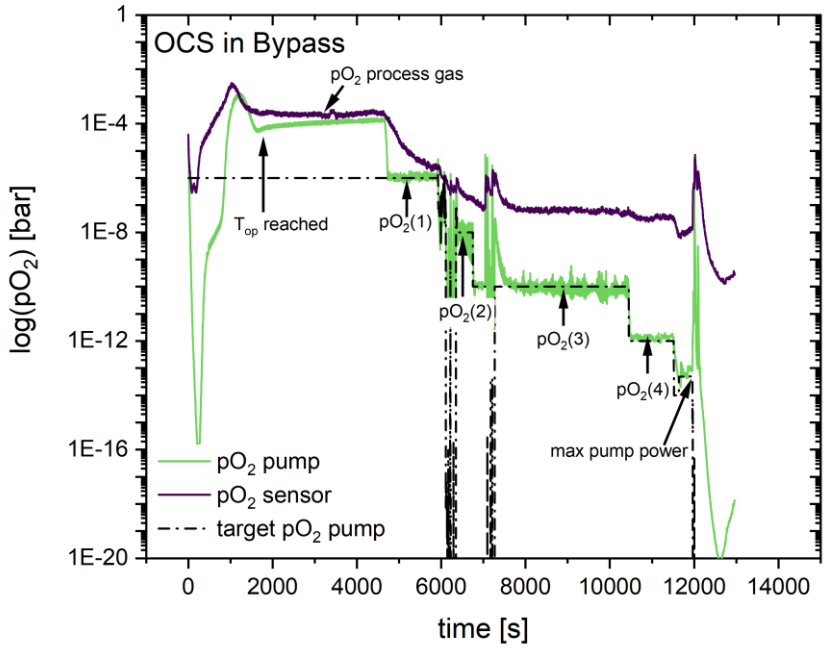

Figure 61:Oxygen partial pressure measured at the sensor and pump units of the OCS. The measurement was carried out in a bypass configuration, with the process gas (Ar) circulating solely through the OCS bypassing the EML process chamber. Different target values were set for the oxygen partial pressure at the pump unit.

The first thing to notice is that two distinct partial pressures of oxygen are displayed. As introduced in sec. 3.2.2 the OCS consist of two YSZ units able to measure the oxygen partial pressure. While the 'sensor' unit is only capable of measuring the partial pressure, the 'pump' can additionally introduce an oxygen flow into the processing chamber effectively 'pumping' oxygen into the chamber or out of it. At first glance it can be quite confusing that both units are able to measure the oxygen partial pressure. When investigating the measurement results, one has to always keep in mind the relative position of the respective unit. The 'sensor' unit is located right at the 'entrance' were the atmosphere is introduced from the EML chamber into the OCS. The 'pump' unit is located at the gas 'exit' where the gas is introduced back into the EML chamber after passing through the OCS. For the 'pump' unit itself, the measuring part of the YSZ tube is located right behind the 'pumping' part of the tube, relative to the gas flow.

With this in mind Figure 61 can be analyzed. The OCS needs roughly 20 min. (1200 s) to heat the YSZ tubes to the operation temperature $T_{\mathrm{op}} = 873$ K. After that, an almost steady partial pressure of $\approx 10^{-4}$ bar can be observed in the OCS. This partial pressure lies slightly higher than the partial pressure expected for the 750 mbar process gas of Ar (99.9999 vol. pct. purity Ar) which would be expected to have a partial pressure of oxygen between 10^{-6} bar and 10^{-5} bar. The observed partial pressure can be attributed to a poor conditioning of OCS atmosphere, as will be shown later.

After roughly 30 min. of measurement a first target value for the partial pressure measured at the pump was set to $pO_2(1) = 10^{-6}$ bar. It can be seen, that the value is reached almost immediately for the pump

while the partial pressure measured at the sensor follows with a certain inertia. The same can be observed for the second target ($pO_2(2)$) set. For the third and forth target set ($pO_2(3), pO_2(4)$), the partial pressure could be reached at the pump but the signal at the sensor did not follow. This behavior illustrates one big challenge of the OCS. In this first test the target partial pressure was adjusted over 6 orders of magnitude which is quite challenging for any PID control to perform. When setting the third target partial pressure, $pO_2(3)$, a spike in partial pressure measured at the pump appears in Figure 61. Instead of decreasing the partial pressure in the OCS, an increase in pO_2 can be observed in the sensor signal, which shows that oxygen was briefly pumped into OCS instead of out of the OCS. Even though the PID control could afterwards quickly adjust the partial pressure to the target value for the pump the brief increase in oxygen generated an offset between the partial pressure measured at the pump and the sensor. For a short moment the partial pressure pumped into the OCS was about 4 orders of magnitude higher than the target value set. These changes in order of magnitudes make a precise PID even more necessary, so that the experiment is not influenced by such spikes caused by poor controls.

Before the end of the experiment the PID control was circumvented by setting the lowest possible value as target pO_2 at the pump. In this way both signals could be decreased drastically. A partial pressure of $pO_2 = 10^{-20}$ bar could be reached at the pump and $pO_2 = 10^{-10}$ bar could be reached with the expected inertia at the sensor. This shows that the oxygen partial pressure in the process gas can be adjusted to very low orders of magnitude.

Summarized, the first test showed that:

1. The basic operational function was proven. A steady, consistent partial pressure could be measured which matches roughly with the expected value for pure Ar. The differences between the signals of the pump and sensor unit need to be considered when evaluating the oxygen partial pressures.
2. The partial pressure at the pump could be adjusted between $10^{-4} > pO_2 > 10^{-20}$ bar. At the sensor a minimal $pO_2 = 10^{-10}$ bar could be set.
3. The PID control parameters need to be adjusted to allow an operation over the immense measurement range. The effects of an experimental range over more than 15 orders of magnitude need to be considered when evaluating the results.

A similar test was performed with the OCS connected ‘in-line’ with the EML process chamber. The results can be seen in Figure 62. The first difference between the two tests is the steady partial pressure that is reached after the operation temperature is set. The $pO_2 < 10^{-5}$ bar observed are much closer to the partial pressure expected for the 750 mbar pure Ar in the process chamber. In contrast to the previous ‘bypass test’ the chamber atmosphere was conditioned before the experiment. To do so, the complete system including EML and OCS were first evacuated down to a total pressure of 10^{-5} mbar. The system was then flushed twice with pure Ar gas. Subsequently, the system was evacuated over night to a total pressure of 10^{-6} mbar before being filled with the process atmosphere of 750 mbar pure Ar. This conditioning reduced the initially observed oxygen partial pressure by over one order of magnitude. One possible explanation would be that residue with high oxygen share, such as CO, CO_2 or H_2O, adsorbed at the chamber walls are flushed out by the procedure.

After letting the OCS equilibrate, the target partial pressure at the pump was first set to $pO_2 = 10^{-7}$ bar, and after almost no response was observed by the sensor unit, it was set to the lowest possible value to achieve the highest possible O_2-pumping performance. While the partial pressure at the pump decreased rapidly, the partial pressure measured at the sensor only decreased slowly from $pO_2 = 10^{-5}$ bar to $pO_2 = 10^{-6}$ bar over more than 100 minutes. The slow response by the sensor can be attributed to different effects. First, the chamber gas volume adds a significant inertia to the system since its gas volume is large compared to the total pumping power of the OCS. Secondly, the OCS has to ‘pump against’ the leak rate of the system. Every real vacuum system has an effective leak rate > 0 bar/s. In the case of the OCS, ambient air is leaking into the system carrying roughly 21 vol.-% oxygen. This leak rate translates to a constant increase in oxygen partial pressure over the course of the experiment.

Especially in scenarios with extremely low oxygen partial pressures ($pO_2 < 10^{-7}$ bar) can this leak rate heavily influence the measured values. Combined with the large chamber volume this leads to immense timespans needed to reduce the 'chamber oxygen partial pressure' measured by the sensor unit. It takes roughly 90 minutes to decrease the oxygen partial pressure (measured with the sensor) from 10^{-5}bar to 10^{-6}bar.

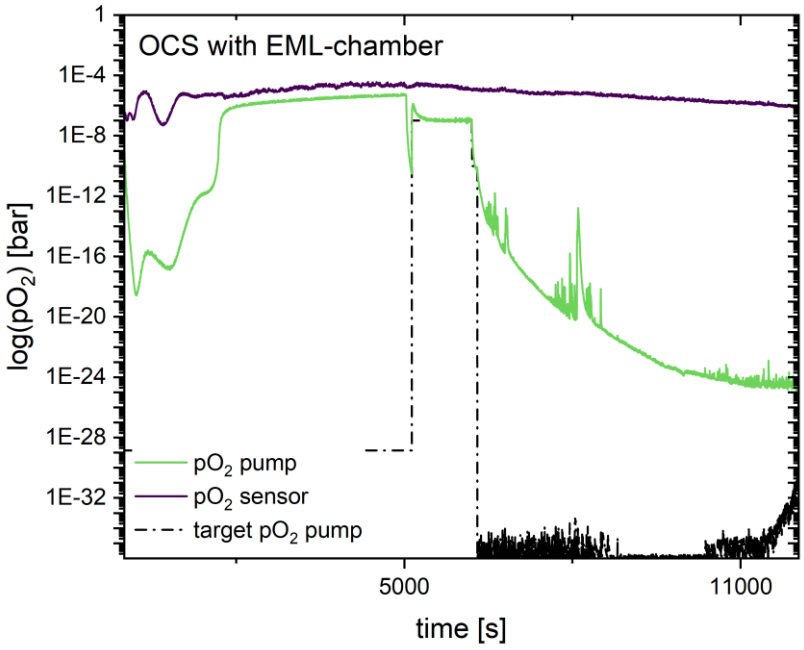

Figure 62: Oxygen partial pressure measured at the pump and sensor unit with the OCS connected in-line with the EML process chamber. The target partial pressure at the pump was set to the lowest possible value in order to achieve maximum pumping power. No levitation experiment was carried out.

To quantify the leak rate and its influence on the partial pressure measured, different pO_2 are set at the pump and the OCS, connected in-line with the EML chamber, and the system is given some time to equilibrate. Afterwards, the pump is turned off and the response by both sensor and pump oxygen partial pressure is recorded in Figure 63.

Three different target partial pressures, $pO_2 = 10^{-8}; 10^{-12}; 10^{-13}$ bar, are set at the pump. After equilibrating for at least 2h, the O_2 pump is turned off. The three different experiments are shown in on graph in Figure 63 with the same color for the partial pressure at the pump and the corresponding sensor pressure for each individual measurement. The partial pressure measured at the pump unit is depicted as a solid line, the partial pressure at the sensor is depicted as a dash-dotted line in the same color for the respective target partial pressure set. Between the measurements of Figure 62 and this measurement, an optimization of the PID parameters was conducted. Compared to the earlier measurements, the pump target partial pressure is reached much quicker and with much less over- or undershooting. For the sensor signal the same general trend as in Figure 62 can be observed. The partial pressure decreases very slowly for each target partial pressure set at the pump unit. The partial pressure trend recorded with the sensor unit is independent from the target value set. When turning the O_2 pump off, the oxygen partial pressure suddenly increases before it slowly approaches a value of $pO_2 = 10^{-3}$ bar. This trend can be observed for both sensor and pump unit starting simultaneously with the stop of the oxygen pump. From Figure 63 the O_2 leak rate can be estimated from the increase in partial pressure as roughly 10^{-7} bar/s. In everyday terms such a leak rate would refer to a 'gas tight' system. Regarding vacuum technology, it would correspond to a $3 \cdot 10^{-6}$m hole, resembling a minor leak in a vacuum system. As a comparison, a leak rate of 10^{-14} bar/s represents the lower detection limit of modern helium leak detectors. The

almost identical response after stopping the oxygen pump in all three cases shows that the leak rate is independent of the target partial pressure set at the pump. It is also important for the operational use of the OCS, that the oxygen partial pressure response of the sensor unit during the 2 h equilibrating phase is nearly independent of the target value set at the pump. Since the sensor unit sits right at the chamber exit, it stands to reason that the oxygen partial pressure in the chamber is closely resembled by the partial pressure measured with the sensor unit. With this in mind two possible explanations become apparent. Either the pumping power needed to reach the target value set at the pump does not greatly differ for target values between 10^{-8} bar and 10^{-13} bar. Or the oxygen partial pressure in the chamber does not change significantly with changing pumping power.

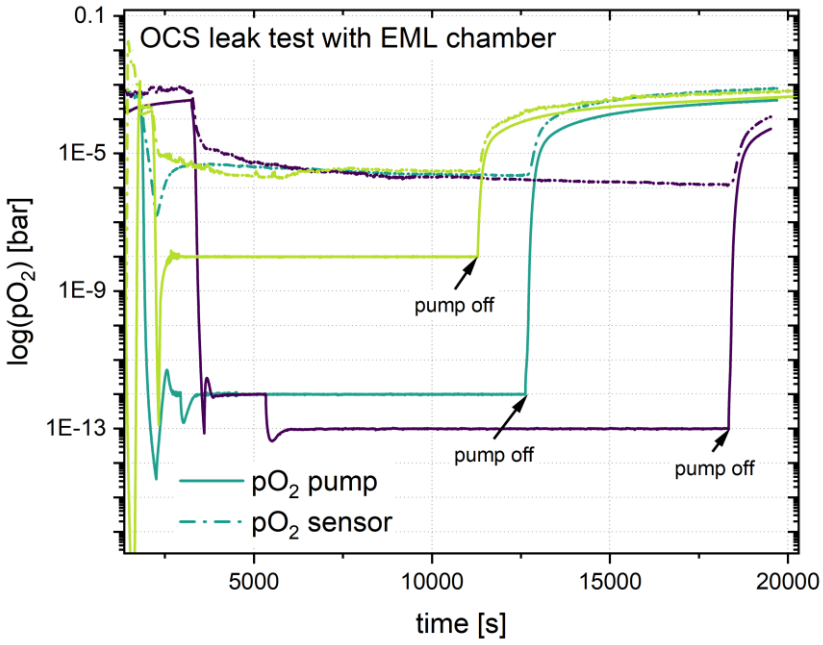

Figure 63: Leak test with the OSC in-line with the EML chamber. Three target partial pressures are set at the pump and the response in partial pressure at the sensor and pump are recorded over time.

Figure 64 shows the O_2 pump power needed to reach the target partial pressure set for the pump in percent of the maximum pump power. Bearing in mind the earlier consideration, two things become apparent. Firstly, the pump power needed to adjust the partial pressure at the pump is very low with around 0.15 percent. Secondly, the power needed to reach the target set, tends towards the same value for each target set. In the concrete experimental context this means, that only a small gas volume is pumped down to the target partial pressure bevor it is put through the sensor part of the pump unit (which is located at the same YSZ tube right behind the pump part) before it is introduced into the EML chamber.

All these considerations regarding the PID control, the conditioning, the inertia caused by the chamber and the leak rate are done in order to reach the 3rd milestone introduced at the beginning of this chapter. To carry out meaningful measurements of the surface tension under the influence of oxygen, it is essential to develop an experimental procedure that minimizes disturbing influences by the measurement method itself. The first step in doing so is to identify possible disturbing influences and experimental challenges, as done above. The possible most impactful challenge might be posed by so called ‘buffer gas’ reactions taking place in the system atmosphere.

Combining the high number of different, possible buffer gas reactions and the huge range of possible oxygen partial pressure, the topic of buffer gas reactions is way too complicated to be investigated here

in its entirety. It is rather the aim of this work to introduce the topic and get a sense of its influence on the measurement principle, so that it can be considered when designing further measurements. When looking at the topic in a very simplified way using the reaction of hydrogen H_2 and oxygen O_2 to water H_2O, the equilibrium of the gas reaction in Eq. 71 has to be considered.

$$H_2 + \frac{1}{2} 0_2 \leftrightarrow H_2O \qquad (71)$$

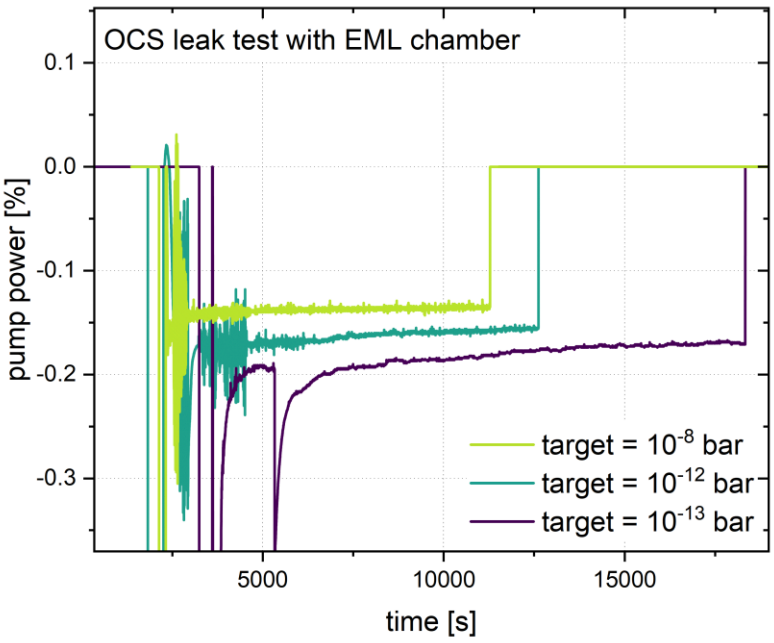

Figure 64: O_2 pumping power needed to reach the target set at the pump unit in Figure 63 as a function of time.

Assuming a fixed initial partial pressure of hydrogen in the system, three regions can be distinguished. In the case of very low oxygen partial pressure almost all added oxygen will react with the present hydrogen to form water vapor. In this scenario, pumping oxygen into the atmosphere using the OCS would barely change the observed oxygen partial pressure until the stoichiometric composition of H_2 and O_2 is reached. Upon reaching the equivalence point, a further increase in oxygen can result in a sudden change in oxygen partial pressure by several orders of magnitude comparable to a chemical titration. Further increasing the oxygen partial pressure above the equivalence point, shifts the reaction equilibrium leading to a steady increase of oxygen partial pressure measured. Ref. [79] explains in greater detail how such buffer gas reactions can influence the OCS and its electrical control specifically.

Buffer gas reactions can be crucial for the interpretation of data obtained by the OCS. The previous exemplary considerations were carried out assuming a fixed temperature at which the buffer gas reaction takes place. However, the chemical equilibrium of the reaction shifts with changing temperature. This is vital in the context of the OCS since the sample temperature can vastly differ from the operating temperature of the YSZ tubes in sensor and pump unit. This in turn means that different equilibria might be present for the same buffer gas reaction, subsequently leading to a discrepancy between the partial pressure measured at the YSZ tubes and the partial pressure in the vicinity of the sample.

The oxygen partial pressure of the gas atmosphere, p_{O_2}, has been calculated in dependence of the temperature, T, of the gas atmosphere and for different partial pressures measured at the sensor temperature of 873 K, $p_{O_2}^{873\,K}$, in Figure 65. The calculations are based on Ref. [79] and the equilibrium constant *K(T)* of the reaction described in Eq. (71), which reads as:

$$K(T)=\frac{(p^0_{H_2O}+\Delta p_{H_2O})}{(p^0_{H_2}+\Delta p_{H_2})(p^0_{O_2}+\Delta p_{O_2})^{1/2}} \qquad (72)$$

In Eq. (72), $p^0_{H_2O}$, $p^0_{H_2}$, and $p^0_{O_2}$ describe the partial pressures of water vapor, hydrogen and oxygen before any reaction takes place. For the calculations an initial partial pressure of hydrogen of $p^0_{H_2} = 10^{-7}\ bar$ was assumed. First Eq. (72) is solved for $p_{O_2} = p^0_{O_2} + \Delta p_{O_2}$ and subsequently $p^0_{O_2}$ is adjusted until different $p^{873\,K}_{O_2}$ (acting as 'starting values') are obtained. Afterwards, the temperature is varied while keeping the previously obtained $p^0_{O_2}$ and the assumed $p^0_{H_2}$ fixed. The calculated temperature dependent partial pressures p_{O_2} are displayed as the black solid lines. The corresponding $p^{873\,K}_{O_2}$ values can be obtained by finding the value of the calculated black solid lines at 873 K. A more detailed description of the calculations can be found in Ref. [79]. The calculations (black solid lines) show, that for partial pressures measured above $p^{873\,K}_{O_2} = 10^{-7}$, there is no significant impact of the temperature on the partial pressure p_{O_2}. For measured partial pressures $p^{873\,K}_{O_2} < 10^{-7}$ there is a strong temperature dependence. In those cases, corrections need to be carried out, which strongly depend on the initial hydrogen partial pressure $p^0_{H_2}$.

In a first attempt to quantify possible buffer gas reactions in the present EML-OCS setup, the oxygen partial pressure was measured in the system filled with 750 mbar Ar, while changing the operating temperature of the YSZ in both pump and sensor unit. The obtained results are included in Figure 65 as the dark solid dotted lines. Figure 66 shows the oxygen partial pressure measured as a function of the sensor and pump temperature in more detail for one test run. The insert shows the corresponding temperature profile for both pump and sensor. To clarify the course of time, three timestamps are marked in Figure 66 as t_{start}, t_5 and t_{end}. In Figure 65 two distinct test runs at different oxygen partial pressure levels are included as the dark lines connecting the individual data points. Additionally, a test run by Airbus Space and Defense on their ISS OCS prototype is included as bright solid line.

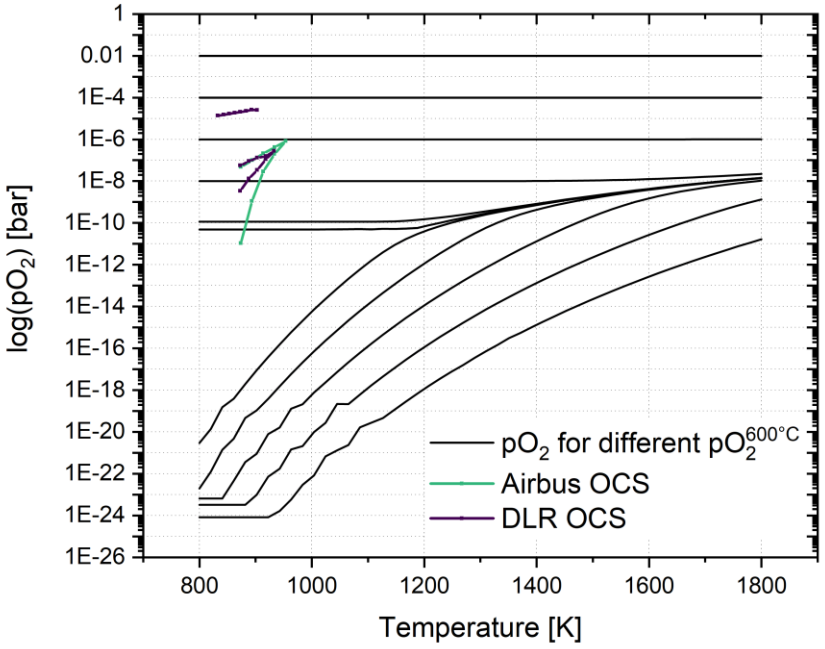

Figure 65: Temperature dependence of the oxygen partial pressure for a process gas for different partial pressure measured with the OCS. An initial hydrogen partial pressure of $p^0_{H_2} = 10^{-7}$bar was assumed. The calculations follow Ref. [79]. Several test runs at different operating temperatures carried out at the DLR OCS and by Airbus Space and Defense on their ISS OCS prototype are included.

For no buffer gas, or for oxygen partial pressure levels $pO_2^{873\,K} > 10^{-7}$, no change in partial pressure would be expected with a changing temperature. The first test run at higher partial pressures confirms this expectation. The slight increase in partial pressure during this test run can be associated with the previously mentioned leak rate of the system. Apart from the increase caused by the leak rate no change can be observed when altering the operation temperature.

The second test run, as well as the test run by Airbus Space and Defense, do not match in the same way with the expectations from the calculations made. Both test runs show a surprisingly similar increase in partial pressure measured when increasing the temperature, followed by a decrease in partial pressure when the temperature is decreased again. The measured partial pressure course rather resembles the trend calculated for much lower oxygen partial pressures. Considering the leak rate of the system, a subsequent decrease of the partial pressure with decreasing temperature strongly indicates the presence of a buffer gas reactions. The leak rate could also explain the different partial pressures in Figure 66 for t_{start}, and t_{end}. For the partial pressure range at which the test runs were carried out no such significant influence of temperature was expected for the partial pressure under the assumptions made for the calculations of Figure 65. The derivations could be caused by inaccurate assumptions made for the calculations or different gas reactions taking place. The calculations were only carried out for the hydrogen, oxygen and water reaction. However, different gas mixtures containing O_2, CO_2 or CO could lead to different buffer gas reactions as the here considered H_2 and H_2O mixture. Figure 65 raises the question, if initial input conditions exist, so that the calculations would match the experimentally observed results. Answering this question with further investigations would therefore yield valuable insight for the process atmosphere. Testing the OCS-EML operation with different gas atmospheres could offer highly interesting research insights (especially regarding a future use of the ISS-OCS) that go far beyond the scope of this work.

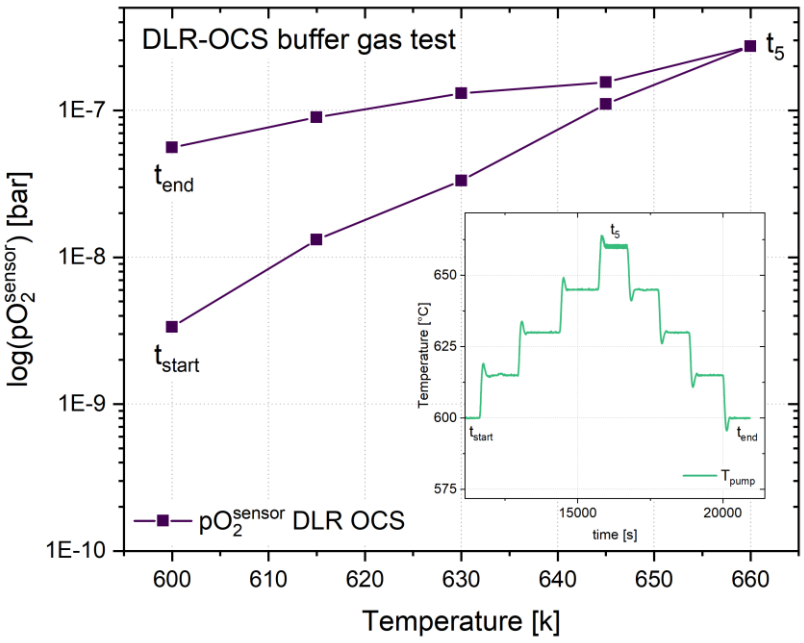

Figure 66: Temperature dependence of the oxygen partial pressure measured during the second test run carried out at the DLR OCS. The inset shows the temperature-time profile of the sensor and pump unit during the test run.

The buffer gas reactions that are present in the experimental setup cannot be fully explained by the exemplary calculations made for the reaction depicted in Eq. 71. Together with the previous investigations on the leak rate and the chamber inertia this shows that a special operating procedure needs to be designed in order to obtain meaningful measurements with the OCS. Therefore, later in this

work a well-defined process procedure is developed to ensure the comparability of the obtained results. With no existing standardized measurement procedures, many particularities have to be considered when designing an EML experiment including the OCS. The previous investigations gave a first impression of the general behavior of OCS measurement principle. The next needed step is to evaluate the general interaction of a levitating sample with the OCS setup, before the two blocks can be combined to find a suitable measurement course.

To do so, a pure liquid vanadium sample was levitated and molten while the OCS measured the oxygen partial pressure in the experimental system. Figure 67 shows the oxygen partial pressure measured during an EML experiment with pure vanadium against the time. The vanadium was levitated and molten simply by turning the generator to 95% power. In this way the sample could be held at an isothermal temperature of 2200 K after melting. The sample needed roughly 120 s to reach thermal equilibrium. The arrows in Figure 67 mark when the generator was turned on and when melting of the sample could be observed. Before the generator was started a constant oxygen partial pressure was measured. The partial pressure dropped sharply when the generator was started and after the melting of the sample the slope of the decrease changed. After an additional change in slope, the oxygen partial pressure approached an equilibrium value. The equilibrium was reached after roughly 35 min ($t > 2000$ s).

This behavior is somewhat expected for liquid vanadium since it has a high affinity and high solubility for oxygen. As soon as the vanadium is heated it starts to absorb oxygen from the surrounding atmosphere until an equilibrium is reached. A similar oxygen partial pressure trend can be observed when levitating pure titanium. Titanium is known as a so called ‘getter material’ used to remove residual gases, especially oxygen, from evacuated systems. Figure 67 shows a similar ‘getter effect’ for pure vanadium. The inset shows that after a sufficient timespan an equilibrium is reached. Vanadium is used in commercially available multicomponent ‘Non-Evaporable-Getter’ materials (NEG) which are used in ultra-high vacuum applications [123]. These alloys are known to, apart from oxygen (O_2), also getter CO, N_2 and H_2 gasses. Removing these gases from the process atmosphere could potentially influence the observed oxygen partial pressure. Inside the chamber atmosphere different gas phase reactions are taking place. To give an example, hydrogen reacts with oxygen to form water. If, in this case, hydrogen is removed from the atmosphere via the getter effect of the liquid vanadium, the equilibrium is shifted. Subsequently, less oxygen can be ‘bound’ as water and the observed oxygen partial pressure in the chamber increases. There are numerous possible reactions taking place whose effect can experimentally not be separated without exceeding the scope of this work. Investigating the reactions taking place in the process chamber would form a highly interesting research topic itself. However, the multitude of possible reaction inside the process atmosphere needs to be considered when interpreting the observed oxygen partial pressure trends.

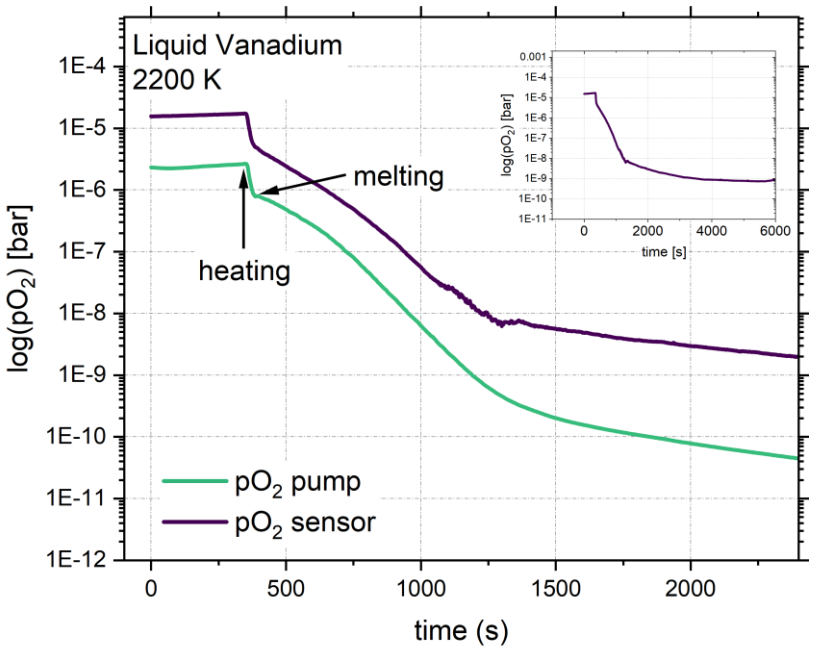

Figure 67: Oxygen partial pressure versus time during an EML experiment with pure vanadium. The vanadium sample was levitated at 95% generator power and thereby held at an isothermal temperature of 2200 K. *The inset shows that after a sufficient timespan an equilibrium is reached.*

For the design of the later experiments two things become apparent from the trend observed in Figure 67. Firstly, the sample needs a sufficient time at an isothermal temperature (35 min) before the oxygen partial pressure measured has reached an equilibrium. Secondly, both vanadium and titanium show a strong gettering effect, reducing the oxygen partial pressure in the process atmosphere. When trying to carry out oxygen partial pressure dependent measurements it makes sense to measure such samples from low to high oxygen partial pressures by successively increasing the oxygen partial pressure in the atmosphere.

With all the previous considerations in mind, two different process modes were developed to measure thermophysical properties in dependence of the oxygen partial pressure. The oxygen partial pressure profile for the first process mode, called ‘pumping mode’, can be seen in Figure 68. The process called ‘titration mode’ is depicted in Figure 69. In both cases the sample is given a substantial time to reach an equilibrium oxygen partial pressure, before the controlling of the atmosphere by the OCS starts. The only difference between the two process modes is which measured value the OCS is regulating towards. In the pumping mode the oxygen pumping power is adjusted so that a set target value is reached for the partial pressure measured at the pump unit. For the titration mode, the OSC adjusts the pumping power so that the measured value at the sensor reaches a set target value. Expressed abstractly, the pumping mode controls the atmosphere which is introduced into the chamber while the titration mode controls the current oxygen partial pressure measured in the process chamber. Before this background the differences in both figures can be explained by the inertia of the gas volume of the sample chamber. For the pumping mode, only a small gas volume has to be adjusted to meet the target. Therefore, the partial pressure measured by the pump is quickly controlled to match the target value in Figure 68. It needs to be noted, that between the measurements of Figure 61 and Figure 68 several PID parameter optimization processes were carried out. As a result, the actual value is now adapted very quickly to match the target value over a range of nine orders of magnitude. For the titration mode, the PID control is much less precise, which is hardly surprising considering the chamber volume.

Thermophysical property measurements, in the framework of this work mainly surface tension measurements, can be carried out at any time during this oxygen profile. The measured surface tension can subsequently be connected to the respective oxygen partial pressure. In this fashion, by understanding the basic operational principles of the OCS, and reaching the 2nd postulated milestone, two measurement processes to investigate the surface tension in dependence of the oxygen partial pressure could be developed.

In the next step, the pumping mode and titration mode processes are applied to the simple model system of pure liquid vanadium to reach the 3rd milestone needed to build the foundation towards investigating the influence of oxygen on the surface tension of the Al-Ti-V system.

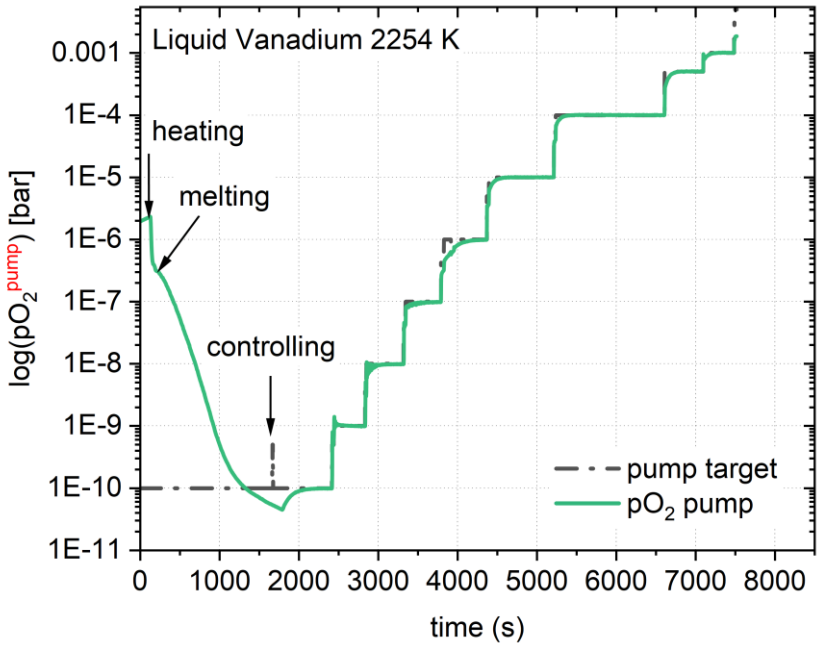

Figure 68: Oxygen partial pressure versus time for the 'pumping mode' process type.

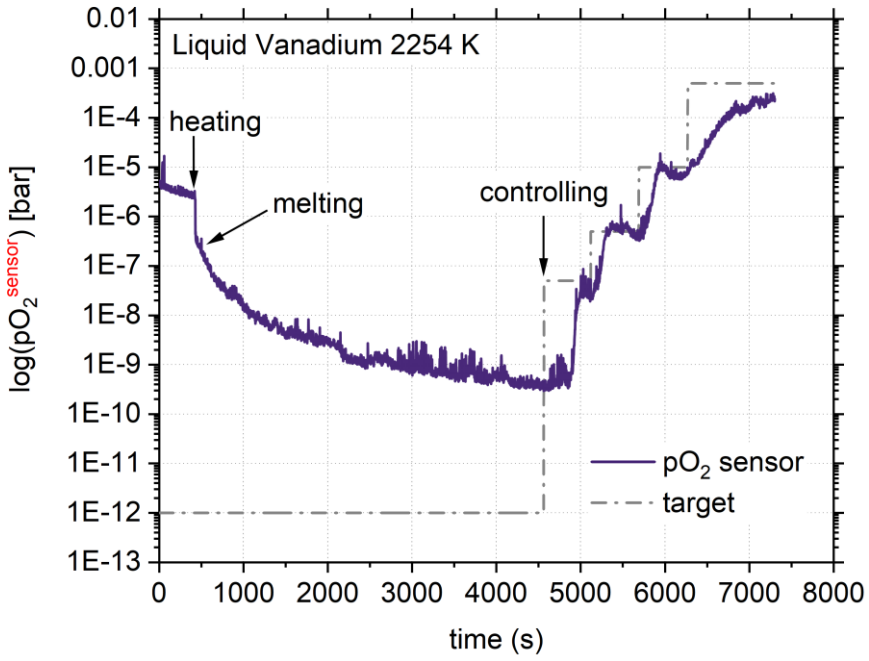

Figure 69: Oxygen partial pressure versus time for the 'titration mode' process type.

4.5.2 Results – Surface Tension in Dependence of Oxygen Partial Pressure

The surface tension of pure liquid vanadium is measured in dependence of the oxygen partial pressure by applying the pumping mode and titration mode process while the sample droplet is levitated at a constant temperature. Pure vanadium is chosen to act as a model system to investigate the fundamental interactions between the liquid metal and oxygen.

The measured surface tension at 2250 K during the pumping and titration mode is shown as a function of the oxygen partial pressure in Figure 70 and Figure 71 respectively. In each graph the surface tension for pure vanadium at 2250 K calculated from Table 17 is included as a dash-dotted line. For clarity the oxygen partial pressure profile measured at both, sensor and pump are included in Figure 72 for the pumping mode. The arrows mark the times at which surface tension measurements have been carried out.

A very similar surface tension trend can be observed for both, the pumping and the titration mode. For oxygen partial pressures $pO_2 < 10^{-7}$bar, the surface tension is close to the expected value of the previous measurements. Upon further increasing the partial pressure a starting decrease in surface tension can be observed. Since no significant difference between the pumping and titration mode is noted, the pumping mode was chosen as modus operandi for the following investigations, since it is more reliably reproducible and easier to optimize regarding the PID control.

A decrease in surface tension upon increasing the partial pressure above 10^{-7} bar is expected, since investigations show, that already small amounts of oxygen can drastically decrease the surface tension of liquid metals [36]. Typically, for liquid metals 'sigmoid' shape curves are expected when investigating the surface tension in dependence of the oxygen influence [124] as shown in the schematic in Figure 73 taken from Ref. [36]. In this schematic, the normalized surface tension, $\frac{\gamma}{\gamma_0}$, is depicted as a function of the oxygen bulk mole fraction of the sample, x_0. The curve can be subdivided into three

regions with changing oxygen segregation conditions. Going through these regions the surface changes from a virtually oxygen free surface to reaching a saturation of oxygen. If a bulk liquid metal is in contact with a gaseous phase containing a certain oxygen partial pressure, some oxygen is dissolved in the metal. In region 1, the oxygen mole fraction is very close to zero. Therefore, a very dilute solution is considered and the surface tension of the mixture is close to the surface tension of the pure metal. In this low concentration range, the number of available surface sites for the solute oxygen to segregate to is very large compared to number of solute atoms. Therefore, the equilibrium constant for the oxygen surface segregation is not dependent on composition (interactions between adsorbed atoms can be neglected) [124] and the surface tension of the mixture can be calculated based on the constant. In region 2, the oxygen concentration increases and the number of available surface sites decreases. In this region, the interaction between the adsorbed atoms have to be considered when calculating the surface tension of the mixture from the equilibrium constant. Once a maximum adsorption, $\chi_{\Gamma max}$, is reached in region 3, calculating the surface tension using the equilibrium constant for the surface segregation is no longer valid. In region 3 the surface tension decrease has to be attributed to the changing bulk oxygen concentration and the surface tension decreases with a decreasing slope until the saturation point, χ_{sat}, is reached. At the saturation point most metals form oxides, whose composition does not change and as a result the surface tension stays constant. It needs to be mentioned, that those solid oxides usually float on the surface making a reliable surface tension measurement with the oscillating drop method nearly impossible.

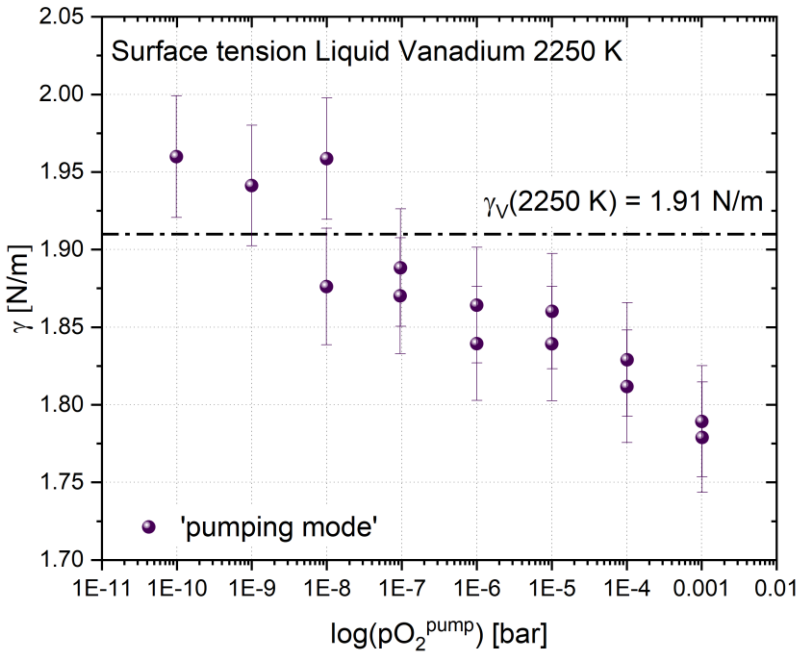

Figure 70: Surface tension of pure liquid vanadium at 2250 K *as a function of the oxygen partial pressure adjusted using the pumping mode. The surface tension for vanadium at* 2250 K *calculated from Table 17 is included for reference.*

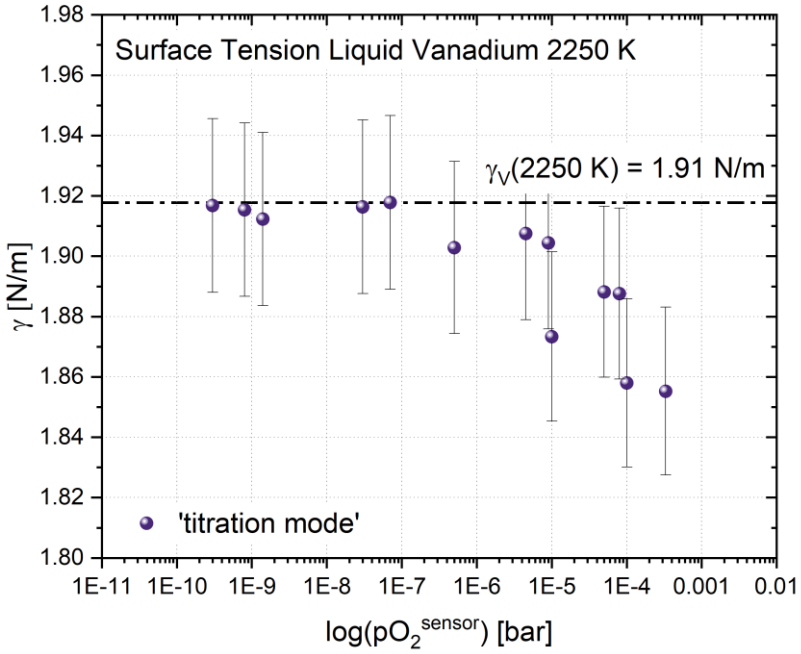

Figure 71: Surface tension of pure liquid vanadium at 2250 K *as a function of the oxygen partial pressure adjusted using the titration mode. The surface tension for vanadium at* 2250 K *calculated from Table 17 is included for reference.*

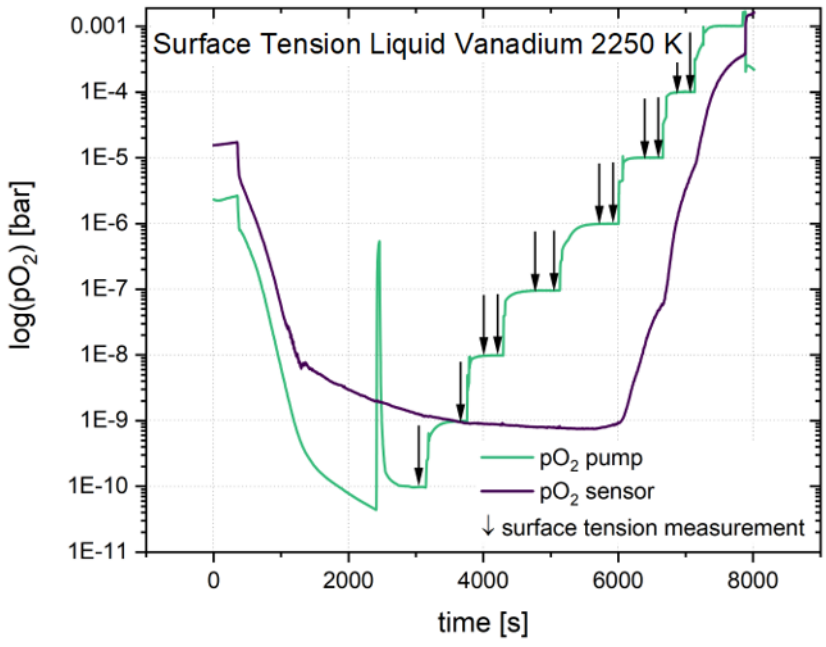

Figure 72: Oxygen partial pressure adjusted by the OCS pump over the course of a pumping mode experiment. The 'response' partial pressure measured by the sensor is included as a dark line. The arrows mark where surface tension measurements were carried out.

So far, the surface tension was solely investigated as a function of the oxygen partial pressure in the process chamber. The so observed decrease in surface tension in Figure 70 and Figure 71 is small compared to the total value. It is therefore not possible to ultimately identify if pure liquid vanadium follows the behavior introduced by [124] and depicted in Figure 73. Additionally, the oxygen mole fraction of the sample, which the surface tension is shown as a function of in Figure 71, is experimentally not connected with the oxygen partial pressure.

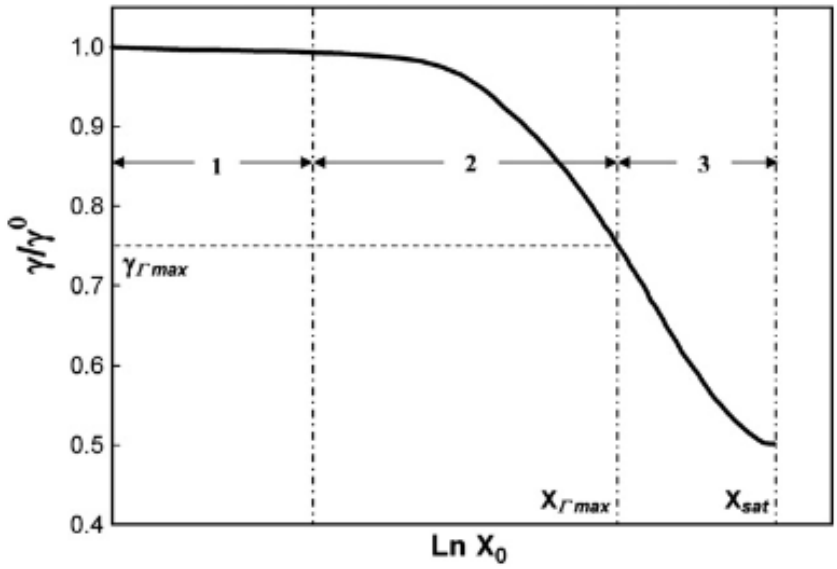

Figure 73: Schematic course of the surface tension of liquid metals as a function of oxygen mole fraction. Taken from Ref. [36].

The trend observed in Figure 70 and Figure 71 depicts the behavior for a surface with a very small oxygen mole fraction (associated with region 1) and a further increase in oxygen mole fraction of the sample could cover a larger area of Figure 73 experimentally. That would allow the previous results to be better placed within the scope of already existing investigations.

Since the oxygen partial pressure introduced into the process atmosphere cannot be increased above $pO_2 = 10^{-3}$ bar, due to the limitations in pumping power (current) of the OCS, a different approach has to be chosen in order to increase the oxygen present. Since the use of special, oxygen rich, process gases would require further setup modifications an increase in oxygen presents in the sample is achieved in other ways. However, the use of specifically modified process gases could yield not only scientific insight but also process related benefits (e.g. for calibration means) and are therefore highly interesting for future research.

4.5.3 Results – Surface Tension in Dependence of Bulk Oxygen Mole Fraction

Instead of trying to increase the oxygen atomic concentration via the process atmosphere using the OCS, the oxygen is introduced into the sample as bulk oxygen during the preparation. As explained in section 3.1, the oxygen is introduced into the samples by alloying pure vanadium together with vanadium(V)-oxide powder. In this way, almost 18 at.-% bulk oxygen atomic concentration can be achieved. After sample preparation, the samples were analyzed by the '*Elektrowerk Weisweiler GmbH'* regarding their oxygen content with the carrier gas hot extraction (CGHE) method. Table 24 show the analysis results.

Table 24: Sample target composition during sample preparation and actual sample composition measured by the 'Elektrowerk Weisweiler GmbH' *via CGHE method for the samples in the V-O system.*

Sample	target composition [at.-% oxygen]	actual composition [at.-% oxygen]
V	0	0.08
$V_{99}O_1$	1	1.21
$V_{97}O_3$	3	3.27
$V_{94}O_6$	6	6.28
$V_{88}O_{12}$	12	12.34
$V_{12}O_{18}$	18	18.38

After preparing samples with different bulk oxygen mole fractions, the surface tension of each sample is measured as a function of temperature, following the same analysis procedure as for the binary alloys in section 4.3.2. The resulting surface tension measurements are shown in Figure 74 versus the temperature. A reference temperature of 2100 K is marked for future analysis. Linear fits are carried out for each composition, since the data exhibits a linear temperature dependence. For clarity reasons, these linear fits are shown instead of the individual measuring points for samples with less than 1 at.-% oxygen, since they show very similar surface tension values. The surface tension measured for the pure vanadium (99.99% vanadium without any oxide power see section 3.1) sample shows very good agreement with the previous measurements of pure vanadium in sec. 3.3.1. Starting with samples containing 0.5 at.-% oxygen, the surface tension decreases noticeable with an increasing oxygen mole fraction.

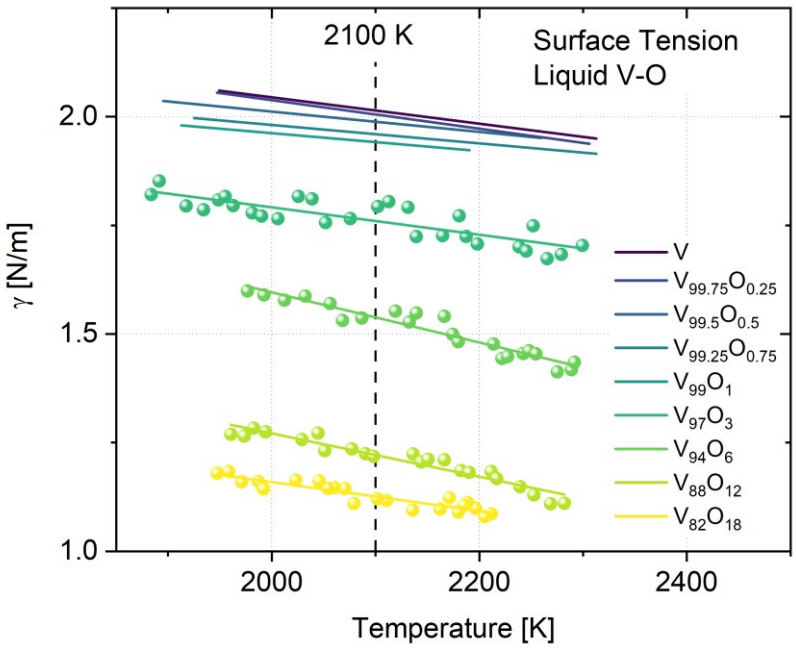

Figure 74: Surface tension versus the temperature for liquid vanadium samples containing different mole fractions of oxygen.

The measurements in Figure 74 were conducted temperature dependently by cooling with an inert gas flow of Ar. This means the OCS could not be used during the experiment. As a result, the surface tension is directly linked to the oxygen mole fraction of the sample but the oxygen partial pressure could not be experimentally connected with the results. This first experiment shows very well the necessity for the setup modifications made in section 3.3 and 3.4. As heating and positioning is coupled in EML, a cooling

gas flow is needed to control the sample temperature. This cooling gas flow undermines the operating principle of the OCS by constantly changing the process atmosphere. The heating laser was implemented to the EML setup in order to minimize this conflict. Combined with a coil design aimed at maximum levitation force and minimal heating input into the sample, the temperature control can be achieved with the newly implemented laser. Nevertheless, additional experiments are needed to connect all four different parameters of oxygen partial pressure, oxygen atomic concentration, surface tension and temperature.

In a first step, the two previous experiments are simply combined. The surface tension was measured for samples prepared with different oxygen atomic concentrations while simultaneously applying the pumping mode process with the OCS. This allows for an experimental connection of oxygen partial pressure, oxygen mole fraction and surface tension.

The results are shown in Figure 75. The surface tension is shown as a function of the oxygen partial pressure for vanadium samples prepared with different amounts of oxygen. For samples with oxygen atomic concentration of up to 6 at.-% almost no dependence of the surface tension from the oxygen partial pressure can be observed. For samples prepared with higher oxygen mole fraction, a starting decrease in surface tension at very high oxygen partial pressures can be seen. The decrease in surface tension between the different samples matches that expected from Figure 74. As for the previous pumping mode experiments the sample was held isothermal at 2250 K after melting.

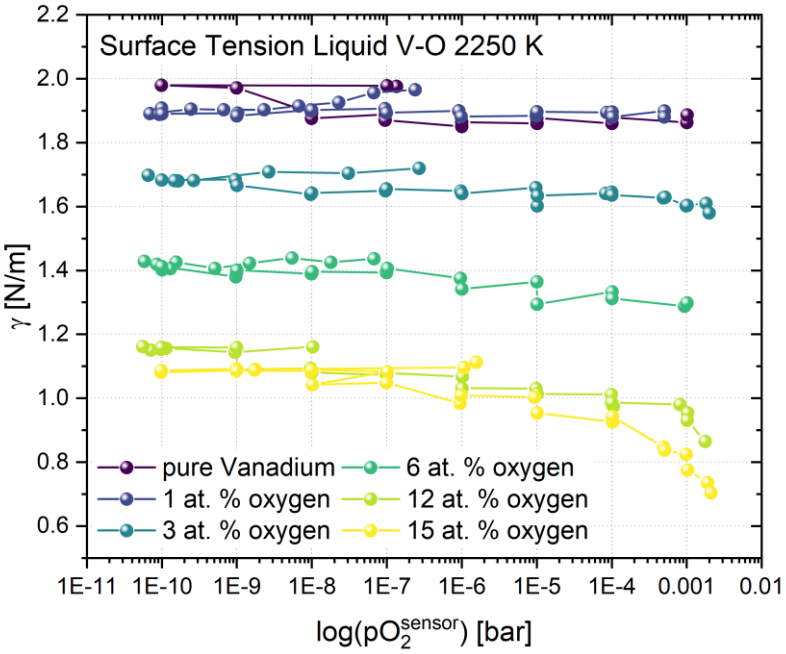

Figure 75: Surface tension as a function of the oxygen partial pressure (sensor) for samples prepared with different oxygen bulk mole fraction. The samples were held at 2250 K *over the course of the experiment.*

In Figure 75 the surface tension data is obtained using the pumping mode since it is a much better controllable operating mode. The surface tension is then only plotted versus the partial pressure measured at the pump unit for simplicity. To verify, that no information is lost, Figure 76 exemplary shows the surface tension measured for the sample containing 3 at.-% oxygen plotted against the partial pressure measured with the sensor and the pump unit. The jump in the surface tension values for low oxygen partial pressures can be explained when considering the experimental path (exemplary depicted in Figure 72). In the early experimental stages (about 30 min), no equilibrium is reached yet. This results in identical surface tension values measured while the oxygen partial pressures are still decreasing

towards the equilibrium. As observed earlier, an offset (around half an order of magnitude) between the sensor and pump unit exists for low partial pressures ($pO_2 < 10^{-8}$ bar) which disappears for higher partial pressures. However, it can be easily seen, that the trend observed is almost identical. When evaluating the data measured with the pumping mode, there is no significant difference between the oxygen partial pressure recorded at the sensor and the pump unit.

With the results from Figure 75 the surface tension of pure liquid vanadium can be correlated to both the oxygen partial pressure (measured at the sensor unit) in the process atmosphere and the bulk oxygen mole fraction. This connection was visualized in Figure 77. The surface tension of a pure liquid vanadium sample at 2250 K is shown in dependence of the bulk oxygen mole fraction and the oxygen partial pressure (sensor). This connection lays the foundation for reaching the final research goal of this work. Based on these results the previously measured thermophysical properties can be reassessed towards the influence of oxygen and first insights on the fundamental interactions between oxygen and a liquid vanadium droplet can be gained.

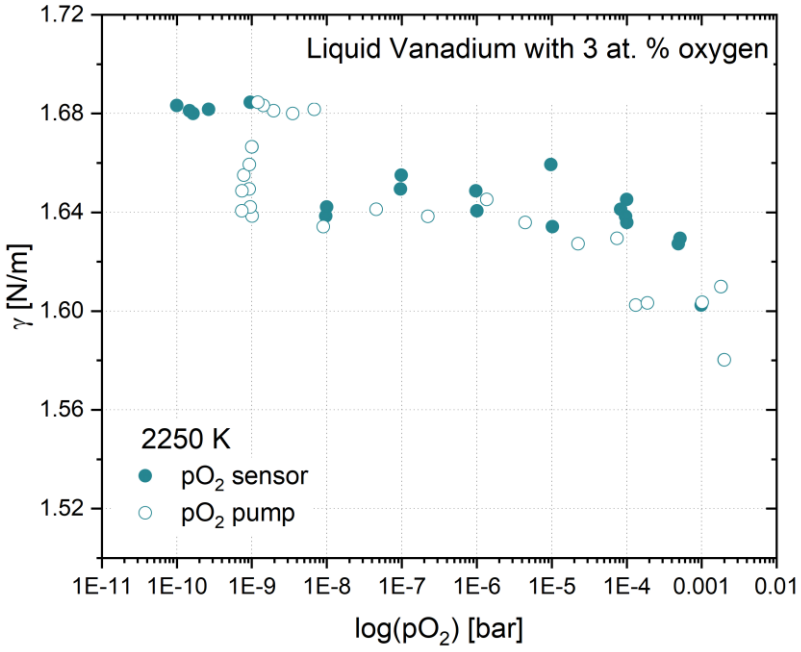

Figure 76: Surface tension of liquid vanadium with 3 at.-% oxygen at 2250 K *versus the oxygen partial pressure measured with the sensor and the pump unit.*

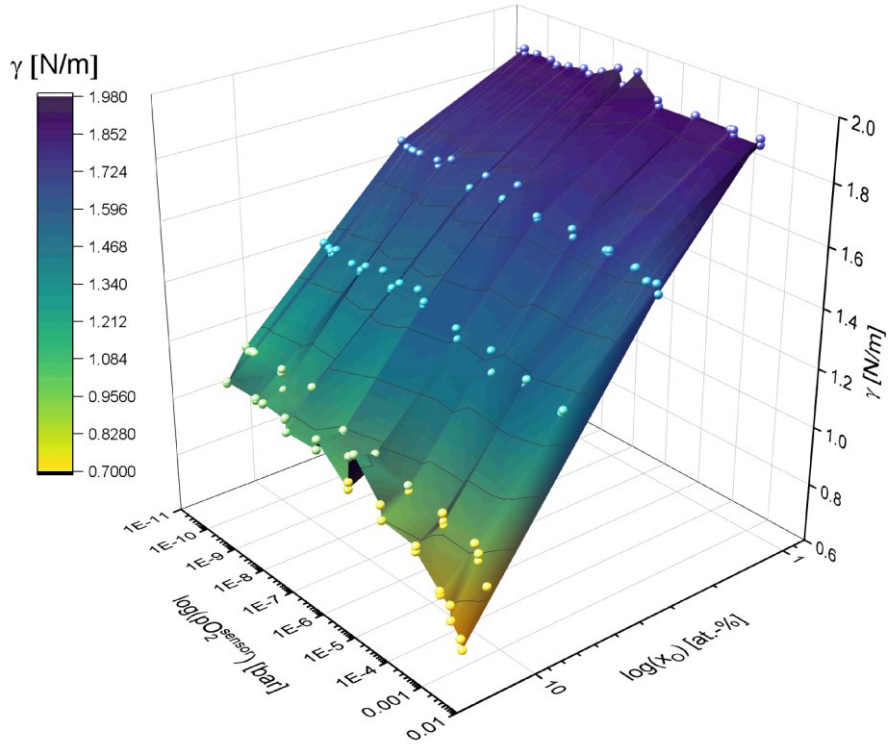

Figure 77: Surface tension of a pure liquid vanadium sample at 2250 K *as a function of both bulk oxygen mole fraction and the oxygen partial pressure measured at the sensor unit.*

A consecutive experiment aims to now connect surface tension, oxygen mole fraction, oxygen partial pressure and surface tension all together. A first example of how such temperature dependent OCS measurements can look like is provided in Figure 78. In this experimental series the liquid vanadium samples with different bulk oxygen atomic concentrations were processed similar to the experimental series shown in Figure 75 under use of OCS, but this time the samples were additionally superheated using the heating laser. By reducing the laser power, the surface tension of the sample is subsequently measured during cooling, while simultaneously observing the oxygen partial pressure in the chamber. In Figure 78 both the sample temperature as well as the oxygen partial pressure recorded with the sensor unit are depicted.

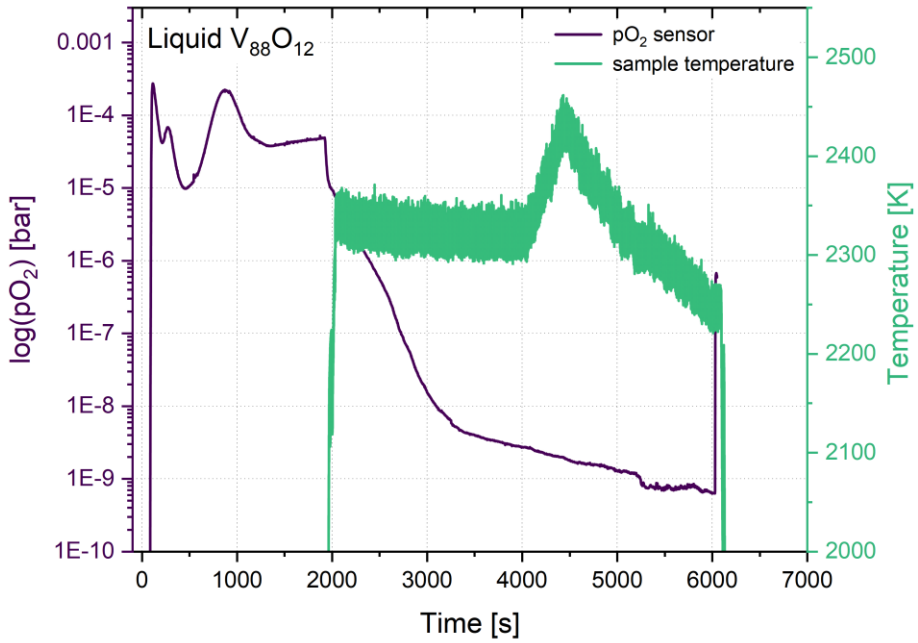

Figure 78: Oxygen partial pressure and sample temperature over the course of an EML surface tension measurement of liquid $V_{88}O_{12}$. To enable a temperature dependent oxygen partial pressure measurement the sample temperature was varied using the equipped heating laser. The surface tension was measured during subsequent cooling by reducing the laser power.

Figure 79 and Figure 80 show the corresponding surface tension and oxygen partial pressure for all samples in the experimental series. The results agree very well with the previous findings depicted in Figure 75 and Figure 77. A linear temperature dependence has been observed for all measured samples. Therefore, linear fits following Eq. (22) are included. The corresponding fit parameters are summarized in Table 25.

The experimental series shows that the parameters oxygen partial pressure and temperature can be adjusted independently of each other. With this, experimental access to all relevant parameters (temperature, oxygen partial pressure and bulk oxygen concentration) is possible in a single measurement, which lays the foundation for a systematic and comprehensive investigation of the interaction between the liquid Al-V-Ti system and oxygen.

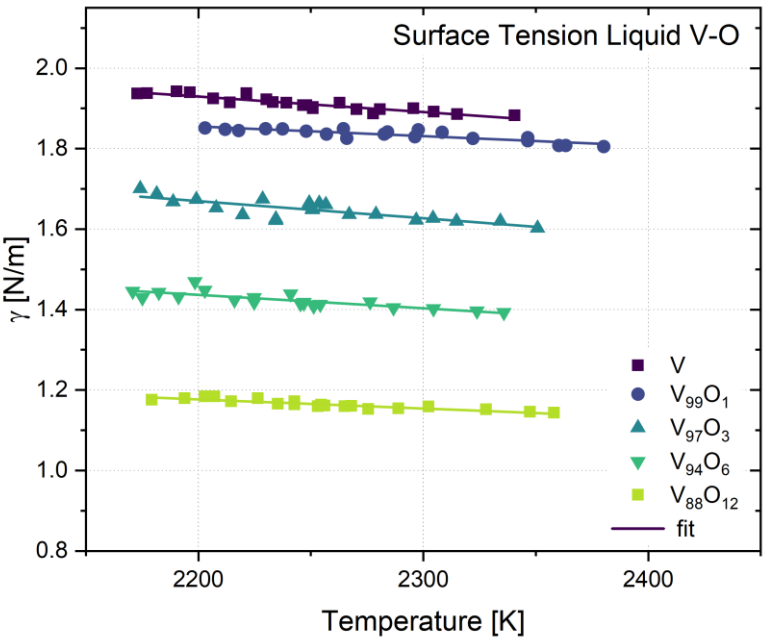

Figure 79: Surface tension of liquid vanadium with varying bulk oxygen mole fraction. Temperature dependent measurements were carried out while simultaneous recording the oxygen partial pressure with the OCS. The sample temperature was adjusted by using a heating laser.

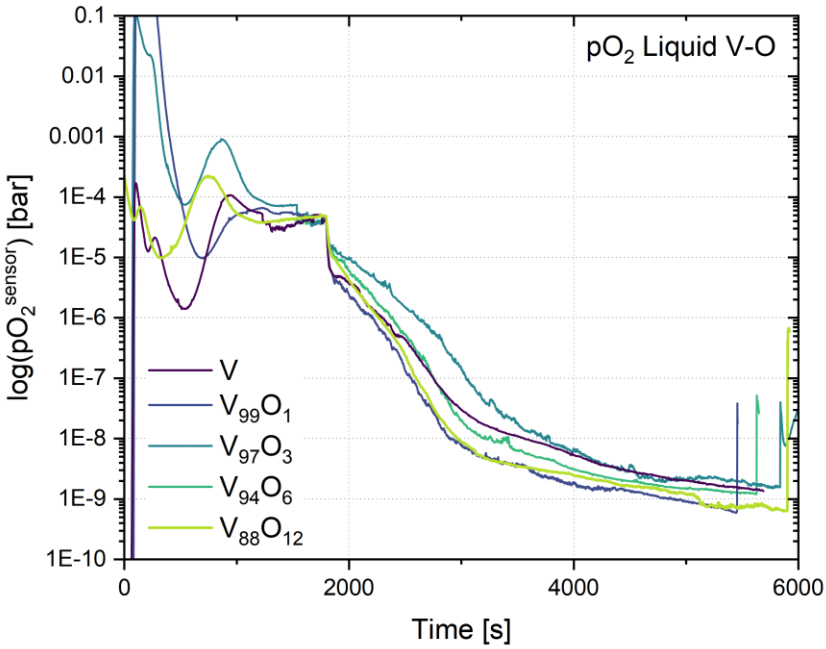

Figure 80: Oxygen partial pressure measured at the sensor versus time corresponding to the surface tension measurements in Figure 79.

Table 25: Parameters T_L, γ_L, γ_T and $\gamma(2100\,K)$ for all investigated compositions within the V-O system. The liquidus temperatures, T_L, were taken from the phase diagram introduced in [67].

Composition	T_L[K]	γ_L[Nm^{-1}]	γ_T[10^{-4}Nm^{-1}K^{-1}]	$\gamma(2100\,K)$[Nm^{-1}]
V	2183	1.93±0.07	-3.85±0.36	1.962
$V_{99}O_1$	2183	1.86±0.04	-2.42±0.32	1.880
$V_{97}O_3$	2178	1.68±0.08	-4.25±0.70	1.713
$V_{94}O_6$	2173	1.45±0.09	-3.33±0.53	1.474
$V_{88}O_{12}$	2123	1.13±0.07	-2.26±0.24	1.135

4.5.4 Discussion - The Influence of Oxygen on the Surface Tension of Liquid Vanadium

One major motivational aspect for combining the EML with the OCS was to make it possible to evaluate the oxygen influence on thermophysical property measurements made in electromagnetic levitation. That is one reason why an OCS is not only integrated into the DLR-EML but will also be added to the ISS-EML. Based on the measurements on pure liquid vanadium we can draw conclusions about the credibility of the thermophysical property measurements made for the ternary Al-Ti-V system.

When talking about 'the influence of oxygen' two cases are experimentally distinguished depending on where the oxygen is admitted to the liquid sample. Oxygen can be present in the process atmosphere surrounding the liquid sample or oxygen can already be present in the sample bulk before the experiment. In this work the surface tension is investigated under the influence of oxygen. The surface tension is largely determined by the oxygen concentration in the surface phase. Therefore, in total three different locations for oxygen are important for this work. Oxygen can be present in the gas atmosphere, the surface phase or the bulk phase of the sample. The interactions of the oxygen transfer between these locations are the main focus of this work.

In a first step in sec. 4.5.2 the liquid vanadium sample was 'exposed' to oxygen from the side of the gas atmosphere. Figure 72 shows how the liquid sample interacts with the gas atmosphere regarding the oxygen exchange. The first information found in Figure 72, is that the oxygen partial pressure is between 10^{-5} bar and 10^{-6} bar before the sample is levitated, depending on the conditioning of the process chamber. At first glance this seems trivial, since this is the oxygen partial pressure expected for high purity argon used in the EML furnace, but this represents an important experimental validation of the often-made purity assumption during levitation experiments. This does not only strengthen the meaningfulness of surface tension measurements, but all thermophysical property measurements made in EML which are susceptible to an oxygen influence. This provides a valuable knowledge especially for the reevaluation of the previously obtained thermophysical property data. The further course of the oxygen partial pressure recorded in Figure 72 provides additional insights for this aspect.

Upon heating and subsequently melting of the sample, the oxygen partial pressure in the EML chamber strongly decreases until an equilibrium value is reached. This shows, that the melting the sample removes oxygen from the surrounding atmosphere in a 'getter-effect' expected for liquid vanadium. Combining the course of the oxygen partial pressure with the constant surface tension measured for partial pressures up to $10^{-7} - 10^{-6}$ bar it can be concluded that the oxygen removed from the atmosphere mainly moves to the sample bulk. If the oxygen would be present at the sample surface a decrease in surface tension could be observed. These findings compare very well with Ref. [25] showing a similar behavior of the surface tension of liquid titanium exposed to different oxygen partial pressures. For liquid titanium in Ref. [25] no dependence of the surface tension on the oxygen partial pressure has been observed. For pure liquid vanadium, only a minor decrease in surface tension by three percent was visible for high partial pressures of oxygen $pO_2 > 10^{-4}$ bar. It can be assumed that, in the liquid sate,

both elements absorb oxygen mainly into the bulk, while no effect on the surface can be experimentally seen.

Both aspects, of comparably low oxygen partial pressure in the process gas and an oxygen free surface for liquid titanium and liquid vanadium support the reliability of the previous thermophysical property measurements. Especially for samples with high titanium and vanadium mole fractions, the oxygen present during the EML experiments does not have a substantial influence on the surface tension measured, since all possibly present oxygen is absorbed into the sample bulk. A use of the thermophysical properties measured in the present EML setup as a database for titanium, vanadium and Al-Ti-V alloys with high titanium and vanadium mole fraction is possible considering the observed oxygen influence.

For alloys with a high aluminum mole fraction a different behavior could be evident. As previous works show [125, 126], the surface tension of aluminum rich alloys is strongly affected by the adsorption of oxygen. It was also shown in these works, that the surface condition of pure liquid aluminum regarding the oxygen coverage is temperature dependent. At high temperatures a removal of oxide particles can lead to a deoxidized surface state compared to the oxidized aluminum surface observed at lower temperatures [126]. The opposite surface-oxygen-interaction for liquid Ti/V and liquid Al opens up many highly interesting future research possibilities. Based on the previous results, it could for example be assumed that the surface state of an Al-Ti-V alloy possibly changes as a function of both aluminum mole fraction and temperature. The EML in combination with the OCS, both terrestrial and on board the ISS, is perfectly suited to lead investigations aimed in this direction.

The findings of this work can be valuable groundwork for such future research. If a possible change in surface state needs to be investigated in compositional dependence, first the possible surface states of the pure components need to be known. Therefore, five different parameters need to be connected to fully understand the surface state of a liquid regarding the oxygen influence: the temperature, the oxygen partial pressure, the surface oxygen mole fraction, the bulk oxygen mole fraction and the surface tension. The correlation between these parameters can be vastly different for the individual components of the Al-Ti-V system. Ref. [126] laid the foundation for pure aluminum, Ref. [25] for liquid titanium, and it is the goal of this work to do the same for liquid vanadium.

So far only the experimental connection between oxygen partial pressure and surface tension was discussed. In Figure 74 the surface tension of liquid vanadium is depicted as a function of the temperature for samples with different bulk oxygen atomic concentrations. Similar to the discussions in section 4.3.2, the surface tension can be shown as a function of the bulk oxygen mole fraction at a fixed reference temperature of 2100 K. The result is shown in Figure 81.

In this way, the surface tension for liquid vanadium can be shown as a function of the bulk oxygen mole fraction. The experimental data (light round symbols) is compared to model data for an ideal V-O mixture (light, dashed line, Eq.(51)) and a non-ideal mixing V-O system (light, solid line, Eq. (52)). The same approach was taken in Ref. [25] for liquid titanium, where the model calculations are explained in greater detail. The corresponding data was taken from Ref. [25] and included in Figure 81 for better comparability (dark squares and lines). For the V-O system additional measurements under microgravity conditions were carried out for pure vanadium and vanadium with 5at.-% bulk oxygen atomic concentration in the TEMPUS-EML facility. A comparison of the TEMPUS measurements with the DLR-EML results can be found in Figure 82. The surface tension at the reference temperature of 2100 K, measured in microgravity, are included in Figure 81 as diamond symbols.

The measurements made in the DLR-EML facility and in the TEMPUS-EML facility are in excellent agreement with each other for the respective compositions. Thereby, the measurements are a great tool to validate each other and to complement each other. With the TEMPUS facility several disturbing influences that occur during a ground based EML measurement can be avoided. Without gravitational forces the deviation of the sample shape from the ideal spherical shape is very small. In contrast to that,

ground-based EML allows for an easy repetition of experiments, enabling more significant statistics. The minor differences in both measurement results can easily attributed to statistical deviation. The DLR-EML results represent averaged measurements, while only individual measurements can be reported for the TEMPUS results. The similar results for both facilities, show that the assumptions made to address the sample shape deviation during terrestrial EML are valid. The use as reference data is further enhanced by the good agreement of both data sets.

Not only does the usability as reference data of the results presented in this work benefit from the repeatability of the measurements in different setups, but with both facilities generating such similar data, this work can help to better assess the process atmosphere in the TEMPUS facility and thereby be of great benefit for all past and future TEMPUS experiments. The results show how well both facilities can be used complementary. While the TEMPUS-EML is capable of producing highly precise 'singular' measurements, the ground based DLR-EML furnace allows for a more comprehensive approach due to the smaller experimental effort when compared with the parabolic flight experiments.

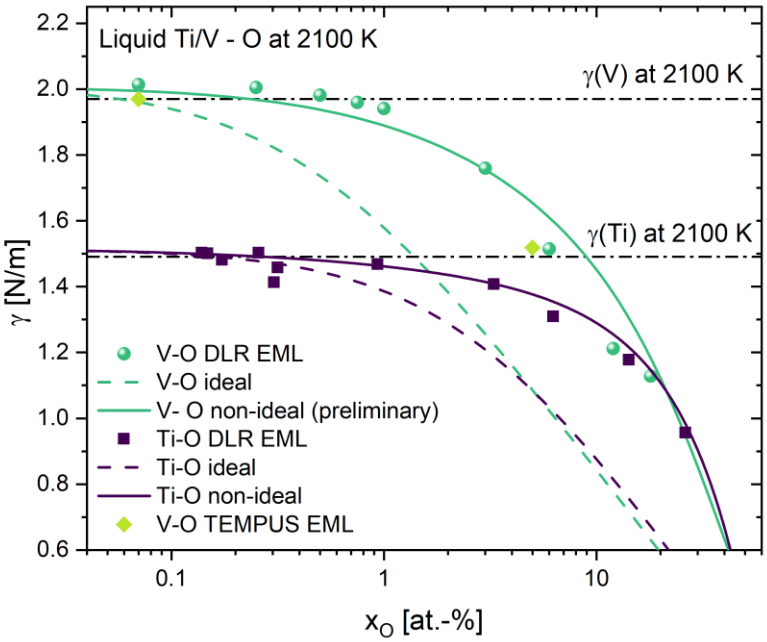

Figure 81: Surface tension of liquid Ti and V as a function of the bulk oxygen mole fraction. Calculations for the ideal and non-ideal solution case by solving the Butler equation are shown as dashed and solid lines. Microgravity measurements in the TEMPUS facility are included as diamond symbols.

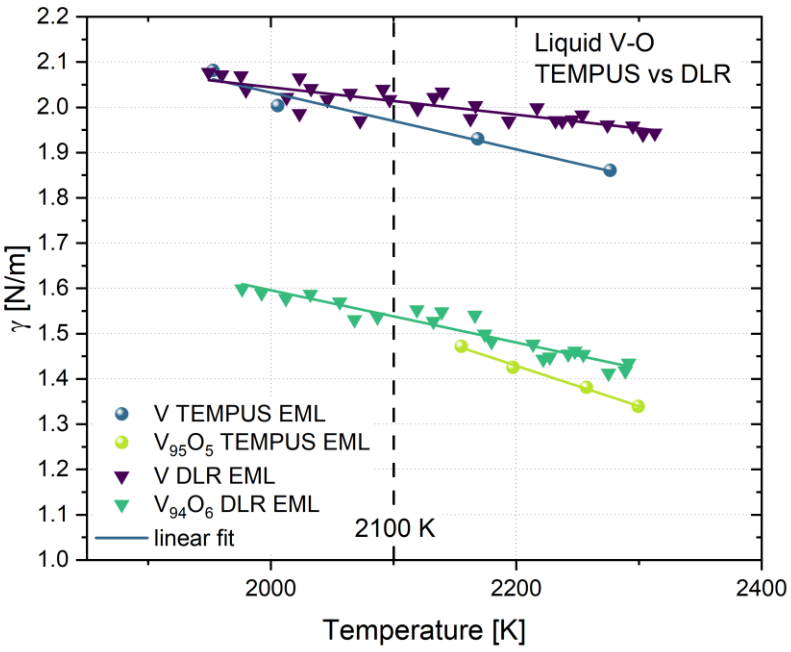

Figure 82: Surface tension versus the temperature measured for pure liquid vanadium and vanadium with 5 at.-% oxygen in the TEMPUS-EML facility in microgravity. The results are compared to measurements of pure vanadium and vanadium with 6 at.-% oxygen measured at the DLR-EML setup.

The similarities between Ti and V, when mixed with oxygen become apparent at first glance. For bulk oxygen atomic concentrations of up to ≈1 at.-%, the measured surface tension is equal to the surface tension measured for the pure elements at the corresponding temperature. The values measured in this work for the pure elements are included as dash-dotted horizontal lines. In both cases the surface tension decreases strongly when adding more than 1 at.-% oxygen. The measured data is well described by the model calculations including non-ideal interactions, while the ideal mixing approach underestimates the experimental data.

As discussed in Ref. [25], Figure 81 shows that for both titanium and vanadium a dissolution of oxygen in the liquid bulk is favored, while the segregation of oxygen is suppressed. Compared to other pure metals [41, 125] comparably large amounts of oxygen are needed to effectively reduce the surface tension of liquid titanium and vanadium.

Similar to this work, Ref. [25] also included surface tension measurements for pure liquid titanium in dependence of the oxygen partial pressure. There, no substantial influence of the oxygen partial pressure on the surface tension could be observed. In an explanatory attempt, it was assumed that the liquid samples are not in equilibrium when processed in the DLR-EML and therefore not enough oxygen can be transported into the process atmosphere by the OCS to effectively change the surface oxygen concentration and subsequently the surface tension. This assumption matches very well with the oxygen partial pressure course for liquid vanadium observed in Figure 72 and the surface tension measured in Figure 70 and Figure 71. A time of over 1 hour is needed to reach a constant oxygen partial pressure measured by the sensor unit, which proves that the sample is not in equilibrium. After starting the partial pressure control, the partial pressure measured by the sensor only increases after the pumping unit introduces a partial pressure of 10^{-6} bar into the process chamber, which matches with the point in Figure 70 where the surface tension starts to lightly decrease. This is a first difference between vanadium and titanium. While for Ti no change in surface tension was evident with regards to the experimental accuracy [25] when changing the oxygen partial pressure, for V a starting decrease in surface tension could be seen. This ‘onset’ of the surface tension decrease might be corresponding to the starting

decrease in surface tension for samples containing 1 at.-% oxygen observed in Figure 81. For liquid vanadium this indicates, that the OCS effectively changes the bulk oxygen, as well as the surface oxygen concentration. However, due to the relatively small oxygen pumping capability of the OSC in relation to the chamber volume this would entail very long pumping times.

With this, an experimental connection of the surface tension, the partial pressure and the bulk oxygen mole fraction can become possible. The results shown in Figure 75 and Figure 77 establish an experimental design to achieve the connection. Above a bulk oxygen atomic concentration of 6 at.-% a dependence of the surface tension from the oxygen partial can be observed that resembles the general course of the surface tension in dependence of the bulk oxygen mole fraction. This indicates, that some sort of oxygen solubility threshold is reached for high bulk oxygen mole fractions. Above this threshold oxygen pumped into the atmosphere is not dissolved into the sample bulk but segregates to the surface and thus reduces the surface tension. The surface oxygen mole fraction is therefore dependent on the oxygen partial pressure of the surrounding atmosphere and the bulk oxygen mole fraction.

The model calculations included in Figure 81 are an attempt to predict this dependence. For these calculations the Butler model introduced in sec. 2.3.1 and 2.3.2 was expanded to the Ti-O system and the V-O system respectively. In the case of the ideal mixture the Langmuir-isotherm [53] is combined with the Conventional Butler model to calculate the oxygen coverage (the oxygen concentration in the surface). In the non-ideal case, additional energy barriers for the movement of metal or oxygen atoms from the surface to the bulk and vice versa need to be considered. These energy barriers correspond to the excess free energies of oxygen. For the Ti-O system these free energies can be calculated when assuming that only TiO_2 'associate' species are present for the Ti-O system. The resulting Butler equation can then be solved to any combination of surface tension, oxygen coverage, bulk oxygen mole fraction and oxygen partial pressure. In Figure 81 this would translate to a specific oxygen partial pressure for each point on the solid lines, in Figure 77 the model would predict a singular line on the measured plain.

For the Ti-O system the assumption of only one TiO_2 species is reasonable, but for the V-O system four different possible associate species can form (see section 2.4.1). This complexity drastically increases the modeling effort drastically. The solid line in Figure 81 represents a first attempt in modeling which species is present in which quantity and subsequently solving the corresponding Butler-equation system introduced in section 2.4.1. The model is labeled 'preliminary' since an extensive modeling was not possible in the timeframe of this work. Instead, an approximation has been developed only considering one oxide associate (VO), estimated based on the total oxygen mole fraction, in the V-O system. Subsequently the monoatomic model described in section 2.4.1 was applied to the resulting system regarding only a single excess energy following Ref. [64]. This concept underlying the approximate model itself is still debatable [63] and the algorithm used for its solution is far from optimized. Nevertheless, is the model reproducing the experimental data for both liquid titanium and liquid vanadium remarkably well. It thereby lends itself to be a reasonable starting point for further evaluation and interpretation. Simultaneously, more in depth modeling, which would by far exceed the limits of this work, is needed.

Figure 83 shows the oxygen partial pressure measured by the sensor unit as a function of time for all samples with different bulk oxygen mole fractions. All samples show a very similar pO_2 trend, with the equilibrium partial pressure being almost identical for all compositions investigated at 7.5^{-10} bar. The observed equilibrium oxygen partial pressure is very close to the equilibrium oxygen partial pressure reported in the Ellingham diagram [62] for the $\frac{4}{3}V+O_2 \leftrightarrow \frac{2}{3}V_2O_3$ reaction which is 6.7^{-10} bar. This forms quite a contrast to the considerations previously done. With the model it would be predicted, that each composition shows a different equilibrium oxygen partial pressure. So far, no distinct explanation could be found why all compositions show the same equilibrium partial pressure that would be expected for pure vanadium.

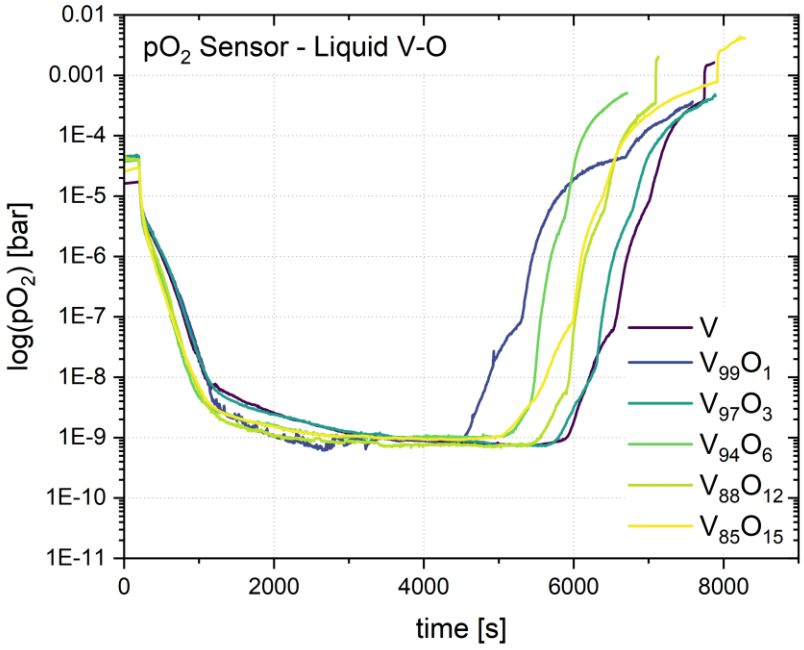

Figure 83: Oxygen partial pressure measured by the OCS sensor unit as a function of time measured during the surface tension measurements of vanadium samples with different bulk oxygen concentrations. Each curve corresponds to a single surface tension measurement depicted in Figure 75.

The results in Figure 83 show how hard it is to connect all the different parameters when investigating the influence of oxygen on the surface tension both experimentally and in model calculations.

The same becomes even more evident when evaluating the temperature dependent OCS measurements reported in Figure 79 and Figure 80. The adsorption of oxygen can not only drastically reduce the surface tension of a liquid metal but can also change the temperature coefficient and even change the sign of the temperature coefficient [36]. In these cases, a 'boomerang' or 'elbow' shape is observed when plotting the surface tension over the temperature [127]. The experimental setup created during the course of this work provides a great tool for the investigation of such temperature dependent phenomena since it is possible to measure surface tension, temperature and oxygen partial pressure simultaneously. Figure 84 three dimensionally summarizes the temperature dependent OCS measurements shown section 4.5.3. It becomes evident, that the temperature coefficient of the surface tension does not change significantly with temperature for all investigated samples. Furthermore, there is only a minor difference in the temperature coefficient for the different oxygen mole fractions. As shown in Figure 85, the temperature coefficient changes between $2.25 \cdot 10^{-4}$ N m^{-1}K^{-1} (for $V_{88}O_{12}$) and $4.24 \cdot 10^{-4}$ N m^{-1}K^{-1} (for $V_{97}O_3$) and does not follow a distinct trend. This matches very well with previous investigations that suggest that the oxygen influence on the temperature coefficient becomes less apparent with low oxygen partial pressure [36]. This fits well with the low oxygen partial pressure ($\approx 10^{-9}$ bar) observed during the measurements.

Even though no clear trend is observed, a more elaborate investigation of the temperature coefficient in the liquid V-O is highly interesting. Most works [128, 129] connect a change in the sign of the temperature coefficient for the surface tension to a large difference in the surface tension of the components of a system. The results show, that this is also the case for the V-O system. Yet no significant change in the temperature coefficient becomes apparent. At the same time, the general agreement [128] is that, if a change in temperature coefficient is present, it will decrease with increasing temperature. Figure 84 shows that, in the current setup, only a relatively high temperature range is experimentally available (T_l-50<T<T_l+100 K). Further setup modifications could make a wider

temperature range available. Possible changes in the temperature coefficient could be become more prominent at lower temperatures. Since some works [130, 131] connected the change in the temperature coefficient sign to segregation effects, while others [132] attributed it to a so-called ‘surface phase transition line’ it would be highly rewarding to investigate the temperature coefficient of V-O at lower temperatures. The great benefit would thereby be, that the temperature coefficient can not only be determined in relation to the temperature and bulk oxygen mole fraction but also in relation to the oxygen partial pressure.

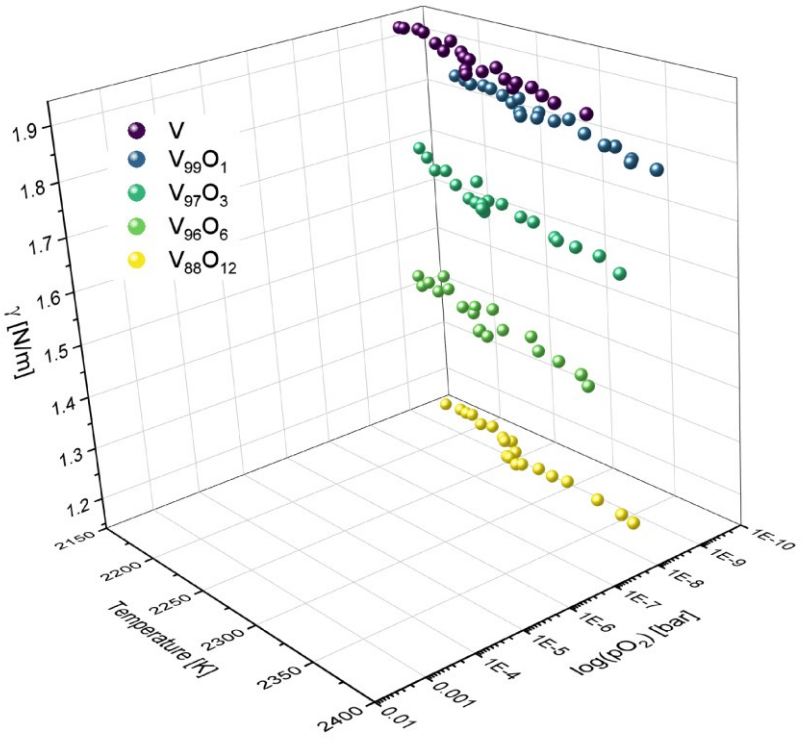

Figure 84: Surface tension, temperature and oxygen partial pressure of liquid vanadium containing different amounts of oxygen.

In the same work, [36], the surface tension of pure molten silver is modeled in dependence of both the temperature and surface tension. Figure 86 shows the results taken from Ref. [36]. With the scaling of Figure 84 chosen to roughly match the scaling of the model, it can be seen that both show the same general trend for pure liquid vanadium. This suggests, that the temperature coefficient is depending more on the oxygen partial pressure of the process atmosphere than on the bulk oxygen mole fraction.

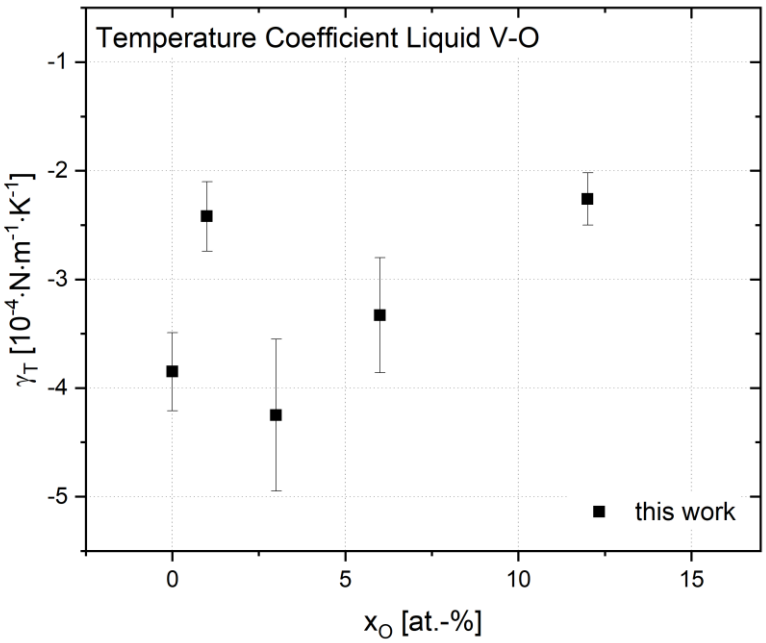

Figure 85: Temperature coefficient, γ_T, as function of the bulk oxygen mole fraction for the liquid V-O system.

A comparison of both graphs also shows the experimental potential of the EML setup built in this work. By extending the experimental work and varying the oxygen partial pressure during the experiment it could be possible to experimentally map the thermodynamic model shown in Figure 86 in a single experiment.

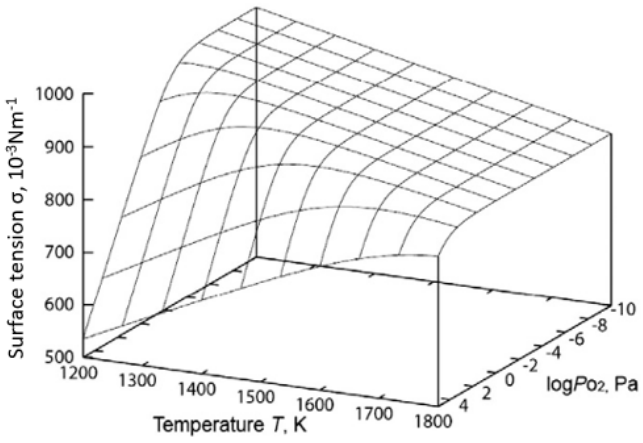

Figure 86: Three-dimensional map of surface tension, temperature and pO_2 for molten silver. The figure is taken from Ref. [36].

Current investigations revolve around refining the model calculations drafted in this work based on the experimental procedures designed in this work. Additionally, metallographic investigations are currently ongoing to analyze the sample condition in dependence of the processing route.

5. Conclusion

The results for liquid vanadium under the influence of oxygen, which conclude the experimental investigations of this work, close the circle back to the first of three research goals proposed in this work. A systematic thermophysical database was established for the Al-Ti-V system by providing density and surface tension data. The foundation therefore was laid by measurements on the pure components. On this basis the reliability of the EML measurement methods were validated by contextualizing the results for the pure elements with already existing literature data. Subsequently, all binary sub-systems were investigated following the same systematical approach. Finally, a representative section through the ternary system was investigated. Together with previously existing data [13, 26] a systematical database, including temperature dependent data for density and surface tension for over 40 different liquid alloys in the Al-Ti-V system, was created. The reliability of this database was then validated in the context of possible oxygen influence to enable the use as reference data or input for following research. In this way the first core part of this work, establishing a reliable, comprehensive and systematical database, could successfully be completed.

Building on that core part, different models for the thermophysical properties were established, first for the binary sub-systems and later for the ternary section through the Al-Ti-V system. Establishing these models serves two different goals. First, the mathematical models fill the gaps in the experimentally generated database. Combining models with experimental data, comprehensive temperature and compositional dependent databases can be produced. Second, the thermodynamic models hold diverse information on the mixing behavior of the different systems.

For the Ti-V system no significant excess volume was observed, which leads to the assumption of an ideal mixing behavior of Ti-V caused by their close proximity in the periodic table and the resulting similarities. This hypothesis was later confirmed by the results for the surface tension. This situation changes when mixing aluminum and vanadium. For the liquid Al-V, a highly non-ideal behavior was observed in density and surface tension. Based on the different thermodynamical models, the surface segregation could be examined for the different systems. Expectedly, in all systems the component with the smaller surface tension segregates to the surface. The segregation behavior could be fit into already existing classifications [14] based on the excess free energy ${}^{E}G$. For Ti-V the segregation follows the trend predicted for a linear mixing, which the surface enriching with Ti, following the trend of many other titanium containing alloy systems. For Al-V less aluminum segregation as predicted for an ideal system is evident. Additionally, the segregation behavior, as well as the overall mixing behavior, is very similar regarding their deviation from the ideal mixing behavior for Al-Ti and Al-V further strengthening the assumption of an exchangeability of titanium and vanadium when mixed with aluminum.

These results were then transferred to the ternary system based on the $Al_xTi_{(1-x)0.5}V_{(1-x)0.5}$ section. The main question here was if the thermophysical properties of the ternary system could be calculated solely from its binary sub systems, or if a ternary contribution needs to be considered. Both for the density and for the surface tension it was shown, that the experimental data is best described by models considering a ternary contribution. The mathematical descriptions underlying the respective models hint towards a possible change in surface atom coordination moving from the binary to the ternary system. The latter results show, that the 2nd core part and research goal of this work, understanding and predicting the mixing behavior of the Al-Ti-V system, could so be achieved for the binary sub-systems. In doing so a stable foundation for following investigations in the ternary system was created. Further investigations are needed to confirm that the observations for the $Al_xTi_{(1-x)0.5}V_{(1-x)0.5}$ section are transferable to the complete ternary system.

The 3rd and last goal of this research was to establish an experimental framework to investigate the oxygen influence on the thermophysical properties of liquid metals and carry out first investigations on liquid vanadium in the context of the Al-Ti-V system. By successfully integrating the OCS into the EML furnace an experimental platform was created that allows for container-less thermophysical property measurements in dependence of the oxygen partial pressure.

To begin with, it was shown how complex the measurement mechanism of the OCS is. The OCS is not comparable to an industrial available sensor system with precisely known measurement interactions. At the same time the high complexity of the systems enables many different experimental possibilities. Exemplary, two different operation modes in the titration and pumping mode were crafted and evaluated during EML measurements. With this, an experimental foundation for future EML investigation including the OCS was created. However, it was also shown that much more system-oriented research is needed regarding the OCS, especially considering a future use of a similar OCS system onboard the international space station. First considerations regarding buffer gas reactions showed how complex the OCS operation can be. A groundwork was laid on which parameters from process gas, leak rate or chamber conditioning need to be considered during the OCS operation. At the same time the operational potential of the OCS in combination with the EML was demonstrated, opening up a whole future research field of its own. Many future works can build on the fundamentals carved out in this work to establish the OCS, especially the OCS planned to be integrated into the ISS EML, in the scientific community. The first experimental implementation of the OCS into the EML framework shows just how complex the device is. This work has helped to identify some of the experimental conditions that need to be considered during an OSC process. Valuable insight in the interactions with the process atmosphere and possible buffer gas reactions, leak rates and temperature dependencies have been gained during the course of this work. All of these have been evaluated before the background of an OCS operation during an EML experiment. With the experimental procedures developed first scientific reliable oxygen partial pressure dependent surface tension data could be obtained for liquid vanadium. With the preliminary model, a first step towards a reasonable interpretation of this data has been taken.

A first application of the OCS in EML measurements on liquid vanadium showed the enormous potential of the system. Five different parameters were experimentally connected: the surface tension, the oxygen partial pressure, the oxygen coverage, the temperature and the bulk oxygen concentration in one thermodynamic model. By creating a preliminary model an experimental framework could be created which can provide the data basis needed for such a modelling. The scientific potential enabled through the experimental framework is manifold. By successively expanding the oxygen centered investigations from the pure elements to the binary sub-systems, eventually the whole Al-Ti-V can be characterized.

The different parameter that were experimentally connected in the presented setup and a more fundamental understanding of the interaction of oxygen and liquid metals was gained. This was demonstrated using the example of pure liquid vanadium. Liquid vanadium shows a very similar interaction with oxygen as liquid titanium in previous investigations [25]. Present oxygen is predominantly dissolved in the sample bulk while it's segregation to the surface is suppressed. As a result, the surface tension of liquid vanadium and titanium is unaffected up to comparably high oxygen atomic concentrations of about 1 at.-%. This forms a contrast to many other liquid metals [41] amongst others aluminum [126] which shows a significant decrease in surface tension for very small oxygen mole fractions already. In the context of the Al-Ti-V system this suggests, that the surface oxygen state of ternary alloys might change as a function of temperature and composition. It is therefore highly interesting to apply the experimental procedure introduced in this work onto ternary Al-Ti-V to further investigate a possible change in surface oxygen interaction. The EML-OCS setup of this work provides the experimental data needed. The EML-OCS setup provides even more experimental possibilities which have not been fully exhausted in this work. An example for this was given by the temperature dependent measurements. The addition of the heating laser to the setup allowed to conduct temperature dependent measurements including the OCS. With this addition many more experimental paths became possible.

6. Outlook

As for most meaningful research, laying a sound foundation for future research is the core of many goals proposed in this work. With the successful achievement of these goals it is now reasonable to take a closer look at these investigations of which some are already being pursued.

The most obvious continuation of this work is the expansion towards the Al-Ti-V system. This work provided a first insight into the general mixing behavior of the ternary system. More comprehensive data can be obtained by simply expanding this work onto different alloy compositions. This can have both high fundamental and practical use. A larger data base is vital for the understanding of the mixing behavior of the complete Al-Ti-V alloy system, while more data simultaneously increases the quality of thermodynamic models used to improve the performance of all sorts of industrial foundry or manufacturing processes. The systematical investigations on the binary sub-systems provided in this work thereby greatly benefits the interpretation of future ternary alloy data.

However, by far the largest opportunity for future research is provided by the successful implementation of the OCS into the EML setup. As already mentioned in the respective result sections, further applications for the OCS are manifold. Based on the results of this work more facility studies are possible. This is especially interesting in the context of microgravity EML experiments onboard the International Space Station (ISS). The DLR-EML with the implemented OCS offers an easily accessible and reliable experimental platform. As shown for the TEMPUS-EML experiments presented in this work, microgravity experiments greatly benefit from complementary ground-based research. The high precision of microgravity experiments comes with the cost of the extremely high experimental effort. A ground-based facility is therefore the perfect addition in order to achieve significant science. The DLR-EML and the results of this work offer a great starting position in order to achieve an optimal application of the OCS that will expand the ISS-EML in the near future. The results of this work help interpreting obtained data as well as identify experimental potential of science utilizing the ISS-EML.

Regarding ground-based research, the potential of the OCS is far from being exhausted. Especially, temperature dependent measurements including the OCS are currently planned. By experimentally connecting surface tension, oxygen partial pressure, oxygen mole fraction and temperature the interaction mechanisms between oxygen and liquid metals can be better understood. The current optimization of the thermodynamic model applied to the V-O system pursues the same goal. Collaborations with modelling experts will hopefully allow for the development of even better prediction tools which are not only interesting for fundamental science but could potentially also have great practical use. Metallographic investigations on the processed samples are currently being carried out. Combing these, while simultaneously expanding the database can help understanding the behavior of oxygen inside the liquid sample.

In the process of achieving the goals of this work many highly interesting research possibilities can been identified. Mentioned here are only the paths that are currently pursued and result immediately from this work. This work only scratches the surface in understanding the interactions between oxygen and liquid metals but in doing so lays a solid foundation for future research inching closer to a true understanding.

References

[1] A. Wilson, The Living Rock, Cambridge, England: Woodhead Publishing Limited, 1994.

[2] D. Raabe, C. C. Tasan and E. A. Olivetti, "Strategies for improving the sustainability of structural metals," *Nature,* no. 575, pp. 64-74, 2019.

[3] S.-Y. Sung and Y.-J. Kim, "Modeling of titanium aluminides turbo-charger casting," *Intermetallics,* vol. 15, pp. 468-474, 2007.

[4] Q. Wang, W. Zhang, S. Li, M. Tong, W. Hou, H. Wang, Y. Hao, N. M. Harriso and R. Yang, "Material Characterisation and Computational Thermal Modelling of Electron Beam Powder Bed Fusion Additive Manufacturing of Ti2448 Titanium Alloy," *materials,* vol. 14, pp. 1-23, 2021.

[5] E. Flender and J. Sturm, "Thirty years of casting process simulation," *International Journal of Metalcasting,* pp. 7-23, 2010.

[6] M. J. Donachie, Titanium A Technical Guide, Novelty: ASM International, 2000.

[7] M. Peters, J. Kumpfert, C. H. Ward and C. Leyens, "Titanium Alloys for Aerospace Applications," *Advanced Engineering Materials,* no. 6, pp. 419-427, 2003.

[8] H. Rack and J. Qazi, "Titanium alloys for biomedical applications," *Materials Science and Engineering,* pp. 1269-1277, 2006.

[9] D. R. Sumner and J. O. Galante, "Determinants of Stress Shielding: Design Versus Materials Versus Interface," *Clinical Orthopaedics and Related Research,* pp. 1976-2007, 1992.

[10] V. S. D. Herzog, E. Wycisk and C. Emmelmann, "Additive manufacturing of metals," *Acta Materialia,* pp. 371-392, 2016.

[11] T. Zhang and C. Liu, "Design of titanium alloys by additive manufacturing: A critical review," *Advanced Powder Materials,* pp. 1-11, 2022.

[12] L. Goumiri, J. Joud, P. Desre and J. Hicter, "Tensions superficielles d'alliages liquides binaires présentant un caractère dimmiscibilité: Al-Pb, Al-Bi, Al-Sn et Zn-Bi," *Surface Science,* pp. 471-486, 1979.

[13] J. J. Wessing and J. Brillo, "Density, Molar Volume, and Surface Tension of Liquid Al-Ti," *The Minerals, Metals & Materials Society and ASM International,* vol. 48, pp. 898-882, 2016.

[14] J. Brillo, Thermophysical properties of multicomponent liquid alloys, Berlin/Boston: Walter de Gruyter GmbH, 2016.

[15] J. Brillo and G. Kolland, "Surface tension of liquid Al-Au binary alloys," *J. Mater. Sci.,* 2016.

[16] M. Leitner, T. Leitner, A. Schmon, K. Aziz and G. Pottlacher, "Thermophysical Properties of Liquid Aluminum," *Metallurgical and Materials Transactions A,* pp. 3036-3045, 2017.

[17] E. S. Levin, D. Ayushina and G. P., "Density and surface-energy polytherms of liquid (molten) aluminum," *High Temperature 6,* no. 3, p. 416, 1968.

[18] T. Ishikawa, P.-F. Paradis, T. Itami and S. Yoda, "Non-contact thermophysical property measurements of refractory metals using an electrostatic levitator," *Measurement Science and Technology,* vol. 16, pp. 443-451, 2005.

[19] G. Pottlacher, High Temperature Thermophysical Properties of 22 Pure Metals, Graz: edition keiper, 2010.

[20] T. Saito, Y. Shiraishi and Y. Sakuma, "Density Measurement of Molten Metals by Levitation Technique at Temperatures between 1800°C and 2200°C," *Transactions of the Iron and Steel Institute of Japan,* no. 2, pp. 118-126, 1969.

[21] K. Thurnay, "Thermal Properties of Transition Metals," Forschungszentrum Technuk und Umwelt, Karlsruhe, 1998.

[22] B. Reiplinger and J. Brillo, "Density and excess volume of the liquid Ti–V system measured in electromagnetic levitation," *Journal of Material Science,* pp. 1-11, 2022.

[23] B. Reiplinger, Y. Plevachuk and J. Brillo, "Surface tension of liquid Ti, V and their binary alloys measured by electromagnetic levitation," *Journal of Materials Science,* pp. 21828-21840, 2022.

[24] J. T. Okada, T. Ishikawa, Y. Watanabe and P.-F. Paradis, "Surface tension and viscosity of molten vanadium measured with an electrostatic levitation furnace," *J. Chem. Thermodynamics,* no. 42, pp. 856-859, 2010.

[25] J. Brillo, J. Wessing, H. Kobatake and H. Fukuyama, "Surface tension of liquid Ti with adsorbed oxygen and its prediction," *Journal of Molecular Liquids,* pp. 1-12, 2019.

[26] J. J. Wessing, "Thermophysical properties of liquid Al-Ti alloys under the influence of oxygen," *Doctoral dissertation, RWTH Aachen Chair for Foundry Science and Foundry Institute,* 2018.

[27] R. Novakovic, D. Giuranno, E. Ricci, A. Tuissi, R. Wunderlich, H. Fecht and I. Egry, "Surface, dynamic and structural properties of liquid Al–Ti alloys," *Applied Surface Science,* vol. 258, no. 7, pp. 3269-3275, 2012.

[28] M. Mohr, R. Wunderlich, R. Novakovic, E. Ricci and H. Fecht, "Precise Measurements of Thermophysical Properties of Liquid Ti–6Al–4V (Ti64) Alloy On Board the International Space Station," *Advanced Engineering Materials,* no. 22, pp. 1-10, 2020.

[29] I. Egry, D. Holland-Moritz, R. Novakovic, E. Ricci, R. Wunderlich and N. Sobczak, "Thermophysical Properties of Liquid AlTi-Based Alloys," *International Journal of Thermophysics,* no. 31, pp. 949-965, 2010.

[30] H. Fukuyama and Y. Waseda, High Temperature Measurements of Materials, Berlin: Springer, 2009.

[31] B. J. Keene, "Review of data for the surface tension of pure metals," *International Materials Reviews,* vol. 4, no. 38, pp. 157-192, 1993.

[32] B. C. Allen, "The Surface Tension of Liquid Transition Metals at their Melting Points," *Trans. AIME,* no. 227, p. 1175, 1963.

[33] I. Egry, A. Diefenbach, W. Dreier and J. Piller, "Containerless Processing in Space Thermophysical Property Measurements using Electromagnetic Levitation," *International Journal of Thermophysics,* vol. 22, p. 569–578, 2001.

[34] D. Herlach and D. Matson, Solidification of Containerless Undercooled Melts, Weinheim: Wiley-VCH, 2012.

[35] C. Notthoff, H. Franz, M. Hanfland, D. Herlach, D. Holland-Moritz and W. Petry, "Electromagnetic levitation apparatus for investigations of the phase selection in undercooled melts by energy-dispersive x-ray diffraction," *Review of scientific instruments,* pp. 3791-3796, 2000.

[36] I. Egry, E. Ricci, R. Novakovic and S. Ozawa, "Surface tension of liquid metals and alloys - Recent developments," *Advances in Colloid and Interface Science,* pp. 198-212, 2010.

[37] L. Goumirir and J. Joud, "Auger electron spectroscopy study of aluminium-tin liquid system," *Acta Metallurgica,* pp. 1397-1405, 1982.

[38] R. Murarka, W. Lu and A. Hamielec, "Effect of dissolved oxygen on the surface tension of liquid iron," *The Canadian Journal of Metallurgy and Materials Science ,* 1975.

[39] A. Kasama, A. McLean, W. Miller, Z. Morita and M. Ward, "Surface Tension of Liquid Iron and Iron-Oxygen Alloys," *The Canadian Journal of Metallurgy and Materials Science ,* pp. 9-17, 1983.

[40] B. Gallois and C. Lupis, "Effect of Oxygen on the Surface Tension of Liquid Copper," *Metallurgical Transactions B,* pp. 549-557, 1981.

[41] M. Abbasi, J. Lee, M. Shin, Y. Kim and Y. Kang, "Effect of oxygen adsorption on surface tension of liquid copper: Experiments and thermodynamic models," *Applied Surface Science,* pp. 116-122, 2014.

[42] V. Agarwala and T. Fort, "Nature of the stable oxide layer formed on an aluminum surface by work function measurements," *Surface Science,* pp. 60-70, 1976.

[43] E. Yousefi, Y. Sun, A. Kunwar, M. Guo, N. Moelans and D. Seveno, "Surface tension of aluminum-oxygen system: A molecular dynamics study," *Acta Materialia,* pp. 1-12, 2021.

[44] L. Beyanchikov, *Russian Metallurgy,* pp. 1156-1163, 2010.

[45] R. Boyer, G. Welsch and E. Collings, Materials Properties Handbook: Titanium Alloys, ASM Internatinal, 1994.

[46] D. A. Porter, K. E. Easterling and M. Y. Sherif, Phase Transformations in Metals and Alloys, 3 ed., T. a. F. Group, Ed., Boca Raton: CRC Press, 2009.

[47] H. Baehr, Thermodynamik, Berlin: Springer, 2002.

[48] R. Schmid-Fetzer and J. Gröbner, "Focused Development of Magnesium Alloys Using the Calphad Approach," *Advanced Engineering Materials,* pp. 947-961, 2001.

[49] K. Mukai, Interfacial Physical Chemistry of High-Temperature Melts, Boca Raton: CRC Press, 2020.

[50] R. K. Dadashev, Thermodynamics of Surface Phenomena, Cambridge: Cambridge International Science Publishing, 2008.

[51] E. Guggenheim, "The Principle of Corresponding States," *The Journal of Chemical Physics,* pp. 253-261, 1945.

[52] G. Kaptay, "Extension of the Gibbs-Duhem relation to partial molar surface thermodynamic properties of solutions," *Langmuir,* 2022.

[53] G. Kaptay, "The partial surface tension of components of a solution," *Langmuir,* vol. 31, pp. 5796-5804, 2015.

[54] T. Tanaka and T.Iida, "Application of a thermodynamic database to the calculation of surface tension for iron-base liquid alloys," *Steel Research International,* no. 65, pp. 21-28, 1994.

[55] I. Egry, "Surface tension of compound forming liquid binary alloys: A simple model," *Journal of Material Science,* no. 39, pp. 6365-6366, 2004.

[56] E. Ricci, E. Arato, A. Passerone and P. Costa, "Oxygen tensioactivity on liquid-metal drops," *Advances in Colloid and Interface Science,* pp. 15-32, 2005.

[57] R. Gasser and G. Ehrlich, An introduction to chemisorption and catalysis by metals, Oxford university Press, 1987.

[58] H.-D. Dörfler, Grenzflächen und kolloid-disperse Systeme: Physik und Chemie, Springer, 2002.

[59] G. R. Belton, "Langmuir adsorption, the Gibbs adsorption isotherm, and interfacial kinetics in liquid metal systems," *Metallurgical Transactions B,* pp. 35-42, 1976.

[60] K. Mukai, Z. Yuan, K. Nogi and T. Hibiya, "Effect of the OxygenPartial Pressure on the Surface Tension of Molten Silicon and Its Temperature Coefficient," *ISIJ International,* pp. 148-152, 2000.

[61] Massachusetts Institute of Technology, "web.mit.edu," [Online]. Available: https://web.mit.edu/2.813/www/readings/Ellingham_diagrams.pdf. [Accessed 18 07 2024].

[62] S. Seetharaman, Treatise on Process Metallurgy, Volume 1: Process Fundamentals, Oxfrod: Elsevier, 2013, p. 508.

[63] J. Brillo, J. Wessing, H. Kobatake and H. Fukuyama, "Surface tension of liquid Ti with adsorbed oxygen and a simple associate model for its prediction," *High Temperatures - High Pressures ,* pp. 89-105, 2019.

[64] Z. Cao, S. Li, W. Xie, G. Du and Z. Qiao, "Critical evaluation and thermodynamic optimization of the V–O system," *Calphad,* pp. 241-251, 2015.

[65] H. Okamoto, "Al-V (Aluminum-Vanadium)," *Journal of Phase Equilibria and Diffusion,* no. 33, p. 491, 2012.

[66] J. L. Murray, "The Ti-V (Titanium-Vanadium) system," *Bulletin of Alloy Phase Diagrams,* no. 2, pp. 48-55, 1981.

[67] H. Wriedt, "The O-V (Oxygen-Vanadium) System," *Bulletin of Alloy Phase Diagrams,* pp. 271-277, 1989.

[68] P. R. Rony, "The electromagnetic levitation of metals," in *Trans. Vacuum Met. Conference*, Boston, 1964.

[69] J. Brillo, G. Lohofer, F. Schmidt-Hohagen, S. Schneider and I. Egry, "Thermophysical property measurements of liquid metals by electromagnetic levitation," *International Journal of Materials and Product Technology,* 2006.

[70] G. Lohöfer, "Force and Torque of an electromagnetically levitated metal sphere," *Quarterly of Applied Mathematics,* pp. 495-518, 1993.

[71] G. Lohöfer, "Theory of an Electromagnetically Levitated Metal Sphere I: Absorbed Power," *SIAM Journal on Applied Mathematics,* pp. 567-581, 1989.

[72] W. Wien, "On the division of energy in the emission-spectrum of a black body," *The London, Edinburgh, and Dublin Philosophical Magazine and Journal of Science,* pp. 214-220, 1897.

[73] J. Brillo, I. Egry and I. Ho, "Density and Thermal Expansion of Liquid Ag–Cu and Ag–Au Alloys," *International Journal of Thermophysics,* vol. 27, pp. 494-506, 2006.

[74] S. Krishnan, G. P. Hansen, R. H. Hauge and J. L. Margrave, "Spectral emissivities and optical properties of electromagnetically levitated liquid metals as functions of temperature and wavelength," *High temperature science,* no. 29, pp. 17-52, 1990.

[75] J. Lee, D. M. Madson, S. Binder, M. Kolbe, D. Herlach and R. Hyers, "Magnetohydrodynamic Modeling and Experimental Validation of Convection Inside Electromagnetically Levitated Co-Cu Droplets," *The Minerals, Metals & Materials Society,* pp. 1018-1023, 2014.

[76] S. Sauerland, "Messung der Oberflächenspannung an levitierten flüssigen Metalltropfen".*Ph.-D. thesis (RWTH Aachen, Germany, 1993).*

[77] J. Priede and G. Gerbeth, "Oscillatory Instability of Electromagnetically Levitated Solid Bodies," *IEEE transactions on magnetics,* pp. 354-357, 2000.

[78] H.-J. Fecht and M. Mohr, Metallurgy in Space - Recent Results from ISS, The Minerals, Metals and Materials Society 2022, 2022.

[79] M. Schulz, J. Brillo, C. Stenzel and H. Fritze, "Oxygen partial pressure control for microgravity experiments," *Solid State Ionics,* pp. 332-336, 2012.

[80] G. Lohöfer, M. Beckers, T. Blumberg, D. Bräuer, S. Schneider, T. Volkmann and A. Meyer, "TEMPUS - A microgravity electromagnetic levitation facility for parabolic flights," *Paper appears in Rev. Sci. Instrum. (2024),* pp. 1-6, 2024.

[81] G. Lohöfer and J. Piller, "40th AlAA Aerospace Sciences Meeting and Exhibit," in *The new ISS Electromagnetic Levitation Facility: 'MSL-EML'*, Reno, NV, 2002.

[82] V. Pletser and J. Harrod, "The science of gravity: A new era of ESA experiments on parabolic flights," *ESA bulletin. Bulletin ASE. European Space Agency,* pp. 22-30, 2014.

[83] J. Brillo and I. Egry, "Density Determination of Liquid Copper, Nickel, and Their Alloys," *International Journal of Thermophysics,* no. 24, pp. 1155-1170, 2004.

[84] J. Brillo, T. Schumacher and K. Kajikawa, "Density of Liquid Ni-Ti and a New Optical Method for its Determination," *The Minerals, Metals & Materials Society and ASM International,* vol. 50, pp. 924-935, 2018.

[85] S. Amore, J. Horbach and I. Egry, "Is there a relation between excess volume and miscibility in binary liquid mixtures," *The Journal of Chemical Physics,* vol. 134, pp. 044515-(1-9), 2011.

[86] L. Soldi, A. Quaini, S. Gosse, J. Brillo and M. Roskosz, "Thermodynamic and thermophysical properties of Cu-Si liquid alloys," *High Temperatures - High Pressures,* vol. 49, pp. 155-171, 2020.

[87] L. Rayleigh, "On the conditions of instability of electrified drops," *Proc. Roy. Soc,* no. 29, pp. 71-83, 1879.

[88] J. Schmitz, "Untersuchung der Anisotropie im Benetzungsverhalten flüssiger Al-Cu Legierungen auf einkristallinen orientierten Al2O3-Substraten," *PhD thesis, RWTH Aachen ,* 2011.

[89] I. Egry, G. Lohöfer, I. Seyhan, S. Schneider and B. Feuerbach, "Viscosity and Surface Tension Measurements in Microgravity," *International Journal of Thermophysics,* no. 20, pp. 1005-1015, 1999.

[90] I. Egry, L. Ratke, M. Kolbe, D. Chatain, S. Curiotto, L. Battezzati, E. Johnson and N. Pryds, "Interfacial properties of immiscible Co–Cu alloys," *Journal of Materials Science,* pp. 1979-1985, 2010.

[91] D. L. Cummings and D. A. Blackburn, "Oscillations of magnetically levitated aspherical droplets," *Journal of Fluid Mechanics,* no. 224, pp. 395-416, 1991.

[92] F. Busse, "Oscillations of a rotating liquid drop," *Journal of Fluid Mechanics,* pp. 1-8, 1984.

[93] J. Brillo, G. Lauletta, L. Vaianella, E. Arato, D. Giuranno, R. Novakovic and E. Ricci, "Surface tension of liquid Ag-Cu binary alloys," *ISIJ International,* vol. 54, pp. 2115-2119, 2014.

[94] M. J. Assael and K. Kakosimos, "Reference Data for the Density and Viscosity of Liquid Aluminum and Liquid Iron," *Journal of Physical and Chemical Reference Data,* no. 35, pp. 285-300, 2006.

[95] J. Brillo, I. Egry and J. Westphal, "Density and thermal expansion of liquid binary Al – Ag and Al – Cu alloys," *International Journal of Materials Research,* vol. 2, no. 99, pp. 162-167, 2013.

[96] E. S. Levin, D. G. Ayushina and V. P. Geld, "Density and surface-energy polytherms of liquid (molten) aluminum," *High Temperature 6,* no. 3, p. 416, 1968.

[97] P. M. Smith, J. W. Elmer and G. F. Gallegos, "Measurement of the density of liquid aluminum alloys by an X-ray attenuation technique," *Scripta Materialia,* no. 40, pp. 937-941, 1999.

[98] V. Sarou-Kanian, F. Millot and J. C. Rifflet, "Surface Tension and Density of Oxygen-Free Liquid Aluminum at High Temperature," *International Journal of Thermophysics,* pp. 277-286, 2003.

[99] H. P. Wang, S. J. Yang and B. B. Wei, "Density and structure of undercooled liquid titanium," *Chinese Science Bulletin,* no. 57, pp. 719-723, 2012.

[100] P. F. Zou, H. P. Wang, S. J. Yang, L. Hu and B. Wei, "Density Measurement and Atomic Structure Simulation of Metastable Liquid Ti-Ni Alloys," *The Minerals, Metals & Materials Society,* no. 49, pp. 5488-5496, 2018.

[101] G. Pottlacher, High Temperature Thermophysical Properties of 22 Pure Metals, Graz: Edition Keiper, 2019.

[102] S. Ozawa, Y. Kudo, K. Kuribayashi, Y. Watanabe and T. Ishikawa, "Precise Density Measurement of Liquid Titanium by Electrostatic," *Materials Transactions,* no. 58, pp. 1664-1669, 2017.

[103] P.-F. Paradis and W.-K. Rhim, "Non-contact measurements of thermophysical properties of titanium at high temperature," *The Journal of Chemical Thermodynamics,* vol. 32, pp. 123-133, 2000.

[104] E. Ntonti, S. Sotiriadou, M. J. Assael, M. L. Huber, B. Wilthan and M. Watanabe, "Reference Correlations for the Density and Thermal Conductivity, and Review of the Viscosity Measurements, of Liquid Titanium, Zirconium, Hafnium, Vanadium, Niobium, Tantalum, Chromium, Molybdenum, and Tungsten," *International Journal of Thermophysics ,* pp. 1-40, 2024.

[105] V. Raghavan, "Al-Ti-V (Aluminum-Titanium-Vanadium)," *Journal of Phase Equilibria and Diffusion,* pp. 276-279, 2005.

[106] S. Amore, S. Delsante, H. Kobatake and J. Brillo, "Excess volume and heat of mixing in Cu-Ti liquid mixture," *The Journal of Chemical Physics,* vol. 139, pp. 064504-(1-6), 2013.

[107] M. Watanabe, M. Adachi, M. Uchikoshi and H. Fukuyama, "Densities of Pt–X (X: Fe, Co, Ni and Cu) binary melts and thermodynamic correlations," *Fluid Phase Equilibria,* vol. 515, pp. 112596-(1-11), 2020.

[108] M. Watanabe, M. Adachi and H. Fukuyama, "Densities of Fe–Ni melts and thermodynamic correlations," *Journal of Materials Science,* vol. 51, pp. 3303-3310, 2015.

[109] J. Brillo, M. Watanabe and H. Fukuyama, "Relation between excess volume, excess free energy and isothermal compressibility in liquid alloys," *Journal of Molecular Liquids,* vol. 326, pp. 114395 1-35, 2021.

[110] A. Kostov and D. Živković, "Thermodynamic analysis of alloys Ti–Al, Ti–V, Al–V and Ti–Al–V," *Journal of Alloys and Compounds,* vol. 160, pp. 164-171, July 2008.

[111] Y. Plevachuk, I. Egry, J. Brillo, D. Holland-Moritz and I. Kaban, "Density and atomic volume in liquid Al–Fe and Al–Ni binary alloys," *International Journal of Materials Research,* no. 98, pp. 107-1011, 2013.

[112] J. Brillo, R. Brooks and I. Egry, "Density and viscosity of liquid ternary Al-Cu-Ag alloys," *High Temperatures - High Pressures,* pp. 371-381, 2008.

[113] H. Kobatake, J. Brillo and J. Schmitz, "Density and viscosity of ternary Al–Cu–Si liquid alloys," *Journal of Materials Science ,* pp. 3541-3549, 2014.

[114] K. Zhou, H. Wang, J. Chang and B. Wei, "Experimental study of surface tension, specific heat and thermal diffusivity of liquid and solid titanium," *Chemical Physics Letters,* pp. 105-108, 2015.

[115] P.-F. Paradis, T. Ishikawa, G.-W. Lee, D. Holland-Moritz, J. Brillo, W.-K. Rhim and J. T. Okada, "Materials properties measurements and particle beam interactions studies using electrostatic levitation," *Materials Science and Engineering: R: Reports,* vol. 76, pp. 1-53, 2014.

[116] S. Amore, J. Brillo, I. Egry and R. Novakovic, "Surface tension of liquid Cu–Ti binary alloys measured by electromagnetic levitation and thermodynamic modelling," *Applied Surface Science,* pp. 7739-7745, 2011.

[117] H. M. Lu and Q. Jiang, "Surface Tension and Its Temperature Coefficient for Liquid Metals," *The Journal of Physical Chemistry B,* pp. 15463-15468, 2005.

[118] I. Ansara, A. T. Dinsdale and M. H. Rand, COST 507: Thermochemical database for light metal alloys. Vol.2, 2 ed., Office for Official Publications of the European Communities, 1998, pp. 297-299.

[119] B. Lindahl, X. Liu, Z. Liu and M. Selleby, "A thermodynamic re-assessment of Al–V toward an assessment of the ternary Al–Ti–V system," *Calphad,* no. 51, pp. 75-88, 2015.

[120] G. Kaptay, "An improved derivation of the Butler equations for surface tension of solutions," *Langmuir,* no. 33, p. 10987–10992, 2019.

[121] X. Lu, N. Gui, A. Qiu, G. Wu and C. Li, "Thermodynamic Modeling of the Al-Ti-V Ternary System," *The Minerals, Metals & Materials Society and ASM International 2014,* pp. 4155-4164, 2014.

[122] T. Tanaka, K. Hack and T. Iida, "Application of Thermodynamic Databases to the Evaluation of Surface Tensions of Molten Alloys, Salt Mixtures and Oxide Mixtures," *Zeitschrift für Metallkunde,* pp. 380-389, 1996.

[123] C.Benvenuti and P.Chiggiato, "Pumping characteristics of the St707 nonevaporable getter (Zr 70 V 24.6-Fe 5.4 wt %)," *Journal of Vacuum Science & Technology A Vacuum Surfaces and Films,* 1996.

[124] E. Ricci, A. Passerone and J. Joud, "Thermodynamic study of adsorption in liquid metal-oxygen systems," *Surface Science,* pp. 533-553, 1988.

[125] H. Kobatake, J. Brillo, J. Schmitz and P. Pichon, "Surface tension of binary Al–Si liquid alloys," *Journal of Materials Science,* pp. 3351-3360, 2015.

[126] J. Molina, R. Voytovych, E. Louis and N. Eustathopoulos, "The surface tension of liquid aluminium in high vacuum: The role of surface condition," *International Journal of Adhesion and Adhesives,* pp. 394-401, 2007.

[127] X. Xiao and J. Brillo, "Surface tension of liquid Fe-Ni, Fe-Cr, and Ni-Cr with physics-informed statistical modeling on the influence of oxygen content," *Journal of Molecular Liquids,* 2022.

[128] M. Soledade, C. Santos, J. Carlos and R. Reis, "Surface tension of liquid mixtures and metal alloys. Thermodynamic conditions for the occurrence of a positive temperature coefficient," *Journal of Alloys and Compounds,* pp. 1-11, 2021.

[129] I. Egry, "The Surface Tension of Binary Alloys: Simple Models for Complex Phenomena," *International Journal of Thermophysics,* pp. 931-939, 2005.

[130] P. Desre and J. Joud, "Surface tension temperature coefficient of liquid alloys and definition of a "zero marangoni number alloy" for crystallisation experiments in microgravity environment," *Acta Astronautica,* pp. 407-415, 1981.

[131] J. Lee, W. Shimoda and T. Tanaka, "Surface Tension and its Temperature Coefficient of Liquid Sn-X (X=Ag, Cu) Alloys," *Materials Transactions,* pp. 2864-2870, 2004.

[132] G. Kaptay and C. Mekler, "Calculation of surface tension and surface phase transition line in binary Ga-Tl system," *Materials Science and Engineering A,* pp. 65-69, 2008.